Structural Studies of Surfaces and Interfaces by Scanned-Angle X-ray Photo-Electron Diffraction.

by

Michael A. Gleeson, B.Sc. (Hons.)

A Thesis presented to Dublin City University for the degree of Doctor of Philosophy.

This work was carried out under the supervision of Dr. Colin Barnes, School of Chemical Sciences, at Dublin City University.

September, 1996

I hereby certify that this material, which I now submit for assessment on the program of study leading to the award of Ph.D. is entirely my own work and has not been taken from the work of others save and to the extent that such work has been cited and acknowledged within the text of my work.

Signed : Michael Gleeson **ID No. :** 92700250

MICHAEL GLEESON

Date : 26/9/96

ACKNOWLEDGEMENTS:

I wish to thank my supervisor, Dr. Colin Barnes, for his help and guidance during this work.

I would also like to express my gratitude to:

my fellow postgraduate students and the academic and technical staff in the School of Chemical Sciences at DCU.

Dr. Peijun Hu (Queens University, Belfast) and Prof. Marco Torinni (University of Florence, Italy), for the provision of single scattering cluster calculation programs.

Dr. Mark Newton for the provision of the experimental XPD data, measured from the CuPd [85:15] {110} bulk alloy, which was analysed in chapter VI.

The members of the physics department at the Technical University of Tampere, especially Janne Aaltonen for helping me drink Leipzig dry.

The members of the surface science group at the chemistry department of the University of Florence, especially Andrea Atrei and Ugo Bardi for three memorable collaborations.

The members of my laboratory group, Caroline, Jim and the transients, Sinead, Santiago and Steffi, for tea and sympathy.

Mark Surman and Dave Teehan, for invaluable assistance during my periods at the Daresbury synchrotron radiation source, affectionately known as Hell.

The fellow members of my household, Mick T., Mick L., Mick M., Spencer, Joe, Brian and Shane, for their forbearance.

My family, and all others who helped keep me sane in an insane world

An especially heartfelt note of thanks goes to my sister Catherine, for being there in a time of need.

CONTENTS:

ABSTRACT

Scanned-angle X-ray photo-electron diffraction (XPD) was examined as a candidate for use in the qualitative determination of the surface crystallography of a variety of surface systems of chemical and physical relevance, including the growth of strained ultra-thin metal films, the co-adsorption of CO with alkali metals and the geometry/compositional profile of bi-metallic alloy surfaces. Where appropriate, ancillary techniques such as Near Edge X-ray Absorption Fine Structure (NEXAFS), Low Energy Ion Scattering Spectroscopy (LEISS) and Angle-Resolved Ultra-violet Photo-emission Spectroscopy (ARUPS) were used to further characterise these surface systems.

The effect of strain on the structure of ultra-thin metal films grown on fcc substrates was examined by XPD. Cobalt films grown on Pd {100} and {111} substrates were shown to have a Volmer-Weber growth mode, and to be initially strained in-plane by the substrate. In both cases the Co overlayers were shown to grow in an fcc structure, rather than the normal hcp phase adopted by Co at room temperature. In the case of Pd {100}, the Co overlayers grew in a novel highly tetragonally distorted fcc layer structure (c/a=1.11-1.15; fcc c/a=1.41, bcc c/a=1.0), which persisted to high coverages (>20 eML). On the {111} plane, the Co adlayers relaxed more rapidly toward their bulk fcc lattice parameters with complete relaxation occuring in the 1-5 eML coverage range. There was again evidence of a distorted lattice structure induced by the Pd substrate for very thin Co films.

In contrast, Cu was shown to grow on Pd {110} at 300 K in the Stranski-Krastanov growth mechanism with flat clusters growing above a 1 ML pseudomorphic Cu slab. Again XPD indicated evidence of growth of a distorted fcc structure. The fcc structure of the Cu films was studied by angle-resolved photo-emission using synchrotron radiation. The strain imposed by the Pd substrate manifested itself by changes in the film electronic structure relative to bulk Cu {110}.

A range of stoichiometric K/CO co-adsorbed monolayers on Co $\{10\bar{1}0\}$ were studied by NEXAFS, XPS and XPD, including a c(2x4)-(K+CO), a c(2x2)-(K+CO) and a

p(3x1)/c(2x2)-(K+CO) mixed phase. The orientation of the CO molecule and changes in the CO bondlength were determined via NEXAFS. The CO was found to be upright on the c(2x4) and c(2x2) overlayers. However, evidence for a tilted CO species on the p(3x1)/c(2x2) phase was found. Co-adsorption with K was shown to induce a lengthening of the CO molecular bond (monotonically increasing with K:CO stoichiometry) of up to ~0.13 Å relative to CO on clean Co. Various co-adsorption induced NEXAFS features, such as the appearance of an additional resonance with π-symmetry ~11.7 eV above the Fermi level and a splitting of the characteristic CO π-resonance, were identified as being consistent with a direct chemical bonding interaction between the K 4s-resonance and the CO $2\pi^*$ orbitals. Low-energy scanned-angle XPD was utilised to determine the structure of the c(2x2)-(K+CO) overlayer. The overlayer was found to consist of an intimately mixed K/CO phase, with the potassium and oxygen species nearly co-planar and at a lateral separation of ~2.9 Å, which is consistent with a K-O chemical bonding distance. The results indicate that low-energy scanned-angle XPD has definite potential as a quantitative structural analysis tool for complex systems containing two or more co-adsorbates.

The surface structure of two CuPd alloys, a $Cu_{0.85}Pd_{0.15}$ {110} bulk crystal and a Cu{100}-c(2x2)-Pd surface alloy was examined by polar XPD. In the case of the surface alloy (formed by deposition of ~0.5 ML of Pd on Cu {100}, XPD clearly demonstrated that the alloy was not a homogeneous, single layer structure, but was composed of domains of c(2x2) CuPd alloy and areas of pure Cu {100}. Approximately 50% of the Pd atoms were found to reside in the *second* layer of the selvedge. In the case of the bulk alloy, polar XPD clearly demonstrated that the alloy surface *did not* adopt a simple fcc lattice structure. Various models consistent with the observed XPD measurements have been proposed, which should be tested by independent structural determination techniques.

Scanned angle XPD was shown to be a rapid and reliable method of obtaining the major aspects of the surface geometry for a wide variety of surface systems. The use of a single scattering approximation in the analysis of scanned-angle measurements was found to be sufficient. The results of the co-adsorption study indicate that even at relatively low kinetic energies (~120 eV), single scattering modelling can still yield reliable results.

Chapter I

Introduction.

Surfaces represent the interface between a condensed phase of matter (i.e. solid or liquid) and another phase (solid, liquid or gas). While in a bulk material, surface atoms are in the minority, and generally represent less than $1x10^{-7}$ of a typical sample, their influence vastly outweighs their statistical occurrence. For instance, surfaces atoms are responsible for heterogeneous catalysis and for the corrosion characteristics of the material. Some of the technologically important areas in which surfaces play a crucial role include catalysis, magneto-optical film production, micro-electronics/semi-conductor fabrication, electrochemistry and corrosion passivation [1-3].

"Surface science" is motivated by the aim of achieving a fundamental understanding of the physical and chemical properties of surfaces. By gaining an understanding of the processes that occur at surfaces on an atomic/molecular level, macroscopic surface properties can be better understood and, potentially, controlled. Surface science generally entails the study of 'single crystal' materials in an ultra-high vacuum (UHV, $<1x10^{-9}$ torr) in order to maintain the surface in a constant, well-defined state during the experimental measurements.

Single crystal materials have atoms arranged in a regular, repeating lattice structure. For, example, metals adopt close-packed crystal structures such as *face-centred-cubic*, fcc (e.g. Cu, Ni, Pd), *body-centred-cubic*, bcc (e.g. Fe, Cr, Mo) and *hexagonal-close-packed*, hcp (e.g. Co, Ti, Ru). Figure 1 shows the unit cell of an fcc lattice. Different cross-section cuts through a bulk fcc crystal yield different surface atomic arrangements, which are identified by their 'Miller indices' [4]. Figure 1 illustrates the planes through the fcc unit cell that correspond to the three low Miller index surfaces of this crystal structure, (001), (011) and (111). These are the simplest and most commonly studied surfaces of fcc metals. The geometry of such surfaces, once atomically cleaned in UHV, is uniform (other than a low concentration of defect sites such as surface steps, which only occur every ~100 Å) hence aiding the interpretation of experimental data.

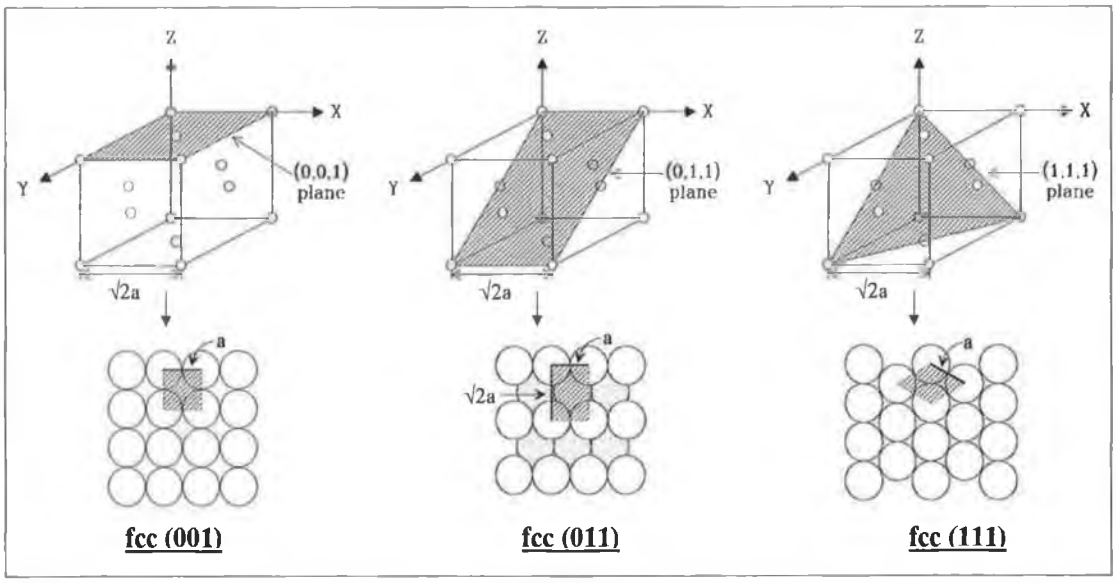

Figure 1: The fcc unit cell structure and the cross-sections which correspond to the three low Miller index planes. **a** is the length of the primitive surface unit cells shortest side. In this case, it also corresponds to the nearest-neighbour inter-nuclear separation.

It is readily apparent that surface atoms have a different environment from atoms in the bulk of the crystal structure since they have all lost nearest-neighbour atoms. For example, in the case of fcc crystals, atoms in a (001) surface have lost 4 nearest neighbours, while atoms in a (011) surface have lost 5 nearest neighbours and atoms in a (111) surface have lost 3 nearest neighbours. This fact manifests itself in the (011) plane generally being the most reactive of the low index faces, and also the most likely to "reconstruct" in order to maximise surface atom co-ordination and compensate for the loss in bonding.

One of the primary aims of surface science is to elucidate the geometric structure of surfaces and interfaces, and to correlate this with the corresponding chemical and electronic properties of the surface/interface. The term "geometric structure" refers to the local atomic arrangement of surface atoms, which may differ from the bulk atomic structure. Clean metal surfaces often undergo multi-layer surface relaxations, which involve a contraction of the outermost inter-layer spacing and an accompanying expansion of the second inter-layer spacing. This arises from the need of the atoms in the outermost layer to increase their effective co-ordination due to the loss of neighbours at the solid-vacuum interface. Hence, they move towards their second

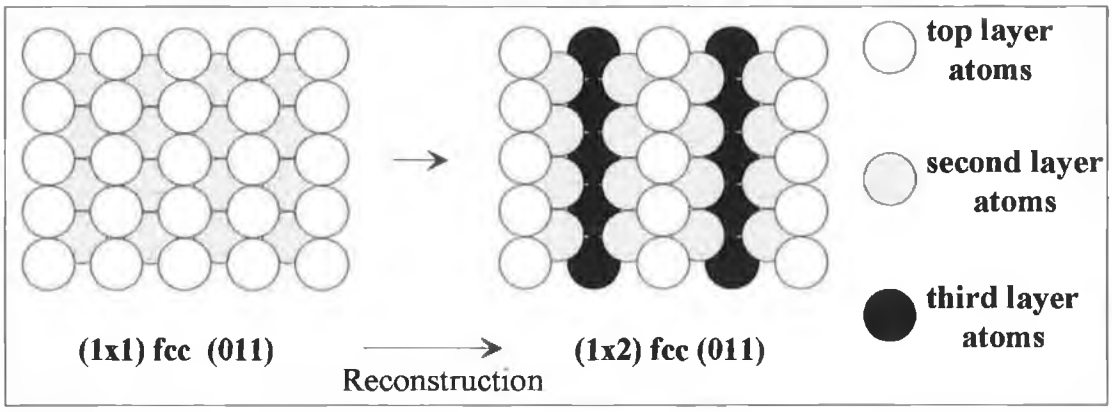

Figure 2: Typical reconstruction of an fcc (011) surface from a bulk truncated (1x1) structure to a (1x2) missing row surface.

layer neighbours. This leads to an effective 'over-co-ordination' of the second layer atoms, which respond by pushing third layer atoms away and thereby creating a second-to-third layer expansion. This effect proceeds deeper into the selvedge, being progressively damped with distance from the surface. A more radical reaction to the creation of a surface is "reconstruction" in which the surface structures re-arrange with a lateral periodicity different from that which would be expected on the basis of a 'bulk truncated' structure. A common reconstruction at fcc (011) crystal faces is the (1x1)→(1x2) missing-row reconstruction, which is illustrated in figure 2. This can occur on clean single crystal surfaces (e.g. Au, Pt), or it may be induced by adsorbates (e.g. alkali metals, hydrogen on Pd, Ni {110}).

In addition to the 'low-index' crystal faces shown in figure 1, single crystals can be cut so as to deliberately form a high density of atomic steps on the surface. A schematic of a fcc (331) stepped surface is shown in figure 3. This surface has an extremely high step density, with each terrace being only three atoms wide. Stepped surfaces are interesting because of the different chemistry that may occur at step-sites in comparison to terrace-sites. It is clear that step-sites will have a higher co-ordination for adsorbates than terrace sites, leading to differing surface chemistry/reactivity.

Until now the term 'surface atoms' has referred solely to those atoms in the outermost layer of the crystal. As illustrated by the inter-layer spacing changes discussed above, effects due to the existence of the surface are not confined exclusively to these atoms.

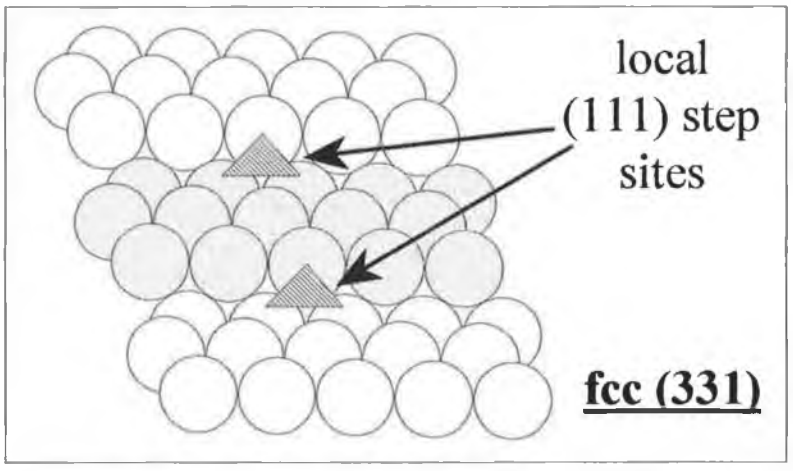

Figure 3: Surface atomic arrangement of a fcc (331) single crystal with (111) terraces and steps.

Atoms beneath the top layer also feel the effect of the absence of surface atoms. In the case of the fcc (001) surface 2nd layer atoms have lost one next-nearest neighbour atom, while for the (111) surface they have lost three. The 2nd layer atoms in an fcc (011) surface have lost a *nearest neighbour* atom as well as two next-nearest neighbour atoms, which again helps explain the enhanced reactivity, and the tendency to reconstruct, of this crystal face. Consequently, surface scientists refer to the 'selvedge' region, which is defined as the region near the surface where the crystal properties are significantly different from those of the bulk. It generally encompasses the top 4-5 layers of the crystal, although the thickness that is relevant is dependent on the property being studied.

In order to understand the catalytic and reactive properties of surfaces, the way in which they interact with adsorbates must be understood. At an atomic level single crystal surfaces have a range of potential adsorption sites, which are distinguished by the number of surfaces atoms that the adsorbate can co-ordinate/bond with. The different sites on the three low Miller index fcc surfaces are illustrated in figure 4. For molecular adsorbates (e.g. CO), any of the adsorption sites is feasible. In the case of metal adatoms the high co-ordination (three- and four-fold hollow) sites are generally preferred (although not always, e.g. sodium adatoms on Cu (111) and Ni (111) adsorb in an "on-top" geometry [5]).

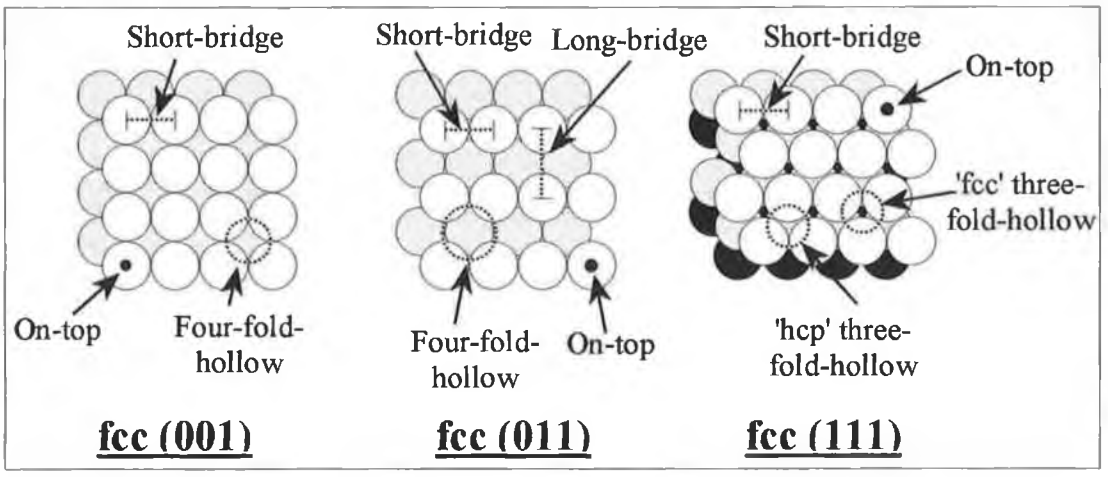

Figure 4: The different high symmetry co-ordination sites on the low Miller index fcc faces.

Molecular adsorbates may physisorb (weak adsorbate-substrate interaction) or chemisorb (strong adsorbate-substrate interaction) at metal surfaces. In the case of chemisorption the molecule may remain intact, or it may dissociate to molecular fragments or to its component atoms. Lateral adsorbate interactions, either direct or substrate-mediated, may lead to an ordering of the adlayer species. It is the combination of the adsorbate-substrate and adsorbate-adsorbate interactions that determine the local adsorption site and long range order of an adsorbate species.

The term 'epitaxial growth' is used when an ordered overlayer structure is formed upon metal deposition on a single crystal. In many cases, such as the adsorption of metals and semiconductors on solid surfaces, adsorption does not terminate upon the completion of a single monolayer and multi-layer structures may be fabricated. In this case, growth of overlayers with a lattice structure (e.g. fcc, bcc, hcp) different from that normally adopted for the bulk structure is possible under the influence of the substrate. Hence, growth of such films offers an exciting range of possibilities for creation of new materials with chemical and physical properties not encountered naturally (e.g. a body-centred-tetragonal (bct) phase of Co grown of Pd {100} c.f. Chapter III).

A range of surface sensitive spectroscopies have been devised to probe quantitatively the crystal structure of surfaces and interfaces. Of these, perhaps the most established method is low energy electron diffraction (LEED) [4], which for ordered surfaces

may provide a full quantitative picture of the geometric structure with bond lengths accurate to within ±0.03 Å. However, LEED is limited at present to the study of equilibrium crystal structures. More recently, scanning tunnelling microscopy (STM) has begun to provide information on complex dynamic processes, such as crystal growth and the mechanism of surface reconstruction. While not being able to equal LEED in terms of accuracy in quantitative structural work, more complex surfaces consisting of domains with differing local geometry may be examined.

Despite the continued dominance of LEED and STM as the primary surface structural tools, they both suffer from two major disadvantages. Firstly, neither technique is chemically specific, leading to potential problems when studying complex surface systems in which several atomic species are present. Secondly, both techniques involve electron flow to and from the surface. Many molecular adsorbates may be severely disrupted by such electron beams, leading to desorption and/or dissociation.

The major part of this thesis is dedicated to the application of a photon-based technique, X-ray photo-electron diffraction, which minimises the aforementioned beam damage and is chemically specific, and hence able to interrogate the local structure around a given adsorbate atomic species. Chapter II outlines the general principles upon which the technique is based, while Chapters III-VI describe the results of its use to study a range of chemically and physically interesting surface systems in an attempt to evaluate future potential areas of utilisation.

REFERENCES:

[1] G.A. Somorjai, Introduction to Surface Chemistry and Catalysis, Wiley interscience, New York, (1994).

[2] T.N. Rhodin and G. Ertl, The Nature of the Surface Chemical Bond, North Holland Physics Publishing, Amsterdam, (1979).

[3] S.R. Morrison, The Chemical Physics of Surfaces, Plenum Press, New York, (1990).

[4] M.A. van Hove, W.H. Weinberg and C.M. Chan, Low Energy Electron Diffraction: Experiment, Theory and Structural Determination, Springer-Verlag, Berlin, (1986).

[5] D.L. Alder, I.R. Collins, X. Liang, S.J. Murray, G.S. Leatherman, K.-D. Tsuei, E.E. Chaban, S. Chandavarkar, R. McGrath, R.D. Diehl and P.H. Citrin, Phys. Rev. B, 48 (1993) 17445.

Chapter II

An Introduction to X-ray Photo-electron Diffraction (XPD).

1. SURFACE STRUCTURE DETERMINATION:

The structural parameters are among the most fundamental properties of surfaces/interfaces that may be studied. A battery of techniques have been developed that allow the geometric parameters of a surface/selvedge to be measured. Among the most commonly used of the techniques available are low energy electron diffraction (LEED, [1-3]), scanning tunnelling microscopy (STM, [4-6]) and X-ray photo-electron diffraction (XPD, [7-9]).

LEED involves probing a single crystal surface with a beam of monochromatic low kinetic energy electrons (40-500 eV) and measuring the elastically back-scattered electrons, which occur as diffraction beams from an ordered surface along well-defined directions, as a function of energy and angle. In order to obtain quantitative structural information from the measured electron diffraction pattern a trial-and-error procedure must be adopted in which structural information is obtained via comparison of the measured diffraction data with theory calculations for a postulated surface structure. With proper analysis, full structural information can be obtained about the selvedge region. The 'surface sensitivity' of the technique is energy-dependent. For KE<100 eV the inelastic mean-free-path (IMFP, a measure of how far an electron can travel un-perturbed in a solid) is at a minimum, and the technique is at its most surface sensitive. In LEED the electron diffraction pattern is not species specific. Any ordered region within the selvedge will contribute to the observed pattern. Until recently it had been assumed that this technique required the surface to possess long range order. However, measurements have been made from disordered overlayers that possess 'lattice gas' properties. An overlayer forms a 'lattice gas' if the adatoms adsorb on the surface in a random fashion but have a similar local environment (short range order). Hence, each atom scatters the incident electrons in a similar (though not identical) fashion and the contribution from each atom is approximately identical. However, LEED cannot be applied to completely random surface structures, where no long or short range order exists.

LEED has the advantages that it is an entirely laboratory based experiment (i.e. no requirement for large-scale research facilities) and hence is easy to perform. It is an extremely well-established technique, and has become the 'workhorse' for structural determination against which other techniques are judged. With full multiple-scattering analysis, LEED can give extremely detailed and accurate information about the structural geometry of highly ordered surfaces. When properly utilised, structural parameters can be determined to an accuracy of <0.03 Å. The main drawback of the technique is that it requires rigorous experimental practice. Exact alignment of normal incidence is required, and external magnetic fields (such as the Earth's magnetic field) must be eliminated. In addition, the study of molecular adsorbates suffers from severe problems due to rapid electron beam damage of the molecular overlayer. Such adsorbates may be subject to e^--beam induced dissociation and/or desorption, making good quality measurements difficult to obtain. LEED analysis is often highly time-consuming, especially for complex overlayers in which several atomic/molecular species are present. Such "co-adsorption" systems, which usually contain at least one beam sensitive molecular adsorbate, are key to understanding complex catalytic processes at solid surfaces. A full multiple-scattering analysis may take many months for such complex systems. However, the recent introduction of approximate methods such as 'tensor-LEED' [10-12], in which small perturbations (within 0.2-0.3 Å) of a model structure may be performed rapidly on the basis of a single full-multiple scattering calculation, are beginning to revolutionise data analysis [13].

STM is the ultimate surface sensitive technique. While LEED probes a surface to a finite depth that is determined by the IMFP of the diffracted electrons, STM is primarily sensitive only to the outermost atomic layer of the sample. The topography of a surface is measured by scanning a sharp (ideally atomically sharp) probe above a surface. The tip is electrically biased relative to the sample such that electrons can tunnel between the probe and the surface with a probability that is determined by the tip-surface separation. The topography can thus be obtained either by measuring the changes in tunnelling current as the tip is scanned above the surface at a constant height, or by measuring the tip deflections required to maintain a constant current as the tip is scanned. STM requires a conducting surface but a similar technique called atomic force microscopy (AFM), which measures probe deflections caused by

attractive van der Waals forces between the surface and the tip, allows non-conducting surfaces to be imaged.

As for LEED, STM is a laboratory based technique. It has the advantage of being a direct technique (no theoretical modelling required). Different atom types can be distinguished in STM images (through changes in the tunnelling probability due to local electronic and work function changes) although currently the technique cannot be used to chemically identify adsorbates. Because STM is a local structural probe, it does not require the sample to be ordered as is the case for LEED. It is possible to achieve lateral atomic resolution of surface features by STM and, with proper calibration, quantitative structural information can be obtained to an accuracy of <1 Å. The main drawback of STM is its inability to probe structural parameters below the outermost surface layer. From an experimental point of view, the requirement to isolate the sample from external vibrations, and problems with reproducibly forming good tips, can make good images difficult to obtain. Care must be taken to ensure that apparent 'structures' on the surface are not artefacts due to the surface-tip interaction. STM is not well suited to the study of molecular adsorbates since interactions between the substrate and the tip predominate, which may perturb adsorbates in STM/AFM. However, it is a very useful technique for studying metal-on-metal overlayers.

XPD involves measuring the intensity variation of X-ray photo-electrons emitted from surface localised atoms as a function of either emission angle (scanned-angle XPD) or emission energy (scanned-energy XPD). The scattering of the electrons by surrounding atoms yields information about the local structure. The diffraction pattern arises from coherent interference of the directly emitted component of an electron wavefront with other components that are elastically scattered by the surrounding atoms. As with LEED, the depth to which XPD probes the surface is determined by the IMFP of the electrons. By careful selection of the X-ray wavelength, and by detecting only electrons of a specific kinetic energy (KE), emission from a given atomic species can be monitored. Of these three techniques, this is the only one that can probe the local environment of a single atomic species in isolation, and it generally

does not suffer the problems with molecular adsorbates that arise with LEED and STM.

The measured diffraction pattern, which is governed mainly by the atoms within ~5-10 Å of the emitting atom, allows the determination of the local structure around the emitting atom. Hence, XPD does not require the surface structures to have long range order, but does require the local structure around the emitting atoms to be the same. XPD can, in principle, be used where the emitting atom type exists in several different local environments. However, the resulting pattern is the sum of the intensities resulting from each of the different local structures. As the number of different structures increases so does the number of different contributions to (and the overall complexity of) the final diffraction pattern. In some cases structural information can be derived directly from XPD scans, but it is generally necessary to model the electron diffraction process and compare theory with experimental results in order to obtain quantitative results. While a full multiple scattering approach to XPD modelling is adopted by some workers, many regard a simpler single or double scattering approach, in which higher order multiple scattering paths are ignored, to be sufficient for most structural determinations.

From an experimental point of view, scanned-angle XPD can be readily performed with a laboratory X-ray photo-electron spectroscopy (XPS) chamber. All that is required, beyond the standard XPS instrumentation, is to ensure that the analyser has a small acceptance angle and to have some means of changing the electron detection angle (usually by sample rotation). The measurements are reasonably simple to perform, requiring only that normal precautions with regard to sample alignment and XPS peak normalisation be taken. The main drawback of laboratory-based XPD is that the electron kinetic energies are determined by the core level binding energies of the emitting species and the photon energy of the available X-ray sources (typically Al K_α (1486.6 eV) and Mg K_α (1253.6 eV)).

In order to perform scanned-energy XPD, or to obtain a greater range of emission energies for scanned-angle XPD, a variable photon energy source (i.e. a synchrotron radiation source) is required. Consequently, these experiments are more expensive to

perform, and measurements can generally only be made for relatively short time periods. However, the enhanced beam intensity, and the greater range of measurements that can be taken, makes synchrotron based XPD experiments more versatile than the laboratory based equivalent. XPD has now developed to a state where it can yield a full structural determination via the scanned-energy technique of Woodruff [14, 15]. With the application of theoretical modelling, recent scanned-energy XPD studies have demonstrated that structural parameters can be determined to an accuracy rivalling that of LEED. However, the requirement for synchrotron radiation still makes such studies relatively rare.

Full understanding of the structure of a surface is generally only possible when the results from different studies are combined to provide an overall picture of the surface structure. Despite the areas of overlap, the three techniques outlined above should be regarded more as complementary rather than as competitive. These techniques, and a battery of others developed to probe the structural, chemical and electronic nature of surfaces, are available for characterising the large number of surfaces/interfaces that can be prepared [16]. It is difficult for any single worker to be able to apply a full range of techniques to a given surface. Hence, full surface characterisation of a given system is generally obtained by combining results from various workers who concentrate on the use of a select number of techniques.

This thesis deals with the use of XPD to study surface systems of chemical and physical interest. In particular, the aim of this work was to investigate the potential of scanned-angle XPD for the quantitative structural analysis by studying a range of surface and interface problems including:

(a) the initial stages of formation of metal-metal interfaces.

(b) the geometry and structure of catalytically relevant, co-adsorbed overlayers on single crystal surfaces.

(c) the surface structure and compositional profile of bulk and surface binary alloys.

In addition to XPD, a range of other surface sensitive spectroscopies, including near-edge X-ray absorption fine structure (NEXAFS), angle-resolved ultra-violet photo-

emission spectroscopy (ARUPS) and low-energy ion scattering spectroscopy have been applied where necessary. This chapter deals with the theory, practical requirements and analysis of scanned-angle XPD before proceeding to the chapters dealing with the experimental measurements.

2. INTRODUCTION TO XPD:

2.1. History:

X-ray photo-electron diffraction (XPD) is the name given to emission intensity modulations that are observed if photo-emitted electrons from a sample surface are measured as a function either of their emission angle for a constant photon energy ('angle-resolved') or as a function of the photon excitation energy for a constant emission angle ('energy-resolved'). Polar XPD (i.e. the electron emission intensity measured as a function of polar emission angle measured w.r.t. the surface normal) was first observed from a single crystal surface in 1970 during X-ray photo-electron spectroscopy (XPS) studies of NaCl {100} by Siegbahn and co-workers [17, 18]. However the core level and Auger peak intensity enhancements, which were observed at well defined polar emission angles, were incorrectly attributed to electron channelling phenomena that are seen in transmission electron microscopy, termed Kikuchi bands. It was not until this misunderstanding was corrected by Egelhoff [19, 20], and the actual origin of the enhancements was understood, that XPD began to be developed as a tool for studying the short range order of atoms in single crystal surfaces and thin film overlayers. XPD from adsorbed atoms and molecules was first reported in 1978 by a number of different groups [21-23]. The technique developed slowly at first but has gained increasing attention in recent years. The origin of the diffraction process is now well understood and may be modelled accurately by electron scattering programs which utilise the LEED scattering formalism developed by Pendry [1]. Careful measurement of XPD patterns coupled with theoretical modelling of the diffraction process is now a powerful tool in the study of surface structure [14, 19].

2.2. Measuring Photo-Electron Diffraction Spectra:

In general either photo-emitted or Auger electrons may be used for XPD studies (the obvious exception being that Auger emission cannot be used for scanned-energy experiments). The excitation processes that are involved in both X-ray photo-emission

and Auger emission are outlined in figure 1. Photo-emitted electrons have a kinetic energy defined by the photon energy of the excitation source, while the kinetic energy of Auger electrons is characteristic of the atom from which they are emitted.

In order to perform XPD experiments a source of X-rays is required. In laboratory based systems this is typically a dual anode X-ray source utilising the Al K_α (1486.6 eV) & Mg K_α (1253.6 eV) lines. An electron energy analyser capable of measuring electrons at a specific kinetic energy is required. For XPD measurements a small acceptance angle, typically ~2° half angle cone, is required. Finally, there must be some means of altering either the position of the analyser relative to the sample (scanned-angle XPD) or the kinetic energy of the emitted electron (scanned-energy XPD). The sample-analyser orientation can be varied either by mounting the sample on a manipulator which allows rotation in the desired direction (polar and/or azimuthal) or by having a moveable analyser within the experimental chamber.

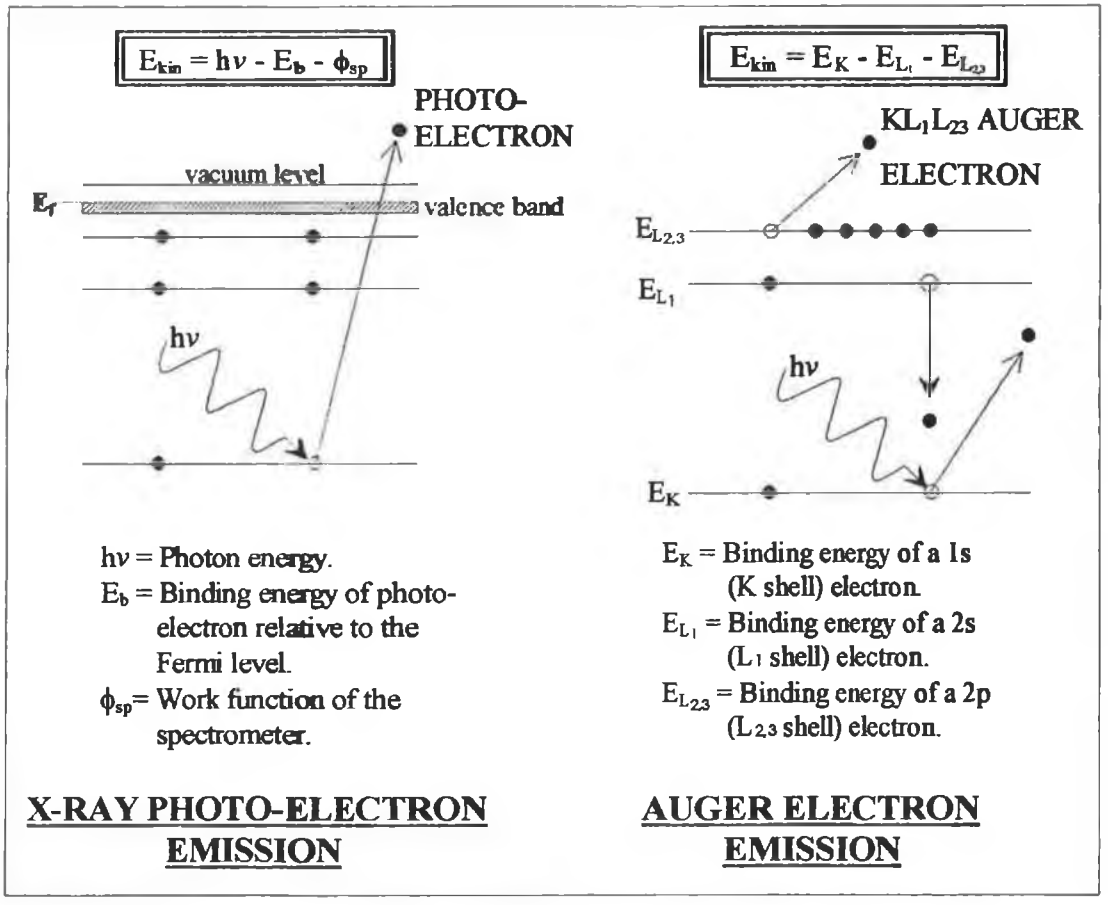

Figure 1: Photo-electron and Auger electron emission processes.

Varying the electron kinetic energy obviously requires a variable-energy photon source, hence, such experiments can only be performed at a synchrotron radiation source.

The different types of photo-electron diffraction measurements that can be made are illustrated in figure 2. Scanned-angle measurements are taken by varying the angle of electron detection relative to the surface in either a polar or an azimuthal fashion. Polar scans involve varying the emission angle, θ, which is measured with respect to the surface normal. They are generally taken from $\theta=0^{\circ}$ (normal emission) out to as large a value of θ as is feasible (electron intensity usually drops off quite sharply for $\theta>70^{\circ}$). Azimuthal scans are done at a fixed polar angle, θ. The crystal is rotated around the surface normal (varying the azimuthal angle, ϕ). $\phi=0^{\circ}$ is arbitrarily defined, usually with respect to one of the high symmetry azimuths of the single crystal surface. Full 360° azimuthal scans can be obtained, however usually scans of only 90° or 120° are sufficient due to symmetry of single crystal surfaces.

Scanned-energy photo-electron diffraction requires a tuneable X-ray source (i.e. synchrotron radiation). In this case the source, sample and analyser are maintained at a fixed geometry relative to each other while the photon excitation energy (and hence the kinetic energy of photo-emitted electrons) is varied. The emission intensity of a given photo-electron is monitored as the photon energy is varied. Clearly, scanned-energy XPD cannot utilise Auger emission since the kinetic energy of Auger electrons is fixed. Two forms of scanned-energy XPD are distinguished depending on whether the detection direction is normal (NPD) or off-normal (OPD) relative to the sample surface [24]. In this thesis only scanned-angle photo-electron diffraction studies are utilised. For a review of scanned-energy XPD see [25].

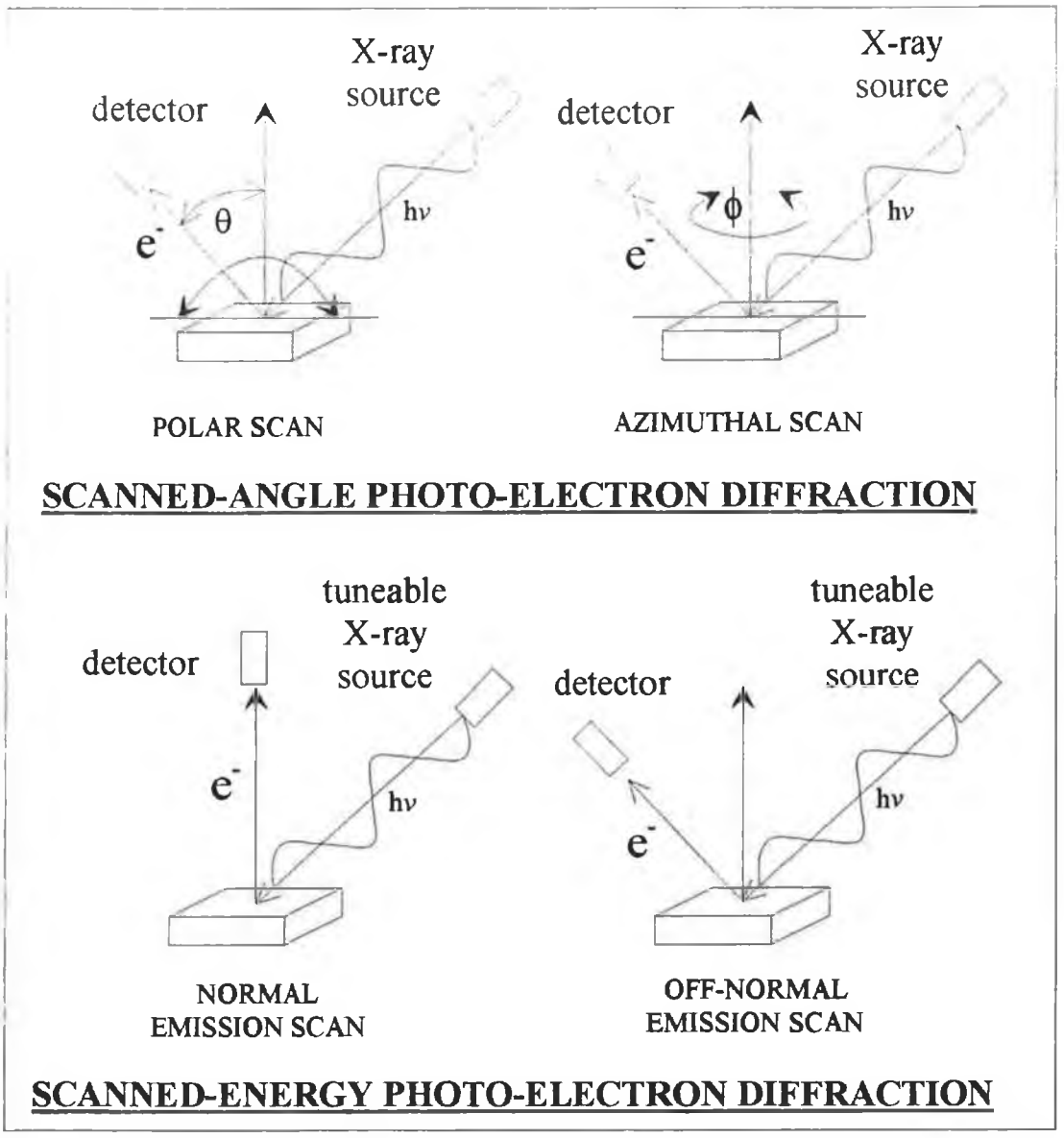

Figure 2: Different modes of XPD.

2.3. Origin of XPD Features:

In scanned-angle XPD, enhanced emission intensity is observed if the electron emission angle lies along an emitter/near-neighbour inter-atomic axis. The intensity enhancement is due to scattering of the emitted electrons by the atoms surrounding the emitter atom. Two modes of scattering can be distinguished, forward scattering (if the electron is scattered <90° from its initial trajectory) and back-scattering (if the electron is scattered >90°). The scattering strength and the observed angular intensity variation are energy dependent. At high outgoing kinetic energies (>200 eV) forward scattering is the dominant process. At lower kinetic energies back scattering becomes

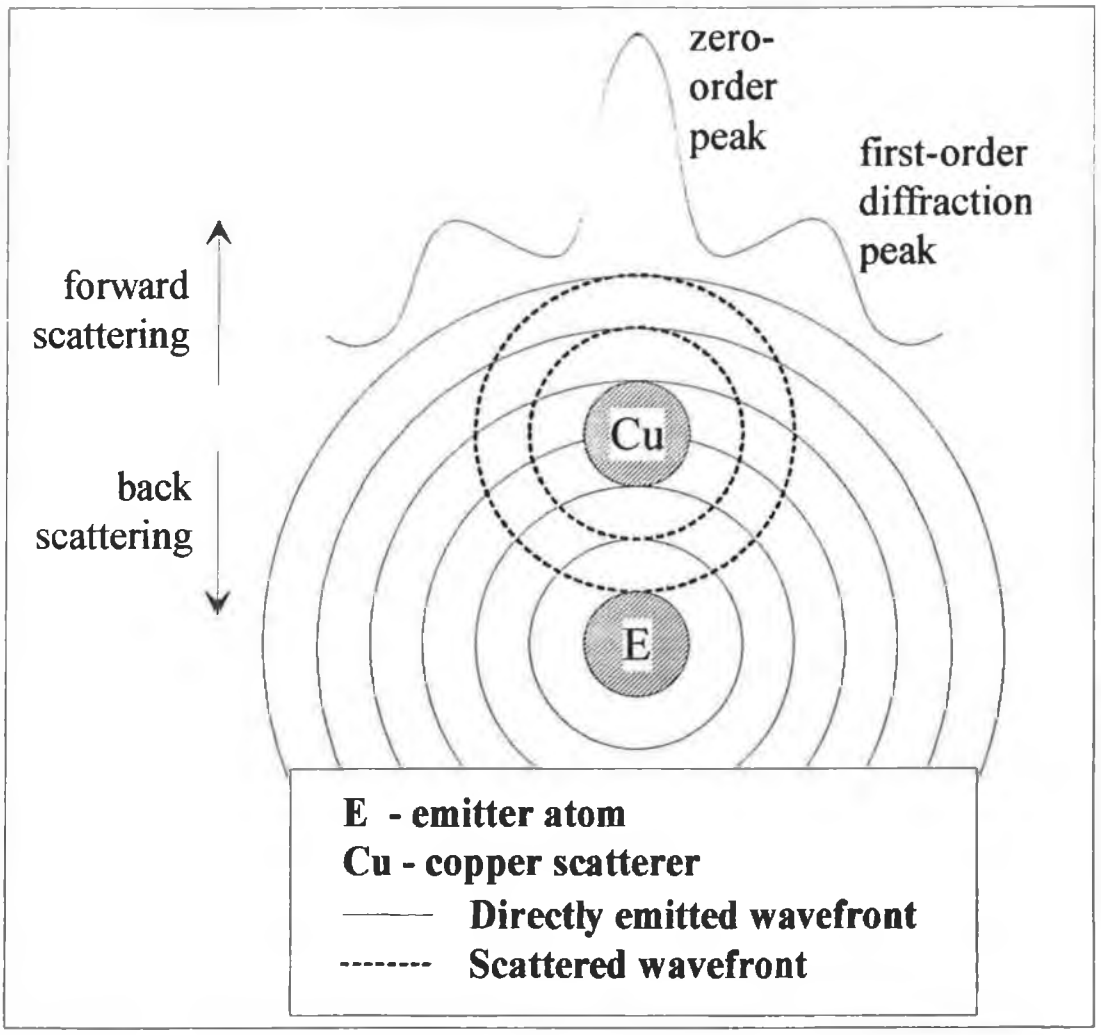

Figure 3: Representation of the scattering of a emitted electron wave by an adjacent atom.

progressively more prominent, although forward scattering remains the most significant process. A useful discussion of the XPD process can be found in [26].

Figure 3 shows an over-simplified yet useful representation of the scattering that occurs when an emitted electron encounters an atom. The emitted electron can be considered as a spherical wavefront propagating out in all directions from the emitter atom (E). When it encounters the scattering atom (Cu) part of the wavefront remains un-perturbed, while part is scattered generating a new wavefront that is centred on the Cu atom. Both wavefronts are spatially and temporally coherent, hence they can interfere generating directions of enhanced and diminished electron intensity.

The main constructive interference occurs along the emitter-scatterer direction ("forward focusing" [27]) resulting in enhanced intensity along the inter-atomic axis, termed the "zero-order" diffraction peak. In the forward direction there is no path length difference between the directly emitted wave and the scattered wave, hence this peak contains little information regarding the emitter-scatterer bondlength, but it is a direct "real space" indicator of the bond direction. As scattering angle moves away from the zero-order position the electron intensity goes through a series of minima and maxima (higher-order peaks), which are due to the directly emitted and the scattered wavefronts interfering destructively and constructively as a function of scattering angle. The scattering cross-section and its angular distribution is dependent on the kinetic energy of the electron and on the atomic species doing the scattering.

Figure 4 shows how the normalised scattering factor amplitude (scattering power) of a Ni atom varies with electron kinetic energy as a function of the scattering angle, θ_{Ni} [25]. It can be seen that at high outgoing kinetic energies (1320 & 505 eV) forward focusing (θ_{Ni}=0°) is the dominant process, while the atom has little scattering power

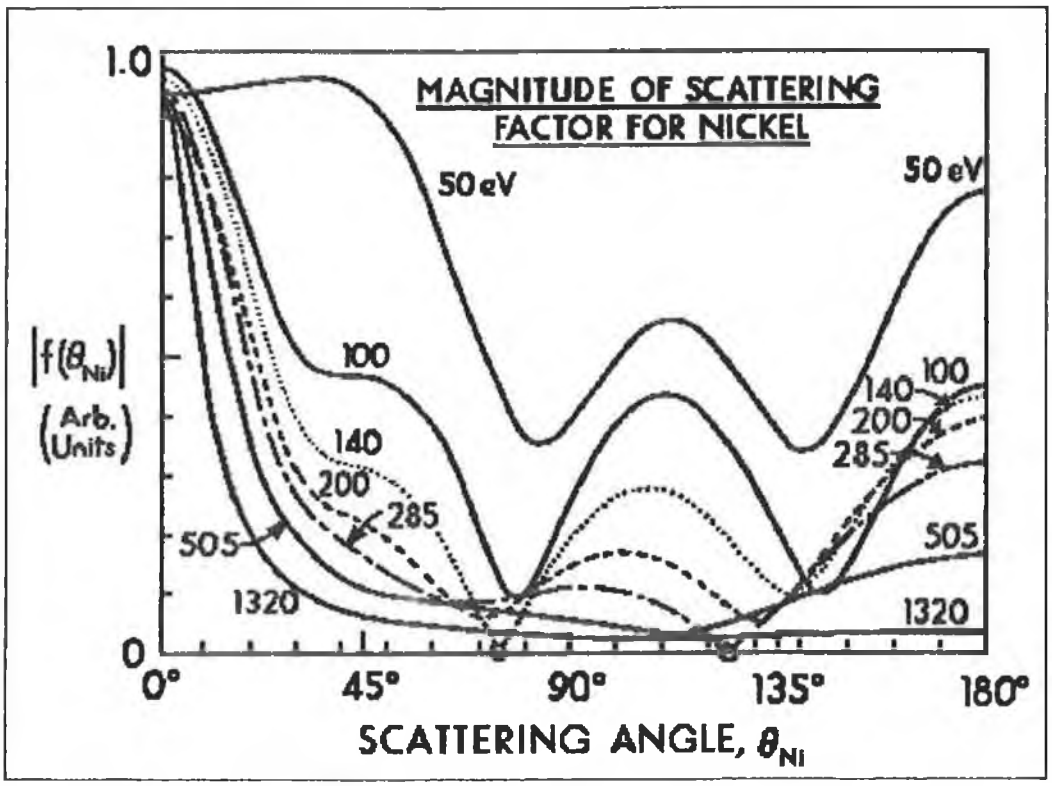

Figure 4: Nickel plane-wave scattering factor amplitudes $|f(\theta_{Ni})|$ as a function of scattering angle (θ_{Ni}) and electron kinetic energy (from [25]).

as the scattering angle moves away from 0°. The magnitude of the scattering factor in the forward direction at high energies is the origin of the enhanced intensity along bond axes in XPD spectra. As the energy decreases, the scattering factor for larger values of θ becomes more significant relative to θ_{Ni}=0°. There is a noticeable increase in the scattering strength at θ_{Ni}=180° (back-scattering) as the kinetic energy decreases. However, even at the lowest kinetic energy (50 eV) forward focusing remains the strongest scattering effect.

In order to understand how the higher-order diffraction features shown in figure 3 occur, a simple scattering process between an emitter and a single scatterer can be considered. Figure 5 illustrates that constructive interference between a scattered and an un-scattered wave occurs when:

$$n\lambda = \text{path length difference} = (a - a(\cos\theta))$$

which can be rearranged to:

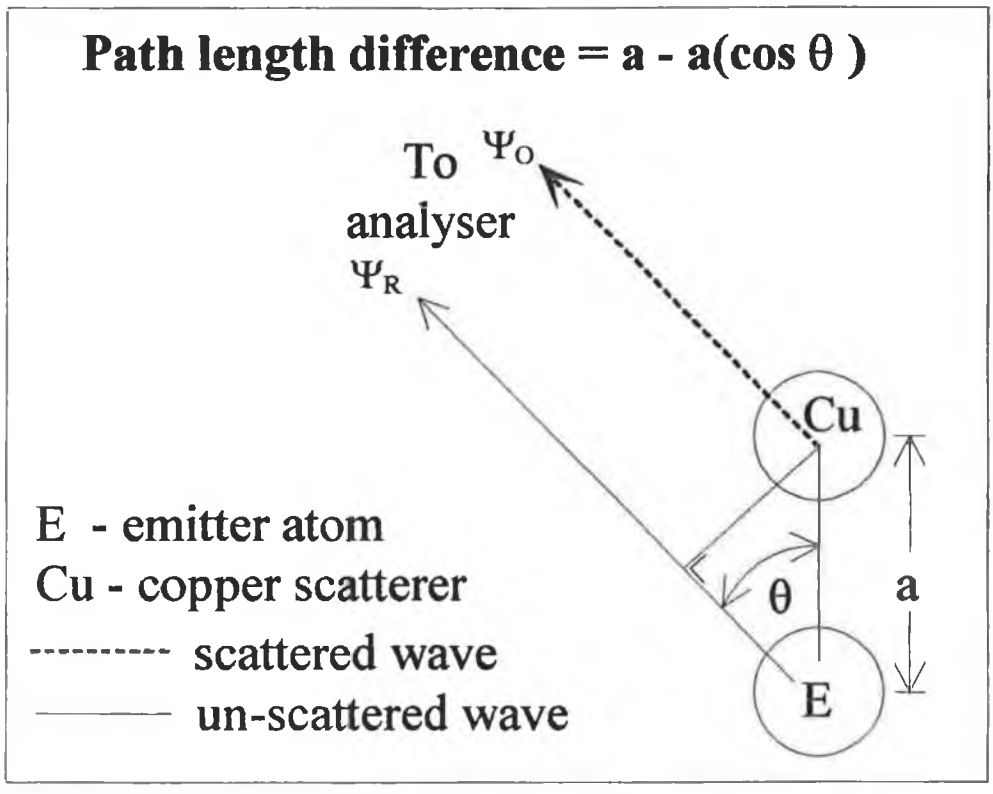

Figure 5: Path length difference between the scattered and un-scattered wavefronts as a function of θ.

Emitter-Scatterer separation (Å)	Electron kinetic energy (eV)	λ (Å)	Polar angle, θ (degrees) n=1	n=2	n=3
2	100	1.225	67.2	103.0	146.9
	500	0.548	43.5	63.1	79.7
	1000	0.387	36.3	52.2	65.2
4	100	1.225	46.1	67.2	85.4
	500	0.548	30.3	43.5	53.9
	1000	0.387	25.4	36.3	44.8
6	100	1.225	37.3	53.7	67.2
	500	0.548	24.7	35.2	43.5
	1000	0.387	20.7	29.4	36.3

Table 1: Position of higher-order diffraction features with emitter-scatterer separation and outgoing kinetic energy.

$$\theta = \cos^{-1}\left(1 - \frac{n\lambda}{a}\right)$$

where n is an integer, λ is the de-Broglie wavelength of the emitted electron and (a-a(cos θ)) is the difference between the distance travelled by the un-scattered portion of the electron wavefront and the distance travelled by the scattered portion. When this difference equals an integral number (n) of electron wavelengths, then constructive interference occurs. When it equals (n+½) wavelengths, destructive interference occurs. Using the equations for the de-Broglie wavelength:

$$\lambda = \frac{h}{mv}$$

and electron kinetic energy:

$$E = \tfrac{1}{2}mv^2$$

where h is Planck's constant (6.62×10^{-34} Js), m is the rest mass of an electron (9.1096×10^{-31} Kg) and v is the velocity of the electron, a relationship between the electron wavelength and its kinetic energy can be derived:

$$\lambda = \frac{h}{\sqrt{2mE}}$$

Substituting in the constants, the wavelength (Å) is related to the kinetic energy (eV) by the equation:

$$\lambda = \frac{12.253}{\sqrt{E}}$$

By substitution into the equation for the path length difference, shown in figure 5, the criterion for constructive interference can be rewritten in terms of the scattering angle, θ, and the electron kinetic energy, E:

$$\theta = \cos^{-1}\left(1 - \frac{n(12.253)}{a\sqrt{E}}\right)$$

This equation can be used to illustrate how the position of the higher-order diffraction features (θ) should vary with the emitter-scatterer separation and with the outgoing electron kinetic energy. Table 1 lists the expected variation of the 1st, 2nd and 3rd higher-order peak positions with emitter-scatterer separation and electron kinetic energy. Clearly the higher-order peaks occur closer to the zero-order peak (θ=0°) with increasing emitter-scatterer separation and also with increasing electron kinetic energy. This simple analysis illustrates that for scanned-angle XPD experiments, which are done at fixed electron kinetic energies, higher-order diffraction features carry information regarding emitter-scatterer bond lengths.

However, although the physical basis of the XPD can be easily visualised by the previous analysis, it is an extreme simplification of the diffraction process. It is based on the assumption that the phase of the scattered wave is un-perturbed during the scattering process, and hence that the phase difference between the two wavefronts arises solely from the distance travelled. However, the scattered electron wave will

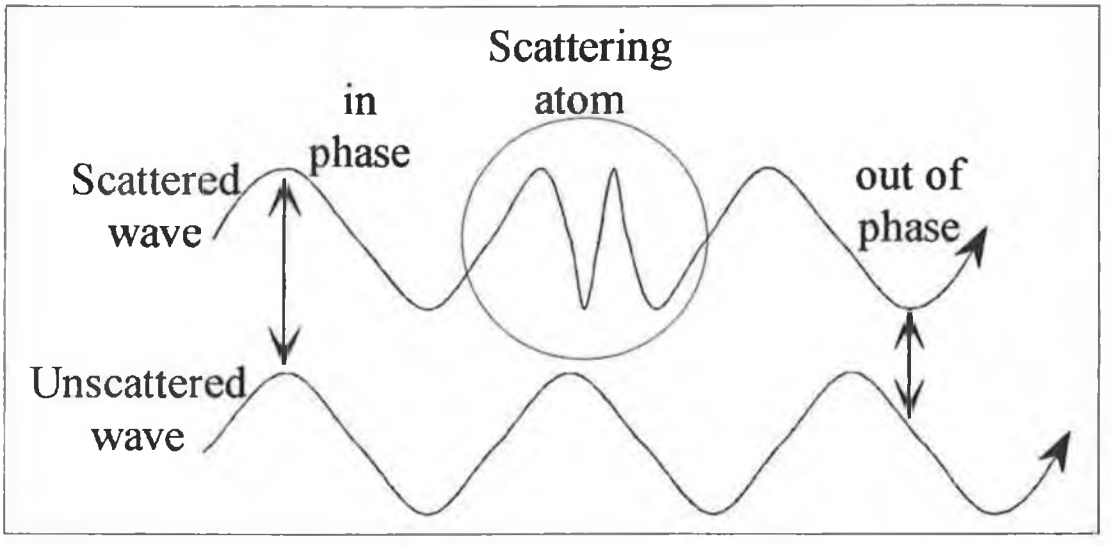

Figure 6: Phase shift induced in electron wave by scattering atom.

undergo a scattering-angle-dependent phase shift as it passes through the complex potential energy wells of the scattering atom. Hence the position of the higher-order diffraction features is determined by a combination of the emitter-scatterer separation and the phase shift of the scattered electron wave.

As the outgoing electron penetrates the electron orbitals of the scattering atom, there is a Coulombic attraction between it and the atomic nucleus. This attraction causes the potential energy of the electron to decrease, and consequently its kinetic energy increases in order to conserve total energy. As the kinetic energy increases the de-Broglie wavelength decreases, hence as the electron approaches closer to the nucleus its begins to undergoes rapid oscillations (very short wavelength). This results in the scattered electron wavefront moving out of phase relative to the un-scattered wave. Figure 6 illustrates how this process works. The scattered wavefront is shown as maintaining its direction while its phase is altered. In reality, fractions of the electron wave are scattered through all angles. The phase shift experienced by the electron wave differs with the scattering angle, which is itself dependent on how deep the wavefront penetrates through the electron shells of the scattering atom. The phase shift is also dependent on the atomic species causing the scattering.

Figure 7 shows the scattering strength of, and the phase shift induced by, a Ge atom as a function of the electron kinetic energy and the scattering angle. The forward focusing nature of the scattering atom, particularly at high kinetic energies as previously shown for Ni in figure 4, is also readily apparent for Ge. The phase shift induced by the Ge is relatively small for small scattering angles ($\theta<30^{o}$). At high kinetic energies the phase shift increases steadily with the scattering angle. At low kinetic energies the phase shift variation with scattering angle is more complex undergoing sharp modulations as a function of the scattering angle.

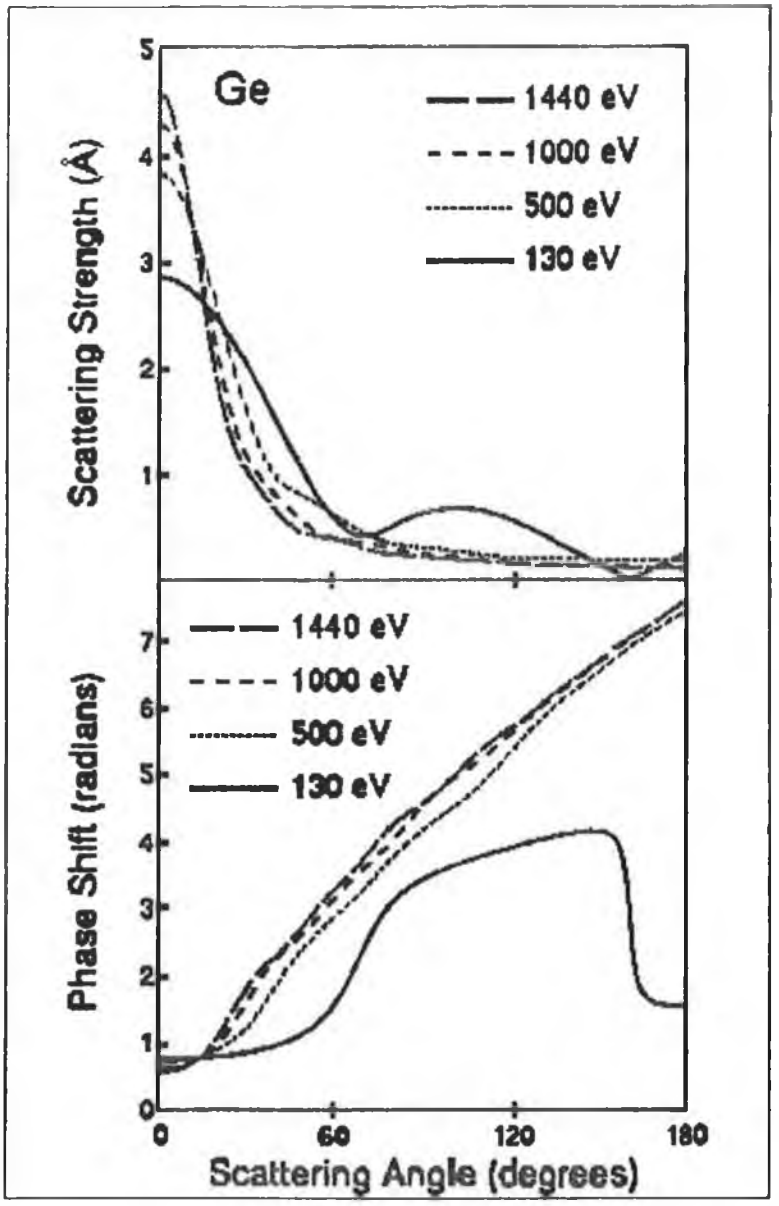

Figure 7: Scattering strengths and phase shifts as a function of scattering angle and electron kinetic energy for Ge computed, using the plane-wave approximation, for a muffin-tin scattering potential (from [28]).

It is clear that, for a two atom model, the phase shift introduced by the scattering atom complicates a direct determination of bond length. The phase shift caused by a given atom at a given kinetic energy may be calculated from a full quantum mechanical treatment of the scattering of an electron by the complex potentials within the atom, thus raising the possibility of being able to determine the inter-atomic separation. However, in reality there are two major complications to such a determination:

1. On a surface there are a large number of scattering atoms within the surface region, hence requiring summation over many scattering paths and making determination of isolated bond lengths difficult.
2. Electrons may be scattered more than once (multiple scattering), further complicating the origin of the higher-order features and the resulting XPD pattern.

2.4. Photo-Electron Diffraction Modelling:

The directionality of the zero-order intensity enhancements (along atom-atom axes) means that structural information can often be obtained from scanned-angle XPD measurements without recourse to computer modelling. In practice this is only reliable at high electron kinetic energies where forward focusing is dominant. Also, while visual inspection will give broad structural information, it does not take full advantage of the information available in the measurements. For more precise quantification of the data, especially at lower kinetic energies, modelling of the scattering process is necessary. A number of factors require consideration in photo-electron diffraction modelling:

2.4.1. The Initial State of the Emitted Electron:

For direct photo-emission, the final state, and hence the shape of the outgoing electron wave, is determined by the dipole selection rules. For an initial state with angular momentum number ℓ, two final state wave channels are available ($\ell\pm1$). The simplest case is for emission of an s-electron ($\ell=0$) in which case only a p-wave channel is available ($\ell=1$). For all other initial states two channels are available. The relative weighting of the two channels is determined by a radial matrix element [29]. A common approximation when carrying out cluster calculations is to treat the outgoing electron wave as a spherically symmetric (s-) wave, which simplifies the calculations involved. Auger emission is generally modelled as a s-wave.

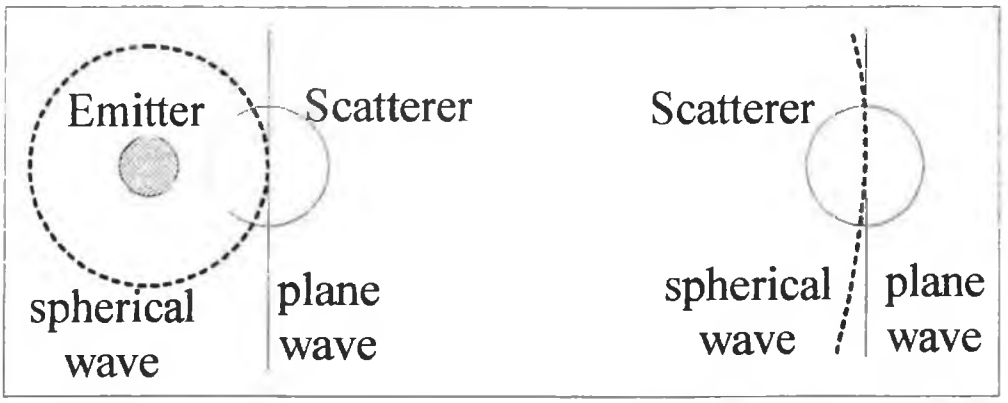

Figure 8: Illustration of how a plane wave better approximates a spherical wave as the emitter-scatterer separation increases.

2.4.2. Plane Wave versus Spherical Wave:

A s-wavefront is spherical (i.e. all points on the surface of the sphere are in-phase), and the more rigorously correct scattering programs take this into account. However a widely used approximation is to treat the wavefront as a plane wave (i.e. all points along a plane surface are in-phase). Use of a curved wavefront results in a substantial increase in the computational time required to calculate a diffraction pattern relative to the calculations for a plane wave. A plane wave only requires the phase of the wavefront to be calculated once for each scattering atom, whereas for a spherical wave it must be repeatedly calculated at different points along the wavefront for a single scatterer.

Use of a plane wave is not a good approximation when the scatterer is near the emitter. The shorter the emitter-scatterer separation, the greater the portion of the outgoing wave (and hence the more spherical the wave) that encounters the scatterer. Cluster calculations have shown that the use of a plane wave results in the over-estimation of the zero-order forward focusing peak [25, 30]. The plane wave approximation steadily improves with increasing separation between the scatterer and the emitter. Figure 8 illustrates how, for two identical scattering atoms, a spherical wave appears more planar in nature to the scatterer which is furthest from the emitter.

The diffraction of electrons results from their Coulombic interaction with the core electrons and the nucleus of the scattering atom. Hence, the sections of the electron wavefront that merely pass through the outer electron shells of the scattering atom are

less affected (due to screening) than those that penetrate the inner electron shells. As the electron kinetic energy increases, the Coulombic force required to scatter a given part of the wavefront through a fixed angle increases. Hence, at higher kinetic energies the parts of the electron wavefront that pass close to the nucleus are less scattered than they would be at lower energies. At very high energies only the portion of the wavefront that passes very close to the atom nucleus is scattered to a significant degree. Because this is a much smaller section of the wavefront, it is almost planar in nature and the plane wave approximation is more valid. Hence, the plane wave approximation also improves as the outgoing kinetic energy of the electron increases, although the over-estimation of zero-order peak remains [30]. Spherical wave corrections for the plane-wave approximation have been published [30, 31]. These allow a very good approximation of true spherical wave calculations without incurring the full computational cost in terms of processing time.

2.4.3. Single versus Multiple Scattering:

Photo-electron diffraction is a multiple scattering process. As shown in figure 3, the portion of the electron wavefront scattered by the Cu atom acts as a new wavefront centred on that atom. Considering just the two atom model in figure 3, the second wavefront (Cu) may now be re-scattered by the emitter atom generating a third wavefront. This wavefront can in turn be scattered by the Cu atom and so on, theoretically ad infinitum. Of course there are limits to the number of scattering paths that are significant. With each successive scattering, the fraction of the total electron intensity that is involved in the scattering becomes progressively smaller. This, coupled with electron loss due to inelastic scattering (via phonon and plasmon excitation in the solid), means that the more scattering paths an electron wave undergoes before it is summed to the overall electron intensity, the less it contributes to the resultant diffraction features.

Precise modelling of the XPD process requires multiple scattering. However, this is complex and computationally time-consuming to implement. Many investigators use simpler, single scattering programs to simulate photo-electron diffraction, based on the assumption that the bulk of the observed diffraction features are due to photo-electrons that undergo only a single scattering process before reaching the detector

[9]. The single scattering approximation has proved reliable at high electron kinetic energies where forward focusing is the dominant process (figures 4 & 7). At high KE the electron intensity is very strongly concentrated along the emitter-scatterer direction, while higher-order diffraction effects become far less significant. Multiple scattering paths that involve scattering through at least one large angle (i.e. away from the emitter-scatterer axis) result in a significant drop in the electron intensity involved in the scattering process and have little effect on the XPD features. The main drawback of single scattering theory at high kinetic energies is that it does not predict an effect, termed 'defocusing' [32], which is outlined below.

Consider a high kinetic energy photo-electron excited from an emitter atom that is at the end of a row of several scatterer atoms (all along the same axis). The electron wave is scattered when it encounters a neighbouring atom. Because the electron has a high kinetic energy, the phase shift caused by a single scattering process along the zero-order direction is small (<40°), and the interference between the scattered and the un-scattered wave is largely constructive (hence the XPD zero-order enhancement). In single scattering theory, once an electron has undergone scattering, the scattered portion of the wavefront is considered as having reached the detector. Hence, only the directly emitted wave can be scattered by each atom along the row of atoms, and each of the scattered waves constructively interfere to give a strong zero-order feature.

However, in a multiple scattering formalism the scattered waves may be re-scattered by each neighbouring atom. With each successive scattering, the wave is shifted further out of phase relative to the directly emitted (un-scattered) wave and the interference process becomes more destructive in nature. Scattering along a row of atoms is the one situation where multiple scattering occurs without scattering through a large angle. As a result, the scattered wavefronts retain a significant electron intensity, particularly at high kinetic energies (i.e. they have a non-trivial effect). The consequence of adopting a single scattering model is that the calculations will predict a larger zero-order feature along a row of atoms than would be predicted by multiple scattering, or would be observed experimentally. Figure 9 illustrates the effect for cluster calculations done along 'chains' of Cu atoms using single and multiple

scattering [33]. As the number of atoms in the Cu chain is extended the single scattering calculations show a small increase in the intensity of the forward focusing peak. Conversely, for multiple scattering calculations the intensity of the forward focusing peak is strongly reduced by defocusing as the chain length is increased and it is virtually eliminated by a chain of 4 Cu scatterers.

For zero-order peaks defocusing is only a problem of relative peak intensities rather than one of peak position. However, each additional scattering will also generate an additional set of higher-order features. These will modify the higher-order features on the XPD curves. Hence single scattering theory will also be somewhat deficient in predicting the position and shape of features which do not arise from zero-order scattering. It can be seen that the inclusion of multiple scattering does alter the higher-order features in figure 9.

The strength of defocusing along a chain of atoms is material dependent. For the Cu chain, shown in figure 9, the effect is very strong for a chain of five atoms, corresponding to a length of ~10 Å. However, a comparative study of defocusing by Al and Cu chains, done by Aebischer *et al* [34], has shown that defocusing is not necessarily as strong for other materials. In the case of Al scatterers a defocusing effect equivalent to that of Cu was found to occur for chains of 7-8 atoms (17-20 Å), which is 1.5-2 times longer than Cu. Aebischer *et al* concluded that factors such as the electron kinetic energy, lattice constant and the ratio of the electron wavelength to lattice constant were relatively unimportant in determining the defocusing behaviour of the atoms. The difference was found to be mainly due to the scattering potentials (which determine the phase shift of the scattered wave) of the atoms. Hence, the defocusing effect is material dependent, and it is incorrect to assume that equivalent chain lengths of different atoms will have the same effect.

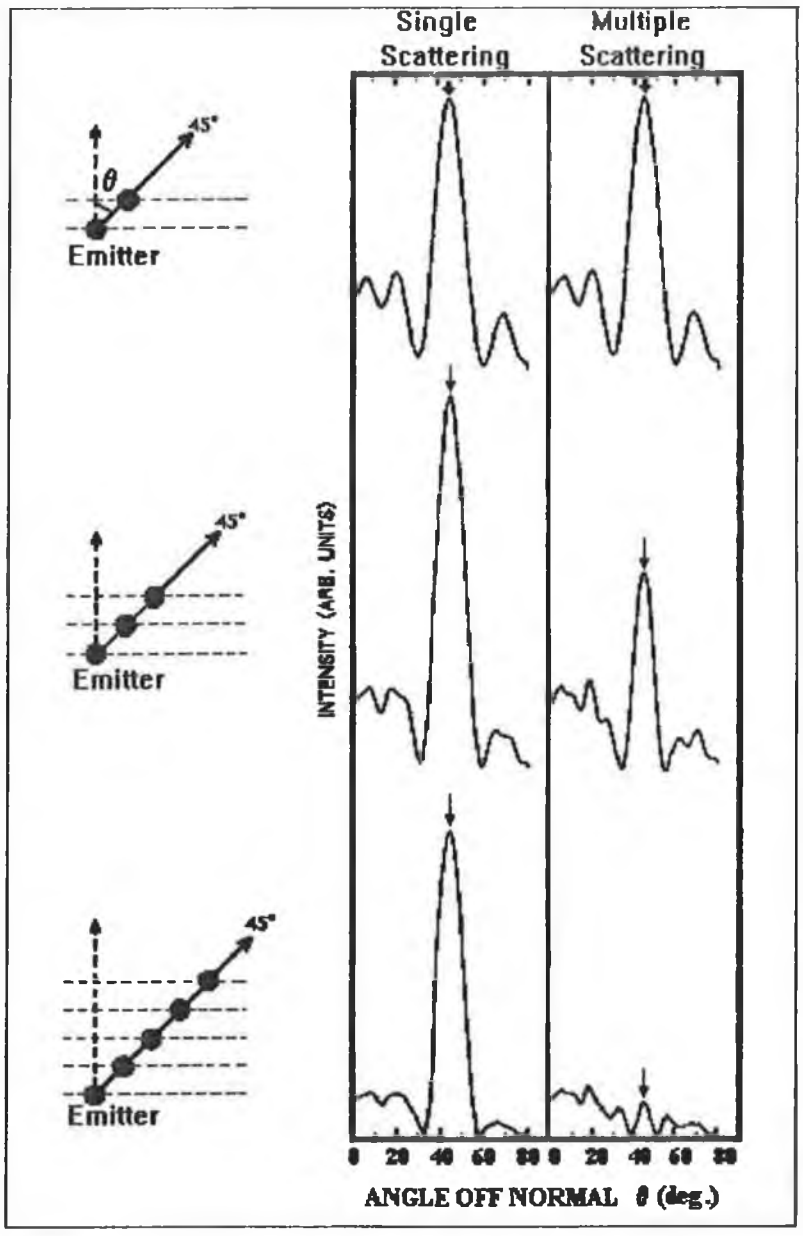

Figure 9: Cluster calculations for Cu Auger emission at KE=917 eV from a point source at the end of a Cu chain (from [33]). The left-hand diagrams indicate the chain geometries used. The arrows on the plots indicate the forward focusing peak.

For emission at high electron kinetic energies, the neglect of defocusing by single scattering theory can be minimised by using relatively small clusters [35, 36]. In this case, there will only be short atom chains within the cluster and so no important multiple scattering paths will exist. The calculated curves from such clusters are dominated by single scattered forward focusing peaks in both single and multiple scattering theory. Small clusters will often be adequate for modelling XPD processes since the diffraction pattern tends to be dominated by 'near-neighbour' scatterers.

However, use of a small cluster in not always valid. For instance, proper determination of the Si (111)-$\sqrt{3}\times\sqrt{3}$-Ag structure by scanned-angle XPD has been shown to require large clusters and multiple scattering theory [36]. Where possible convergence tests on large and small clusters should be performed before deciding on an adequate cluster size.

It becomes more important to use a multiple scattering treatment as the electron kinetic energy is reduced. At low energies, significant electron intensity will be scattered through large angles, and back-scattering becomes a much more significant process (figure 4). Even if an electron undergoes multiple scattering it may still retain sufficient intensity to significantly affect the diffraction pattern. Hence, changing from a single to a double, or triple, scattering model may have a significant affect upon the calculated XPD curves.

2.4.4. Lattice Vibrations (Phonons):

Within a surface an atom may vibrate with a given amplitude about its equilibrium position. The amplitude of vibration is dependent on the sample temperature (i.e. the higher the temperature, the greater the vibrational amplitude). Since the vibration period is usually $>10^{-13}$ sec and the photo-emission process happens on a significantly shorter time scale ($<10^{-15}$ sec), the XPD measurement will average the atomic position of the scatterers over a range of positions during their vibrational motions. This has the effect of introducing "disorder" since the electron wave is scattered at a range of positions for a given scattering atom, leading to a smearing/broadening of the diffraction features. Most scattering programs include some element of lattice vibration within their structure by means of a Debye-Waller factor.

2.4.5. Analyser Acceptance Angle:

All electron energy analysers have a finite angular acceptance. Although a vanishing slit width is the experimental ideal for accuracy in structural determination, the practical requirement of obtaining measurements within a reasonable time-scale means that there must be a trade-off between high angular resolution and electron count rates. For experimental measurements the acceptance aperture is generally ~2° half-angle. This also has the effect of 'smearing' the XPD diffraction features with the

possible loss of fine structure. Inclusion of angular averaging within a cluster calculation formalism is desirable to better approximate experimental results. Failure to include an acceptance angle will result in an increase in the fine structure on the calculated spectrum relative to experimental measurements. Such structure, while not incorrect, would none-the-less be impossible to detect experimentally (at least using the X-ray source intensities and analyser resolutions currently available).

2.4.6. The Angle between the Source and the Analyser:

This is a fixed parameter for scanned-angle experiments that involve rotation of the sample, which is the most common procedure for varying the emission angle. Rotation of the sample results in a change in the angle of incidence of the X-ray photon beam. For initial states other than the spherical 1s orbital, this will result in a change in the photo-ionisation cross-section of the atomic orbitals (i.e. the probability of photo-emission changes). As a result the electron intensity will vary. In order to properly calculate XPD curve shapes, this effect should be accounted for.

3. XPD MODELLING:

3.1. XPD Calculations:

The program used to calculate the theoretical XPD curves in this chapter was written by Dr. Peijun Hu [37]. The program calculates the photo-electron diffraction spectra based on a cluster of atoms surrounding a single emitter and it can be set to calculate to either a single or a double scattering approximation. The code was modified at DCU to enable calculations from large clusters to be performed with greater ease and also to facilitate the study of simple molecules, such as carbon monoxide. In addition, a program to automatically calculate the energy dependent phase shifts (up to a maximum of 35) of the scattering atoms was incorporated within the scattering code. The phase shifts are calculated from atomic wave-functions [38] based on a user specified electron kinetic energy. This eliminated the necessity to separately calculate and manually input the phase shifts for each new kinetic energy and allows the possibility of calculating scanned-energy XPD curves with only minor modification of the code.

The program calculates the diffraction pattern for a single emitter at a time. In situations where multiple emitters are called for (i.e. a multi-layer crystal structure), they are accounted for by summing curves calculated for clusters with the emitter located in different layers (one calculation for each unique site occupied by an emitter atom). The initial state of the emitted electron can be specified with correct weighting of the inter-channel interference between the ℓ-1 and the ℓ+1 outgoing waves by using appropriate radial matrix elements [29].

The program accounts for atomic vibrations within the cluster via a Debye temperature for each unique atomic species and the source-to-analyser angle can be set at the required value. The inelastic mean free path (IMFP), which ensures convergence of calculated curves at large cluster sizes, is calculated by an in-built empirical routine discussed on page 47. Excitation by either polarised or un-polarised light can be selected. This is done within the program by considering un-polarised

light as being composed of two polarised light beams with orthogonal electric (E) vectors. The appropriate beam is neglected for calculations involving polarised light.

The position of atoms within the cluster are represented by Cartesian co-ordinates (x, y and z). The emitter atom is located at (0,0,0). All other atoms are located by their displacement (Å) from the emitter. The z-direction is treated as the surface normal and positive z-values are in the direction of the cluster surface. Negative z-values represent atoms below the emitter (i.e. away from the cluster surface). During calculation of scanned-angle spectra, the cluster orientation is changed about the origin (the emitter) to simulate polar or azimuthal rotation as required. For polar scans, $\theta=0^{o}$ is when the z-direction of the cluster is pointing directly at the analyser (normal emission). Positive polar angles involve tilting the z-axis away from the analyser towards the source, while negative polar angles involve tilting in the opposite direction. For polar scans the crystal is always rotated in the plane defined by the source and analyser axes. For azimuthal scans a fixed polar angle is selected. An azimuthal angle of 0^{o} is defined when the source-analyser plane is parallel to the plane defined by the x & z axes of the cluster. When polarised radiation is used the E-vector of the light is parallel to the source-analyser plane.

A second cluster calculation program has also been used in this thesis. This was provided by Prof. Marco Torrini [39]. This program allowed only single scattering to be considered and assumed a s-wave emission (i.e. the initial and final states of the electron could not be specified). The program had similar feature to those outlined above (e.g. option for polarised or un-polarised light, spherical wave correction), and the diffraction patterns calculated by the two programs were in good agreement. In all cases similar diffraction feature shapes and positions were reproduced. The program of Prof. Torrini had one advantage in terms of experimental XPD studies. A single data file could be used to calculate diffraction patterns for a large range of different cluster structures. For a given structural parameter (e.g. a cluster inter-layer spacing) a range of possible values could be specified. The program would generate the relative atom positions in the cluster for each interval within this range, and calculate the corresponding XPD curve. This served to automate the process of calculating

diffraction patterns in situations where a large range of structural parameters required testing.

In order to illustrate the effect that various parameters, such as the emitter-scatterer separation and the outgoing electron kinetic energy, have on polar XPD features, single scattering cluster calculations (SSCC's) have been carried out using a series of simple clusters. The most basic of these involves an emitter atom and a single Cu scatterer as shown in figure 3. By systematically varying one parameter while keeping all others constant, the effect of various structural and experimental parameters on the calculated XPD spectra can be investigated. The program of Dr. Hu was used for this purpose.

3.1.1. Atom Type:

Figure 10 illustrates the effect that changing the atom type of the scatterer has on the SSCC XPD spectra. Three different scatterers are used (oxygen, copper and palladium), each located 2.0 Å from the emitter (Cu) atom along the positive z-direction. The source-analyser angle is fixed at 55°. The polar angle XPD spectra are calculated at two outgoing electron kinetic energies, 100 eV and 1000 eV. The only input parameters that change at a given energy are the atomic mass and the calculated phase shifts of each scatter (i.e. the Debye temperature was left unchanged for the different atom types). The initial state is set as an s-orbital (i.e. emission into a p-wave). Un-polarised light and single scattering, including the spherical wave correction, was used.

The calculated curves at KE=1000 eV show the characteristic features of an emitter and single scatterer cluster. The most prominent feature is the forward focusing peak at $\theta=0°$. As the polar angle is changed a series of higher-order diffraction features are observed. Although all the curves have the same general features, a number of trends can be identified as the atomic weight of the scatterer is increased (O(16.00 amu)→Cu(63.55 amu)→Pd(106.40 amu)). The forward focusing peak becomes stronger and narrower with increased atomic weight. This can be attributed to the increase in the nuclear charge of the atoms as the atomic weight increases. The Coulombic attraction between the nucleus and the electron is greater, and so forward

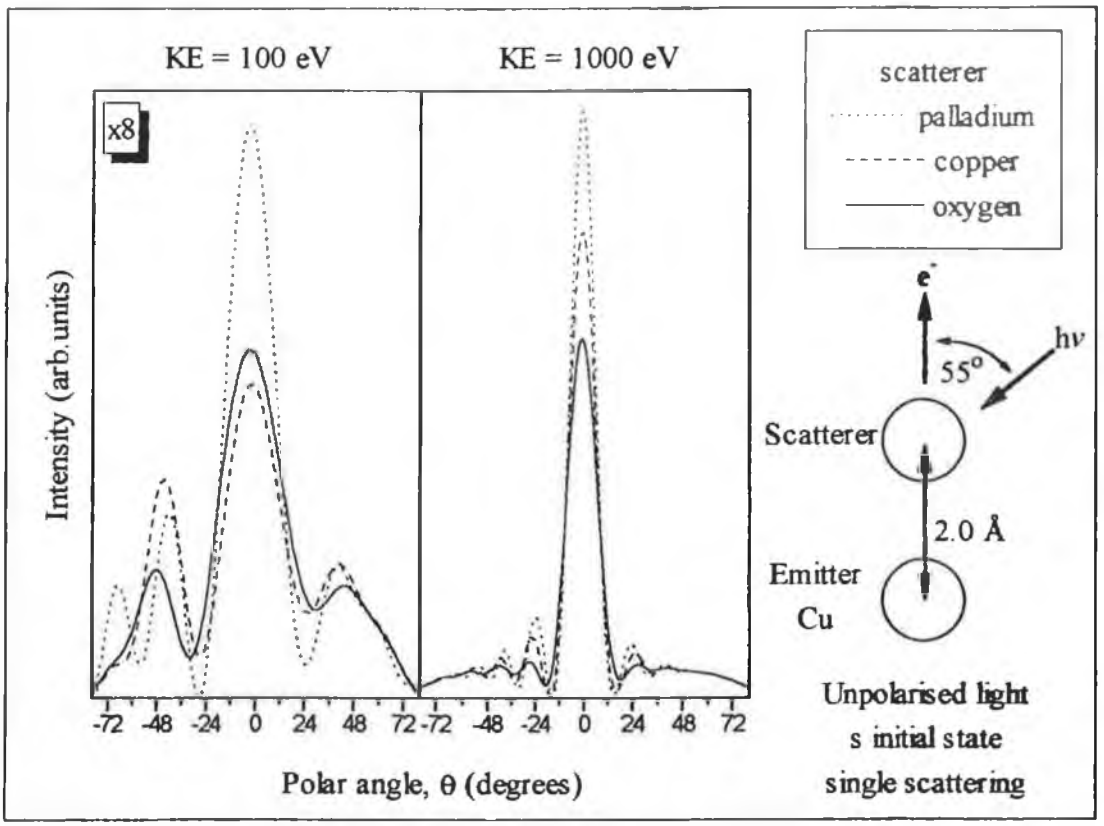

Figure 10: Variation of SSCC XPD pattern with scatterer type.

focusing becomes more dominant. In addition, the higher-order features become stronger as the scattering power increases. There is a small shift of the higher-order features towards smaller polar angles as the atomic mass of the scatterer increases.

The SSCC's at 100 eV kinetic energy are markedly different from those at 1000 eV. The first point to note is that the calculated intensities are a factor of 8 smaller in comparison to the curves calculated at KE=1000 eV. The forward focusing peak is still present but it is less dominant and significantly broader. The higher-order diffraction features are now more prominent relative to the zero-order peaks. Consequently, changes in the scattering features with atom type are much more apparent at low kinetic energies. The forward focusing peaks no longer increase systematically with the atomic mass of the scatterer, since the oxygen zero-order peak is now larger than that of copper.

The dominance of the zero-order feature at KE=1000 eV illustrates why single scattering is a good approximation of the diffraction process at high kinetic energies.

Clearly scattering along inter-nuclear axes will dominate the XPD curve features, while the electron intensity scattered away from the axes is relative weak and will contribute little to the diffraction features. Conversely, at low kinetic energies the scattering is much more isotropic. Hence, more scattering paths are capable of contributing significant intensity to the XPD curve features.

One notable aspect of the calculated curves is their non-symmetry about normal emission, which can be seen most clearly in the KE=100 eV spectra. The orientation of the scatterer directly above the emitter should lead to a symmetric forward focusing peak centred about $\theta=0^{\circ}$. The non-symmetry arises from the incidence direction of the X-ray radiation. At normal emission ($\theta=0^{\circ}$) the X-ray source subtends an angle of 55° to the z-axis of the cluster. When the analyser is measuring at a polar angle of $\theta=-10^{\circ}$ the source to z-axis angle increases to 65°. However, when the analyser is measuring at $\theta=10^{\circ}$ (structurally symmetric from the point of view of the cluster) the source to z-axis angle decreases to 45°. The non-symmetry observed is due to changes in the probability of electron excitation by the incident photons into different p type final states (p_x, p_y and p_z) as the angle of incidence of the photons to the emitting atom changes (cross-sectional effects, see later).

3.1.2. Emitter-Scatterer Separation:

Figure 11 shows the effect on the SSCC curves of using a single copper scatterer at different inter-atomic distances (2, 4 and 6 Å) from the emitter atom for outgoing kinetic energies of 100 eV and 1000 eV. The curves follow the same trends with increasing separation for emission at both 100 eV and 1000 eV. However, the absolute intensity of the SSCC's at KE=100 eV is a factor of 12 smaller compared to those for KE=1000 eV. The absolute intensity of the zero-order ($\theta=0^{\circ}$) peaks decreases with increasing atomic separation. The intensity at $\theta=0^{\circ}$ for a=6 Å is ~20% of that for a=2 Å. This can be attributed largely to the fact that at larger separation less of the outgoing electron wave is encountered by the scattering atom. For a spherical wave the electron intensity should decrease as a function of the inverse of the surface area of a sphere $[(4\pi r^2)^{-1}]$. Hence less of the wave is scattered and weaker diffraction features are observed.

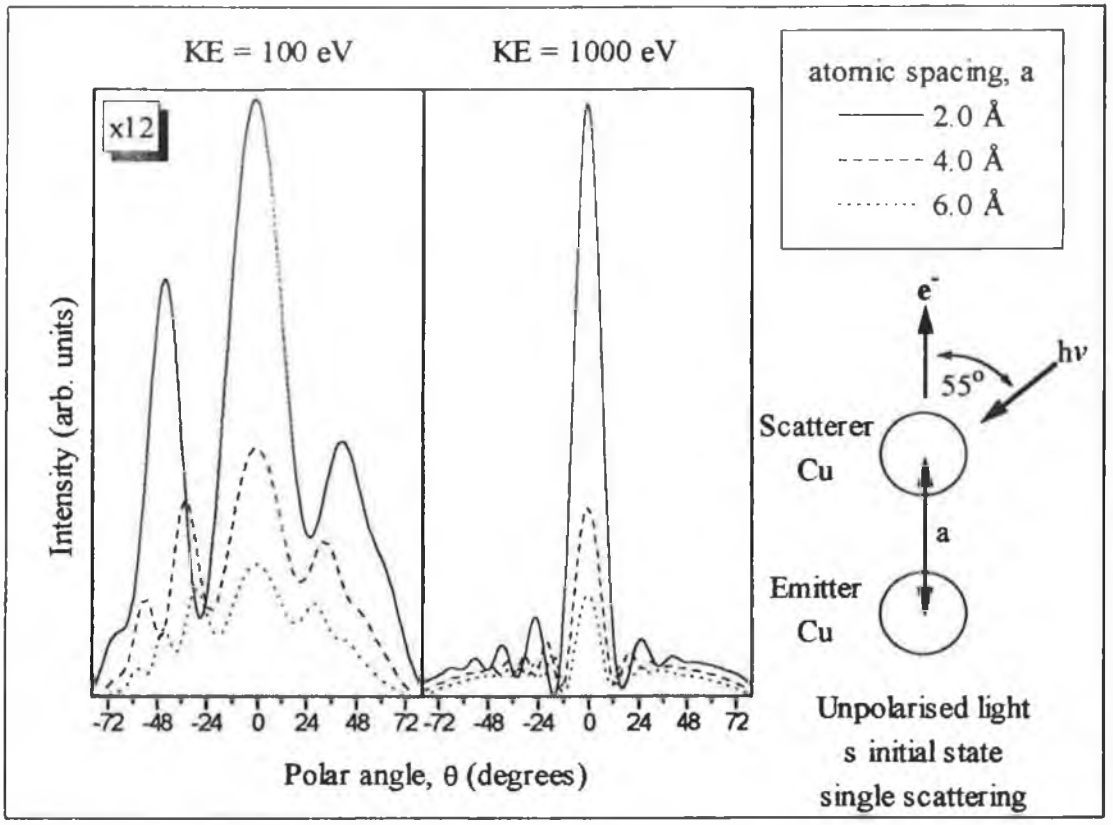

Figure 11: Variation of SSCC XPD pattern with scatterer type.

As is apparent in figure 11 and table 1, for a fixed kinetic energy the higher-order diffraction features occur closer to the zero-order feature when the emitter-scatterer separation increases. Consequently, the first minimum (destructive interference) falls closer to the zero-order maximum, reducing the angular width of the zero-order peak. This can be illustrated by again considering the two atom situation shown in figure 5. The largest path length difference that can occur between the directly emitted and the scattered wave is for $\theta=180°$. In this situation, the phase shift due solely to atom separation (again ignoring the scatterer induced phase shift) is as a result of a path length difference of 2a (twice the emitter-scatterer separation). Substituting into the equation for constructive interference:

$$n_{max}\lambda = a - a(\cos(180°))$$

and by rearranging

$$n_{max} = 2a/\lambda$$

where n_{max} is the maximum number of higher-order diffraction features that can occur for given values of a and λ. Table 2 shows the largest integer value of n for given

	E (eV) / λ (Å)	100 / 1.23	1000 / 0.39
		n_{max}	
Separation (Å)	2	3	10
	4	6	20
	6	9	30

Table 2: Variation of n_{max} with the energy (wavelength) of the outgoing electron and with the emitter-scatterer separation.

values of a and λ. It is clear that as either the electron kinetic energy or the emitter-scatterer separation increases, more diffraction features will occur in the same angular range and consequently the features themselves become narrower. Figure 11 shows that, as the emitter-scatterer separation increases, the forward focusing peaks have significantly less intensity than the forward focusing peaks due to atoms closer to the emitter. Hence, the XPD curves will be dominated by features originating from the nearest- or next-nearest-neighbouring atoms surrounding the emitter atom.

3.1.3. Angle Between Source and Detector:

As was shown in figures 10 & 11, working with a fixed angle between the X-ray source and the electron analyser results in an asymmetric XPD curve about the normal emission direction. This arises from changes in the cross-section for excitation of the initial to final states transition as the source-cluster geometry varies. It is necessary to gain some idea of the affect that changes in the source-detector angle may have on measured XPD curves.

Figure 12 shows SSCC's for different source-to-analyser angles (α) using the two atom Cu cluster at emission energies of 100 and 1000 eV as before. The most notable feature is that for $\alpha=0^\circ$ (i.e. photon incidence and electron detection along the same axis) there is an intensity minimum at normal emission ($\theta=0^\circ$). In this geometry the calculated intensity increases steadily as the polar angle moves away from zero but always remains small compared with the calculations done for $\alpha>0^\circ$. In particular for emission at KE=1000 eV the $\alpha=0^\circ$ curve appears almost flat when plotted against the other calculations on a same-scale figure.

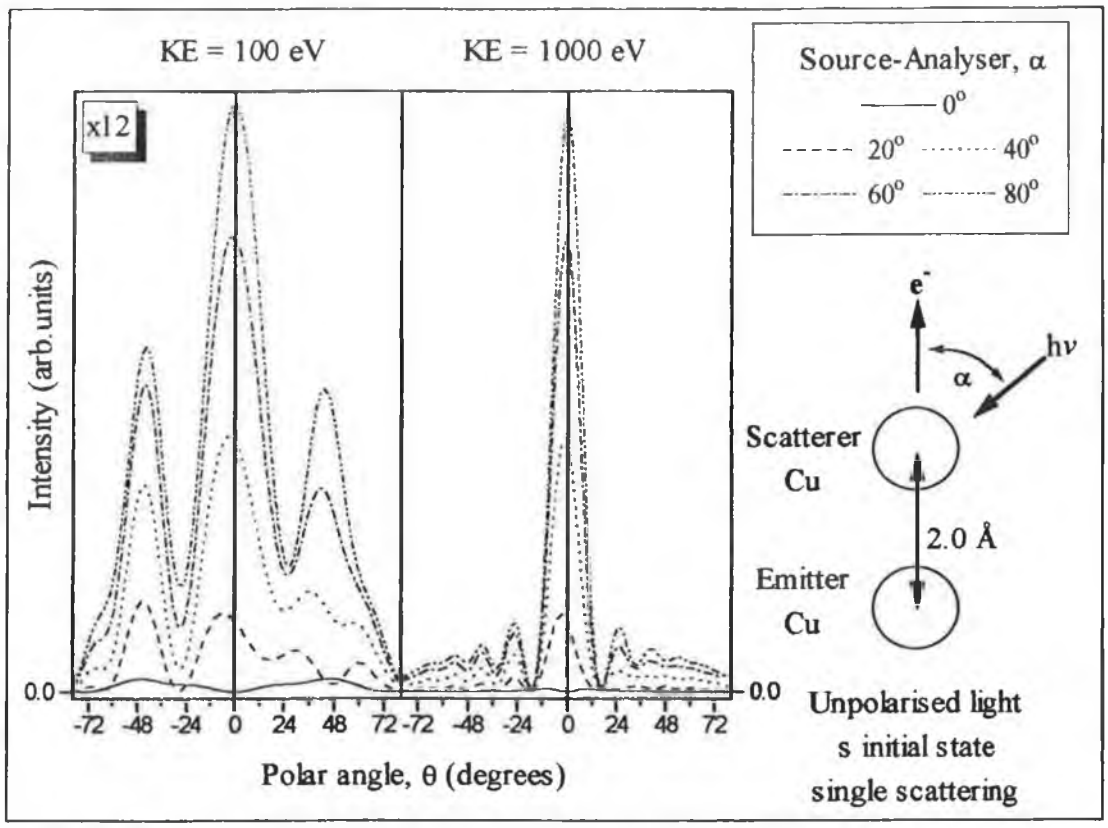

Figure 12: Effect of changing the source-analyser angle on the SSCC XPD pattern.

The lack of intensity at normal emission for $\alpha=0^0$ can be explained by the selection rules that apply to electron transitions. In order for a transition to be allowed, the combination of the initial and final states of the emitted electron, and the E-vector of the exciting photon, should be symmetric (i.e. all three components should be identically symmetric *or* one component should be symmetric and the other two anti-symmetric to any given plane). At normal emission, for an s initial state the outgoing electron wave can be thought of as being in the shape of a p_z orbital (perpendicular to the surface). The p_x and p_y orbitals are parallel to the surface and consequently provide no electron intensity along the surface normal since they have a nodal plane in this direction. The initial state (s) is perfectly symmetric. The final state (p_z) is symmetric about any plane containing the z-axis. However the E-vectors of the light at $\theta=0°$ will be asymmetric with respect to a plane containing the z-axis. As a result emission into a p_z type wavefront is symmetry forbidden and no intensity will be seen

at normal emission. The intensity increases as θ moves away from 0° due to emission into the p_x and p_y states and a partial lifting of the forbidden transition to the p_z state.

Another noticeable feature of the curves is that, at a given KE, as $\alpha \rightarrow 90°$ the absolute intensity of the XPD forward focusing peak increases substantially. This is also a consequence of the symmetry selection rules. The transition from an s-orbital into a p_z wave will be optimally excited by light with an E-vector that has identical symmetry to the p_z wave. This occurs when un-polarised light is incident at $\alpha=90°$ to the p_z axis (for p_z aligned along $\theta=0°$). As $\alpha \rightarrow 0°$, the component of the E-vector capable of exciting the transition becomes progressively smaller and disappears at $\alpha=0°$.

The asymmetry about $\theta=0°$ does not appear on the SSCC's for $\alpha=0°$ where rotation of the cluster along opposite directions is equivalent. At small source-analyser angles the asymmetry is very pronounced. This is illustrated by the fact that the maximum of the normal emission intensity occurs at non-zero (and increasingly more negative) angles as α decreases. This is a much more pronounced effect for KE=100 eV (peak max.=-6° at $\alpha=20°$) than for KE=1000 eV (peak max.=-3° at $\alpha=20°$). At large polar angles (>40°) the asymmetry in the calculated curves becomes less significant. This is true at both emission energies, although it is less apparent at KE=1000 eV due to the dominance of the zero-order peak.

It is important to note that the changes that occur with α at a given kinetic energy are much more pronounced on the *positive* polar angle side (i.e. rotation from the analyser toward the source) than on the *negative* polar angle side of the SSCC's. In fact, the curve shapes at negative angles are quite similar as a function of α. The standard mode of measuring XPD polar curves is along the *positive* direction. Hence, it is obvious from the changes observed in figure 12 that proper account of the source-analyser geometry should be included in all cluster calculation programs and that this is particularly important for experimental set-ups where α is small (<40°).

From a practical point of view figure 12 indicates that experimental set-ups with small values of α are probably best avoided where possible. If an experimental set-up has a

small angle between the source and the analyser, then locating the sample normal on the basis of the normal emission forward focusing maximum may be unsafe. However, effects such as angular averaging by the analyser aperture and instrument resolution may hide the misalignment of the zero-order peak. As has been the case for all SSCC's the affect of the analyser-source angle is most apparent at low kinetic energies, which clearly require more rigorous treatment in cluster calculation theory.

3.1.4. Initial and Final State Effects:

The large asymmetry about $\theta=0^{\circ}$ and the significant shape changes observed in figure 12 are in fact unique to the s→p transition. If an identical set of calculations is done for a purely p→d transition then the asymmetry is still present. However, it is much less pronounced and the shape of the curves remains effectively constant as a function of α, even at positive polar emission angles. If the calculations are done for a pure p→s transition then there is no asymmetry in the calculated curves (a consequence of the purely symmetric nature of the s final state). Clearly the initial and final state of the emitted electron can play a significant role in determining the shape of the calculated curve.

In order to estimate the affect of initial and final states upon the resulting photo-electron diffraction spectra, SSCC's have been performed using a two atom cluster as before. The importance of correctly accounting for these states can be judged by varying the initial and final states of the emitted electron for a fixed kinetic energy. Figure 13 shows a series of SSCC's from a two atom cluster with well defined initial and final states. The calculations are done for emission from p, d and f initial states and the curves corresponding to the transition into the ℓ-1 and ℓ+1 channels are shown separately.

The SSCC's shown in figure 13 were done at KE=100 eV. Similar calculations done at KE=1000 eV are not shown. As was the case for all previous calculations, at KE=1000 eV the SSCC's were dominated by the zero-order forward focusing peak. Apart from changes in the absolute intensity calculated, the different initial to final state combinations were virtually identical. The changes in the higher-order features

were negligible relative to the size of the zero-order peak. Clearly, at high kinetic energies the initial and final states of the outgoing electron are secondary to the forward focusing process.

In the case of KE=100 eV, the comparison of the SSCC's for the various initial states, as seen in figure 13, shows greater differences due to the relative strength of the higher-order features. The 3 curves corresponding to the $\ell \rightarrow \ell$-1 transition compare well with each other. The main difference is an increase in the absolute intensity calculated as the initial state changes from p→f. Similarly, the 2 curves for emission from p and d into the ℓ+1 channels agree well with each other and with the corresponding ℓ-1 channels (although there are shape changes in the higher-order features). The notable exception is the f→g transition. In this case the calculated zero-order peak is smaller than the higher-order features. The shape of the calculated curve can be attributed to the complexity of the g-waveforms.

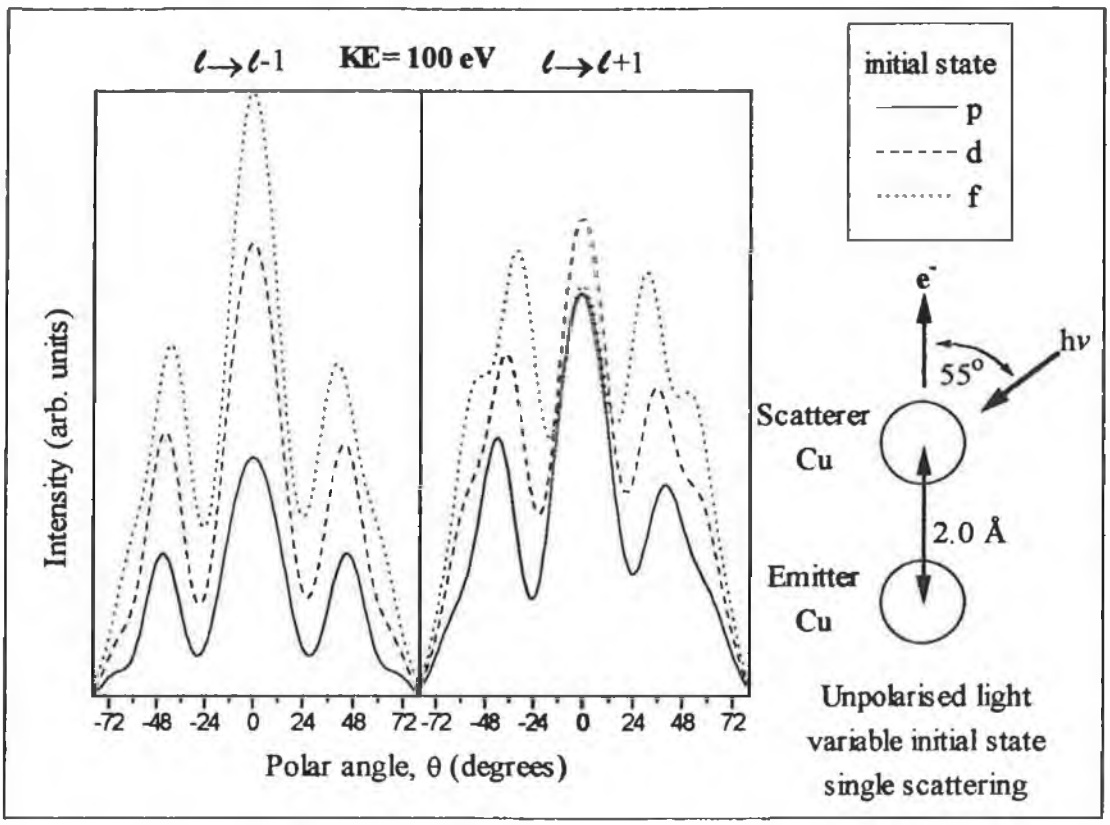

Figure 13: Effect of varying the initial and final states of the emitted electron on the SSCC's.

Given the level of agreement between the various curves in figure 13, it appears that the initial and final states do not have a dramatic effect on the curve shape even at low kinetic energies and that an s-wave approximation should be generally adequate. The main exception is for transitions involving the more complex states (i.e. f→g) [40]. Also, based on the asymmetry shown in figure 12, proper accounting of the states is preferable for the s→p transition. As always the reliability of the higher-order features calculated at low kinetic energies is increased by more rigorous simulation of the actual experimental process [40].

3.1.5. Inelastic Mean Free Path:

As electrons with a given kinetic energy propagate through a solid they lose intensity through inelastic scattering processes, such as plasmon excitation. In SSCC programs this loss in intensity is included by means of an inelastic mean free path (IMFP). This is the distance an electron can travel through the sample before its intensity is reduced to 1/e (~0.37) of its original value. The IMFP varies with the kinetic energy of the electron and the material through which the electron is propagating. Various equations for estimating the IMFP of an electron in different solids have been proposed. One of the most commonly used is the formula of Seah and Dench [41]. This formula calculates an IMFP based on the kinetic energy of the electron and the density of the material through which it is travelling. The form of the equation is:

$$\lambda_m\,(\text{nm}) = \left(538 \times E^{-2}\right) + \left(0.41 \times a_m^{1.5} \times E^{0.5}\right)$$

where:

λ_m = IMFP of the material.

E = electron kinetic energy (eV).

$$a_m\,(\text{nm}) = \left(\sqrt[3]{\frac{A_m}{N \times P_m \times 1000}}\right) \times 10^9.$$

A_m = mean atomic weight of material atoms (g/mol).

N = Avogadro's number = 6.023×10^{23} particles/mol.

P_m = density of material (Kg/m^3).

The SSCC program used in this chapter employs an empirical method of calculating the IMFP based on the electron kinetic energy and the average inter-layer spacing in the solid. The form of the equation is:

$$\lambda_m\,(\text{Å}) = 2 \times \left[\left(\frac{519.0 \times D_{lay}}{E^2}\right) + \left(0.13 \times \left(\sqrt{D_{lay}^3 \times E}\right)\right)\right]$$

where:

D_{lay} = the average layer spacing (Å).

Figure 14 shows the variation in the IMFP with kinetic energy calculated by the Seah and Dench formula for three different atomic solids, Li, Cu and Pd. The shape of the curves is characteristic of the variation of the IMFP with kinetic energy. At low kinetic energies (<30 eV) the electrons have large IMFP's. This is because, at these energies, they are no longer able to excite the dominant plasmon loss mechanisms within solids and hence can travel long distances without loss of energy. The curves pass through a minimum ("Cooper minimum") at ~50-100 eV, where the electrons excite the loss processes within the sample most efficiently. At this energy electrons within a solid are most surface sensitive (smallest escape depth). The IMFP increases with the kinetic energy beyond this minimum. The higher the kinetic energy, the further an electron can travel in a solid before its intensity is reduced by 1/e.

For comparison, the IMFP variation calculated by the formula used in the SSCC program at two values of D_{lay} (1.0 Å and 2.0 Å) are included on figure 14. It can be seen that the IMFP calculated at a given energy increases with the inter-layer spacing. The two curves calculated fall on either side of those calculated using the formula of Seah and Dench. Since most atomic crystal structures have a layer spacing between 1-2 Å, it is clear that this formula will give an IMFP comparable to that of Seah and Dench.

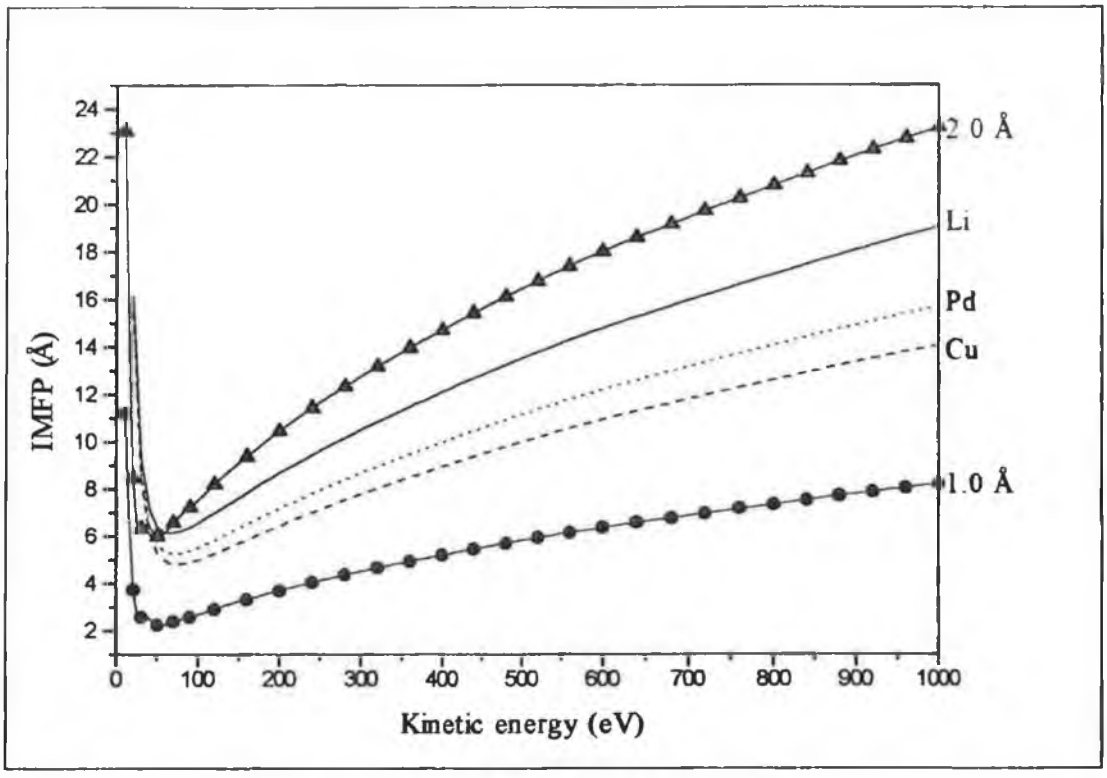

Figure 14: Calculation of IMFP using the formula of Seah and Dench [41] (Cu, Pd & Li) and the SSCC program's empirical equation (1.0 & 2.0 Å).

The function of the IMFP in cluster calculation theory is to provide convergence of the calculations as the cluster size is enlarged. Once an electron wavefront has travelled a distance corresponding to three time its IMFP it will be reduced in intensity to ~5% of its original value. Hence the contribution of scatterers at large distances from the emitter is negligible. The absolute value of the IMFP is not necessarily of vital importance in cluster calculations since it is solely a means of reducing electron intensity. A smaller IMFP than calculated by the Seah and Dench formula can be used in SSCC's as a means of reducing the contribution from distant scatterers in a cluster. As always in such cases, convergence test should be performed to ensure that the use of a 'short' IMFP does not severely distort the calculated curves.

3.2. Comparing SSCC's with Experiment (R-Factor Analysis):

It is important to consider how agreement between an experimentally obtained XPD data and a calculated curve for a given cluster geometry can be judged. The human eye has an excellent ability to judge similarity. However visual comparison of curves has its limitations. If a large number of different calculations are performed on a range of proposed models for a surface system, then there may be too many curves to realistically compare by eye. In addition, visual comparison remains purely subjective and there is no guarantee that different workers will judge the same spectra in a similar fashion. It is preferable to have some method of unbiased mathematical comparison available.

Mathematical comparison can be achieved by means of reliability factors (R-factors). Use of R-factors is routine in LEED analysis, where measured LEED patterns are compared to theoretically calculated patterns. The R-factors used in XPD are derived from those used in LEED. Two of the most commonly used are the Pendry R-factor [42] and the Zanazzi-Jona R-factor [43]. The Pendry R-factor compares the logarithmic derivatives of the experimental and the calculated curves. A logarithmic derivative is the first derivative at a point divided by the intensity at that point. The use of a logarithmic derivative makes the calculation largely insensitive to relative peak heights. The best R-factor (lowest) is returned for the calculated curve that best reproduces the positions of the peaks and troughs in the experimental curve even if there is poor comparison between the relative peak intensities of the two curves. The Zanazzi-Jona R-factor calculates the second derivative of each curve. It is sensitive to peak/trough height as well as position.

In this thesis experimental curves have been compared with theory using the Pendry R-factor. This is more correct from the point of view of SSCC's since single scattering cannot be relied upon to accurately reproduce peak intensities, and will often strongly over-emphasise forward scattering features due to its inability to account for multi-scattering effects, such as defocusing. If full multiple scattering is employed, then use of the Zanazzi-Jona R-factor as a means of evaluation may be

more valid. Multiple scattering calculations are better able to reproduce correct relative intensities in calculated curves. In this case the Zanazzi-Jona R-factor provides an additional criterion upon which to judge the comparison of the curves.

R-factor analysis allows a large number of calculated curves to be quickly compared with experimental measurements. The mode of comparison is free of any subjective bias and is identical for all curves involved. It can very quickly narrow down the range of calculated curves that need be realistically considered as matching the measured data. Comparison between two curves by R-factor analysis yields a number between 0 and 1 (total agreement and no agreement respectively). What constitutes a good R-factor is somewhat arbitrary. Any value above 0.5 is generally termed "poor agreement". R-factors between 0.4 and 0.2 are usually considered "reasonable", while values below 0.2 constitute "good agreement".

4. CONCLUSION:

This chapter has been intended as a simple introduction to the XPD process, and to methods of theoretical modelling required to recover the surface geometry. While it is intended to introduce the basic concepts it is by no means exhaustive. For further details, there are a number of excellent reviews on the subject available [14, 24-26, 28].

Currently, XPD is a fairly well established technique. The relative ease with which scanned-angle XPD measurements can be obtained, using standard laboratory XPS instrumentation, has no doubt contributed to the increasingly wide-spread use of the technique in the present decade. The main advantage of laboratory based XPD at medium (>400 eV) outgoing kinetic energies is the direct nature of the forward focusing process, which allows structural information to be obtained by visual inspection of the diffraction curves. Coupled with SSCC's, quantitative structural information can be obtained. Given good quality data, structural parameters can generally be determined to an accuracy of at least 0.1 Å.

One aspect of XPD that has not yet been fully utilised is the use of synchrotron radiation as the excitation source. Synchrotron radiation allows scanned-energy XPD measurements to be obtained. In addition, low energy (<400 eV) scanned-angle measurements can be made, which have an increased surface sensitivity. As the kinetic energy of the emitted photo-electrons decreases, the sensitivity to scattering by atoms in the plane of, and below, the emitter increases. Hence, low energy measurements contain potentially more information than high energy scans when scattering is strongly peaked in the forward direction, although at low energies cluster modelling is essential (i.e. structural information cannot be reliably obtained by visual inspection of the XPD measurements).

Another option that is made available by the use of synchrotron radiation is the measurement of XPD scans at very high outgoing kinetic energies (> 2 KeV). As the electron kinetic energy is increased, the forward focusing process becomes

progressively sharper and more dominant. Consequently, inter-atomic bond axes are more readily apparent on the XPD curves, and small shifts in the forward focusing peaks due to lattice distortions/relaxations can be more easily identified and quantified.

Perhaps the holy grail of XPD is the development of photo-electron holography into a truly quantitative and reliable structural technique [44-46]. The photo-electron angular distribution can be regarded as a *photo-electron hologram* in as much as it arises from the interference of a reference wave (the directly emitted wavefront) with scattered object waves (from the surrounding scatterers). A complete 3-D image of the surface surrounding the emitter can, in principle, be reconstructed from a full 2-D photo-electron diffraction pattern by Fourier transformation. The technique was first proposed with reference to XPD by Barton [44]. Photo-electron holography is of little use in high-energy scanned-angle XPD when forward focusing peaks dominate the curve, since these peaks carry no path length difference information. However, in back-scattering geometry the technique has more potential. Attempts to reconstruct the local geometry of atomic emitters have yielded some promising results [47, 48], although the structural accuracy is generally $\pm$0.2-0.3 Å at best. Current inversion methods are based on several wide-angle holograms measured at different photo-electron kinetic energies [48-51]. This both increases the experimental time required to obtain a suitable set of data, and necessitates the use of synchrotron radiation. Both of these factors serve to hinder the wide spread use and development of photo-electron holography. At the current state of development, photo-electron holography is perhaps best suited to use as a rapid and direct route to an *approximate* structural determination (e.g. such as determination of adsorption sites) before obtaining a more exact structure using the conventional trial-and-error technique of XPD [46, 52]. However, with further development, the technique may reach a state where 'real' images of the surface structure can be generated directly from measurements of the photo-electron diffraction pattern to a degree of accuracy comparable to the "indirect" photo-electron diffraction methods currently used.

5. REFERENCES:

[1] J.B. Pendry, Low Energy Electron Diffraction, Academic Press, New York, (1974).

[2] M.A. van Hove, W.H. Weinberg and C.M. Chan, Low Energy Electron Diffraction, Springer-Verlag, Berlin, (1986).

[3] G.A. Somorjai and M.A. van Hove in: Investigation of Interfaces and Surfaces, Eds. B.W. Rossiter, J.F. Hamilton and R.C. Baetzold, Interscience Publishers, Rochester, New York, (1990).

[4] H.J. Günterodt and R. Wiesendanger, Scanning Tunneling Microscopy I: General Principles and Applications to Clean and Adsorbate Covered Surfaces, Springer-Verlag, Berlin, (1992).

[5] L.E.C. van de Leemput and H. van Kempen, Rep. Prog. Phys., 55 (1992) 165.

[6] M. Tsukada, K. Kobayashi, N. Isshiki and H. Kagashima, Surf. Sci. Rep., 13 (1991) 265.

[7] C.S. Fadley in: Synchrotron Radiation Research: Advances in Surface and Interface Science, Ed. R.Z. Bachrach, Plenum Press, New York, (1992) pp. 421-518.

[8] D.P. Woodruff in: Angle-Resolved Photoemission - Theory and Current Applications, Ed. S.D. Kevan, Elsevier, New York, (1992) pp. 243-290.

[9] C.S. Fadley, Prog. Surf. Sci., 16 (1984) 275.

[10] P.J. Rous and J.B. Pendry, Surf. Sci., 219 (1989) 355.

[11] P.J. Rous, Prog. Surf. Sci., 39 (1992) 3.

[12] M.A. van Hove, W. Moritz, H. Over, P.J. Rous, A. Wander, A. Barbieri, N. Materer, U. Starke, D. Jentz, J.M. Powers, G. Held and G.A. Somorjai, Surf. Sci., 287/288 (1989) 428.

[13] P. Hu and D.A. King, Phys. Rev. B, 49 (1994) 2791.

[14] D.P. Woodruff and A.M. Bradshaw, Rep. Prog. Phys., 57 (1994) 1029.

[15] R. Davis, D.P. Woodruff, O. Schaff, V. Fernandez, K.-M. Schindler, P. Hofmann, K.-U. Weiss, R. Dippel, V. Fritzsche and A.M. Bradshaw, Phys. Rev. Lett., 74 (1995) 1621.

[16] G.A. Somorjai, Introduction to Surface Chemistry and Catalysis, Wiley interscience, New York, (1994).

[17] K. Siegbahn, U. Gelius, H. Siegbahn and E. Olson, Physica Scripta, 1 (1970) 272.

[18] K. Siegbahn, U. Gelius, H. Siegbahn and E. Olson, Phys. Lett., 32A (1970) 221.

[19] W.F.J. Egelhoff, Phys. Rev. B, 30 (1984) 1052.

[20] W.F.J. Egelhoff, J. Vac. Sci. Technol. A, 2 (1984) 350.

[21] S. Kono, S.M. Goldberg, N.F.T. Hall and C.S. Fadley, Phys. Rev. Lett., 41 (1978) 1831.

[22] S.D. Kevan, D.H. Rosenblatt, D. Denley, B.-C. Lu and D.A. Shirley, Phys. Rev. Lett., 41 (1978) 1565.

[23] D.P. Woodruff, D. Norman, B.W. Holland, N.V. Smith, H.H. Farrell and M.M. Traum, Phys. Rev. Lett., 41 (1978) 1130.

[24] C.S. Fadley, Physica Scripta, T17 (1987) 39.

[25] M. Sagurton, E.L. Bullock and C.S. Fadley, Surf. Sci., 182 (1987) 287.

[26] W.F.J. Egelhoff, CRC Crit. Rev. Solid State Mat. Sci., 16 (1990) 213.

[27] H.C. Poon and S.Y. Tong, Phys. Rev. B, 30 (1984) 6211.

[28] S.A. Chambers, Surf. Sci. Rep., 16 (1992) 261.

[29] S.M. Goldberg, C.S. Fadley and S. Kono, J. Elect. Spec. Relat. Phenom., 21 (1981) 285.

[30] J.M. de Leon, J.J. Rehr, C.R. Natoli, C.S. Fadley and J. Osterwalder, Phys. Rev. B, 39 (1989) 5632.

[31] J.J. Rehr, R.C. Albers, C.R. Natoli and E.A. Stern, Phys. Rev. B, 34 (1986) 4350.

[32] S.Y. Tong, H.C. Poon and D.R. Snider, Phys. Rev. B, 32 (1985) 2096.

[33] M.-L. Xu, J.J. Barton and M.A. van Hove, Phys. Rev. B, 39 (1989) 8275.

[34] H.A. Aebischer, T. Greber, J. Osterwalder, A.P. Kaduwela, D.J. Friedman, G.S. Herman and C.S. Fadley, Surf. Sci., 239 (1990) 261.

[35] T. Abukawa, C.Y. Park and S. Kono, Surf. Sci., 201 (1988) L513.

[36] X. Chen, T. Abukawa and S. Kono, Surf. Sci., 356 (1996) 28.

[37] P. Hu, Chemistry Dept., Queens University of Belfast, Belfast BT7 1NN, Northern Ireland, (1996).

[38] F. Herman and S. Skillman, Atomic Structure Calculations, Englewood Cliffs, N.J. Prentice Hall Inc., New York, (1963).

[39] M. Torrini, Chemistry Dept., University of Florence, Via G. Capponi 9, 50121 Firenze, Italy, (1996).

[40] D.J. Friedman and C.S. Fadley, J. Elect. Spec. Relat. Phenom., 51 (1990) 689.

[41] D. Briggs and M.P. Seah, Practical Surface Analysis, John Wiley & Sons, New York, (1990).

[42] J.B. Pendry, J. Phys. C: Solid State Phys., 13 (1980) 937.

[43] E. Zanazzi and F. Jona, Surf. Sci., 62 (1977) 61.

[44] J.J. Barton, Phys. Rev. Lett., 61 (1988) 1356.

[45] C.S. Fadley, S. Thevuthasan, A.P. Kaduwela, C. Westphal, Y.J. Kim, R. Ynzunza, P. Len, E. Tober, F. Zhang, Z. Wang, S. Ruebush, A. Budge and M.A. van Hove, J. Elect. Spec. Relat. Phenom., 68 (1994) 19.

[46] D.P. Woodruff, Surf. Sci., 299-300 (1994) 183.

[47] S. Thevuthasan, R.X. Ynzunza, E.D. Tober, C.S. Fadley, A.P. Kaduwela and M.A. van Hove, Phys. Rev. Lett., 70 (1993) 595.

[48] L.J. Terminello, J.J. Barton and D.A. Lapiano-Smith, Phys. Rev. Lett., 70 (1993) 599.

[49] J.J. Barton, Phys. Rev. Lett., 67 (1991) 3106.

[50] S.Y. Tong, H. Li and H. Huang, Phys. Rev. Lett., 67 (1991) 3102.

[51] B.P. Tonner, J. Zhang, X. Chen, Z.-L. Han, G.R. Haro and D.K. Saldin, J. Vac. Sci. Technol. B, 10 (1992) 2082.

[52] R. Dippel, D.P. Woodruff, X.-M. Hu, M.C. Asensio, A.W. Robinson, K.-M. Schindler, K.-U. Weiss, P. Gardner and A.M. Bradshaw, Phys. Rev. Lett., 68 (1992) 1543.

Chapter III

The Growth of Ultra-Thin Cobalt Films on Palladium {111} & {100}.

1. INTRODUCTION:

1.1. Thin-Layer Film Growth:

The growth of thin-layer magnetic films is of interest because of their potential applications in the development of reversible data-storage devices based on magneto-optical (MO) technology. The current technology is based on writing magnetic domains of micrometer size in a ferromagnetic thin-film of a rare-earth transition-metal (RE-TM) alloy (e.g. GdTbFe) and retrieving the information via the optical 'polar Kerr effect' [1]. However, the use of RE-TM alloys in such devices has a number of drawbacks. The main problem is the ease with which they can be oxidised [2], resulting in the loss of the magnetic properties (i.e. data recording ability). Addition of protective layers can reduce this problem, but it complicates the film structure and makes manufacturing more difficult. A second limitation of RE-TM alloys is that the Kerr effect of the current alloys decreases as shorter-wavelength lasers, which are required for high density data storage, are used.

The deficiencies of RE-TM alloys have led to metal multi-layers or layered metal structures being considered as possible alternative candidates for use in MO recording devices [3-6]. Cobalt thin-film structures grown with Pt [3, 5-7], Au [8] and Pd [5, 7, 9] have properties that are well suited to such applications. Layered structures that are preferentially magnetised in the direction perpendicular to the film can be readily produced using these metal combinations. These metal layers offer the advantages of a high resistance to corrosion and oxidation and an increasing Kerr effect towards shorter wavelengths [6]. Because of the potential relevance to the development of such devices, structural studies of magnetic thin films (e.g. Co) grown on single crystal metal substrates (particularly Pt, Au and Pd) are of interest. There is also a great deal of interest in the study of the growth of thin metal films on metal substrates in its own right since it represents the first stage of crystal growth [10] and because bimetallic surfaces play an important role in a number of technologically important areas, including catalysis, electrochemistry and corrosion passivation [11].

Thin metal films may exhibit properties quite different from those of the bulk metal. This is most likely to occur when a large lattice mismatch exists between the bulk crystal structure of the adatoms and that of the substrate. This mismatch can result in lattice distortions of the overlayer structure, which may alter its chemical and physical properties. Structural changes that may be induced in the overlayer by the substrate metal include modification of the bulk structure (e.g. fcc versus hcp), growth of layers with a different crystallographic index or changes in the overlayer lattice constants. Deposition of a metal on a single crystal with a significantly larger lattice parameter can result in the growth of overlayers with an expanded in-plane spacing and, as a consequence, a large in-plane strain. This strain may be relieved, in part, by a contraction of the inter-layer spacing to compensate for the expansion [12] resulting in a tetragonally distorted lattice structure. Alternatively, the in-plane expansion may cause the adlayer to adopt a crystal structure other than its normal bulk structure. For instance, Co can be grown in a meta-stable fcc phase on Pt {111} at room temperature, even though the most favourable Co bulk structure at room temperature is hcp [13].

An extreme example of a distorted overlayer structure was suggested by Bain [14], whereby sufficient biaxial expansion of a fcc lattice in the {100} plane would result in a structural transition to a stable bcc or bct (body-centred-tetragonal) phase. Such an expansion could be envisaged to occur as a result of overlayer growth on a fcc {100} substrate with sufficiently large surface lattice parameters to stabilise the transition. Recent papers have proposed the existence of a meta-stable bct phase, both theoretically [15] and experimentally [16, 17] for Cu overlayers grown on Pd {100}. However, doubts have been raised about the validity of the theoretical results [18].

The structure of Co overlayers grown on Cu {111}, {100} and {110} single crystals (~1.7% lattice mismatch) have been widely studied [19-24]. In particular, Co on Cu {111} has received a great deal of attention [21-24]. The initial Co adlayers are found to grow in islands with an fcc lattice structure. The overlayers undergo a fcc→hcp transition at θ_{Co}~4-6 ML as they relax back to their bulk lattice parameters. Pre-adsorption of a surfactant (Sb) was found to delay this transition until θ_{Co}~10 ML

[23]. The Sb was proposed to induce layer-by-layer growth resulting in slower overlayer relaxation as a function θ_{Co}. In the case of Co grown on Cu {100}, the overlayers are found to grow in a fcc lattice structure with a slight tetragonally distortion (expanded in-plane to the lattice parameter of Cu, with an inter-layer contraction of ~0.04 Å) [20]. The deposition of Co on Pt {111} is found to result in a quasi-layer-by-layer growth for ~3 ML followed by island growth [25]. The overlayer structure has been reported as 2-domain fcc {111} [13] or hcp {0001} [25].

Incoherent epitaxial growth of Co on Pd {111}, with the adlayers immediately adopting the bulk Co in-plane lattice spacing, has been reported by Purcell *et al* on the basis of RHEED, AES and LEED measurements [26]. A separate study by Yamazaki *et al* reported an in-plane strains in low θ_{Co} (<2 ML) overlayers on Pd {111}, which was rapidly released as the coverage increased (~3 ML) [27]. In this chapter the results of studies on the growth of Co thin films on Pd {111} and also on Pd {100} utilising scanned-angle XPD and ion-scattering spectroscopy (ISS) are presented. This combination of techniques allows the determination of the initial growth mechanism of the Co overlayers and of the crystal structure of the overlayers up to high coverages (θ_{Co}>20 eML).

The Co atom (radius=1.25 Å) is significantly smaller in size than the Pd atom (radius=1.37 Å) [28]. The difference in atomic size is reflected in the ~9.5% mismatch that exists between the lattice parameters of their bulk crystal structures (i.e. in order for Co overlayers to grow pseudomorphic with a Pd substrate they must undergo an in-plane expansion of ~9.5% from their bulk lattice parameter).The large mismatch between the adatoms and the substrate may result in the growth of Co overlayer with a distorted lattice structure or in a meta-stable fcc phase such as have been observed in the studies outlined above. The forward focusing effect of scanned-angle XPD is useful in probing the structure of metal overlayers [29]. At high electron emission energies (>500 eV) qualitative and semi-quantitative information about the local structure surrounding an emitting atom can be obtained directly from polar XPD scans (e.g. Cu/Ni {001} [30]). Due to the direct nature of the forward focusing peaks

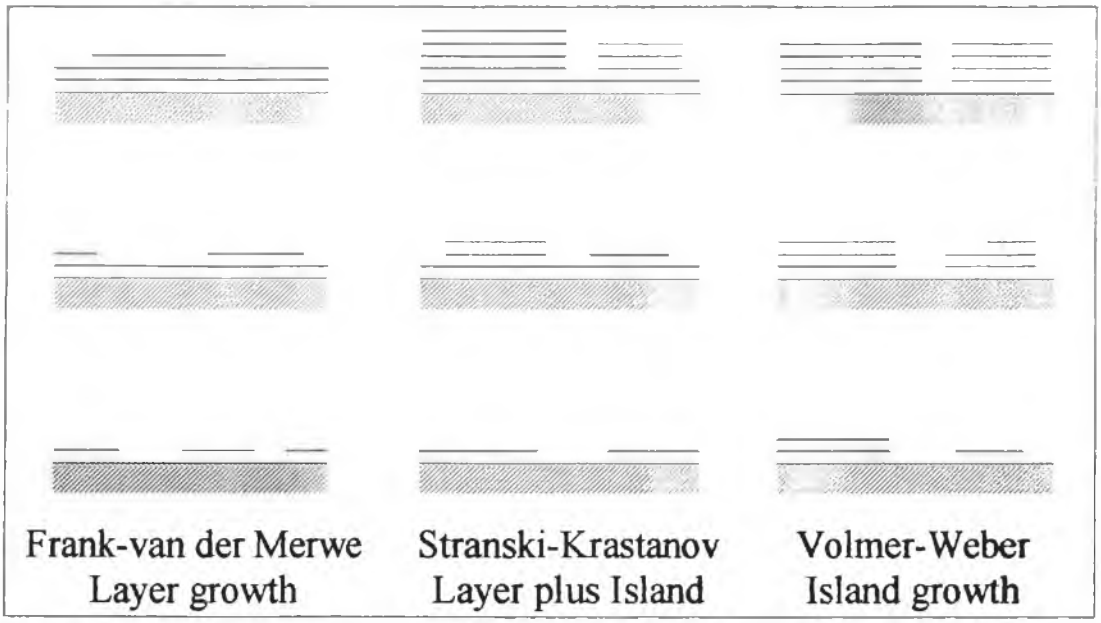

Figure 1: Schematic representation of the 3 crystal growth mechanisms.

observed in XPD, overlayer lattice distortions can be readily identified and quantified using single scattering modelling [31].

1.2. Metal-on-Metal Growth:

Before proceeding to the experimental sections it is pertinent to briefly cover some of the mechanisms and basic terminology used in the growth of ultra-thin metal films on metal substrates. This discussion also has direct relevance to the forthcoming chapter on the growth of Cu on Pd {110} (Chapter IV). Crystal growth on surfaces was first classified into 3 general mechanisms by Bauer [32]. The three growth modes are island (Volmer-Weber, VW), layer plus island (Stranski-Krastanov) and layer (Frank-van der Merwe, FM) growth. Figure 1 shows a schematic representation of the three mechanisms. According to the quasi-equilibrium description given by Bauer [33] these three growth modes are governed by the surface free energies of the deposited film (σ_f) and the substrate (σ_s), the interface free energy (σ_i) and the strain energy (σ_e) [19, 34]. The relative size of the different energies dictates the growth mode.

1.2.1. Layer growth (FM):

The deposited film is expected to grow layer-by-layer when:

$$\sigma_f - \sigma_s + \sigma_i + \sigma_e < 0.$$

If there is a large difference between the two surface free energies (σ_f & σ_s) then these parameters will strongly influence the growth mechanism. In FM growth the adatoms are more strongly bound to the substrate than to each other ($\sigma_f<\sigma_s$). The initial adatoms condense to form a complete monolayer. This is then covered by a less tightly bound second layer. If the decrease in binding is monotonic toward the value for the bulk crystal then layer growth may occur. Whether or not FM growth persists to high coverages is strongly dependent on the strain energy (i.e. lattice mismatch between the substrate and the adsorbate atoms). As σ_e increases FM growth becomes less probable. Of course, FM growth is still possible in systems with a large lattice mismatch *provided* the strain energy within the layers can be relieved (i.e. by defect mechanisms). In reality, true FM growth can only occur for homogenous systems where the strain energy is zero (e.g. Cu grown on Cu).

1.2.2. Layer plus island growth (SK):

If the above inequality reverses with film thickness then the growth mode will be SK. Although represented in figure 1 as being a single layer followed by island growth, the SK growth mode refers to growth of islands following deposition of one *or* more complete monolayers. Any factor that disrupts the monotonic decrease in binding energy with coverage, thereby resulting in a high free energy at the adlayer surface, may cause layer growth to become unfavourable. A large lattice mismatch is one of the more likely reasons for SK growth. Growth in islands increases the relative number of "easy-displaceable" atoms, which serves to minimise σ_e [23].

1.2.3. Island growth (VW):

If the inequality is reversed from the outset of crystal growth then the adatoms grow as three-dimensional islands. In this case the adatoms are more strongly bound to each other than to the substrate ($\sigma_f>\sigma_s$) and small clusters nucleate directly on the surface as crystal growth progresses.

The quasi-equilibrium crystal growth modes predicted by the summation of energies shown above may not always be observed in practice. Non-equilibrium growth can be

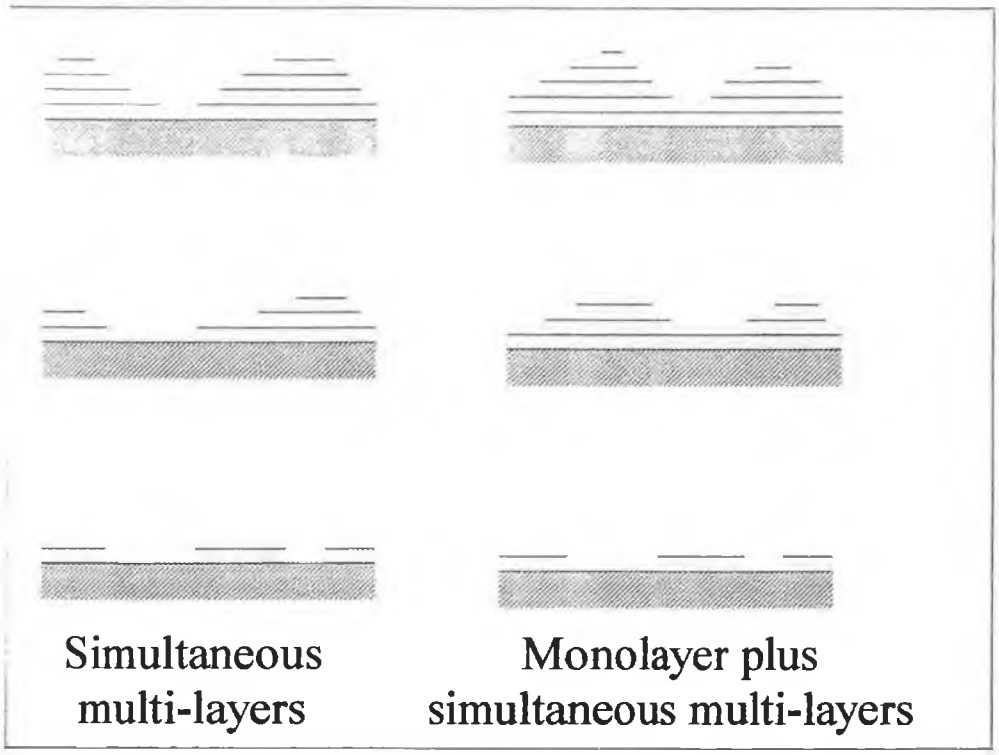

Figure 2: Representation of the SM and MSM growth mechanisms.

envisaged as occur if kinetic factors (such as surface diffusion) are too slow to allow the overlayers to attain local equilibrium during deposition [35]. For example, FM growth requires that atoms impinging and sticking on top of an incomplete adlayer must diffuse to the edge in order to be incorporated in the layer. Surface diffusion processes must be rapid in comparison with the rate of deposition and the time-scale of observation in order for equilibrium crystal growth to occur. Kinetic limitations give rise to the possibility of controlling the growth mode attained by careful control of the sample temperature during deposition [35, 36]. The decisive process that determines the actual growth mode in the kinetic regime is the inter-layer mass-transport [37]. In the absence of rapid (on an experimental time-scale) inter-layer mass-transport VW growth will always be observed.

1.2.4. Simultaneous multi-layers:

In addition to the 3 basic growth modes outlined above, two additional classifications have been proposed, "simultaneous multi-layer" (SM) and "monolayer plus simultaneous multi-layer" (MSM) growth [38, 39]. These are illustrated in figure 2. The SM growth mode (also called the Poisson mode) is an idealised case arising from

negligible adatom surface mobility. Hence, the adatoms 'stick' where they hit the sample and the layers form randomly. Growth of the n^{th} layer can begin once a fraction of the $(n-1)^{th}$ has formed. This is a meta-stable version of the FM mode and has been referred to as pseudo-FM growth. The growth mode can vary in a continuous fashion between SM and true FM depending on the degree of surface mobility and how the mobility varies with coverage. MSM is envisaged as arising when there is a sharp difference between the mobility of the adatoms on the clean substrate and their mobility on the adlayers. In MSM the mobility on the clean surface is rapid enough to allow uniform growth of the first monolayer. Subsequently the mobility drops sufficiently for the growth to become SM-like.

1.2.5. Surface Segregation / Inter-diffusion:

The three idealised growth modes neglect the possibility that substrate atoms are mobile and may segregate to the surface of the adlayer or inter-diffuse with the arriving adatoms during film growth. Alternatively, the arriving "hot" metal atoms may have sufficient energy to undergo "place-exchange" with the substrate atoms. Surface segregation and inter-diffusion are activated by increasing substrate temperature. In order for a process to be significant its rate should be comparable to the film deposition rate.

Inter-diffusion (alloying) at the substrate/overlayer interface can affect the growth mode. Surface stress and surface elasticity play an important role in alloy formation [40]. They usually favour incorporation (alloying) of adatoms larger than the substrate atoms. Formation of surface alloys where the adatom is significantly larger than the substrate atom, such as Pb/Cu [41] and Na/Al [42], have been reported, whereas surface alloys involving adatoms that are smaller than the substrate atoms are rare at room temperature.

Surface segregation can be considered a special form of substrate/adlayer inter-diffusion where whole islands or layers, rather than single adatoms, are buried in the substrate. Surface segregation of the substrate atoms may occur when the substrate surface free energy is lower than the adlayer surface free energy. This situation favours island (VW) growth. The islands, once formed, can lower their energy by

allowing themselves to be coated by a thin film of the substrate atoms. It is difficult to estimate the activation energy for surface segregation because, in addition to the surface free energies, factors such as the heats of solution and the size mismatch also play a role in the process.

2. EXPERIMENTAL:

All measurements were carried out in a standard UHV chamber with a base pressure of ~$2x10^{-10}$ torr. The chamber was equipped with a standard laboratory X-ray source (Al & Mg anodes) and with a multi-channel hemispherical electron/ion energy analyser. The acceptance aperture of the energy analyser was variable. A 3-grid LEED optics was available for checking the surface crystallography and a quadrupole mass spectrometer was used for residual gas analysis.

The Pd single crystals (cut and polished along the {100} & {111} planes) were mounted on a manipulator with mechanised azimuthal and polar motion, which ensured reproducibility in the measurement geometries. Azimuthal motion of 180° was possible. Polar angles were measured with respect to the surface normal (θ=0°) and polar scans could be measured to an angle of 80° off-normal. Polar XPD curves were obtained by rotating the sample around the axis of the manipulator. There was a fixed angle of 55° between the X-ray source (incident light direction) and the analyser (emission direction) in the plane of polar rotation.

Sample cleaning was done by cycles of argon ion bombardment and annealing to ~900-1000 K by resistive heating. The sample temperature was monitored by a chromel-alumel thermocouple, which was spot welded to the side of the crystal. During the initial stages of cleaning residual carbon on the surface was removed chemically by oxygen treatment. This was done by heating the crystal to ~800 K in an oxygen ambient of ~$1x10^{-7}$ torr. Residual oxygen was removed by a short sputter /anneal cycle. Subsequently a clean surface could be routinely obtained by short bombard and anneal cycles. Surface cleanliness was monitored by XPS at normal emission. No contaminants were detectable above the noise level on the clean surface. Reproducible formation of a well-ordered Pd surface was confirmed by LEED.

Cobalt dosing was done using an electron beam evaporator. Coverages were monitored by XPS at normal emission. The evaporation rate was ~1 ML every 3 minutes and the chamber pressure remains below $8x10^{-10}$ torr throughout the

evaporation. Carbon contamination after Co deposition was estimated to be never more than 0.1 ML. In many cases no C 1s XPS signal was detected above the noise level after Co evaporation. All evaporations were done at room temperature.

2.1. He^+ LEISS Measurements:

The energy analyser, set in ion current mode, was used to collect low energy He^+ ion scattering spectroscopy (He^+ LEISS) measurements from the clean and Co covered Pd surfaces. An ion current of ~$1x10^{-8}$ A/cm^2 at 1 KeV energy was used. The incident ion beam was set at ~45° to the surface normal and the scattering angle was ~135°. Under these conditions no variation in the surface composition was observed over the time required to record several complete spectra.

The growth mode of Co during the initial stages of deposition on the Pd crystals was determined using He^+ LEISS. This was done by plotting the decay of the Pd ISS signal (or the evolution of the Co signal) as a function of the Co coverage (θ_{Co}). θ_{Co} was estimated from the background-normalised integrated areas of the Co and Pd core level XPS peaks using the equation:

$$\frac{I_{Co}}{I_{Pd}} = \frac{I^{\infty}_{Co}\left(1 - \exp\left[\frac{-d}{\lambda_{Co}}\right]\right)}{I^{o}_{Pd}\exp\left(\frac{-d}{\lambda_{Pd}}\right)}$$

This equation only holds true for XPS measurements taken at normal emission (as was the case for all measurements) although it can be modified for measurement taken in off-normal orientations. I_{Co} and I_{Pd} are the Co and Pd core level XPS intensities respectively measured after deposition of a certain thickness of Co, d (Å). I^{o}_{Pd} and I^{∞}_{Co} are the XPS intensities measured from the clean Pd crystal and from a thick film coverage of Co (approximating bulk) respectively. λ_{Co} and λ_{Pd} are the inelastic mean-free-paths (IMFP's) of Co and Pd at their respective outgoing kinetic energies calculated using the formula of Seah and Dench [43].

The XPS core level peaks were measured using a large aperture acceptance angle on the energy analyser. This ensured that the measured XPS intensities were not unduly affected by XPD processes. Core level excitation was achieved using Mg K_α radiation (i.e. electron emission energies of ~473 eV for Co and ~917 eV for Pd). IMFP's of 9.4 Å and 13.1 Å were used for λ_{Co} and λ_{Pd} respectively. The above equation is based on the assumption of layer-by-layer growth. If the initial growth is in islands then the equation will under-estimate the actual coverage. The calculated thickness, *d*, can be converted into equivalent monolayers (eML) by dividing by 2.05 Å for a fcc {111} or a hcp {0001} overlayer structures and by 1.77 Å for a fcc {100} structure. These are the inter-layer spacing values of the corresponding bulk Co single crystals [28]. The values calculated represent only an approximation of the actual coverage.

2.2. XPD Measurements:

All XPD measurements were made at room temperature using un-monochromatic Al K_α radiation ($h\nu$=1486.6 eV). XPD curves were acquired by monitoring the electron intensity at a kinetic energy corresponding to the maximum emission from a suitable atomic core level. The most intense Pd core level emission arises from the 3d electron shells. Al K_α excitation results in the emission of electrons from the Pd $3d_{5/2}$ level at a kinetic energy of ~1145 eV. In the case of Co, the most intense emission is from the 2p levels at a kinetic energy of ~700 eV ($2p_{3/2}$). Background normalisation was done by monitoring the electron intensity at a point on the high kinetic energy side of the respective core level emission peaks.

A small acceptance aperture (cone of half-angle ~2°) was used for all XPD measurements. Both the azimuthal and the polar XPD curves were measured in 1° steps. Normal emission (±1°) was located using the maximum of the normal emission forward focusing peak measured from the clean Pd surface. The high symmetry azimuthal directions, along which the polar XPD curves were measured, were located via a combination of the substrate LEED pattern and the symmetry of the azimuthal curves. The azimuthal alignment was accurate to ±2°. All azimuthal curves shown in this chapter have been symmetrised around the ϕ=0° azimuthal angle. The XPD

curves shown in this chapter are plotted as $(I-I_{min})/I_{max}$ to allows direct comparison of the modulation strength (anisotropy) of different curves. Quantitative analysis of the XPD curves was done by comparison with theoretical calculations based on a single scattering cluster-spherical wave (SSC-SW) model.

2.3. Single Scattering Cluster Calculations:

The electron emission from the clean Pd and Co covered surfaces was modelled using single scattering theory. The out-going electron wave was assumed to be s-like in character and a spherical wave correction was applied in the calculations. These approximations are valid at the high out-going kinetic energies being modelled (Co~700 eV; Pd~1145 eV). A total of 23 and 29 phase shifts were calculated for electron emission at 700 eV and 1145 eV respectively, using Herman-Skillman wavefunctions [44]. Bulk Debye temperatures (θ_D) of 385 K for Co and 274 K for Pd were used. An inner potential of 10 eV was assumed.

IMFP's of 11.5 Å and 15.1 Å were calculated for emission from Co and Pd respectively, using the formula of Seah and Dench [43]. The cluster sizes were limited to twice the valve of the IMFP in all directions. Convergence tests on larger clusters showed this to be a valid approximation. In the case of emission from Co, the Pd atoms forming the substrate were set in a bulk terminated lattice structure. The calculations assumed a 2° analyser half-angle acceptance cone.

3. RESULTS:

3.1. The Pd {111} Surface:

Figure 3 shows a model of the Pd {111} single crystal structure. The bulk crystal structure of Pd is fcc, with lattice parameters as shown in figure 3. The primitive surface unit cell (side=2.75 Å) is shown on the surface model. Two different three-fold-hollow (TFH) sites (both indicated in figure 3) can be identified on the {111} surface. The sites are differentiated on the basis of the underlying atoms. The 'hcp' TFH site has a 2nd layer Pd atom directly beneath it. In contrast, the 'fcc' TFH site has a 3rd layer Pd atom directly beneath it. The cross-sections shown in figure 3 are taken along the $(1\bar{2}1)$ azimuths of the crystal surface. Direct forward scattering peaks are most prominent along these azimuths due to the fact that close-packed "chains" of atoms occur in these directions (i.e. the nuclei of the near-neighbour atoms in different layer are aligned along these azimuths). The polar angles at which the main forward

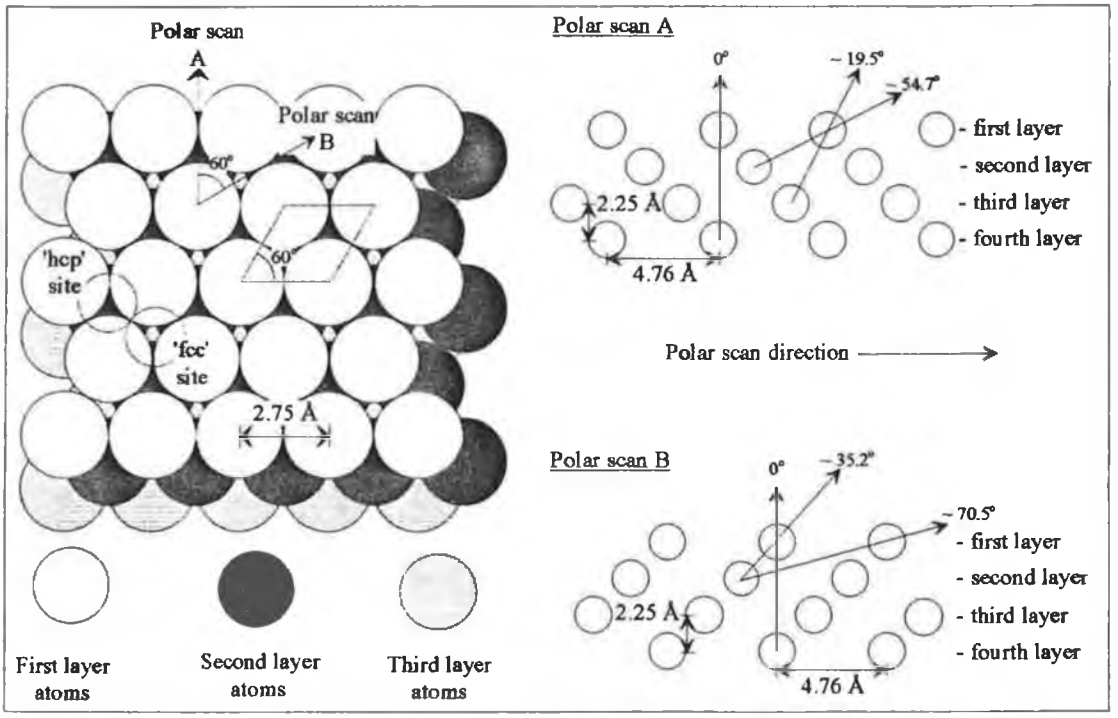

Figure 3: Model of the clean Pd {111} single crystal surface and polar angles of forward focusing peaks based upon a bulk truncation of the sample. No account is taken of refraction due to the inner potential.

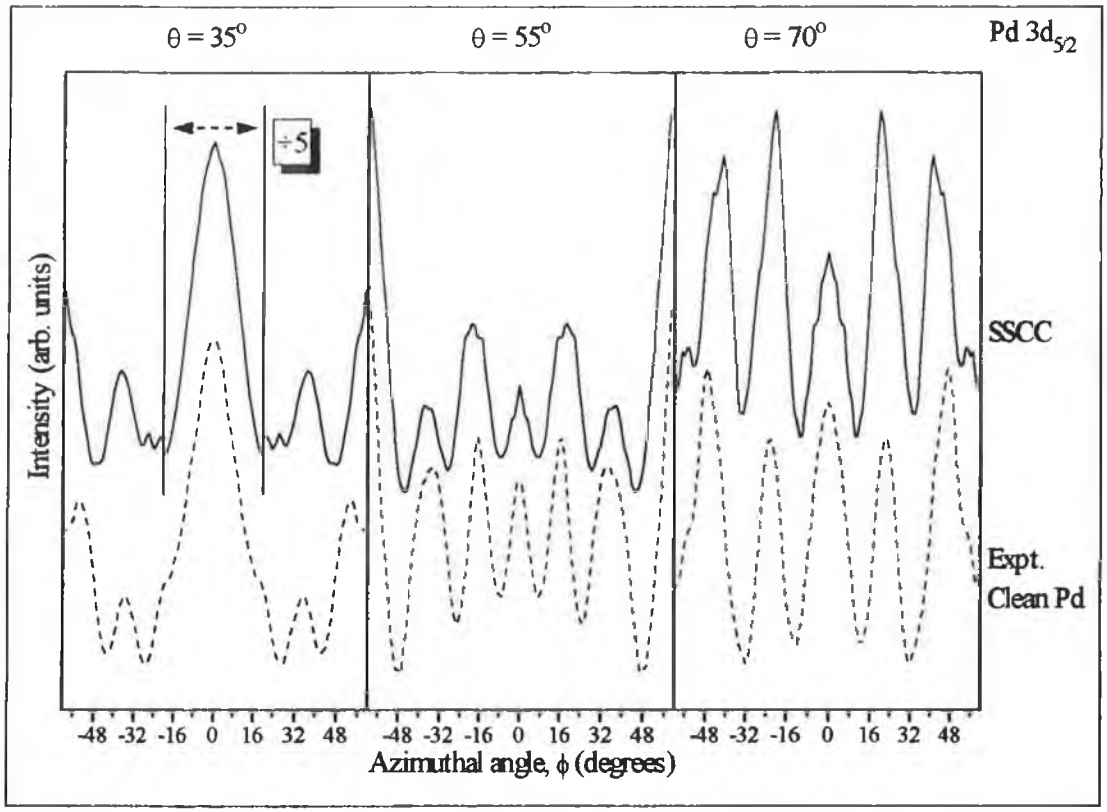

Figure 4: Azimuthal XPD scans measured from the clean Pd {111} single crystal surface. The dashed curves are experimentally measured data and the solid curves are the corresponding SSCC's at polar angles (θ) of 35°, 55° and 70°.

focusing peaks are expected to occur are shown on the cross-sections. These values are calculated on the basis of a bulk terminated crystal structure.

The fcc {111} crystal surface has 3-fold symmetry (i.e. there is an equivalent azimuthal direction on the surface every 120°), which is evident on azimuthal XPD scans measured from the clean Pd {111} surface using $Pd_{5/2}$ emission as shown in figure 4. Azimuthal scans were measured from the clean surface at polar angles (θ) of 35°, 55° and 70°. For the scans taken at 35° and 70° the main forward focusing peaks occurs at an azimuthal angle (ϕ) of 0° (corresponding to 'Polar scan B' $\left([1\bar{2}1]\right)$ in figure 3). In the case of the scan taken at θ=55°, the main forward focusing peak occurs at (the equivalent) ϕ angles of -60° and 60° (corresponding to 'Polar scan A' $\left([2\bar{1}1]\right)$ in figure 3).

SSCC's done for emission from a bulk terminated Pd {111} cluster are included in figure 4 for comparison. Details of the cluster size and other calculation parameters are given in the experimental section. The calculated curves correctly predict the number of peaks observed in the experimental curves and the position of the forward focusing peaks is correctly reproduced. However, the positions and shape of the higher-order diffraction features are less well reproduced. This is particularly evident in the θ=35° SSCC, where the dip observed in the experimental curve at ϕ=-60°/60° is not observed theoretically. The discrepancies between theory and experiment can be largely attributed to the neglect of multiple scattering effects in the SSCC's.

The characteristic over-estimation of the strength of the forward scattering peak by single scattering theory is also clearly evident in figure 4. The forward focusing peak (from ϕ=-19° to 19°) on the SSCC done for θ=35° has been reduced by a factor of 5 relative to the higher-order features to aid visual comparison. No reduction was required for the other two calculations. The over-estimation in the θ=35° SSCC is due to the small separation (~2.75 Å) between the emitter/scatterer atoms that give rise to this forward focusing peak. This results in a large proportion of the emitted wavefront being scattered into the forward direction. In addition, the contribution to this peak due to emission from 3rd and deeper layers is over-estimated due to the neglect of 'defocusing' along a chain of atoms by single scattering theory [45, 46]. A final point to note is that the forward focusing peak on the θ=70° azimuthal scan (at ϕ=0°) is of similar intensity to the higher-order diffraction features. If the crystal structure were not known then this peak could only be identified as a zero-order scattering feature by comparison with SSCC's.

Figure 5 shows polar XPD curves measured along the two high symmetry azimuths shown in figure 3 (ϕ=-60°/60° and ϕ=0°). SSCC's done for a bulk cluster are included as before. The forward focusing features at θ~55° & ~35° have been reduced by factors of 3 & 5 respectively to aid comparison. There is good agreement between theory and experiment, with all the main features of the polar scans being reproduced by the SSCC's. The fact that the position of the forward focusing peaks are in excellent agreement confirms that the polar rotation is calibrated correctly. The

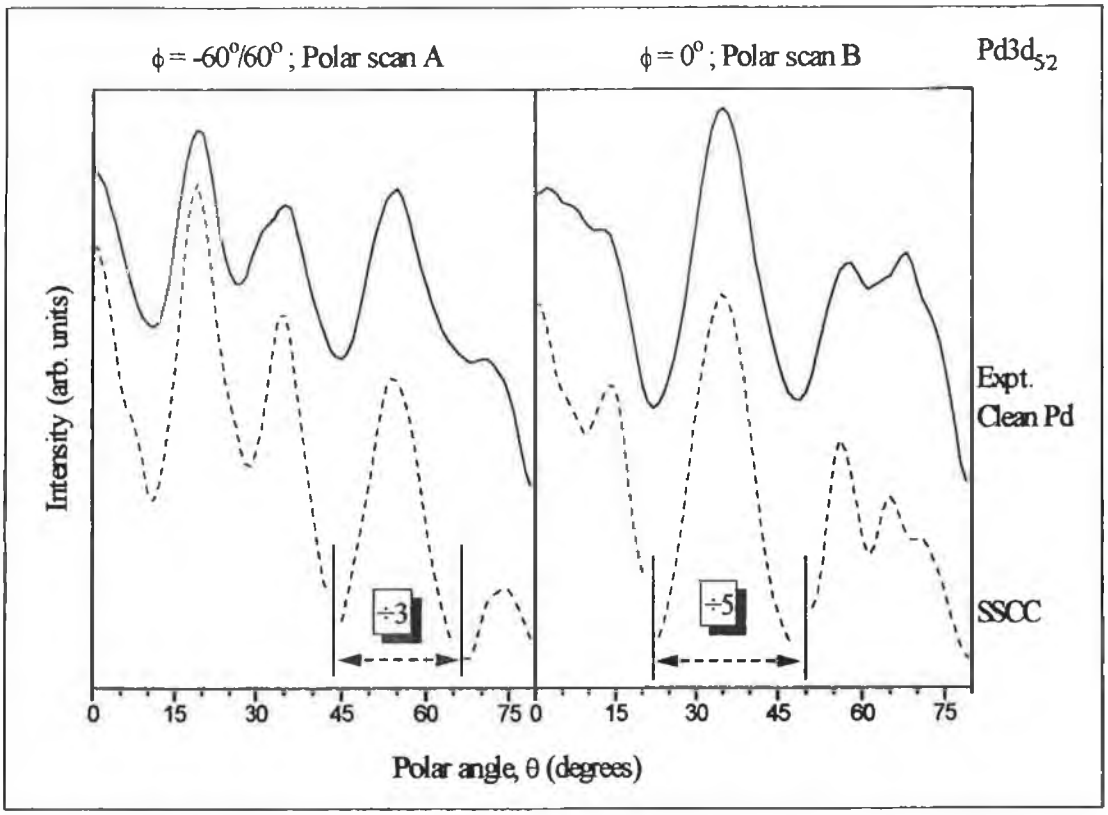

Figure 5: Polar XPD scans measured from the clean Pd {111} single crystal surface along the 2 high symmetry azimuths. The solid curves are experimentally measured data and the dashed curves are the corresponding SSCC's.

normal bulk crystal structure of cobalt at room temperature is hcp. Figure 6 shows a model of the clean hcp Co {0001} crystal structure. The two cross-sections shown are the equivalent directions to those shown in figure 3. Apart from the difference in the crystal lattice parameters, the in-plane surface structure of Co {0001} is identical to that of Pd {111}.

The fcc and hcp bulk crystal structures are distinguished by their stacking order. The stacking in a bulk fcc {111} crystal can be represented as 'ABCABC....', whereas that of a hcp {0001} crystal is 'ABABAB....'. This distinction can be seen clearly in the cross-sectional cuts shown in figures 3 and 6. For the hcp {0001} crystal every second layer is equivalent (directly beneath each other) whereas in the fcc {111} crystal only every third layer is equivalent. Again, there are two distinct TFH adsorption sites on the hcp {0001} surface. Analogous to the Pd {111} surface, the

'hcp' site on Co {0001} is directly above a 2nd layer atom. However, in the case of the hcp {0001} structure there is no bulk atom directly beneath the 'fcc' site.

Unlike the fcc structure, which has prominent forward scattering peaks at θ~20°, ~35°, 55° and ~70°, hcp crystals have only two main off-normal forward scattering peaks (at θ~35° and ~55°). However, these peaks occur along both of the polar scan directions, A and B. As a result, polar scans taken along the two directions are similar. Considering the two azimuthal cross-sections shown in figure 6, a 'perfect' hcp {0001} crystal surface would in theory show three-fold symmetry. However, in reality the crystal will always display six-fold symmetry due to the existence of surface defects and atomic step edges on the surface. Each atomic step on the crystal surface reverses the stacking termination (ABA....→*B*ABA....). The effect of this is to swap the cross-sections of the two polar scan directions shown in figure 6.

Figure 7 illustrates how a step edge results in the conversion of 'Polar scan A' into 'Polar scan B' for a hcp crystal. The shaded atoms represent the additional layer created by the step edge. Of course, a step edge resulting from the removal of 1st layer

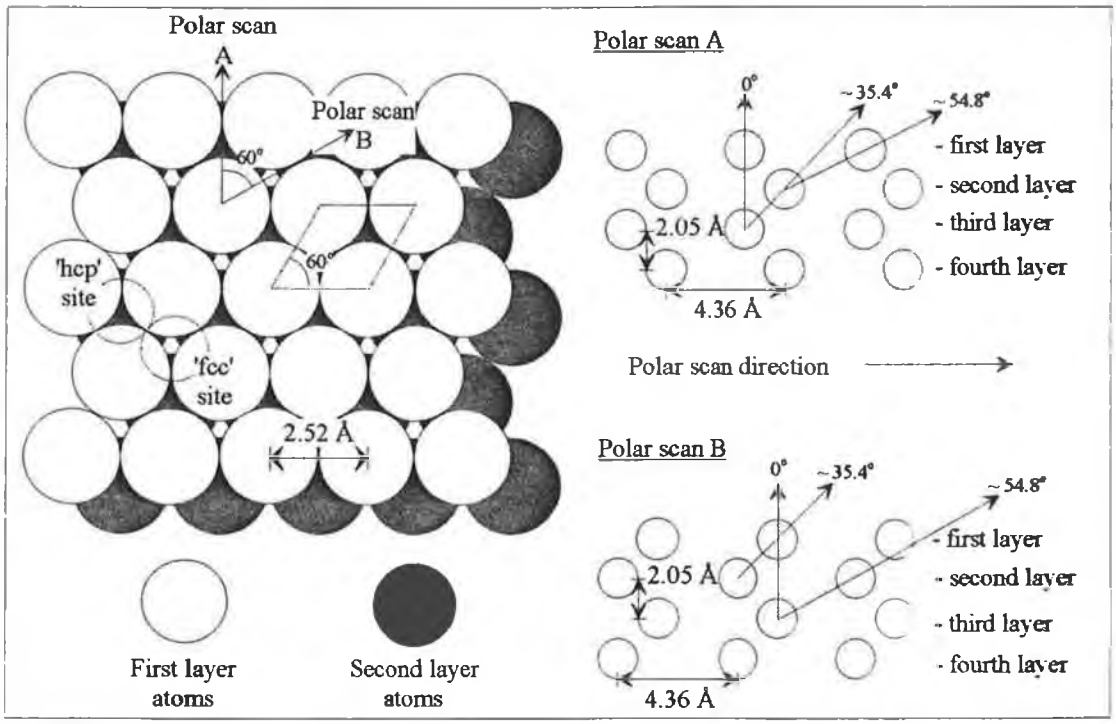

Figure 6: Model of the clean Co {0001} single crystal surface and forward focusing directions based upon a bulk termination of the sample.

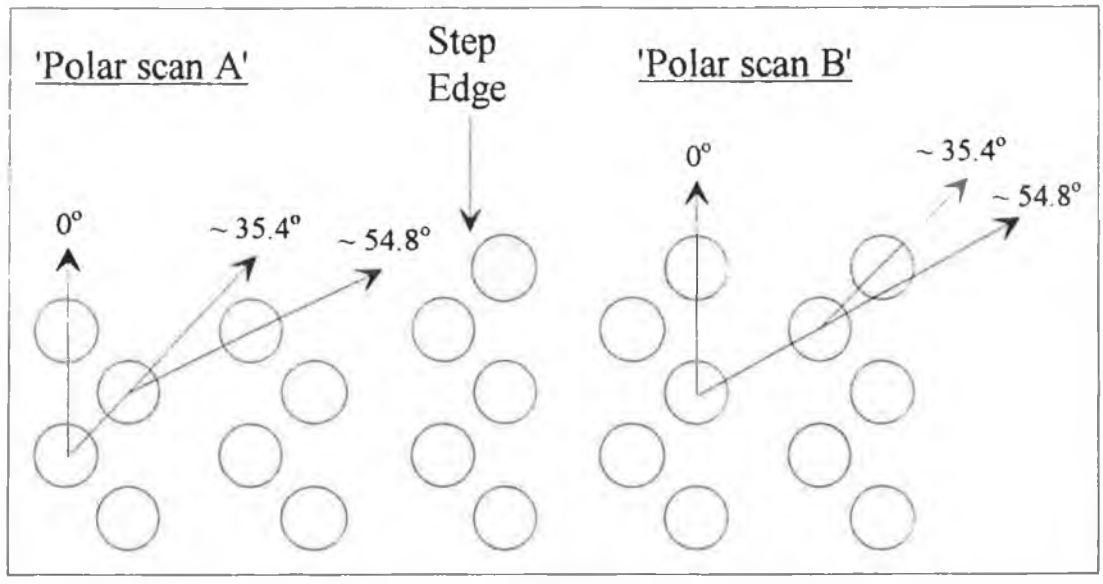

Figure 7: "Swapping" of the polar scan cross-sections as a result of a single-atomic step edge on the crystal surface.

atoms would also have resulted in the conversion of 'Polar scan A' to 'Polar scan B'. This is a consequence of every second layer in the hcp {0001} structure being equivalent. The effect of all step edges and surface defects, averaged across the entire surface, results in an effective six-fold symmetry.

3.2. Cobalt Deposition on Pd {111}:

3.2.1. Growth Mechanism:

One of the first considerations when studying metal-on-metal growth is the initial growth mode. The adsorbed metal may initially form a uniform monolayer (FM or SK growth) or it may form 3-dimensional crystallites/islands (VW growth) [38]. As discussed in the introduction, a number of factors may affect the equilibrium growth mode, including the surface free energy of the substrate and the adsorbate, the surface mobility of the adsorbate and the degree of lattice mismatch between the two metals. In the case of (polycrystalline) Co and Pd, the room temperature surface free energies (γ_i°) have been calculated as 2.709 Jm^{-2} and 2.043 Jm^{-2} respectively [47]. The fact that $\gamma_{Co}^\circ > \gamma_{Pd}^\circ$ favours island growth of Co overlayers on Pd substrates. The Co/Pd lattice mismatch is ~9.5 %, which also favours island growth since pseudomorphic growth of a Co overlayer on Pd {111} would introduce a substantial in-plain strain.

Figure 8 shows the experimentally measured variation of the He^+ LEISS signal with the Co layer thickness (d) calculated on the basis of the XPS core level intensities. The solid line in figure 8 represents the expected decay path of the Pd ISS signal if the first layer were to be deposited as a perfect monolayer. Up to a coverage of ~0.63 eML (d=1.3 Å) the Co deposition is indistinguishable from monolayer growth. However, as further Co is deposited there is clear island growth. At ~1.5 eML coverage roughly 80% of the Pd surface is covered. This percentage gradually increases but complete coverage of the surface is not achieved until >6 eML. This clearly illustrates that Co deposited on Pd {111} has an initial VW-type growth mode.

The dashed curve in figure 8 is a decay curve fitted to the experimental data points. The dotted curve corresponds to the expected ISS decay if the Co deposition were purely random (i.e. addition of Co adatoms to the Pd surface or the developing Co overlayers based purely on the % Co coverage of the surface without a driving force toward either island or monolayer growth). It is clear from the comparison of the

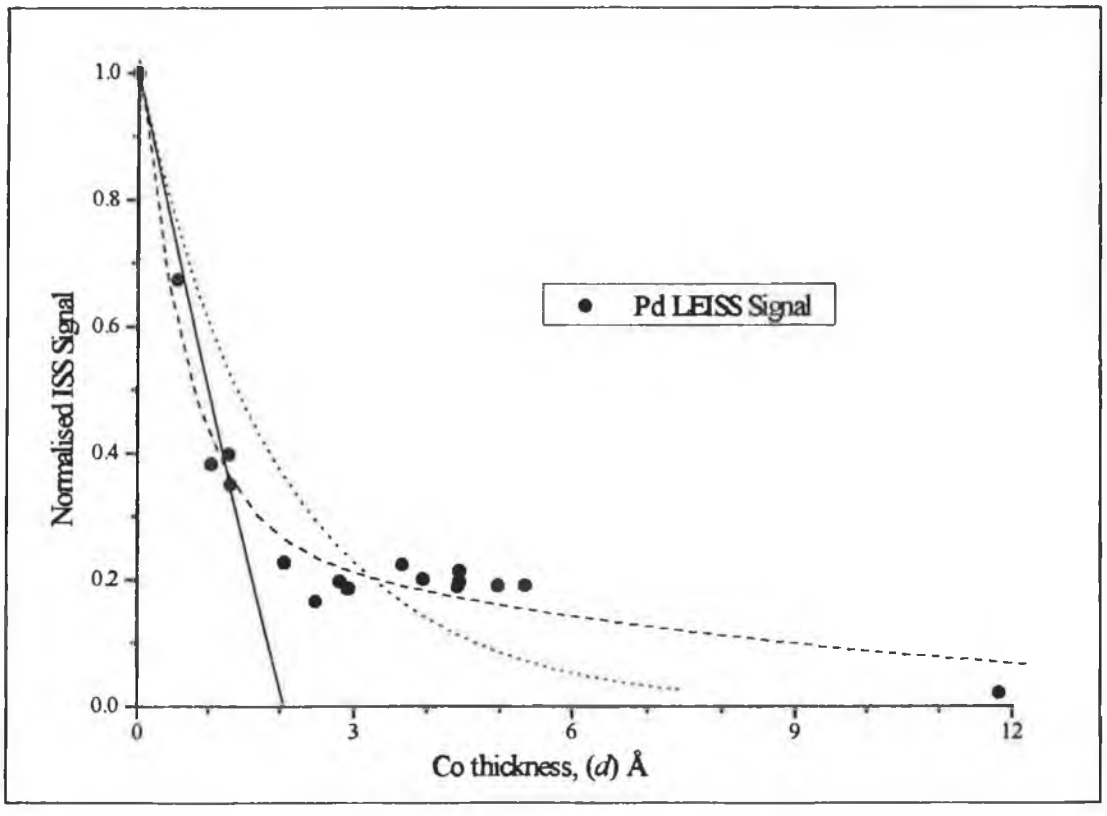

Figure 8: Variation of Pd He^+ LEISS signal of Pd with Co coverage.

'purely random' curve with the experimental data points that the initial sub-monolayer coverages do favour a 'layer-by-layer'-like growth. However, once ~60-70% of the surface is covered the growth mechanism deviates strongly toward island growth and the remaining Pd surface is covered slowly as the islands growth together. This agrees with a previous study that found that the Co 'wets' the Pd substrate well but that there is a significant deviation from layer-by-layer growth before a monolayer is formed [26].

For all θ_{Co} examined the LEED pattern remained p(1x1). However, the background increased and the spots became broader for θ_{Co} up to ~3 eML. No additional LEED spot, as reported in [26], were observed. The LEED pattern improved with additional Co deposition, although the quality was never as good as for the clean Pd {111} surface. The diffraction spots remained relatively sharp with a low background up to the highest coverage studied (~25 eML). A close examination of the diffraction pattern from low θ_{Co} overlayers showed that unit mesh increased in size with increasing coverage. Within experimental error the overlayers adopted the surface unit cell size expected for bulk Co {0001}/Co {111} for Co coverages >6 eML. The high background and diffuse spots at low coverages indicates that the overlayer already begins to relax to a bulk structure at very low coverages.

3.2.2. Cobalt Crystal Structure:

We can distinguish between fcc and hcp crystal growth of the Co overlayers based on the symmetry of the azimuthal scans as discussed earlier. If these scans show six-fold symmetry then the crystal structure must be either hcp or a fcc structure consisting of two equal domains (stacking 'ABCABC....' and 'ACBACB....'). If the azimuthal scans are three-fold symmetric then the structure is a single domain fcc. In this case the stacking of the Co overlayer may follow the substrate (i.e. 'ABCabc....' or 'ABCbca....') or it may be reversed from that of the substrate (i.e. 'ABCacb....' or 'ABCbac....'). In this stacking notation the capital letters refer to the substrate (Pd) and the small letters to the adsorbate (Co). Two stacking notations are given in both cases because the fcc stacking may begin at either a fcc or a hcp site.

Figure 9 shows the azimuthal curves measured at various polar angles from a θ_{Co}~20 eML on Pd {111}. Emission is from the Co $2p_{3/2}$ core level with an outgoing electron kinetic energy of ~700 eV. As was the case for the Pd azimuthal scans, ϕ=0° corresponds to 'Polar scan B' while ϕ=-60°/60° corresponds to 'Polar scan A'. It is immediately evident from the three-fold symmetry of the curves shown in figure 9 that the Co overlayers grow in a single domain fcc structure. The positions of forward focusing features (at ϕ=-60°/60° on the θ=20°/55° scans; and at ϕ=0° on the θ=35° scan) are identical to those of the clean Pd azimuthal scans, showing that the fcc stacking of the overlayer follows the stacking sequence of the substrate. There was no evidence of any transition of the Co overlayers back to its normal bulk hcp phase up to the highest coverage studied (>25 eML).

The SSCC's shown in figure 9 were calculated for bulk-structure Co fcc {111} and hcp {0001} clusters. In the case of the hcp calculation, the surface averaging

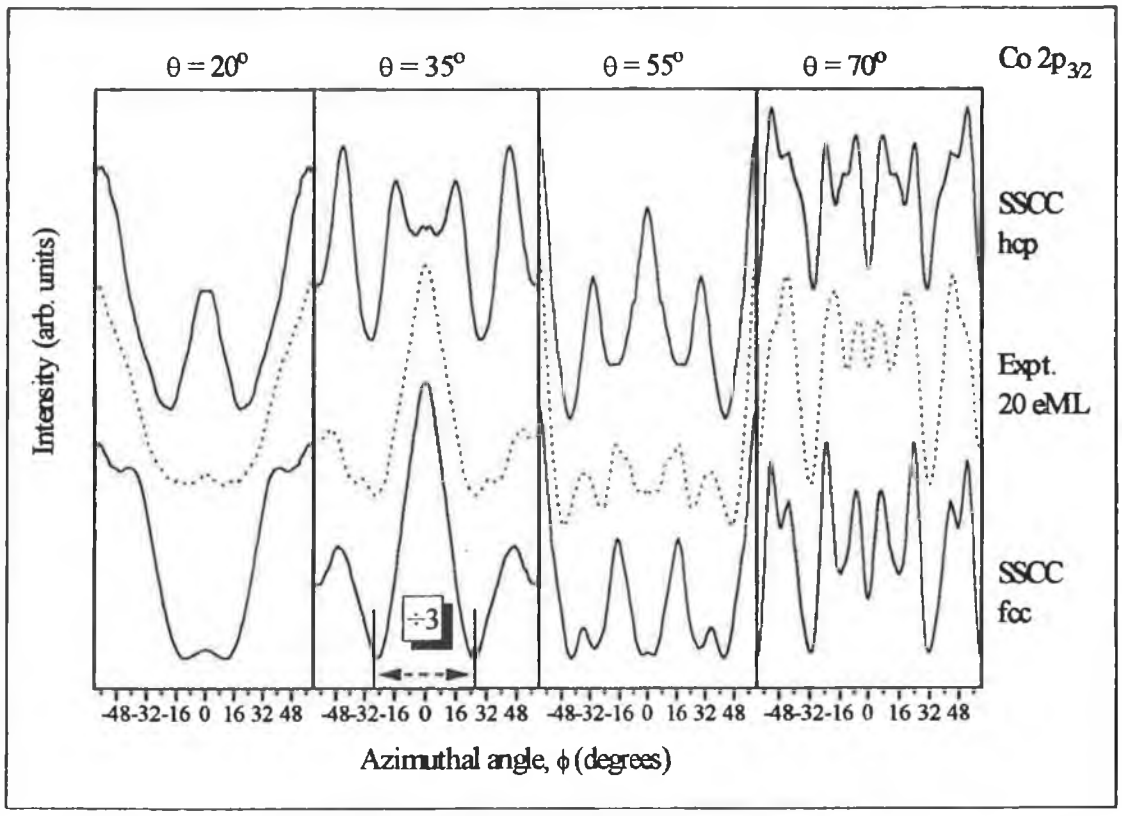

Figure 9: Azimuthal XPD scans measured, using Co 2p emission, from ~20 eML Co on Pd {111} at polar angles of 20°, 35°, 55° and 70°. SSCC's for bulk fcc {111} and hcp {0001} Co are shown for comparison.

discussed previously has not been accounted for in the calculations, hence the theory curves are three-fold symmetric. However, the curves still have elements of six-fold symmetry due to the inherent similarity between the two polar scan directions in the hcp {0001} structure (see figure 6). The forward focusing peaks occur at the same off-normal polar angles along both polar scan directions and differ only in relative intensity.

3.2.3. Co Adsorption Site:

Having determined that the Co overlayers grow in a single domain fcc lattice structure whose stacking follows that of the substrate, the question remains as to whether the Co adatoms in the first adlayer have a favoured adsorption site on the clean Pd {111} surface (either fcc or hcp). There are two possible stacking sequences depending on the adsorption site. For a fcc site the sequence would be 'ABCabc....' whereas for a hcp site it would be 'ABCbca....' in order for the overlayers to follow the Pd bulk

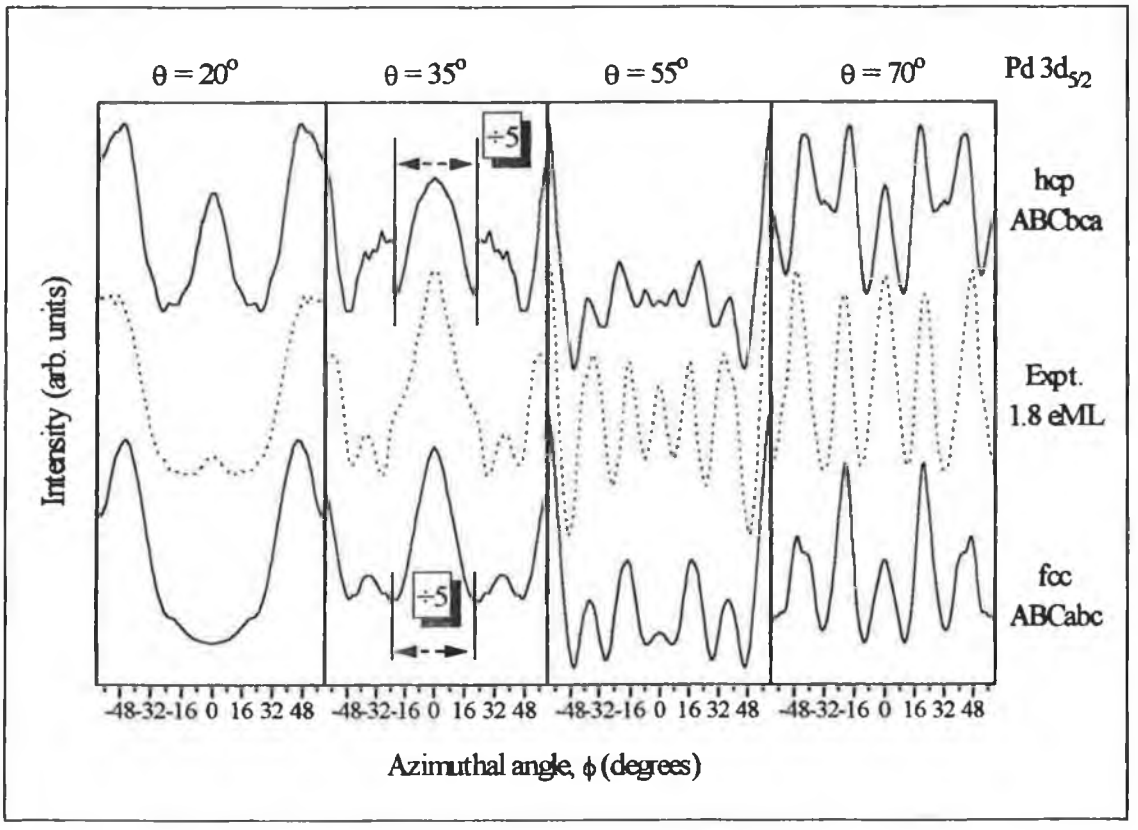

Figure 10: Pd azimuthal XPD scans taken after deposition of ~1.8 eML of Co on Pd {111}. The dotted curves correspond to the experimental scans. The solid curves correspond to azimuthal SSCC's for an 'ABCabc....' and an 'ABCbca....' stacking sequence.

stacking. These two sites cannot be distinguished on the basis of Co emission since both overlayers have an identical stacking structure. However, emission from Pd after adsorption of a small Co coverage should indicate whether or not there is a preferred adsorption site on the surface.

Figure 10 shows the azimuthal XPD scans measured using Pd $3d_{5/2}$ emission following deposition of ~1.8 eML of Co on the clean surface. The SSCC's shown in figure 10 were done for a cluster of two Co monolayers on a bulk Pd {111} substrate. The Co inter-layer spacing used was 2.05 Å and the overlayers were set pseudomorphic with the Pd substrate (in-plane parameter 2.75Å). The two models tested were for preferential adsorption of Co adatoms in a hcp TFH site (ABCbca....) and in a fcc TFH site (ABCabc....). The experimental curves in figure 10 are clearly in better agreement with the SSCC's for Co adsorption in fcc sites than with those for adsorption in hcp sites. We can conclude that the Co adatoms preferentially occupy the 'fcc' sites on the Pd {111} surface.

3.2.4. Coverage Dependent Changes:

Figure 11 shows a series of azimuthal scans measured, using Co $2p_{3/2}$ emission, for a range of θ_{Co} at polar angles of 20°, 35°, 55° and 70°. Changes in the azimuthal curves as a function of θ_{Co} are indicators of changes in the overlayer structure. The fact that the position of the forward focusing features remains constant at all coverages (most evident for the θ=35°/55° curves) proves that the Co overlayers follow the Pd substrate stacking sequence from the outset. If the initial Co layers had adopted a 'reverse' stacking sequence and subsequently switched as θ_{Co} increased, then the forward focusing features would have been displaced by 60° along the x-axis on the low coverage azimuthal scans.

Clearly, apart from changes in the relative peak intensities, there are no gross changes in the azimuthal scans with θ_{Co}. Even at the lowest coverages the curves contain the main structures that persist to >20 eML. However, the azimuthal scans taken at θ=20°, 55° & 70° do show some θ_{Co} dependent changes in the curve features around ϕ=0°. These changes may result from a relaxation (structural transition) of the Co

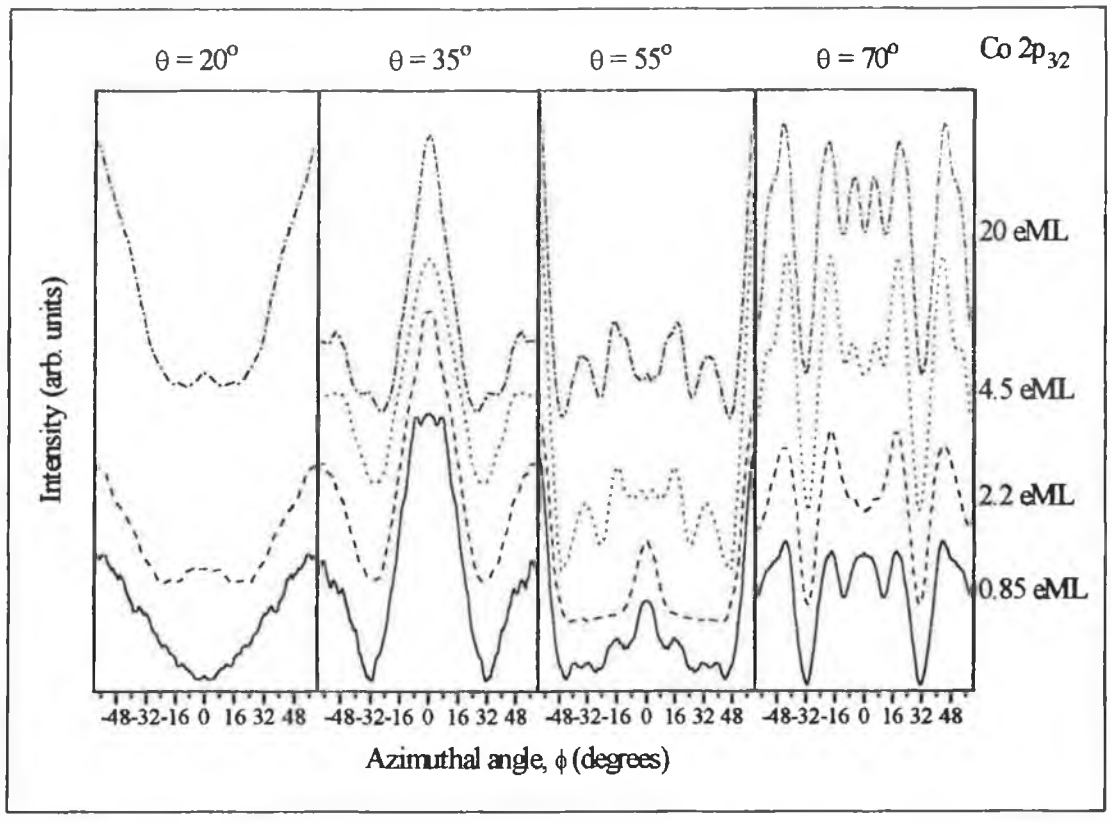

Figure 11: Co azimuthal scans measured as a function of θ_{Co} on Pd {111}.

overlayers from a strained structure at the Co/Pd interface to a more favourable bulk crystal structure as multi-layers develop. Due to the large mismatch between the Co and Pd lattice parameters (~9.5% expansion), the initial Co overlayers may form a distorted fcc structure. Such an in-plane expansion induced by the Pd substrate may result in a corresponding contraction of the Co inter-layer spacing resulting in a tetragonally distorted 'fcc' structure.

Figure 12 shows the evolution of the Co polar XPD features with increasing coverage. The scans were taken along the two high symmetry azimuths shown in figure 3. Again, ϕ=0° corresponds to 'Polar scan B' and ϕ=-60°/60° to 'Polar scan A'. The appearance of direct forward focusing peaks at sub-monolayer coverages (~0.85 eML) confirms that the initial growth is in islands of at least 2-layer thickness.

At low θ_{Co} the forward focusing peaks are shifted to higher polar angles by ~3°. Assuming an in-plane lattice parameter equal to that of the Pd substrate these peak positions correspond to an inter-layer spacing of ~2.0 Å. This value is slightly

contracted (~2.5%) from the bulk Co {0001}/{111} value. It is unlikely that the Co overlayers would sustain such a large in-plain strain (~9.5%) without a corresponding large inter-layer contraction. It is more probable that there is some relaxation of the in-plane strain even during the initial stages of Co growth. The LEED measurements indicate that the overlayers do begin to relax at very low coverages. Hence the in-plane lattice parameter may be less than that of Pd and the contraction of the inter-layer spacing would be correspondingly greater in order to yield the observed peak shift. Intuitively this is the more plausible explanation since it results in the strain being more evenly distributed throughout the overlayer structure. On the basis of pseudomorphic growth the overlayers would have to incorporate a large in-plane strain with only a modest strain perpendicular to the surface.

The forward scattering peaks have already begun to shift back toward their bulk fcc positions at a coverage of ~2.2 eML. At high coverages the forward scattering peaks occur at the expected fcc {111} position indicating that the overlayer has adopted a bulk fcc lattice structure. Hence, the polar scans show that a structural transition from

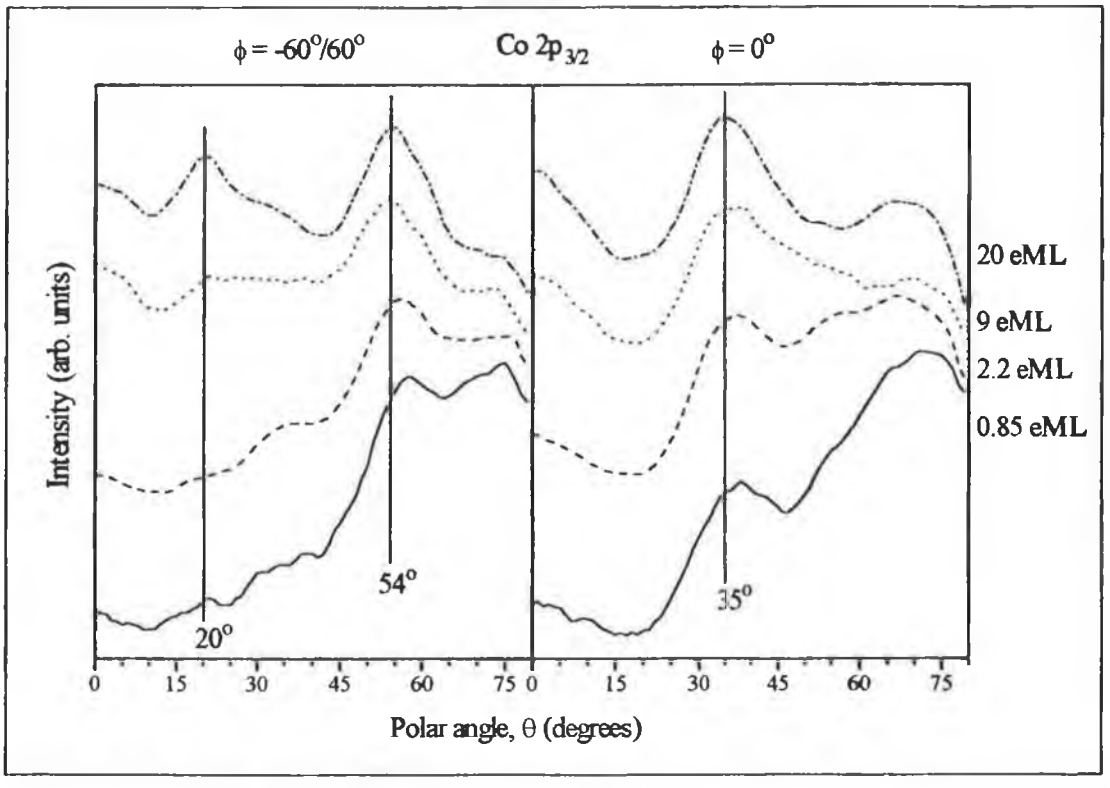

Figure 12: Co polar scans taken as a function of θ_{Co} on Pd {111}.

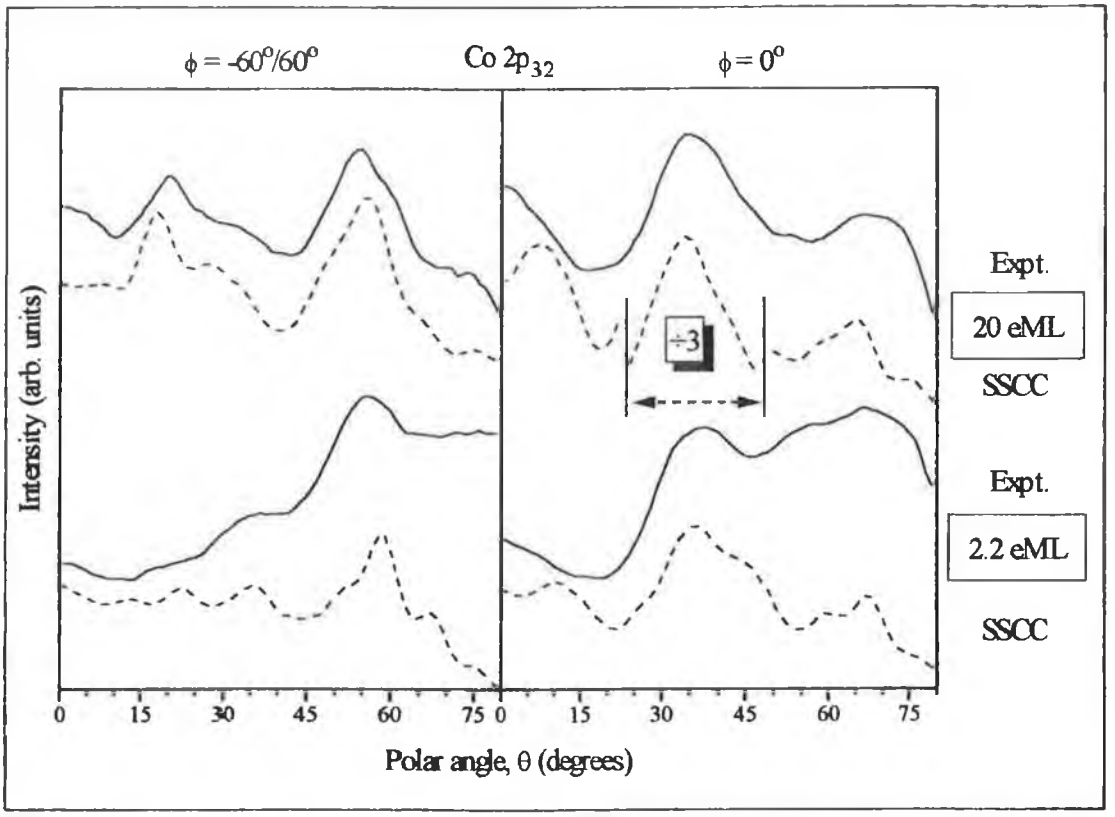

Figure 13: Co polar scans taken after deposition of ~2.2 eML and ~20 eML of Co on Pd {111} (solid curves). The dashed curves correspond to polar SSCC's (see text for details).

a distorted 'fcc' to a bulk fcc structure occurs as θ_{Co} increases. This transition occurs at quite a low Co coverages. Based on the LEED and XPD data it appears to be nearly complete after deposition of ~3-4 eML Co (due to the VW growth mechanism the actual Co coverage on the surface is greater than is indicated by the quoted coverages). This transition can be regarded are the main reason for the θ_{Co} dependent changes observed in the azimuthal scans shown in figure 11. Of course, given the fact that the growth mechanism is VW, a range of different Co thickness' exist on the surface at any given coverage. The different layers will exhibit varying degrees of relaxation resulting in a range of different local structures around the Co emitters. This will also be a factor in the observed changes.

Figure 13 shows a comparison of Co polar XPD scans for a low and high θ_{Co} with corresponding SSCC's. The cluster used for the high coverage (20 eML) SSCC's consisted of 20 layers of Co in a bulk cobalt fcc {111} lattice structure. The low coverage (2.2 eML) cluster consisted of a Co bilayer on a Pd substrate. The Co in-

plane parameter was 2.75 Å and the inter-layer spacing was 2.05 Å. There is reasonably good agreement between theory and experiment in both cases, although the level of agreement is not as good as that obtained for emission from the clean Pd surface (figure 5). The forward focusing features on the experimental curves are broad and not well resolved. This may be indicative of disordered regions within the overlayer.

The main discrepancy between theory and experiment in figure 13 is the dip at normal emission in the 20 eML SSCC done for $\phi=0^{\circ}$. A peak is expected due to the $\theta=0^{\circ}$ forward focusing peak (see figure 3). This splitting can be attributed to the first-order diffraction feature arising from the $\theta=35^{\circ}$ forward focusing peak. Normally the higher-order diffraction features would not have sufficient strength to cause such a large effect. However the fcc {111} surface is a special case. Examining the cross-section through 'Polar scan B' shown in figure 3, it can be seen that there is a large difference between the separation of the adjacent atoms that contribute to the 0° forward focusing peak and the separation of the adjacent atoms that contribute to the 35° forward focusing peak. In the case of Co {111} the respective separations are 6.15 Å and 2.52 Å. The 'splitting' occurs because, due to this difference in the emitter-scatterer separations, the calculated intensity of the 0° forward focusing peak is less than the intensity of the first-order diffraction feature from the 35° forward focusing peak. Hence, as this first-order feature falls at $\theta\sim5\text{-}10^{\circ}$, it splits the normal emission peak. Such an effect is not seen experimentally because both the 35° forward focusing peak and its higher-order features are subject to damping due to defocusing and multiple scattering processes, which are not accounted for in the SSCC's.

3.3. Alloying of Cobalt Films on Pd {111}:

The effect of deliberately annealing a Co on Pd {111} overlayer was examined by LEISS and XPD. Figure 14 shows He^{+} LEISS spectra obtained before and after deposition of ~0.85 eML of Co on Pd {111} and after annealing the overlayer to ~580 K for ~20 minutes. All spectra were measured at room temperature. Based on the reduction of the Pd LEISS signal after deposition, ~60% of the crystal surface is

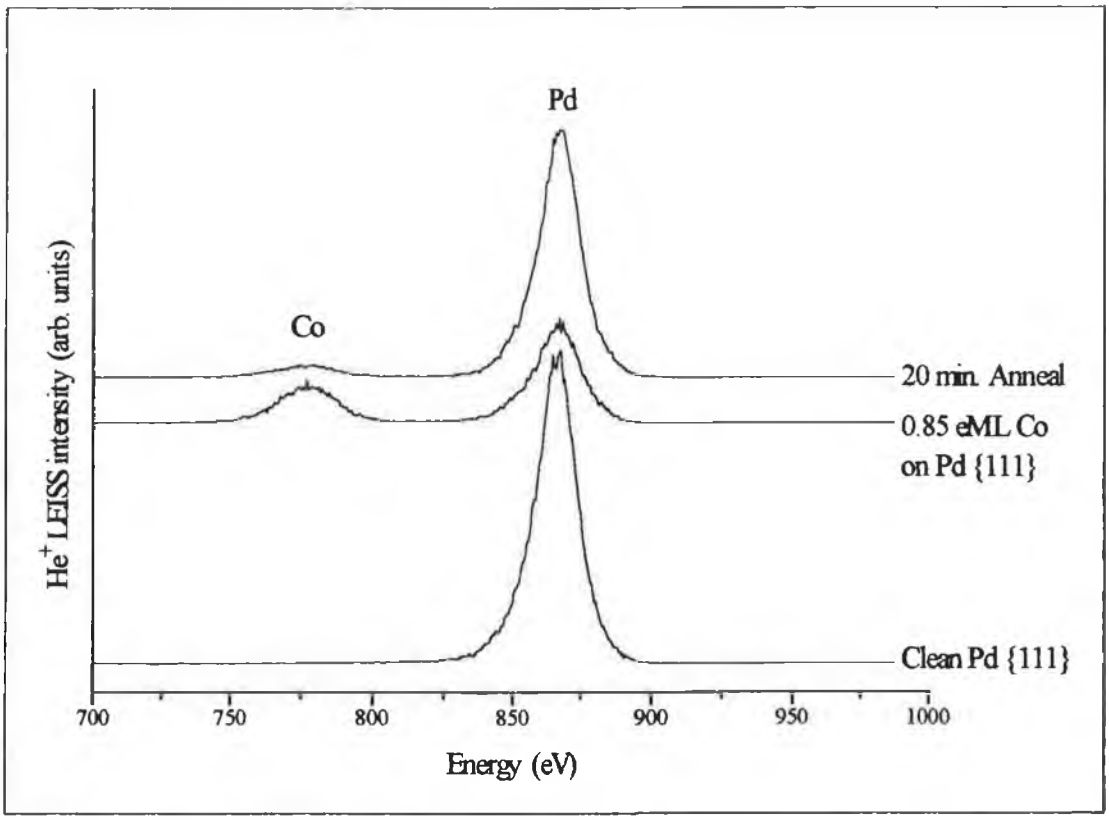

Figure 14: He^+ LEISS spectra obtained from clean Pd, after deposition of ~0.85 eML Co and after annealing to ~580 K for 20 minutes.

covered by Co. At this coverage the Co overlayer should consist of mainly 1- or 2-layer thick islands. This is confirmed by the XPD polar scans taken from this overlayer (shown in figure 12), which show only forward scattering features that can arise from 2-layer thick islands. After annealing the Co surface coverage drops to <20% and the Pd LEISS signal re-emerges strongly, clearly indicating that the bulk of the adsorbed Co has penetrated beneath the top layer of the Pd crystal. The residual Co signal arises from Co within or on-top of the Pd 1st layer.

Figure 15 shows room temperature Co XPD azimuthal scans measured at various polar angles before and after the sample was annealed. After annealing there are changes in the azimuthal features and the forward focusing peaks have significantly greater intensity. In particular, the azimuthal scan measured at θ=55° changes drastically around ϕ=0°. There are also some changes in the θ=35° azimuthal scan around ϕ=-60°/60°.

The increased intensity in the azimuthal features after annealing can be attributed to an increase in the number of Co emitters from which forward focusing can occur. For θ_{Co}~0.85 eML on the Pd surface, a large proportion of the Co adatoms form the 'top layer' and consequently do not contribute electron intensity to the forward focusing features. Upon alloying, most of the Co adatoms are covered by Pd (incorporated in the 2nd or deeper layers of crystal lattice). As a result, a greater proportion of the emitted Co photo-electrons are forward focused (by overlying Pd atoms) resulting in the observed increase in the intensity of the azimuthal features. The fact that an increase is observed in the XPD features is indirect evidence that a substantial amount of the Co atoms remain within the selvedge region where they can contribute to the XPD features.

The structural changes in the higher-order features of the azimuthal plots are also a consequence of alloying. After annealing, the azimuthal curves are similar to those measured from a thick Co overlayer (figure 11). Thus, the changes in the higher-order

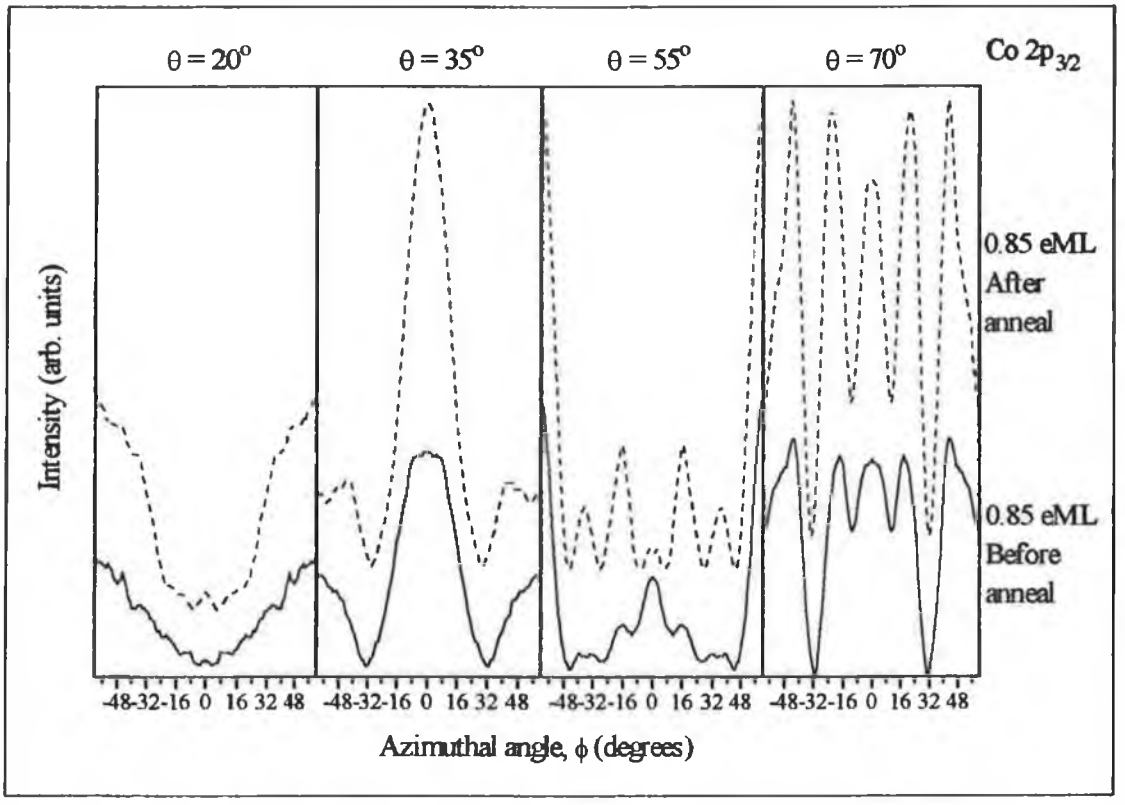

Figure 15: Co azimuthal XPD scans taken before and after annealing ~0.85 eML Co on Pd {111} to ~580 K for 20 minutes.

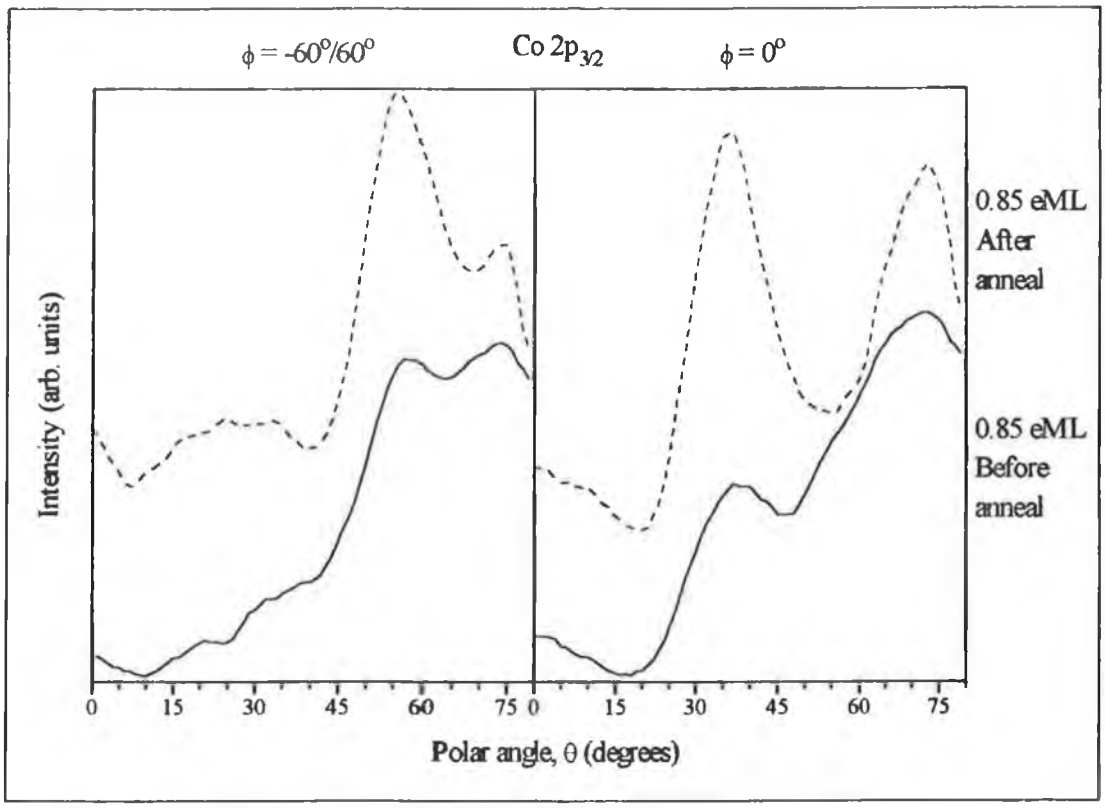

Figure 16: Co polar XPD scans taken before and after annealing ~0.85 eML Co on Pd {111} to ~580 K for 20 minutes.

structure of the azimuthal plots may be indicative of an increased order in the local geometric structure around the Co emitters as a result of direct substitution into Pd atom lattice positions. The changes can be explained as follows. The initial Co layers adsorb with a high degree of disorder as a result of the large Co/Pd lattice mismatch and the progressive structural relaxation with increasing layer thickness. The changes observed in the azimuthal curves measured from low θ_{Co} overlayers (figure 11) reflect the range of different local structures that exist around the Co emitters as the overlayers relax toward a more favourable structure. Once a more uniform local structure has been attained by the Co atoms (either by growing a thick layer coverage (>10 eML) or by alloying of a thin layer coverage) then the azimuthal XPD features become constant.

Figure 16 shows Co XPD polar scans measured from the 0.85 eML Co overlayer before and after annealing. There is clearly a strong increase in the anisotropy of the curves after annealing. The peaks at θ~38° & ~58° on the polar scans taken before annealing, which are due to scattering between 1st-and-2nd layer atoms, are

significantly more prominent after annealing. There is no evidence of a peak at θ~20° (due to 3rd layer Co) on the polar scans taken at ϕ=-60°/60° ('Polar scan A') before annealing. There is a broad peak around θ~20° after annealing which may be due to some 3rd layer Co in the Pd selvedge. However this peak may also be due to the higher-order diffraction feature of the θ~55° forward focusing peak. Enhancement of this peak would also result in stronger higher-order features.

Figure 17 shows a comparison of the 'annealed' polar XPD scans with SSCC's done for a range of alloy clusters. The clusters used had bulk Pd lattice parameters with different distributions of Co in the cluster selvedge region. All clusters contained 0.8 ML Co. For curve A this was located exclusively in the 2nd layer of the cluster. For curve B the Co was distributed 50/50 between the 2nd and 3rd layers of the cluster. In the case of curve C the Co was equally distributed between the top 4 layers of the cluster (0.2 ML per layer), while for curve D it was distributed equally between the top 8 layers (0.1 ML per layer). In all cases the Co was randomly distributed within

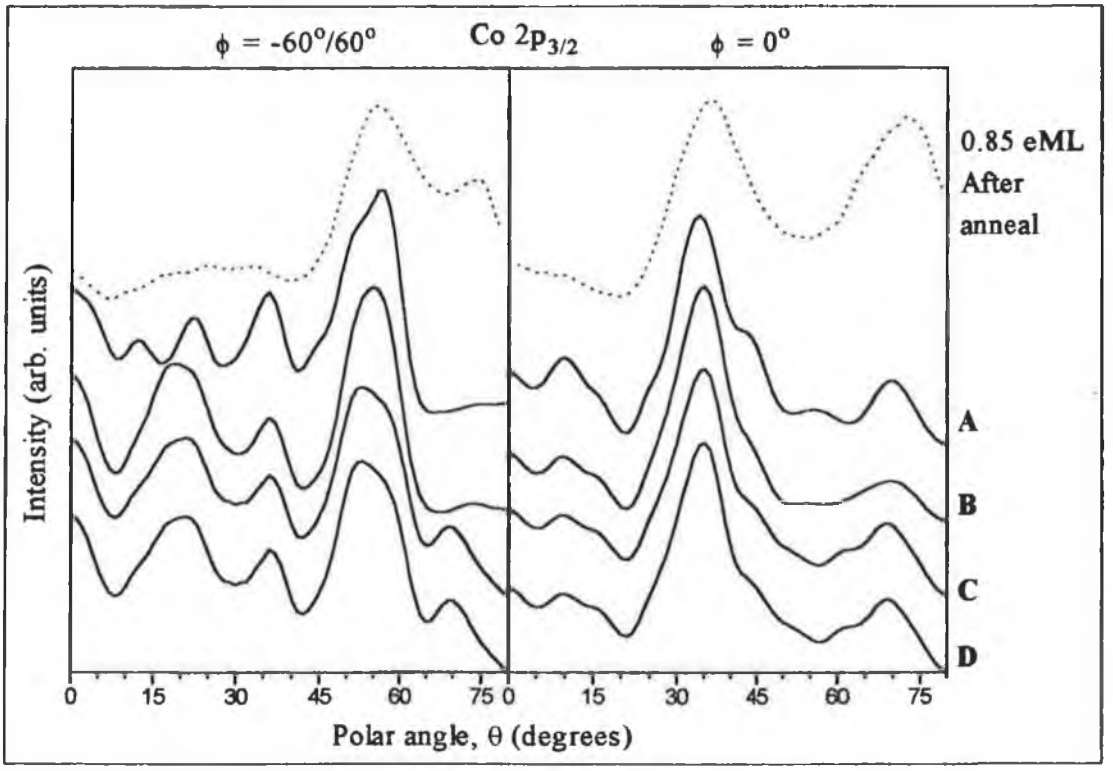

Figure 17: Comparison of Co polar XPD scans for 0.85 eML of Co alloyed with Pd {111} with SSCC's for alloy clusters (curves A-D). See text for cluster details.

the layers and the cluster 'bulk' consisted of pure Pd.

The first point to note is the strong similarity between all four SSCC's for polar scans along $\phi=0^{\circ}$ ('Polar scan B'). This is due to the overwhelming dominance of the 2^{nd}-off-1^{st} scattering process in single scattering theory. Inspection of figure 3 reveals that, for a bulk Pd structure, the adjacent scatterers that contribute to the 0°, 35.2° & 70.5° forward focusing peaks are separated by 6.75, 2.75 & 6.73 Å respectively. The small separation between the scatterers that contribute to the 35.2° peak coupled with the neglect of defocusing along atom chains explains why this peak dominates the SSCC's. The result is that the SSCC's are insensitive to the selvedge composition.

The situation for SSCC's along $\phi=-60^{\circ}/60^{\circ}$ is somewhat better since the adjacent scatterers that contribute to the 0°, 19.5° & 54.7° forward focusing peaks are separated by 6.75, 4.77 & 3.89 Å respectively. In this case the two off-normal peaks arise from scattering by adjacent atoms with comparable separation. Examining figure 17 shows strong similarities between curves B-D. However, curve A has the noticeable absence of a forward focusing peak at $\theta\sim20^{\circ}$ (which arises from 3^{rd} or deeper layer emitters). Instead, this region contains higher-order features arising from the $\theta\sim55^{\circ}$ forward focusing peak. Curve A compares well with the experimental XPD scan, which also shows the noticeable absence of a strong peak at $\sim20^{\circ}$. The three higher-order features on curve A along this scan direction would produce the broad feature observed experimentally if broadened by multiple scattering effects.

On the basis of the peaks observed after annealing (figure 16) and the comparison with SSCC's, the majority of this Co appears to be localised in the 2^{nd} layer of the Pd crystal. Additional evidence for the preferential localisation of the Co within the Pd 2^{nd} layer is provided by the azimuthal scans shown in figure 15. After annealing the forward focusing peaks on the $\theta=35^{\circ}/55^{\circ}$ scans, which arise due to emission from 2^{nd} layer atoms, are significantly more intense. The forward focusing peaks on the $\theta=20^{\circ}$ scans, which require the emission to be from a 3^{rd} or deeper layer, show a significantly smaller increase after annealing, indicating a low concentration of Co in the deeper layers.

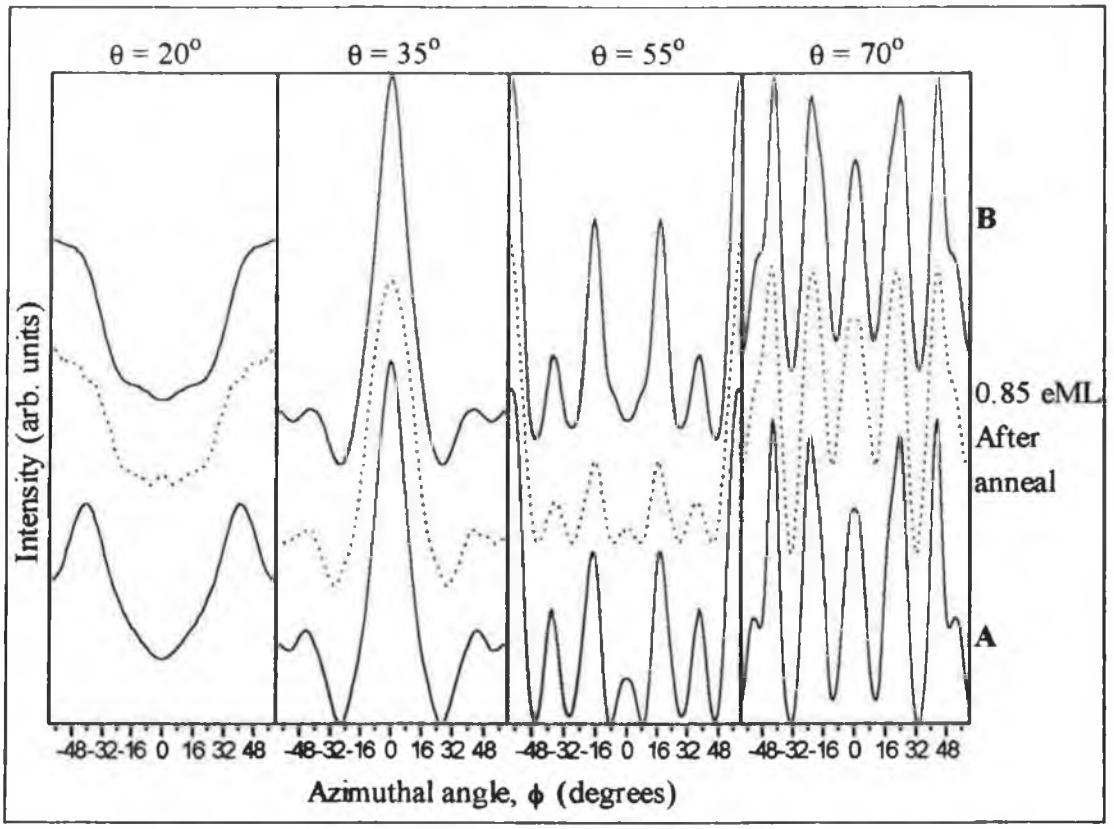

Figure 18: Comparison of SSCC's for annealed clusters A & B with the Co azimuthal XPD curves measured from 0.85 eML Co alloyed with Pd {111}. See text for details of clusters.

Azimuthal SSCC's were performed on alloy clusters A & B (0.8 eML Co in 2nd and 0.4 eML Co in 2nd & 3rd layers respectively) and compared with the experimental curves. The results are shown in figure 18. Unfortunately both alloy clusters agree well with the experimental data. The SSCC's done at θ=35° & 70° are virtually identical. The peaks at ϕ=-40°/40° on the θ=20° SSCC for cluster A can be attributed to higher-order diffraction features of the θ=35° forward focusing peak. It is unlikely that such peak would ever be observed experimentally due to defocusing and multiple scattering effects. There is a difference at ϕ=0° between the SSCC's for θ=55° SSCC's. The presence of a peak on curve A at this position is in better agreement with the experimental curve. However the difference is minor and should not be relied upon in the absence of other evidence capable of distinguishing the two cluster models.

3.4. The Pd {100} Surface:

Figure 19 shows a model of the surface structure of a Pd {100} single crystal. The primitive surface unit cell is shown by the dashed square (lattice parameter=2.75 Å). Two cross-sectional cuts of the crystal are shown along the high symmetry [001] and [011] azimuths. The major XPD forward focusing features from {100} surfaces occur along these azimuths. Note that no forward focusing peaks arise along the [011] azimuth due to 2^{nd}-off-1^{st} layer scattering. Conversely, the [001] azimuth is dominated by a strong 2^{nd}-off-1^{st} scattering peak, which should occur at a polar angle of ~45° for a bulk terminated crystal. The crystal structure of a Co fcc {100} crystal is similar to that of Pd, differing only in its lattice parameters (in-plane parameter=2.503 Å; inter-layer spacing=1.77 Å).

Figure 20 shows azimuthal XPD curves measured from the clean Pd {100} surface and corresponding SSCC's. The azimuthal angles of -45°/45° correspond to the [001] polar scan direction shown in figure 19 and an azimuthal angle of 0° corresponds to

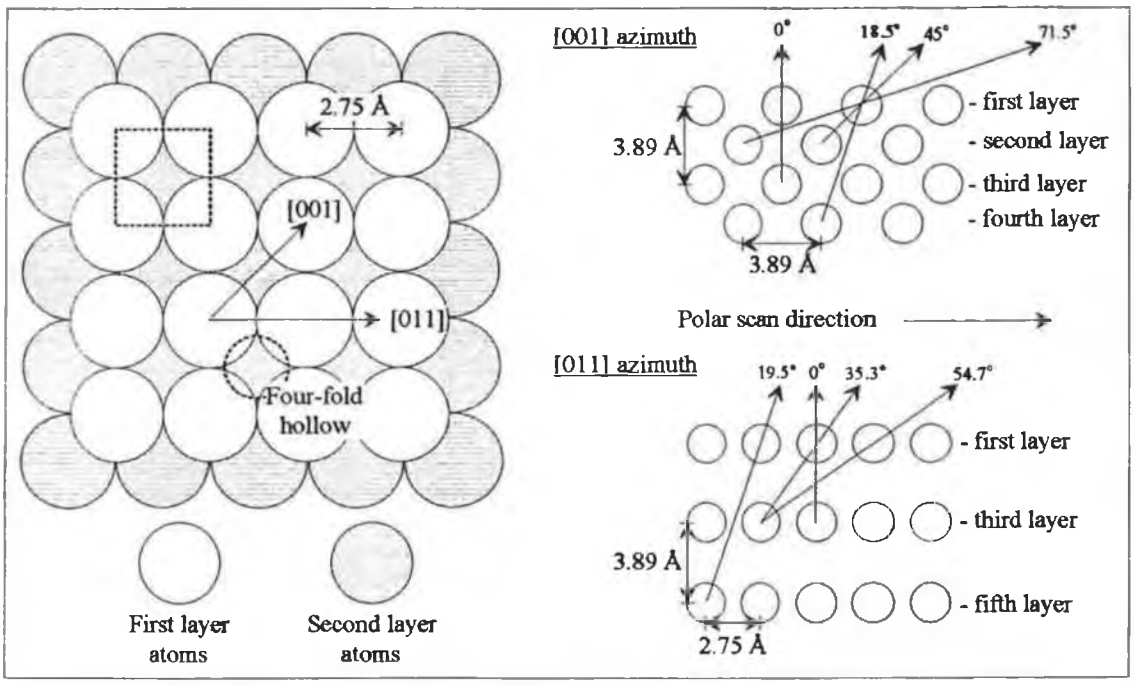

Figure 19: Model of the clean Pd {100} single crystal surface. The main forward focusing features occur at the polar angles shown along the [001] and [011] azimuths, assuming a bulk truncated surface and no refraction effects.

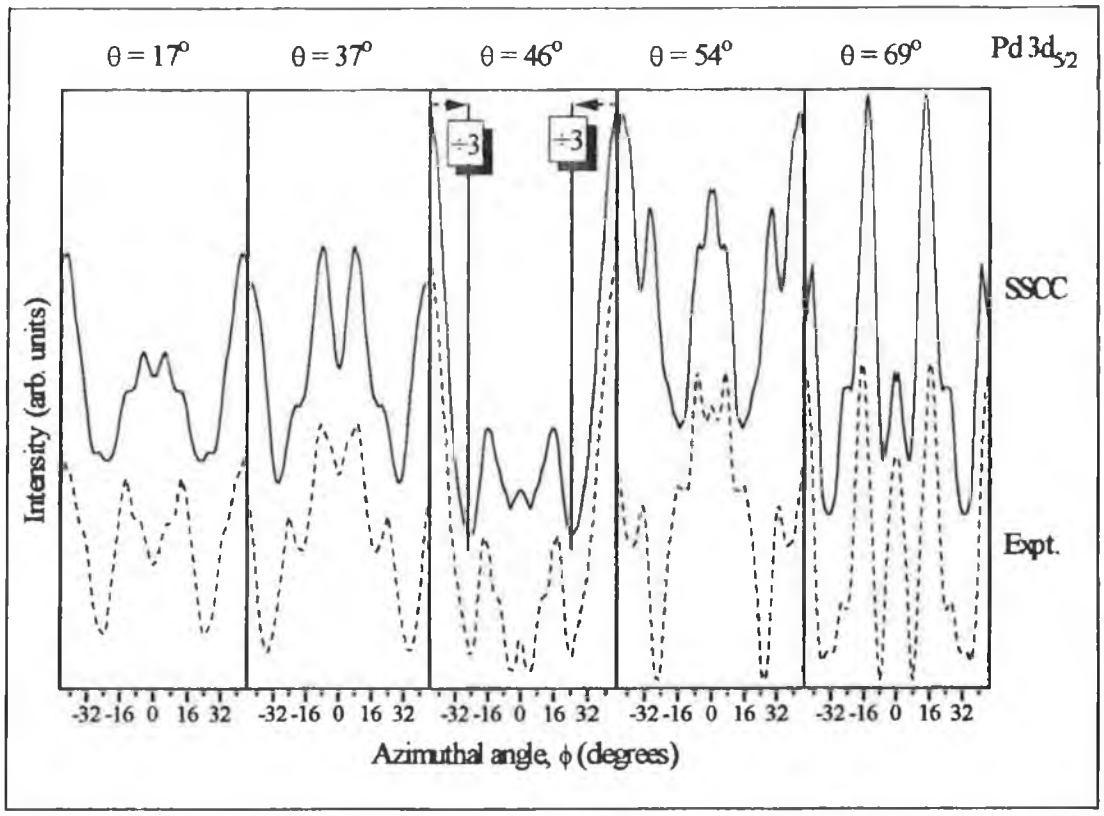

Figure 20: Azimuthal XPD curves measured at various polar angles from clean Pd {100} (dashed curves). The solid curves are SSCC's for a bulk Pd {100} cluster.

the [011] polar scan direction. Note that the forward focusing peaks at ϕ=-45°/45° on the SSCC calculated for θ=45° have reduced by a factor of 3 to aid visual comparison. There is good agreement between theory and experiment at all polar angles. The experimentally observed splitting of the forward focusing peak at ϕ=0° on the azimuthal scan taken at θ=37° is reproduced in the theoretical calculations. This effect can be attributed to scattering by the out-of-plane 2nd layer atoms, which are in close proximity to the direct 3rd-off-1st scattering path along the [011] azimuth. These out-of-plane scatterers are illustrated in figure 21.

3.5. Cobalt Deposition on Pd {100}:

3.5.1. Growth Mechanism:

Figure 22 shows the decrease of the Pd He^+ LEISS signal intensity with increasing θ_{Co} for Co deposition on Pd {100}. The solid line represents the expected decay pattern for layer-by-layer growth. The curve clearly shows that the initial growth is in islands

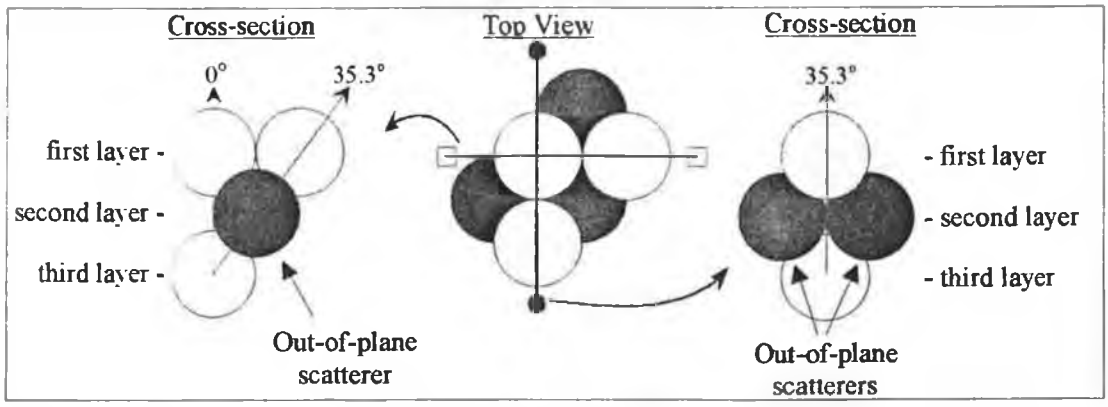

Figure 21: 2nd layer out-of-plane scatterers along the [011] azimuth of the {100} surface.

(VW growth). Hence, the growth mechanism of Co on Pd {100} and Pd {111} is the same. The dashed line is a decay curve fitted to the experimental data points.

The dotted curve in figure 22 corresponds to the expected decay path for 'purely random' Co deposition as previously discussed for the Pd {111} ISS results. Comparison of figure 22 with the equivalent plot for Co deposition on Pd {111} (figure 8) indicates that there is stronger island formation on the Pd {100} surface (i.e. there appears to be a greater driving force toward VW growth on the {100} crystal face of Pd). For the Pd {100} surface all of the experimental ISS data points are above the curve for 'purely random' adsorption indicating preferential island formation. While for Co deposition on Pd {111} the initial sub-monolayer coverages have a quasi-layer-by-layer growth mechanism, in the case of Co on Pd {100} island growth commences from the outset of adsorption. Based on an inter-layer spacing of 1.77 Å (bulk Co {100}), complete coverage of the Pd surface is not achieved until >8 eML of Co has been deposited. The LEED pattern from the Co overlayers remained p(1x1) but the background increased with increasing θ_{Co}. Unlike the situation for Co on Pd {111} the pattern did not improve at high Co coverages. Eventually all diffraction spots disappeared indicating poor long range order.

3.5.2. Cobalt Overlayer Structure:

Figure 23 shows azimuthal XPD curves measured, at θ=45° using Co $2p_{3/2}$ emission, for various θ_{Co} on Pd {100}. Clearly, the azimuthal features are already fully formed at the lowest coverage (~1.5 eML Co). The structure has four-fold symmetry similar

to the azimuthal curves measured from the clean Pd {100} surface, indicating that the Co overlayers maintain a fcc-like structure. There is no significant change in the azimuthal features as θ_{Co} increases, indicating that there are no major structural transitions in the Co overlayers for film thickness' of up to at least 20 eML.

Figure 24 shows polar XPD curves measured before and after deposition of 1.5 eML of Co on Pd {100} using emission from both the Co and Pd core levels. After deposition there is a small shift to higher angles discernible in the off-normal forward focusing peaks (at θ~45° along the [001] and at θ~35° along the [011] azimuth) of the Pd XPD curves. However, the most remarkable result is the position of the equivalent forward focusing peaks on the Co polar scans. Along the [001] azimuth there is a single dominant forward scattering peak due to emission from Co islands of at least 2 layers thickness, which correspond to the clean Pd peak at θ~45°. However, the peak maximum is at θ~51°, strongly shifted from the bulk fcc value and indicative of a severely distorted overlayer structure.

The lack of a prominent forward focusing peak on the Co polar scan measured along the [011] azimuth demonstrates that there is an insufficient amount of 3 (or greater) layer thick Co islands to generate strong focusing features. However there is evidence of a forward scattering features beginning to emerging at θ=0° & ~42.5° due to focusing between 1st-and-3rd layers. Hence, both polar scans indicate that the Co overlayers are growing in a severely distorted fcc-like lattice structure. The small shift of the Pd off-normal forward focusing peaks to higher θ can be attributed to distortion of the normal bulk Pd peak as a result of diffraction by the Co overlayers.

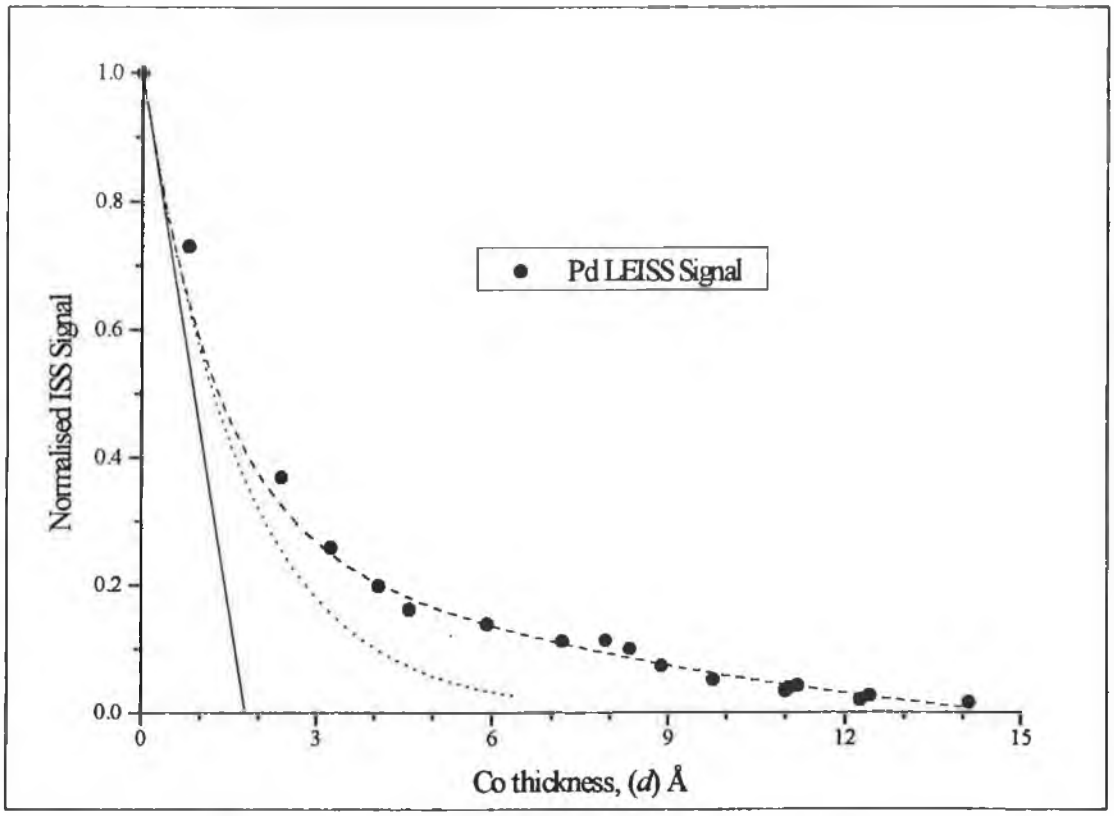

Figure 22: Decay in Pd {100} He^+ LEISS signal with Co coverage.

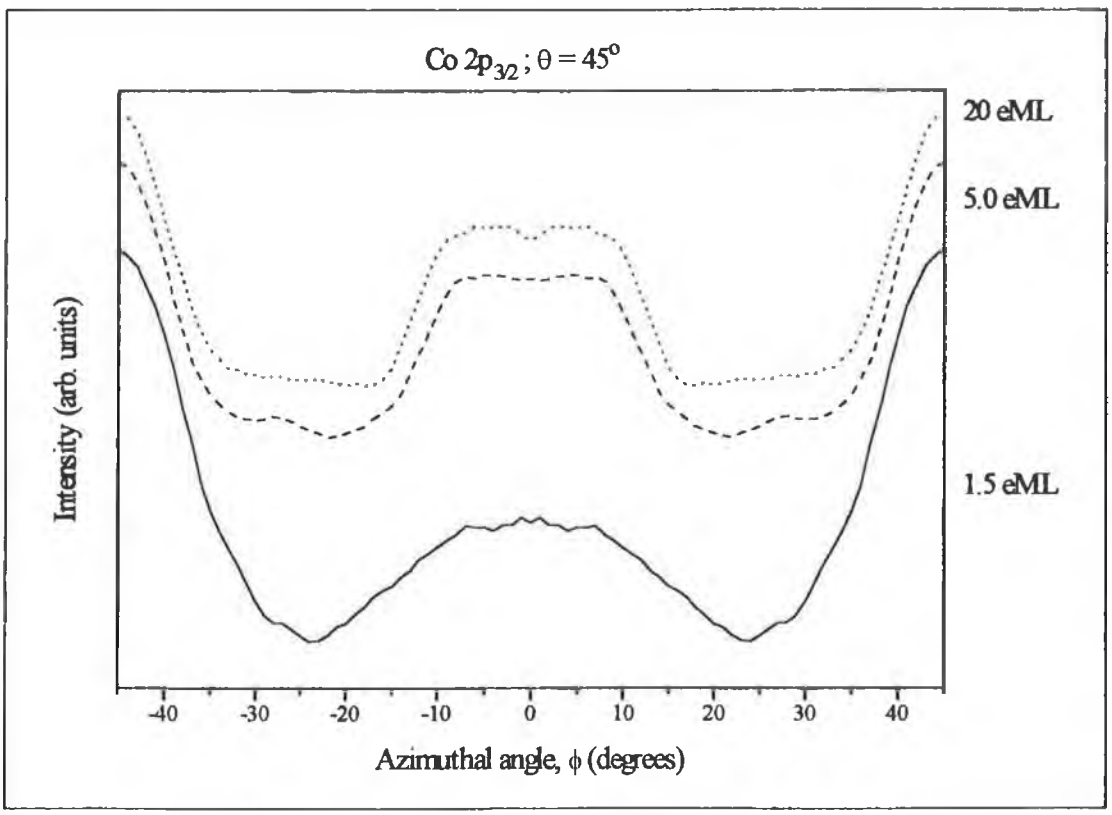

Figure 23: Co azimuthal XPD curves measured from various θ_{Co} on Pd {100}.

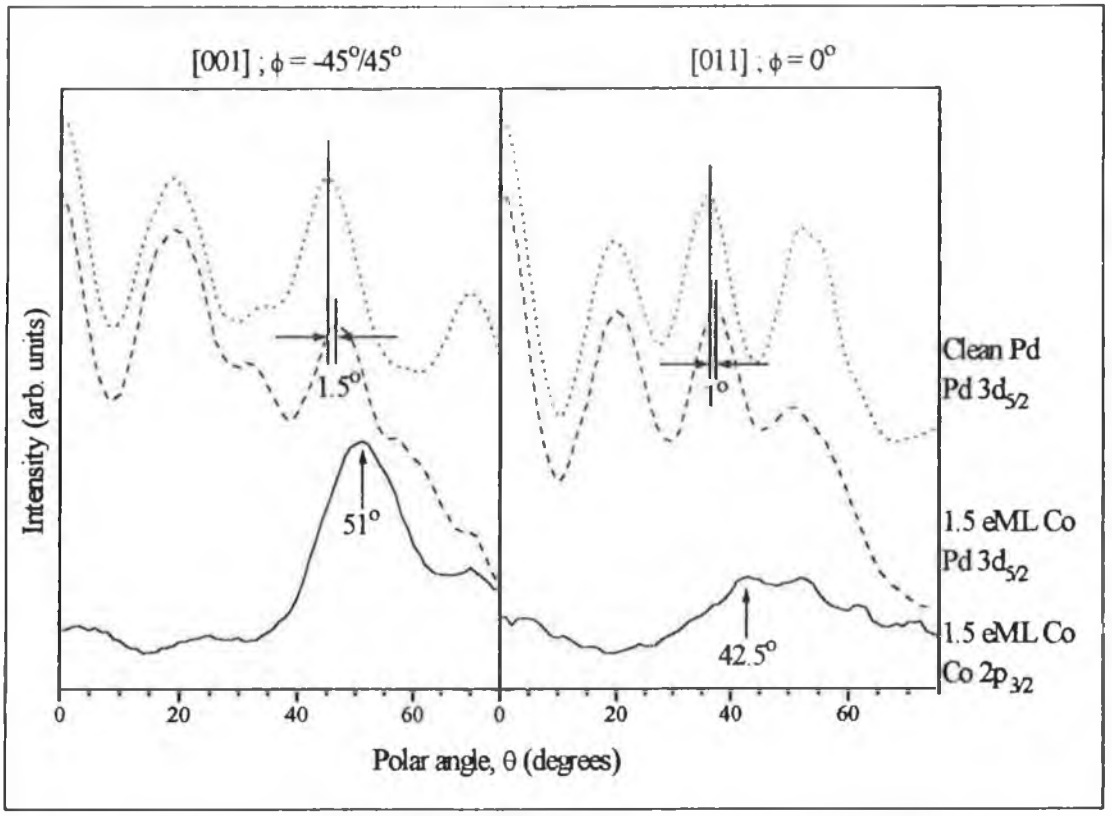

Figure 24: Polar XPD curves measured from clean Pd {100} and from 1.5 eML Co on Pd {100}.

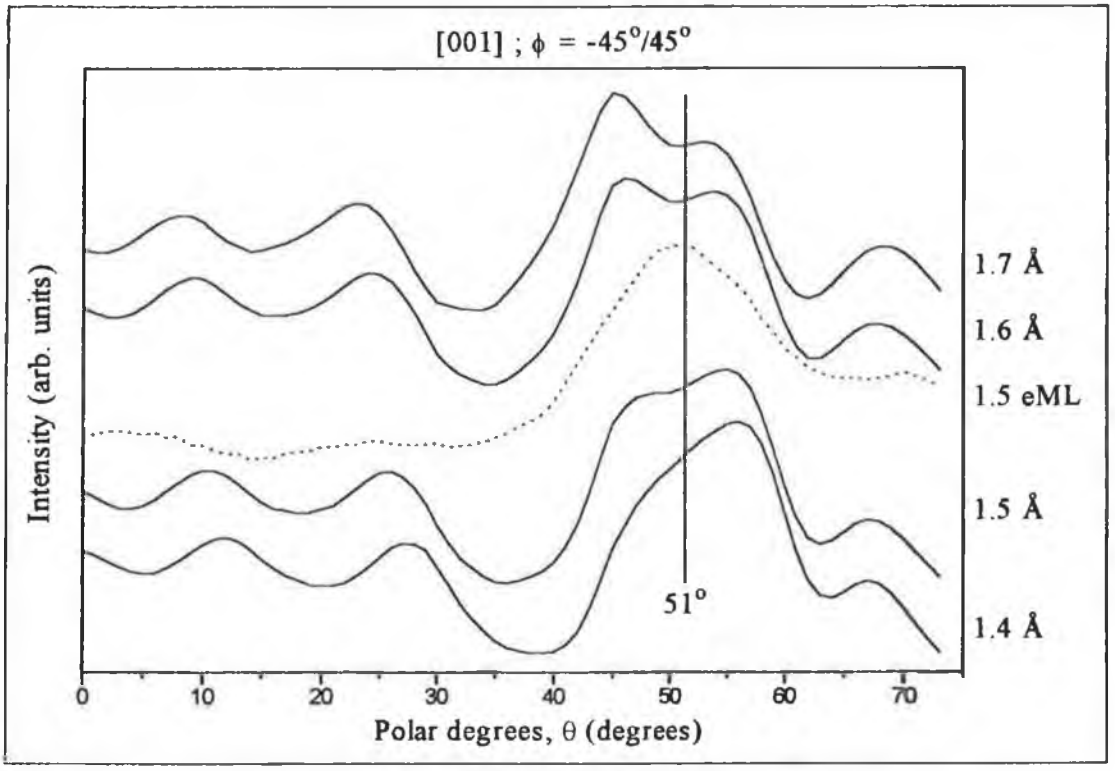

Figure 25: Comparison of the 1.5 eML Co polar XPD curve measured along the [001] azimuth (dotted) with SSCC's done for a cluster of two Co layers on a Pd {100} substrate.

Clearly the bulk of the multi-layer Co on the surface is 2 ML thick. Figure 25 shows a comparison of the 1.5 eML Co polar XPD curve measured along the [001] azimuth with SSCC's done for a cluster consisting of a pseudomorphic 2 ML thick Co adlayer on a Pd {100} substrate (D_{xy}=2.75 Å). The inter-layer spacing (D_z) of the Co was varied as shown in figure 25. As expected, the SSCC's along the [001] azimuth are dominated by a peak at θ~45°-55°. The position of the peak maximum is influenced by the inter-layer spacing. The best agreement between experiment and theory based on peak position is for D_z~1.5-1.6 Å, which corresponds to a contraction of ~11% from the bulk Co {100} inter-layer spacing (1.77 Å). If the in-plane spacing of the Co overlayer is different from that of Pd {100} (not pseudomorphic) then the inter-layer spacing will be correspondingly different in order to preserve peak position (i.e. a larger in-plane expansion (nearer the bulk Co {100} value) would require a smaller inter-layer contraction in order to maintain the forward focusing peak at ~51°).

Some consideration of the implications of the Co polar XPD curve on the overlayer growth mechanism is required. Based on the decay of the PD LEISS signal, ~70% of

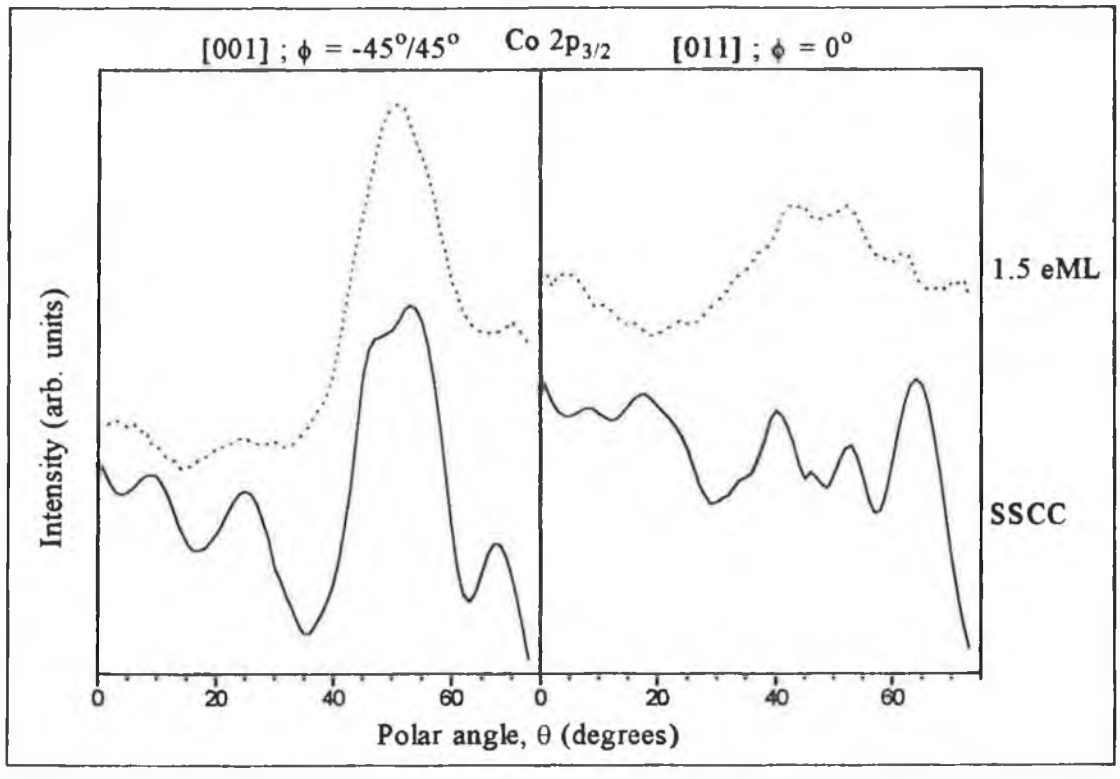

Figure 26: Comparison of the 1.5 eML Co polar XPD scans with SSCC's for a clustering model (see text for details).

the surface is covered by Co after deposition of the 1.5 eML overlayer (i.e. the first Co adlayer contains ~0.7 eML). The remaining ~0.8 eML must form multi-layer thick Co regions. Figure 26 shows a comparison of the 1.5 eML Co polar XPD scans with SSCC's done for a simple cluster model consisting of 0.7 eML in the 1st Co layer, 0.5 eML in the 2nd layer and 0.3 eML in the 3rd layer. The Co inter-layer spacing was set at D_z=1.55 Å. It is clear from figure 26 that there is insufficient 3-layer thick Co in the cluster to produce strong 1st-off-3rd forward focusing features on the SSCC's. This is particularly noticeable along the [011] azimuth, where the off-normal forward focusing peak (θ~41°) is of similar intensity to the higher-order diffraction features that arise for the top two layers of the Co overlayer. The 0.3 eML in the 3rd Co layer of the clusters correspond to a 30% surface coverage and to 20% of the total Co in the cluster. Clearly a greater fraction of the Co overlayer must be 3 or more layers thick before prominent 1st-off-3rd forward focusing peaks begin to appear.

Figure 27 shows the evolution of the Co polar XPD features with increasing coverage. The large shift of the off-normal Co forward focusing peaks from their

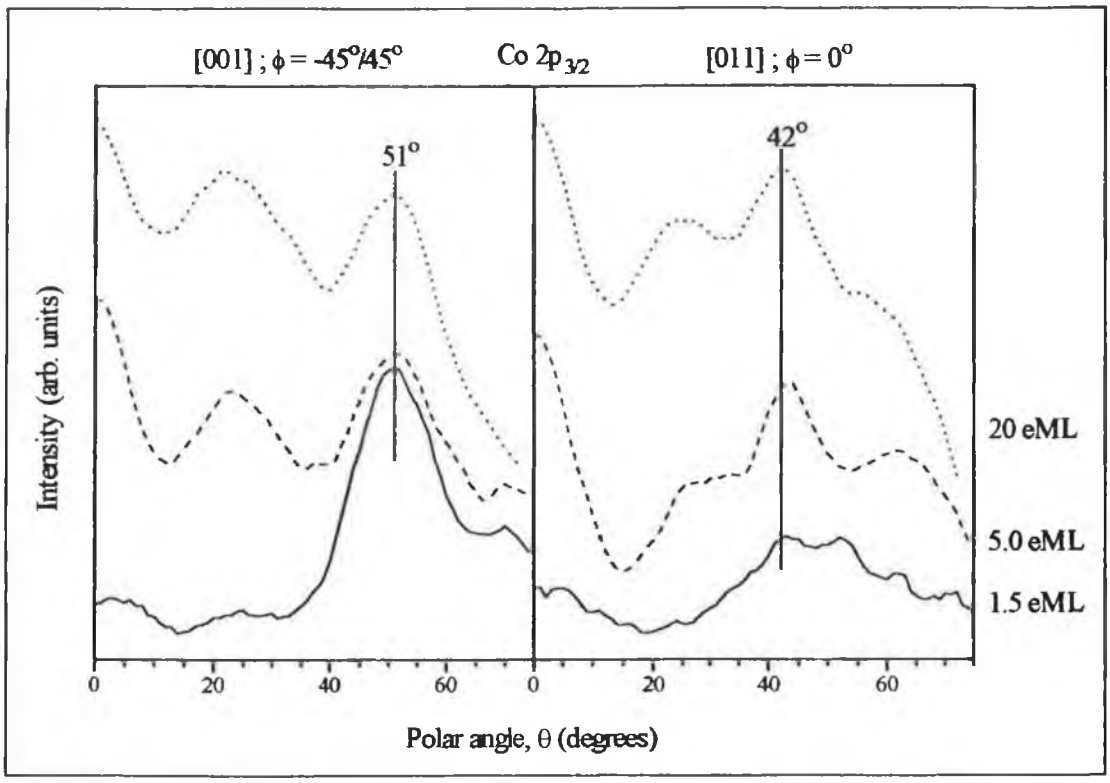

Figure 27: Co polar XPD curves measured for various θ_{Co} on Pd {100}.

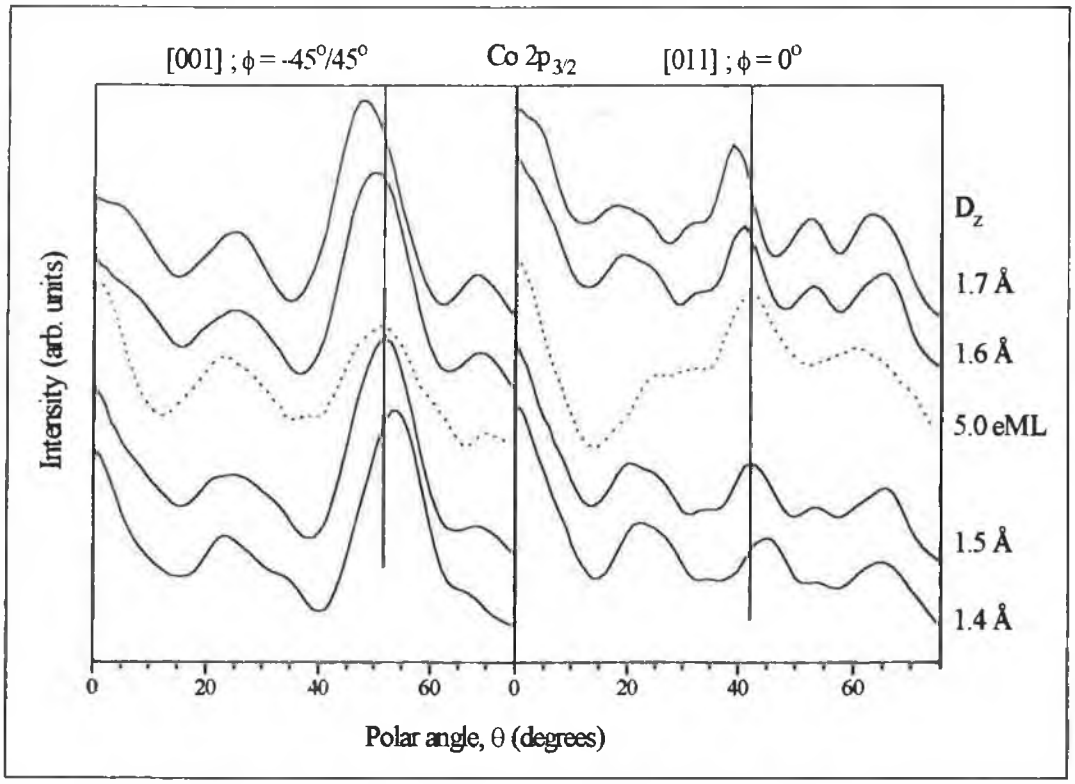

Figure 28: Comparison of SSCC's for different values of D_z with the 5.0 eML Co XPD polar curves.

expected positions is also clearly visible at high θ_{Co} (~20 eML). The main off-normal forward focusing peak occurs at ~51° (±1°) along the [001] azimuth and at ~42° (±1°) along the [011] azimuth. Even at 20 eML there is no evidence of any relaxation of the lattice structure back toward bulk fcc values. Assuming that the positions of the forward scattering peaks on the azimuthal scans correspond exactly to the emitter-scatterer direction, we can obtain qualitative information about the Co overlayer from purely geometric considerations. The position of the forward focusing peaks can be considered as a direct measure of the ratio of D_{xy} (in-plane spacing) to D_z (inter-layer spacing). For bulk fcc lattice structures the value of D_{xy}:D_z is 1.41:1. The corresponding values for the Co overlayers, based on the peak positions observed in figure 27, are 1.74:1 ([001] azimuth) and 1.80:1 ([011] azimuth). This values clearly indicate that the Co lattice is strongly distorted from its bulk fcc values.

The D_{xy}:D_z ratio alone can give no information about the absolute values of the Co lattice parameters. However, it is possible to impose a reasonable lower-limit value on these lattice parameters. The shortest inter-atomic distance in a bulk Co single crystal

is ~2.503 Å [28]. A lower limit can be calculated based on the assumption that the adsorption of Co on Pd {100} does not produce a shorter Co-Co nearest neighbour distance than exists in bulk crystals. Using this assumption, the lowest values of D_{xy} and D_z that are consistent with a ratio of 1.75:1 are 2.75 Å and 1.57 Å respectively. For a ratio of 1.8:1 the corresponding values are 2.78 Å and 1.55 Å. These value represent an in-plane expansion of ~9.9-11.1% and an inter-layer contraction of ~11.3-12.4% relative to bulk Co {100} lattice parameters. This results strongly indicate that the Co overlayers grow pseudomorphic to the Pd substrate, and that they maintain this pseudomorphic growth to high overlayer coverages (>20 eML). A smaller in-plane parameter would require the Co atoms to pack closer together in the overlayer than they do in bulk Co single crystals in order to maintain the forward focusing peak positions.

Figure 28 shows a comparison of SSCC's with the Co polar XPD curves measured from the θ_{Co}~5.0 eML overlayer. It is clear from the comparison of the 5.0 eML and 20 eML curves shown in figure 27 that the 'bulk' overlayer XPD features are already present at the 5 eML coverage. Consequently, a 'bulk' Co cluster was used for the SSCC's. The cluster used consisted of 20 layers of Co. The value of D_{xy} was fixed at 2.75 Å (pseudomorphic to Pd {100}) and D_z was varied as shown in figure 28. Based on the position of the forward scattering peaks the best agreement is for a inter-layer spacing of ~1.5-1.6 Å. This is in agreement with the comparison of the θ_{Co}~1.5 eML experimental curve with SSCC's for a 2 ML thick Co overlayer cluster (figure 25) and confirms the results of the simple geometric analysis.

3.6. Alloying of Cobalt Films on Pd {100}:

Annealing experiments were performed for a Co overlayer on Pd {100} similar to those done for the Co on Pd {111} system. Figure 29 shows the He^+ LEISS measurements taken, at room temperature, from the clean Pd {100} surface, the Co-dosed surface and the annealed surface. The annealing was done in a two-step process. The sample was initially annealed to ~670 K for 8 minutes and subsequently re-annealed to ~670 K for a further 12 minutes. Based on the integrated areas under

the LEISS peaks shown in figure 29, ~80% of the surface is covered by Co after deposition. Upon annealing, the signal due to Co is strongly attenuated, although not completely eliminated. Based on the residual Co ISS signal not more than 5% of the sample surface layer consists of Co atoms after annealing. Clearly alloying with the substrate has occurred. In order to gain a greater understanding of the alloying process XPD measurements were taken before and after the annealing steps.

Figure 30 shows Co polar XPD curves measured before and after the annealing steps. As expected for θ_{Co}~3.7 eML, the polar XPD curves measured before annealing show strong forward focusing features indicating multi-layer thick islands on the surface. The XPD curves undergo significant changes upon annealing. Along the [001] azimuth the forward focusing peak at θ~51° shifts to ~47°, close to its position for a bulk fcc structure. This peak remains strong even after an annealing time of 20 minutes. In contrast, the peak at normal emission (θ=0°) is strongly attenuated. This indicates that the bulk of the Co that remains in the crystal selvedge is localised in the 2nd layer with relatively little in the deeper layers of the selvedge. Migration into the

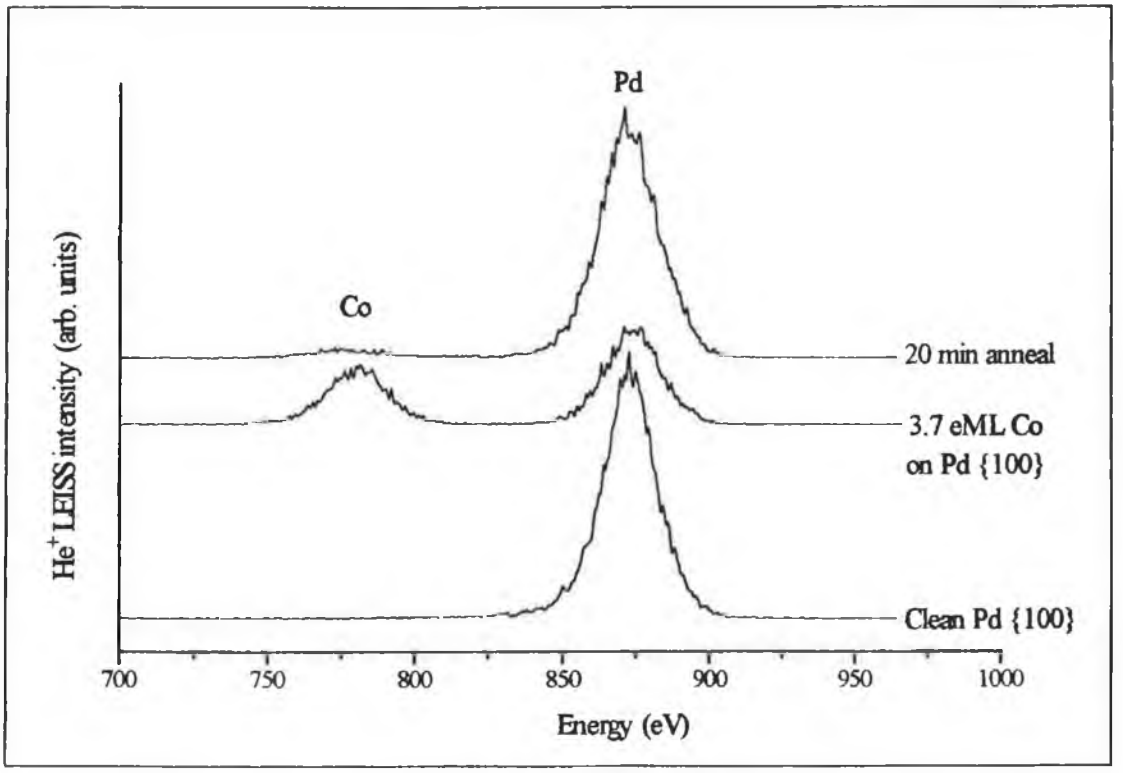

Figure 29: He^+ LEISS spectra obtained from clean Pd, after deposition of ~3.7 eML Co and after annealing to ~670 K for 20 minutes.

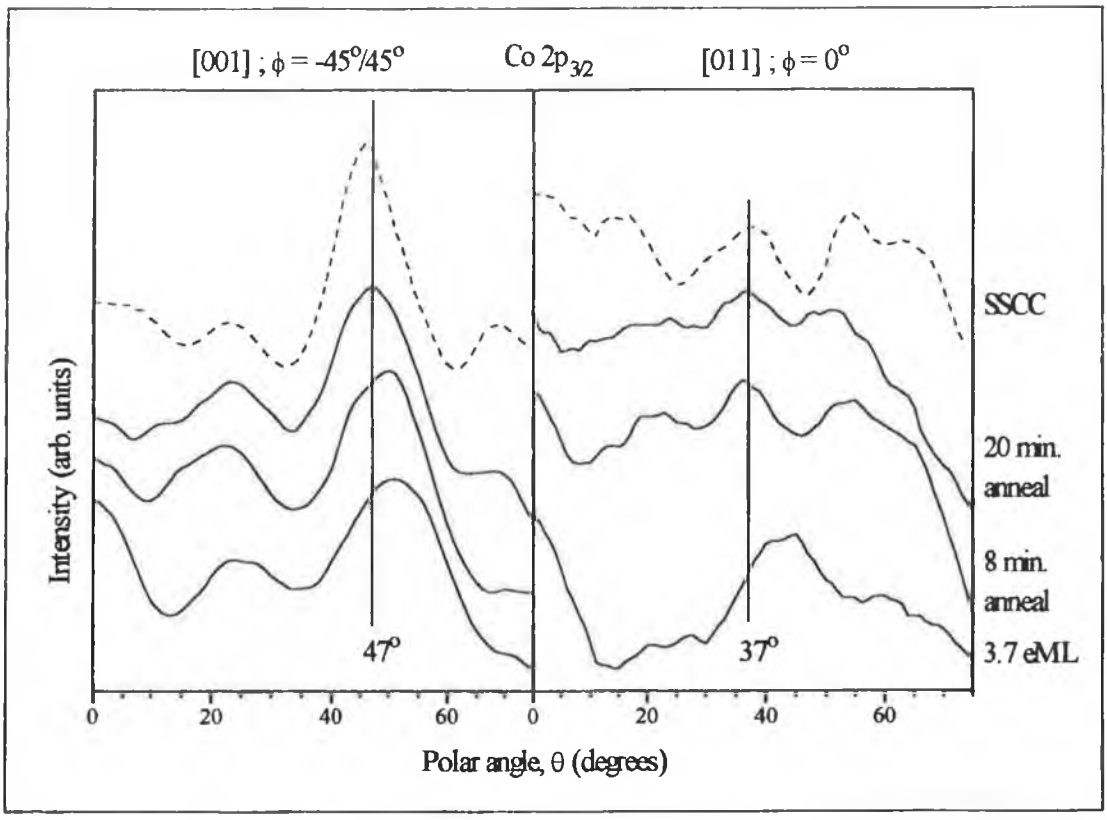

Figure 30: Polar XPD curves measured before and after annealing of 3.7 eML Co on Pd {100}. The theory curves are for an 'annealed' cluster (see text for details).

sample bulk, where it contributes little intensity to the XPD curves, may account for the excess Co.

Further evidence for the lack of Co in the 3rd (or deeper layer) of the Pd selvedge is provided by the polar XPD scans along the [011] azimuth. Along this azimuth all direct forward scattering peaks arise from 3rd or deeper layers. Before annealing there are strong forward focusing peaks, which indicate a multi-layered structure. However, after annealing much of the structure of the XPD curves is lost. Forward focusing peaks are still in evidence at 0° and 37° but they no longer dominate the curve structure. The shift of the off-normal forward focusing peak from ~42° to ~37° after annealing is in agreement with the peak shift for the scans taken along the [001] azimuth.

The SSCC curves shown in figure 30 are for an 'annealed' cluster. This consisted of a Pd lattice structure with 5% Co in the 1st layer, 50% Co in the 2nd layer and 20% Co

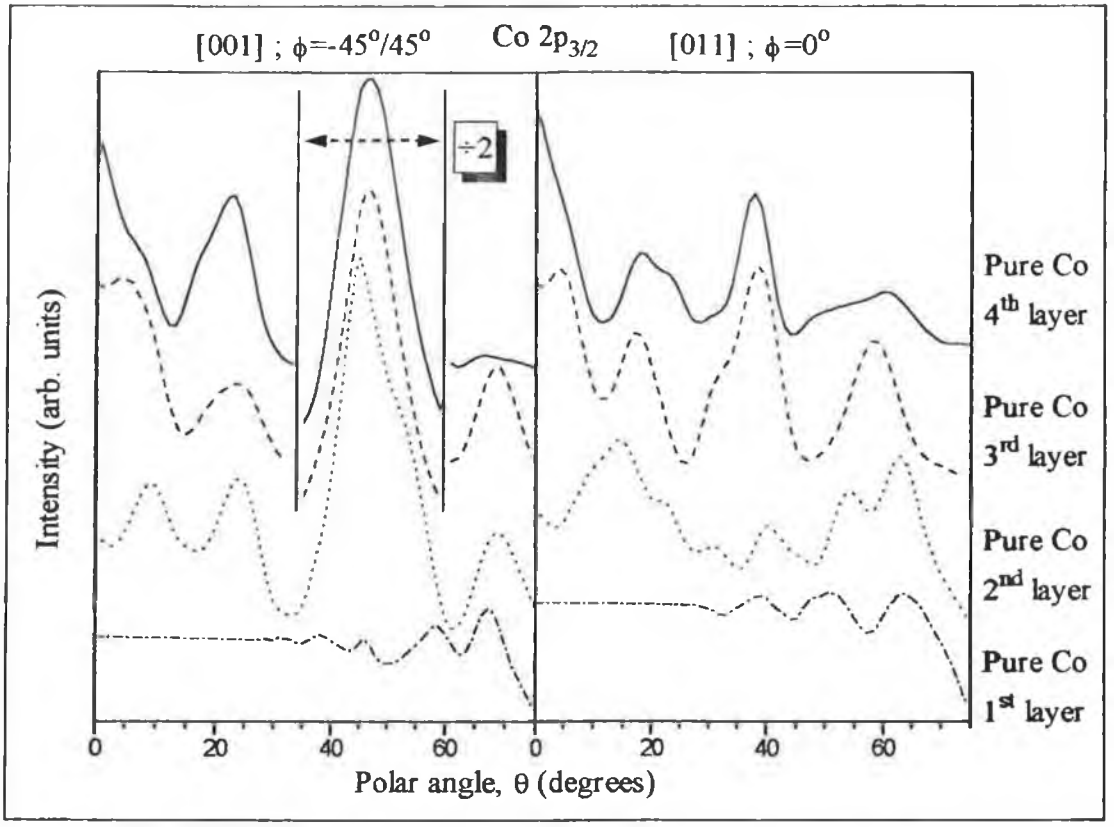

Figure 31: SSCC's done for a pure Co monolayer incorporated into the selvedge of a Pd cluster at the indicated positions.

in the 3rd layer. All additional layers were pure Pd. The in-plane lattice parameter of the cluster was 2.75 Å and the inter-layer spacing, other than for the 1st-to-2nd layer spacing, was 1.945 Å (bulk Pd value). The 1st-to-2nd layer spacing was allowed to vary in order to obtain best agreement between theory and experiment. The best agreement, based on peak position, was obtained for a 1st-to-2nd layer spacing of ~1.8 Å (±0.1 Å), which is the value used for the SSCC's shown in figure 30. This represents a contraction of the outermost layer spacing by ~7.7% from the bulk Pd {100} value.

The results indicate that the Co is preferentially localised in the 2nd layer of the Pd selvedge If the Co atoms were evenly distributed throughout the Pd selvedge, then the polar XPD plots from the annealed surface would have similar features, both in shape and relative intensity, to the polar XPD curves measured from the 5 & 20 eML Co overlayers (figure 27). This is because, for an even Co distribution, the emission from the Co atoms in a given layer of the selvedge would scale relative to the emission

from other layers in a similar fashion to emission from a bulk Co cluster. The fact that the Co emission from the selvedge is being scattered, in the main, by Pd atoms is of little consequence at KE~700 eV.

The forward focusing peak at θ~47° on the [001] azimuth cannot be due to preferential localisation of Co in the 3rd or deeper layers of the crystal selvedge since this would result in strong normal emission forward focusing peaks. Such a strong θ~47° peak relative to the other forward focusing peaks can only arise due to Co in the 2nd layer. This point is illustrated by the SSCC's shown in figure 31. These were done for emission from a bulk cluster with Pd in-plane lattice parameters and an inter-layer spacing of 1.8 Å. The emission was from Co, which was incorporated as a pure monolayer within the selvedge structure. The calculations shown in figure 31 are for this monolayer in the 1st, 2nd, 3rd and 4th layers of the cluster selvedge respectively. As expected, the SSCC's for a pure Co outermost layer are essentially featureless. The important point to note is the strength of the forward focusing features at normal emission along both azimuths, and the strength of the peak at θ~38° along the [011] azimuth, for emission from a Co monolayer in the 3rd & 4th layers of the cluster selvedge. In both cases these features are strong relative to the higher-order diffraction features. Only for emission from Co in the 2nd layer of the selvedge do the SSCC's have a strong peak at θ~47° and weak features at the expected positions of the other forward focusing peaks, as is seen after the 20 minute anneal in figure 30.

The SSCC for the 'annealed' cluster shown in figure 30, which has a high 2nd layer Co concentration, agrees well with the experimental data. However, the Co composition used for the annealed cluster should not be considered as quantitatively accurate. Since the curves are dominated by the contribution from Co in the 2nd layer, there is little sensitivity to the composition of 3rd and deeper layers. The SSCC's can confirm that the bulk of the Co in the Pd selvedge is in the 2nd layer. However, they cannot quantify the absolute amount present.

Figure 32 shows Pd polar XPD curves measured before and after annealing of the 3.7 eML of Co, and from the clean surface. After alloying with the Co overlayer there is a

clear shift of the main Pd off-normal forward focusing peaks to higher polar angles. The shift in peak positions is ~2° (45°→47°, 35°→37°). This shift in the forward scattering peaks is in agreement with the contraction (~7.7%) of the 1st-to-2nd layer spacing found by the SSCC analysis of the Co XPD plots shown in figure 30. This contraction can be attributed mainly to the smaller size of the Co atoms. If a significant proportion of the 2nd layer consists of Co atoms, then a contraction of the 1st-to-2nd and 2nd-to-3rd layer spacing might be expected based purely on size considerations.

The contraction of the outermost inter-layer spacing may indicate that the Co-Pd bond is stronger that the Pd-Pd bond. This would also provide a rational for the preferential localisation of Co within the 2nd layer of the selvedge. The Pd atoms in the outermost layer of a {100} single crystal have lost 4 nearest neighbour. Consequently, any increase in bond strength with the remaining nearest neighbour atoms will compensate for this loss and be energetically favourable. If the Co-Pd bond strength is

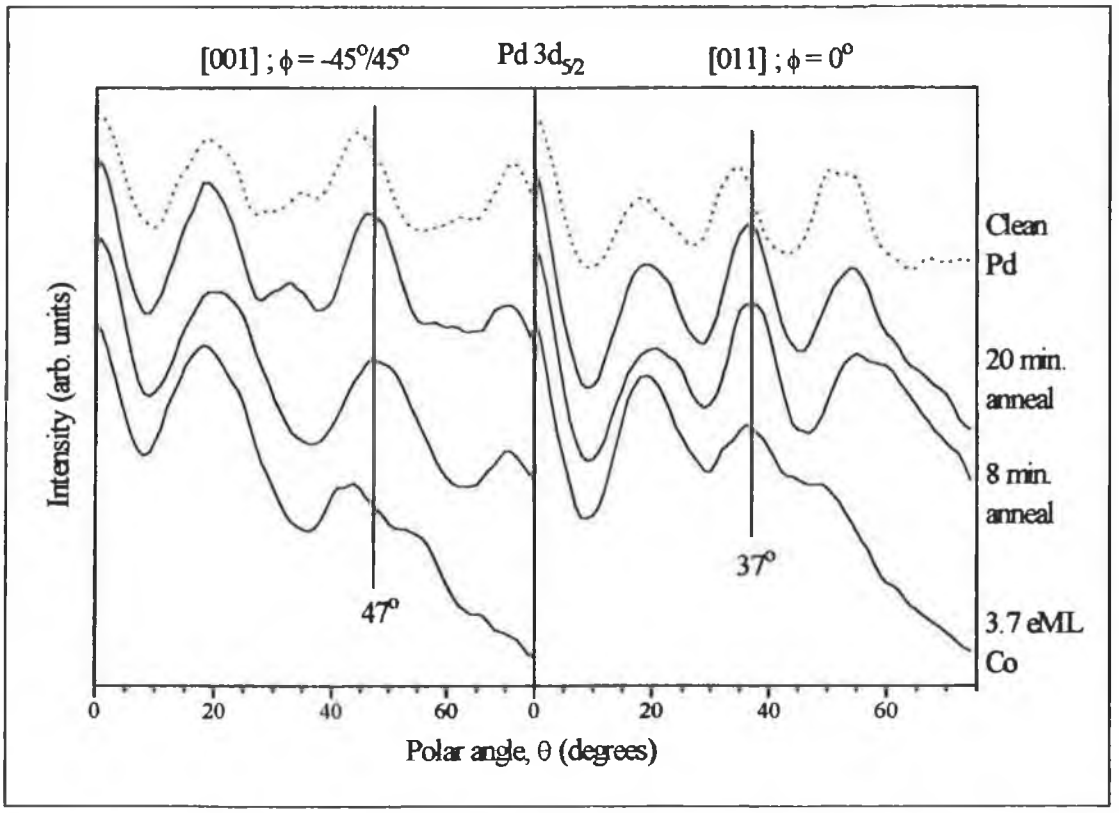

Figure 32: Comparison of Pd polar XPD curves measured from the clean substrate and before and after alloying with a Co overlayer.

significantly greater than that of Pd-Pd, then this would provide an energy barrier to the migration of Co into the crystal bulk and lead to the localisation within the 2nd layer that is observed by XPD.

The Co polar XPD plots shown in figure 30 are relatively insensitive to any 2nd-to-3rd layer spacing change since the bulk of the Co signal comes from the 2nd layer. An indication of a possible contraction of the 2nd-to-3rd layer spacing is provided by the sharpness of the peak at ~37° along the [011] azimuth on the Pd polar scans (figure 32). The two main contributions to this peak are focusing by 1st-off-3rd layers followed by focusing by 2nd-off-4th layers. The contribution becomes progressively weaker for emission from deeper layers. If the 2nd-to-3rd layer spacing is not contracted then the contribution due to 4th-off-2nd scattering would occur at ~35° and the XPD peak would be broadened. The sharpness of the peak suggests that this is not the case, although this can only be considered tentative evidence of such a contraction.

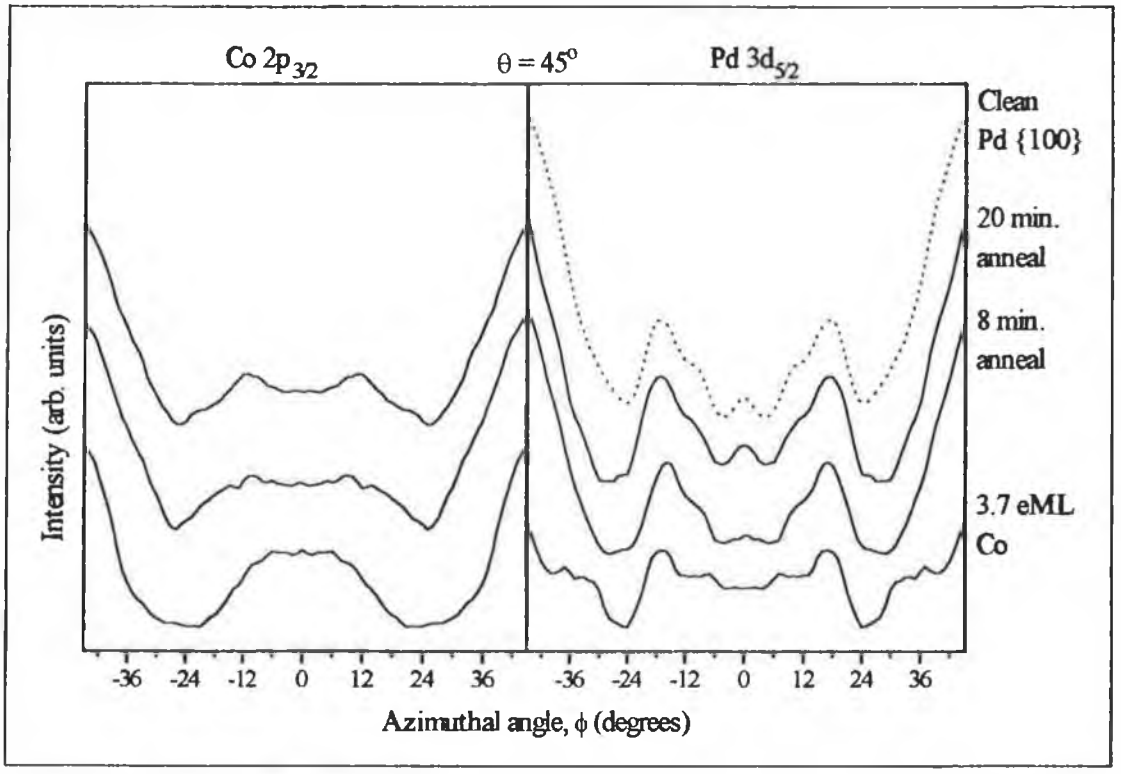

Figure 33: Azimuthal XPD curves measured from Co and Pd before and after annealing of a 3.7 eML Co overlayer on Pd {100}.

Figure 33 shows azimuthal XPD curves measured from the clean Pd surface, and also before and after annealing of the Co overlayer, using both Pd and Co emission. After annealing the Pd azimuthal features, which had been modified and damped by the Co overlayer, re-emerge strongly. The Pd azimuthal curve measured from the annealed surfaces are very similar to those measured from the clean surface. In the case of the Co azimuthal curves there are changes in the azimuthal feature centred at $\phi=0^{\circ}$ upon annealing. The scattering features in this region broadens and forms a doublet structure with maxima at $\phi=-12^{\circ}/12^{\circ}$. This indicates that, at low θ_{Co}, the azimuthal curve can distinguish between an annealed and an unannealed surface. Comparison of the Co XPD curves in figure 33 with those shown in figure 23 is qualitative evidence that significant alloying of Co and Pd does not occur at room temperature.

4. DISCUSSION:

4.1. Co on Pd {111}:

Cobalt deposited on Pd {111} grows in 3-D islands (VW growth). On the basis of the LEISS results, the initial sub-monolayer depositions of Co (<0.7 eML) on Pd {111} do not appear to form islands to any great extent (see figure 8). However, strong island growth commences before the first monolayer is completed. The fact that the substrate LEISS signal does not disappear until θ_{Co}>6 eML indicates that the surface is covered with a high density of islands that do not readily coalesce.

The Co adatoms preferentially occupying the 'fcc' TFH sites on the Pd surface. The overlayers grow in a single-domain fcc lattice structure that follows the stacking pattern of the Pd substrate (i.e. ABCabc....). A structural transition occurs in the Co adlayers during deposition of the first ~5 eML on the surface. This is evidenced by changes in both the Co azimuthal and polar XPD scans with coverage. These changes are complete after deposition of ~5 eML and no other significant changes occur at higher θ_{Co} (>20 eML).

The Co polar XPD scans measured from the low coverage overlayers have their off-normal forward focusing peaks shifted to higher polar angles relative to their expected position for a bulk fcc structure. This is indicative of a tetragonally distorted fcc lattice structure with an expanded in-plane lattice parameter and a contracted inter-layer spacing. The maximum shift in the forward focusing peak position is ~3° (θ_{Co}~0.85 eML). As θ_{Co} increases the peak position reverts to the normal polar angle for a fcc lattice structure.

The structural transition and tetragonal distortion seen in the XPD scans can be attributed to the large lattice mismatch between Co and Pd (~9.5%). The Co atoms in the first layer adsorbed on Pd {111} are forced to adopt an expanded in-plane lattice parameter by the substrate periodicity. This, in turn, results in a shortening of the inter-layer spacing of subsequent adsorbed layers causing the shift of the off-normal

forward focusing peaks to higher polar angles. The expansion of the Co in-plane lattice parameter for pseudomorphic growth results in a large strain in the growing Co overlayers, and so they quickly revert to a bulk fcc-like structure after deposition of ~5 eML. The change in lattice structure appears to occur gradually with coverage, with a reduction of strain in each additional layer, possibly by incorporation of growth defects within the Co overlayers.

It is surprising that the structure of the Co overlayers does not collapse to the lowest energy Co phase at 300 K, i.e. a hcp {0001} crystal structure. However, the Co hcp and fcc crystal structures are energetically quite similar (bulk Co single crystals undergo the hcp→fcc martensitic transition at 706±4 K and the reverse fcc→hcp transition at 691±4 K [48]). Hence, a small expansion of the Co in-plane lattice parameter may be sufficient to stabilise the fcc phase at room temperature (i.e. the persistence of the fcc structure in the high coverage overlayers may be due to a slight distortion of the Co fcc lattice that was not detected by the polar XPD scans). The large mismatch between Co and Pd atoms will result in large interface and strain energies at the Co/Pd interface, which may initially stabilise the fcc phase. These energies relax away with increased θ_{Co}, but may persist to a sufficient extent at high coverage (>20 eML) to create a slight lattice distortion and maintain the stabilisation of the fcc phase. Alternatively, growth defects may become incorporated within the growing overlayers, which may prevent the fcc→hcp transition.

4.2. Co on Pd {100}:

The initial growth of Co on Pd {100} is also in islands (VW growth). However, unlike the growth of Co on Pd {111}, the island growth occurs from the onset of adsorption. The Co adatoms occupy the four-fold-hollow sites on Pd {100} and grow in a fcc stacking pattern. Similar to Co on Pd {111}, the initial Co overlayers have a tetragonally distorted lattice structure. However, in the case of the Pd {100} surface the shift observed in the polar XPD features is much greater (~6°). In contrast to Co on Pd {111}, there is no evidence of any structural transition or relaxation of the overlayer lattice parameters back toward bulk values for θ_{Co} up to ~20 eML. Simple

geometric calculations and SSCC's indicate that the Co overlayers have an inter-layer spacing of 1.5-1.6 Å and a minimum in-plane parameter of ~2.75 Å (pseudomorphic with the Pd substrate).

The lack of any relaxation back toward bulk values indicates that the tetragonally distorted lattice structure of Co on Pd {100} is a meta-stable, bct phase at room temperature. This phase represents a local energy minimum of the distorted fcc lattice structure as it undergoes a 'Bain transition' [14] from an fcc to a bcc structure. A similar body-centred-tetragonal phase (bct) has been proposed for the growth of Cu on Pd {100} [15-17]. This phase was first suggested on the basis of a first principles determination of the phase diagram of Cu [15]. Experimental evidence for the stabilisation of the bct phase for Cu on Pd {100} was presented on the basis of LEED [16] and STM [17] studies.

There is a relatively small (~2%) mismatch between the bulk lattice parameters of Co and Cu. Consequently, it is not exceptionally surprising that a meta-stable bct phase of both atoms is stabilised by the same single crystal substrates. The lattice parameters determined experimentally for the Cu on Pd {100} overlayer were D_{xy}=2.75 Å (pseudomorphic) and D_z=1.55 Å [17]. These values yield a D_{xy}:D_z ratio of ~1.77, which is in good agreement with the ratio determined for the Co on Pd {100} overlayers (1.74-1.80). The existence of such a meta-stable phase is the only plausible explanation for the failure of the Co overlayers to relax back to a bulk structure after deposition of 20 eML.

4.3. Alloying Co on Pd {111} and {100}:

The annealing experiments carried out for Co on Pd {111} and Pd {100} yielded similar results. In both cases the Co was found to alloy readily with the substrate upon annealing to temperatures in the region of 600-700 K. He^+ LEISS confirms that the crystal surface after annealing is predominantly Pd. In both cases, the bulk of the Co in the Pd selvedge was found to be localised in the 2nd layer of the substrate. This is clearly evident for the Pd {100} substrate, where Co emission polar XPD scans along

[011] azimuth of the annealed surface have no strong forward focusing peaks. Forward focusing peaks along this azimuth arise only due to emission from the 3rd or deeper layers of the selvedge. In contrast, the off-normal forward focusing peak along the [001] azimuth, which can originate from 2nd layer emission, is very strong after annealing. In the case of the Pd {111} substrate, both high symmetry azimuths have XPD forward focusing peaks that arise from the 2nd layer. These features are strong after annealing while the XPD peaks that arise from 3rd or deeper layer emission are significantly weaker.

It is possible that the localisation of the Co in the 2nd layer is a purely kinetic effect (i.e. migration to the bulk is thermodynamically favourable but occurs at a slow rate at the annealing temperatures used). However, the annealing experiment done on the Pd {100} crystal suggests that some factor other than simply kinetics is retaining the Co in the 2nd layer of the selvedge. In this case the Co coverage was ~3.7 eML (actually higher given the VW growth mechanism). If kinetics factors were limiting the migration of Co into the bulk, then they should act essentially equally on all layers beneath the top layer. Hence, annealing of ~3.7 eML Co should result in a greater concentration of Co in the 2nd-to-5th layers of the Pd selvedge. However, the Co polar XPD plots after annealing (figure 30) do not show a significant concentration of Co in the 3rd or deeper layers relative to the Co concentration in the 2nd layer. This indicates that some additional factor is causing the retention of Co within the 2nd layer of the Pd crystals.

The reason for the localisation of the Co within the 2nd layer of the Pd {111} and {100} selvedges may be due to the Co-Pd bond strength as discussed earlier. If this is significantly greater than the Pd-Pd bond strength, then retention of the Co within the 2nd layer would partially compensate for the loss of Pd-Pd bonds experienced by the surface atoms. Hence, migration of the Co atoms into the bulk may be thermodynamically favourable but energetically hindered.

5. CONCLUSIONS:

The growth of Co overlayers on Pd {111} & {100} clearly illustrates how the bulk structure of a metal crystal can be modified at room temperature by thin film epitaxy on a substrate of different crystallographic structure/lattice constant. In the case of Co on Pd {111} the overlayers are stabilised in a fcc crystal structure despite the fact that hcp is the normal bulk structure of Co at room temperature. For thin films (up to ~5 eML) XPD indicates a tetragonal distortion of the overlayers. This distortion quickly relaxes as a function of overlayer thickness, and disappears for θ_{Co}>5 eML. At higher θ_{Co} the overlayer structure is undistorted fcc (within the accuracy of detection), and this lattice structure persists to θ_{Co}>20 eML. For Co adsorbed on Pd {100} the overlayers adopt a meta-stable bct structure that persists to high coverages with no evidence of re-crystallisation to a fcc or hcp phase for coverages up to 20 eML. The stabilisation of meta-stable Co crystal structures is due to the large mismatch between the lattice parameters of Co and Pd. In cases where there is only a small lattice mismatch between the substrate and adsorbate, pseudomorphic growth usually occurs with little or no disruption of the overlayer structure. As the mismatch increases, structural changes in the overlayer become more likely in order to stabilise the overlayers.

Alloying of a Co adlayer with the Pd {111} & {100} single crystals results in a preferential localisation of Co in the 2nd layer of the Pd selvedge in both cases. This may indicate that the Co-Pd bond is stronger than the Pd-Pd bond. If this is the case, a high concentration of Co in the 2nd layer would help stabilise the top layer Pd atoms, which have 'lost' some nearest neighbouring atoms.

6. REFERENCES:

[1] M. Hartmann, B.A.J. Jacobs and J.J.M. Braat, Philips Tech. Rev., 42 (1985) 37.

[2] M. Hong, D.D. Bacon, R.B. van Dover, E.M. Gyorgy, J.F. Dillon and S.D. Albiston, J. Appl. Phys., 57 (1985) 3900.

[3] W.B. Zeper, F.J.A.M. Greidanus, P.F. Carcia and C.R. Fincher, J. Appl. Phys., 65 (1989) 4971.

[4] E.R. Moog, C. Liu, S.D. Bader and J. Zak, Phys. Rev. B, 39 (1989) 6949.

[5] Y. Ochiai, S. Hashimoto and K. Aso, IEEE Trans. Magn., 25 (1989) 3755.

[6] W.B. Zeper, F.J.A.M. Greidanus and P.F. Carcia, IEEE Trans. Magn., 25 (1989) 3764.

[7] P.F. Carcia, J. Appl. Phys., 63 (1988) 5066.

[8] F.J.A.den Broeder, D. Kuiper, A.P.van de Mosselaer and W. Hoving, Phys. Rev. Lett., 60 (1988) 2769.

[9] H.J.G. Draaisma and W.J.M. de Jonge, J. Appl. Phys., 62 (1987) 3318.

[10] J.A. Venables, G.D.T. Spiller and M. Hanbücken, Rep. Prog. Phys., 47 (1984) 399.

[11] C.T. Campbell, Annu. Rev. Phys. Chem., 41 (1990) 775.

[12] M. Sambi, E. Pin and G. Granozzi, Surf. Sci., 340 (1995) 215.

[13] M. Galeotti, A. Atrei, U. Bardi, B. Cortigiani, G. Rovida and M. Torrini, Surf. Sci., 297 (1993) 202.

[14] E.C. Bain, Trans. AIME, 70 (1924) 25.

[15] I.A. Morrison, M.H. Kang and E.J. Mele, Phys. Rev. B, 39 (1989) 1575.

[16] H. Li, S.C. Wu, D. Tian, J. Quinn, Y.S. Li, F. Jona and P.M. Marcus, Phys. Rev. B, 40 (1989) 5841.

[17] E. Hahn, E. Kampshoff, N. Wälchli and K. Kern, Phys. Rev. Lett., 74 (1995) 1803.

[18] T. Kraft, P.M. Marcus, M. Methfessel and M. Scheffler, Phys. Rev. B, 48 (1993) 5886.

[19] M.T. Kief and W.F.J. Egelhoff, Phys. Rev. B, 47 (1993) 10785.

[20] J.R. Credá, P.L. de Andres, A. Cebollada, R. Miranda, E. Navas, P. Schuster, C.M. Schneider and J. Kirschner, J. Phys.:Condens. Matter, 5 (1993) 2055.

[21] C.M. Wei, T.C. Zhao and S.Y. Tong, Phys. Rev. Lett., 65 (1990) 2278.

[22] M. Hochstrasser, M. Zurkirch, E. Wetli, D. Pescia and M. Erbudak, Phys. Rev. B, 50 (1994) 17705.

[23] V. Scheuch, K. Potthast, B. Voigtländer and H.P. Bonzel, Surf. Sci., 318 (1994) 115.

[24] P. le Fevre, H. Magnan, O. Heckmann, V. Briois and D. Chandesris, Phys. Rev. B, 52 (1995) 11462.

[25] P. Grütter and U.T. Dürig, Phys. Rev. B, 49 (1994) 2021.

[26] S.T. Purcell, M.T. Johnson, N.W.E. McGee, J.J. de Vries, W.B. Zeper and W. Hoving, J. Appl. Phys., 73 (1993) 1360.

[27] T. Yamazaki, Y. Suzuki, T. Katayama, M. Taninaka, K. Nakagawa and A. Itoh, J. Appl. Phys., 70 (1991) 3180.

[28] J.M. MacLaren, J.B. Pendry, P.J. Rous, D.K. Saldin, G.A. Somorjai, M.A. van Hove and D.D. Vvedensky, Surface Crystallographic Information Service: A Handbook of Surface Structures, D. Reidel publishing company, Dordrecht, Holland, (1987).

[29] W.F.J. Egelhoff, CRC Crit. Rev. Solid State Mat. Sci., 16 (1990) 213.

[30] S.A. Chambers, H.W. Chen, I.M. Vitomirov, S.B. Anderson and J.H. Weaver, Phys. Rev. B, 33 (1986) 8810.

[31] C.S. Fadley, Prog. Surf. Sci., 16 (1984) 275.

[32] E. Bauer, Z. Krist., 110 (1958) S372.

[33] E. Bauer, Applicat. Surf. Sci., 11/12 (1982) 479.

[34] J.A. Venables, Surf. Sci., 299/300 (1994) 798.

[35] D.K. Flynn, J.W. Evans and P.A. Thiel, J. Vac. Sci. Technol. A, 7 (1989) 2162.

[36] T.N. Taylor, R.E. Muenchausen, M.A. Hoffbauer, A.W. Denier van der Gon and J.F. van der Veen, J. Vac. Sci. Technol. A, 8 (1990) 2732.

[37] R. Kunkel, Phys. Rev. Lett., 65 (1990) 733.

[38] C. Argile and G.E. Rhead, Surf. Sci. Rep., 10 (1989) 277.

[39] G.E. Rhead, M.G. Barthès and C. Argile, Thin Solid Films, 82 (1981) 201.

[40] M. Schmid, W. Hofer, P. Varga, P. Stoltze, K.W. Jacobsen and J.K. Norskov, Phys. Rev. B, 51 (1995) 10937.

[41] C. Nagl, O. Haller, E. Platzgummer. M. Schmid and P Varga, Surf. Sci., 321 (1994) 237.

[42] J. Neugebauer and M. Scheffler, Phys. Rev. B, 46 (1992) 16067.

[43] D. Briggs and M.P. Seah, Practical Surface Analysis, John Wiley & Sons, New York, (1990).

[44] F. Herman and S. Skillman, Atomic Structure Calculations, Englewood Cliffs, N.J. Prentice Hall Inc., New York, (1963).

[45] M.-L. Xu and M.A. van Hove, Surf. Sci., 207 (1989) 215.

[46] M.-L. Xu, J.J. Barton and M.A. van Hove, Phys. Rev. B, 39 (1989) 8275.

[47] L.Z. Mezey and J. Giber, Jap. J. Appl. Phys., 21 (1982) 1569.

[48] M.J. Laubitz and T. Matsumura, Can. J. Phys., 51 (1973) 1247.

Chapter IV

The Growth Mechanism, Geometric and Electronic Structure of Ultra-Thin Copper Films on Palladium {110}.

1. INTRODUCTION:

The study of the early stages of the growth of thin metal films on solid surfaces is of interest because it represents the first stage in crystal growth [1], and also because bimetallic surfaces play an important role in a number of technologically important areas including catalysis, electrochemistry and corrosion passivation [2]. Epitaxial growth of one metal on the surface of a different metal opens the possibility of producing ultra-thin films with crystal phases not encountered under normal temperatures and pressure [3]. Much work on metal-on-metal growth has been stimulated by the possibility of modifying and ultimately controlling the magnetic, electronic and catalytic properties of thin films via lattice expansions/contractions or by stabilisation of thermodynamically meta-stable phases induced by the substrate-adsorbate interface.

Copper is one of the most widely studied metal adsorbates. The electronic structure of bulk Cu has been extensively studied [4]. The low density of states at the Fermi level leads to sharp Cu photo-emission features. In addition, surfaces of Cu exhibit a range of surface states and resonances. This makes Cu an ideal prototype metal for studying the effect of lattice strain on electron states. A substantial amount of structural work has been done on the growth of Cu films on the different crystallographic faces of various metal substrates. Growth on substrates with differing lattice constant and bulk structure has been found to produce a range of novel structural modifications in the Cu overlayers. For instance, a bcc phase of Cu has been observed for deposition on Fe {100} [5] and hcp Cu has been grown on Co $\{10\bar{1}0\}$ [6]. Growth of a meta-stable body-centred-tetragonal (bct) phase of Cu on Pd {100} has also been reported [7-9].

In addition to modifications of the bulk crystal structure, lattice strain induced by the substrate may result in surface phase transitions. For example, there is evidence for a reversible $(1\times1)\leftrightarrow(2\times1)$ phase transition upon cooling of ultra-thin fcc Fe films on Cu {100} from 300 to 90 K [10]. The surfaces of fcc {110} transition metals are of particular interest due to the delicate energy balance between the bulk truncated (1×1) phase and the (1×2)-missing-row (MR) geometry [11, 12]. Guillopé and Legrand [13]

predicted, on the basis of tight-binding calculations, that the imposition of strain on {110} surfaces might result in an inversion of the relative stability of the (1×1) and (1×2)-MR surface phases. This study indicated that for Ag an expansive strain of >2% should result in the (1×2)-MR surface being energetically favourable, while for Cu a strain of >5% would be required. Due to the ~7.7% lattice mismatch between Pd and Cu single crystals, pseudomorphic growth of Cu on Pd {110} may result in sufficient in-plane strain to stabilise the (1×1)→(1×2)-MR transition in the Cu overlayers. Due to the large lattice mismatch, the Cu/Pd is an ideal system for investigating the possibility of strain-induced surface transformations. Note however, that the calculations of Guillopé and Legrand were for a distorted Cu lattice, not substrate supported Cu overlayers.

Catalytically, Cu/Pd systems are of interest because Cu-based bimetallic catalysts show improvements in reactivity, selectivity and stability compared with the single component catalysts [14, 15]. Industrially, Cu and Pd are interesting because they are both used as catalysts for methanol synthesis [16] and supported bimetallic CuPd particles have been shown to maintain a high turnover rate for CO oxidation over a much wider temperature range than the elementary catalysts alone [17]. It may be possible to exert control over these properties by tailoring the composition of the bimetallic surface.

The formation of thin layer films of one metal on another is studied with the aim of better understanding catalytic processes at a microscopic level. Thin films may demonstrate catalytic properties different from those of the equivalent bimetallic alloy surfaces. A number of studies have been carried out on the growth of Cu films on the {100} and {111} faces of Pd single crystals. Li *et al* [18] reported, on the basis of LEED measurements, that Cu grows epitaxial but incommensurate with Pd {111} via nucleation of small multi-layer islands on the surface. For Cu grown on a 1500 Å thick Pd {111} slab on mica, Vook *et al* [19] reported that the first 2 ML grew layer-by-layer, followed by cluster growth, on the basis of work function measurements.

Growth of Cu on Pd {100} was reported to proceed via a Stranski-Krastanov (SK) mechanism on the basis of LEED, ARUPS, AES and work function measurements [20]. Based on the Auger signal increase as a function of θ_{Cu}, the first 2 Cu ML were reported to adopt a pseudomorphic and flat (layer-by-layer) growth, with subsequent Cu deposition resulting in the formation of Cu clusters. Cu has been reported to grow in a meta-stable *body centred tetragonal* (bct) phase on Pd {100} [8, 9]. There is a biaxial expansion of the Cu overlayers in-plane to the lattice parameter of Pd (2.75 Å), while the inter-layer spacing is contracted to ~1.55 Å. Pseudomorphic growth is possible because the bct phase (a local energy minimum of the distorted fcc structure [7]) is virtually strain free.

The growth of Cu thin layers on Pd {110} has been extensively studied using STM by Hahn *et al* [21-24]. In particular, this work has dealt with the temperature dependence of the Cu growth mode. The growth mode is reported as changing from Volmer-Weber (VW) at 300 K to Frank-van der Merwe (FM) at 600 K with an intermediate SK growth mode (1 ML & islands) around 400 K [23]. Inter-diffusion of the Cu and Pd was reported above 700 K. The STM images provided a detailed picture of the sub-monolayer growth of Cu on Pd {110} at room temperature. At θ_{Cu}=0.35 ML (coverage determined by STM) Cu formed 2-dimensional islands on the surface, which were elongated along the $[1\bar{1}0]$ surface azimuth. These islands had lengths of up to ~800 Å (300 Cu atoms) and an average width of ~19 Å (5 close-packed rows). The elongation was attributed to the relative ease of adatom migration along the surface troughs ($[1\bar{1}0]$ azimuth) compared with the barrier to migration across the troughs ([001] azimuth) [24]. Increasing θ_{Cu} to 0.7 ML resulted in a filling of the gaps between the islands, thereby increasing the average island width to ~40 Å. At this coverage, growth of the Cu 2nd layer was observed. Above the 1st-layer, the Cu nucleates in small 3-D clusters (10-30 Å in width) with a large micro-roughness. The 3-D islands were still oriented along the $[1\bar{1}0]$ azimuth, although the elongation was less obvious. The diffusion anisotropy along different azimuths was not as marked once the first monolayer formed, indicating a reduced diffusion barrier for Cu on copper surfaces. Embedded atom calculations of the structural and dynamical properties of sub-monolayer θ_{Cu}'s on Pd {110} have found that the formation of 1-

dimensional chains along the [1$\bar{1}$0] surface channels is the most stable structure, in agreement with the STM measurements [25].

In this chapter the results of a LEED, AES, XPD and angle-resolved ultra-violet photo-emission spectroscopy (ARUPS) study on the growth of ultra-thin Cu films on Pd {110} are presented [26]. Information is obtained regarding the growth mechanism and structure of the films as a function of Cu coverage and related to the electronic properties of the overlayer as a preliminary to surface reactivity studies.

2. EXPERIMENTAL:

2.1. LEED, AES and XPD:

These measurements were performed in a VG Scientific ADES-400 electron spectrometer operating at a base pressure of 5×10^{-11} torr. A dual anode (Al & Mg) X-ray source was used for photo-electron excitation. The Pd {110} single crystal was cleaned in-situ by cycles of argon ion bombardment and annealing to ~700 K. A clean surface was demonstrated by a sharp p(1×1) LEED pattern and the absence of any contaminants above the AES and XPS noise level. Copper was deposited from a Vacuum Science Workshops KC3 metal evaporator, which was fitted with a cooled shroud and shutter, at a rate of ~1 ML per hour (see As-*t* plot, figure 2). The chamber pressure never exceeded 1×10^{-10} torr during evaporation. The Cu overlayer was confirmed as being homogenous across the sample surface by AES.

The growth of Cu on the sample was monitored via the Pd $M_{4/5}N_{4,5}N_{4,5}$ and Cu MVV Auger peaks recorded using the LEED optics as a retarding field analyser at modulation voltages of 10 V and 3.5 V respectively. Polar XPD curves were measured along the [001] surface azimuth (±2°, aligned via LEED). Normal emission (±1°) was located using the maximum of the Pd 0° forward focusing peak (Al K_α $3d_{5/2}$ emission, KE~1145 eV). The energy analyser had an acceptance cone of half-angle=1.5°. Cu polar XPD curves were measured in 2.5° steps using Al K_α-excited emission from the $2p_{3/2}$ core level (KE~550 eV).

2.2. ARUPS Measurements:

The ARUPS measurements were performed on beamline 6.2 at the CLRC synchrotron radiation source in the UK. This beamline has a VUV toroidal grating monochromator, a mu-metal UHV chamber with an angle-resolved electron energy analyser (ADES 400) (resolution=0.25 eV). This analyser was rotatable in two planes (horizontal and vertical) about the centre of the chamber. The beamline delivers

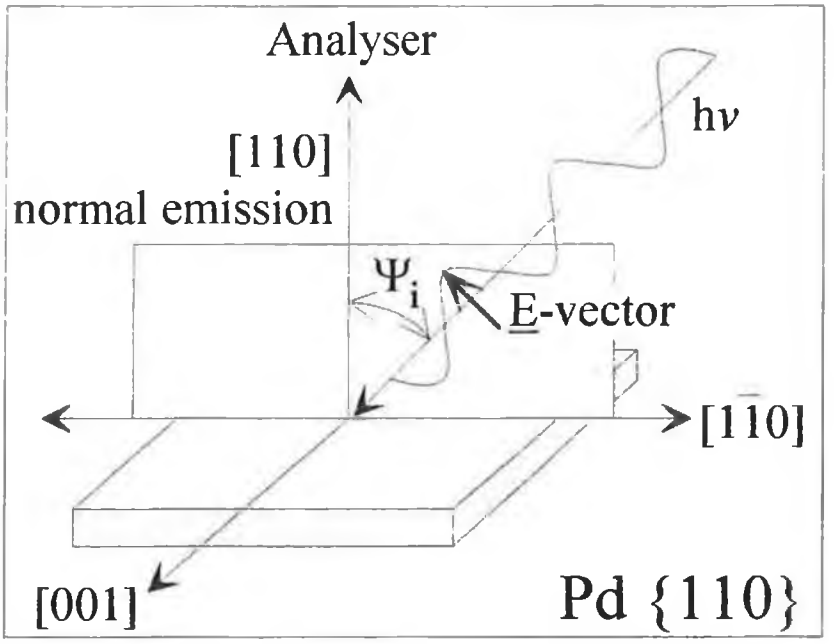

Figure 1: Schematic of the ARUPS measuring geometry. The E-vector remains parallel to the plane defined by the [110] and the [1$\bar{1}$0] directions as a function of Ψ_i.

photons in the energy range 15-110 eV, with the most intense region falling between 19-40 eV. Individual photon energies are set to an accuracy of <0.01 eV.

All ARUPS spectra were measured at normal emission. The crystal was oriented such that the E-vector of the light at normal incidence lay along the [1$\bar{1}$0] surface azimuth. The angle of incidence (Ψ_i) of the light was varied with respect to this azimuthal direction. Measurements were taken at two angles of incidence, 25° (where a large component of the E-vector is parallel to the [1$\bar{1}$0] azimuth) and 60° (where a large component is perpendicular to the [1$\bar{1}$0] azimuth). Figure 1 shows a schematic of the experimental geometry used in the ARUPS measurements.

Copper was evaporated from a Cu wire wound around a tungsten filament. The Cu deposition rate was monitored by measuring the growth of the Cu LMM Auger intensity and the decay of the Pd MNN Auger intensity using a fixed, cylindrical mirror analyser (CMA). The Auger emissions were excited using a 3 KV electron beam at normal incidence to the sample. The analyser had an acceptance cone of half-angle=42.3°±3° (i.e. it accepted electrons with emission angles between 39.3° and

45.3° measured w.r.t. the CMA axis). At normal incidence the CMA axis corresponds to the sample normal. The homogeneity of the Cu deposition was checked by measuring the Cu and Pd Auger emissions at different points on the sample surface.

The Cu coverage was estimated using the equation:

$$\frac{I_{Cu}}{I_{Pd}} = \frac{I^{\infty}_{Cu}\left(1-\exp\left[\frac{-d}{\lambda_{Cu}}\right]\right)}{I^{o}_{Pd}\exp\left(\frac{-d}{\lambda_{Pd}}\right)}$$

where

I_{Cu}/I_{Pd} is the ratio of the Cu LMM signal intensity to the Pd MNN signal intensity for a given θ_{Cu}.

I^{∞}_{Cu} is the Cu LMM signal from a "bulk" Cu overlayer.

I^{o}_{Pd} is the Pd MNN signal intensity from the clean Pd {110} crystal.

λ_{Cu} & λ_{Pd} are the IMFP's of the Cu LMM (KE~920 eV) and the Pd MNN (KE~325 eV) Auger electrons. Using the formulism of Seah and Dench [27] these were calculated as 13.5 Å and 8.1 Å respectively.

d is the distance travelled through the Cu overlayer by the emitted electrons (Å).

In order to convert *d* into θ_{Cu} in monolayers, the emission angle of the electrons with respect to the surface normal (~42.3°) and the Cu inter-layer spacing must be taken into account. This is done using the equation:

$$\theta_{Cu}\ (\mathrm{ML}) = \frac{d\cos(42.3)}{1.3}$$

where

θ_{Cu} is the estimated Cu coverage in ML.

d is the distance calculated using the previous equation.

1.3 is the approximate inter-layer spacing of a bulk Cu {110} single crystal (Å).

The coverage determined is only an estimate since there can be errors of up to 10% in the calculated IMFP's. The equation assumes layer-by-layer growth, hence, if island growth occurs, the absolute coverage will be under-estimated.

3. RESULTS:

3.1. Growth Mechanism and Geometric Structure of Cu on Pd {110}:

3.1.1. Growth Mode:

The growth mechanism of Cu on clean Pd {110} was investigated by monitoring the decrease in the Pd MNN Auger intensity and the increase in the Cu MVV Auger intensity as a function of Cu deposition time. The resultant Auger signal versus time (As-*t*) plot, shown in figure 2, yields information about the growth mechanism. The data can be readily fitted with linear segments and regularly spaced break-points (the distortion of the Cu signal intensity at low coverages is due to a strongly sloping

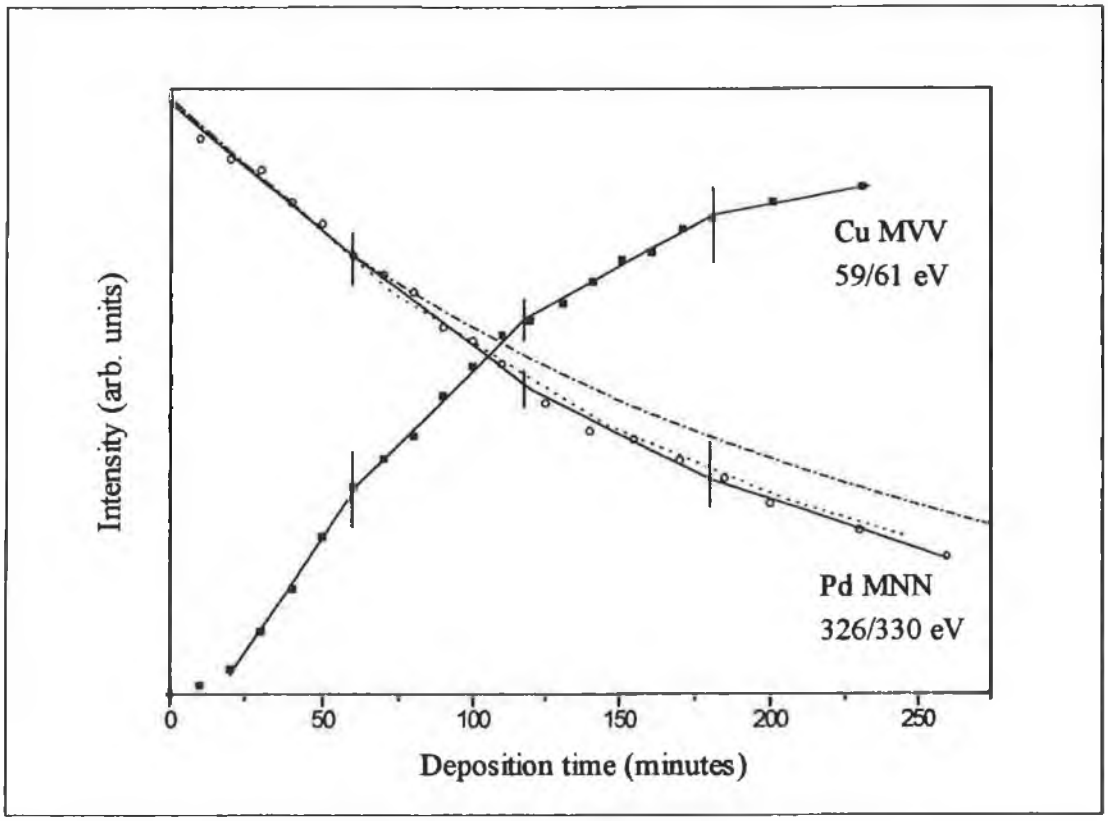

Figure 2: As-*t* plot for the growth of Cu on Pd {110}. The variation of both the substrate (Pd) and adsorbate (Cu) signal with increased deposition time is shown. Linear segments and break points, consistent with layer-by-layer growth, have been fitted to both data sets. The lines fitted to the Pd data points correspond to a 'simultaneous multi-layer' (dotted) and a 'monolayer-simultaneous multi-layer' (dash-dot) growth mechanism (see text for details).

secondary electron background in the experimental data). The As-*t* plot has the characteristic form of the FM (layer-by-layer) growth mechanism [28, 29]. In the FM growth mechanism, each break-point corresponds to the completion of an additional complete monolayer of adsorbate on the substrate surface. On this basis, the deposition rate corresponds to ~1 ML every 60 minutes. The surface free energies of Cu and Pd are 1.934 Jm^{-2} and 2.043 Jm^{-2} respectively [30]. Based solely on these values Cu would be expected to 'wet' a Pd surface, which is consistent with the experimental data. Of course the surfaces free energies alone cannot be used to accurately predict the growth modes. Other factors, such as the strain energy and the interface free energy, may strongly influence the mechanism. In particular, given the ~7.7% mismatch between Cu and Pd, the strain energy may be quite large, and therefore may play an important role in determining the overlayer growth mode.

The shape of the As-*t* plot immediately allows us to rule out the formation of 3-D Cu clusters of significant height on the surface within the first 3-4 ML of growth. The two main growth mechanisms in which clusters are formed are the VW and SK modes as discussed in chapter III. Growth by these mechanisms resulting in the formation of islands with a small base-to-height ratio can be ruled out. However, figure 2 does not confirm that the growth mechanism is 'perfect' FM growth. A model introducing imperfections into the layer-by-layer growth can also produce a good fit to the experimental data. The dotted curve shown in figure 2 correspond to the theoretically calculated Pd MNN intensity variation for a 'simultaneous multi-layer' (SM) growth mechanism. The basis of the SM mechanism is that once a fraction of one Cu monolayer has formed the layer above it may then begin to form. Unlike the VW and SK growth mechanisms, the SM mechanism does not intrinsically assume that formation of multi-layers (clustering) is energetically favoured over the completion of the initial monolayer. SM growth occurs when the surface diffusion of the adatoms on the substrate is slow relative to the time-scale of deposition and measurement (i.e. the formation of layers is kinetically hindered).

The model used to generate the SM curve on figure 2 was based on the initial assumption that the break-points shown correspond to the deposition of approximately 1 equivalent monolayer (eML, i.e. equivalent to a pseudomorphic Cu

monolayer). At the 1st break point the model assumed 80% surface coverage consisting of 60% 1 ML Cu coverage and 20% 2 ML Cu coverage. At the 2nd break-point the first monolayer was considered complete with 20% of the Cu coverage being 2 ML thick and 40% being 3 ML thick. Again, at the 3rd break-point the second monolayer was complete with 20% of the Cu coverage being 3 ML thick and 40% being 4 ML thick. The fit is of a similar quality to that of perfect FM growth, and clearly illustrates that the As-*t* plot is not sufficiently sensitive to determine if there is absolutely 'perfect' FM growth.

The 'clusters' used in the SM model are small in height ('clusters' are only 2 layers thick at any given coverage). Stronger clustering, resulting in the formation of taller islands, would lead to significant deviations of the model from the experimental data. The model used is not 'true' SM growth in the sense that the clusters formed do not have a Poisson distribution [31]. Growth of the Cu overlayers according to a Poisson distribution would lead to significantly taller clusters.

The dash-dot line on figure 2 corresponds to a monolayer-simultaneous multi-layer (MSM) growth mode [29]. This film grows in the SM mode once a complete monolayer of adsorbate has formed (i.e. it is assumed that the motion of the Cu adatoms on a Cu layer is kinetically hindered at room temperature). In the model used to generate the curve shown on figure 2, once the first ML has formed, additional layers grow at a rate that is proportional to the available surface area of the layer beneath (i.e. after the first ML is complete, subsequent Cu atoms adsorb randomly on the available surface). A new layer may immediately begin to grow once of fraction of the layer beneath it has formed. This is true MSM growth, since the island height at any given coverage is dictated by a Poisson distribution.

This MSM model does not agree well with the experimental measurements. Based on the SM and MSM models tested, we can conclude that if clusters do form they have a significantly smaller height than would be expected purely upon the basis of random arrival of atoms at the surface (i.e. there is a tendency for the clusters to 'flatten'). The models clearly indicate that the Cu adatoms tend to form either complete

monolayers or 'clusters' of small height. This is in agreement with the formation of small 3-D clusters of Cu on Pd {110} for θ_{Cu}>0.7 eML observed by STM [22].

The clean Pd {110} surface gives a p(1×1) LEED pattern which persisted during Cu deposition. No super-structures indicative of ordered Cu overlayers with periodicity greater than the substrate, or of a (1×2)-MR reconstruction, were identified even after stepwise annealing of Cu overlayers to 500 K. The intensity of the background increased with increasing θ_{Cu}. There was no evidence during the early stages of layer growth (0-3 eML) of satellite beams from an incommensurate Cu film. Instead, a shift in the maximum intensity from a position typical of Pd {110} to one of pure Cu {110} occurred gradually with coverage. The shift was more evident along the [1$\bar{1}$0] azimuthal direction. At higher θ_{Cu} streaking along the [001] direction was observed, while at the highest coverage studied (20 eML) the surface gave broad diffuse diffraction spots super-imposed on a high background.

3.1.2. XPD Measurements:

Figure 3 shows a structural model of the Pd {110} crystal structure. Also shown is a model of the cross-section through the [001] azimuth of the surface illustrating the origins of the expected forward focusing peaks along this azimuth. Clearly a fcc crystal thickness of at least 3 ML is required in order for forward focusing peaks to

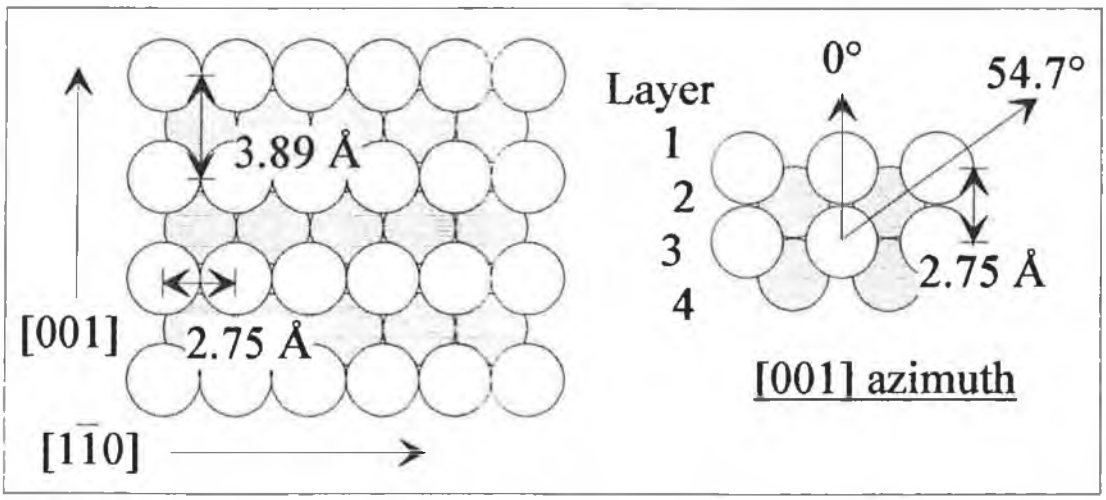

Figure 3: Structural model of the Pd {110} surface and a cross-section through the [001] azimuth.

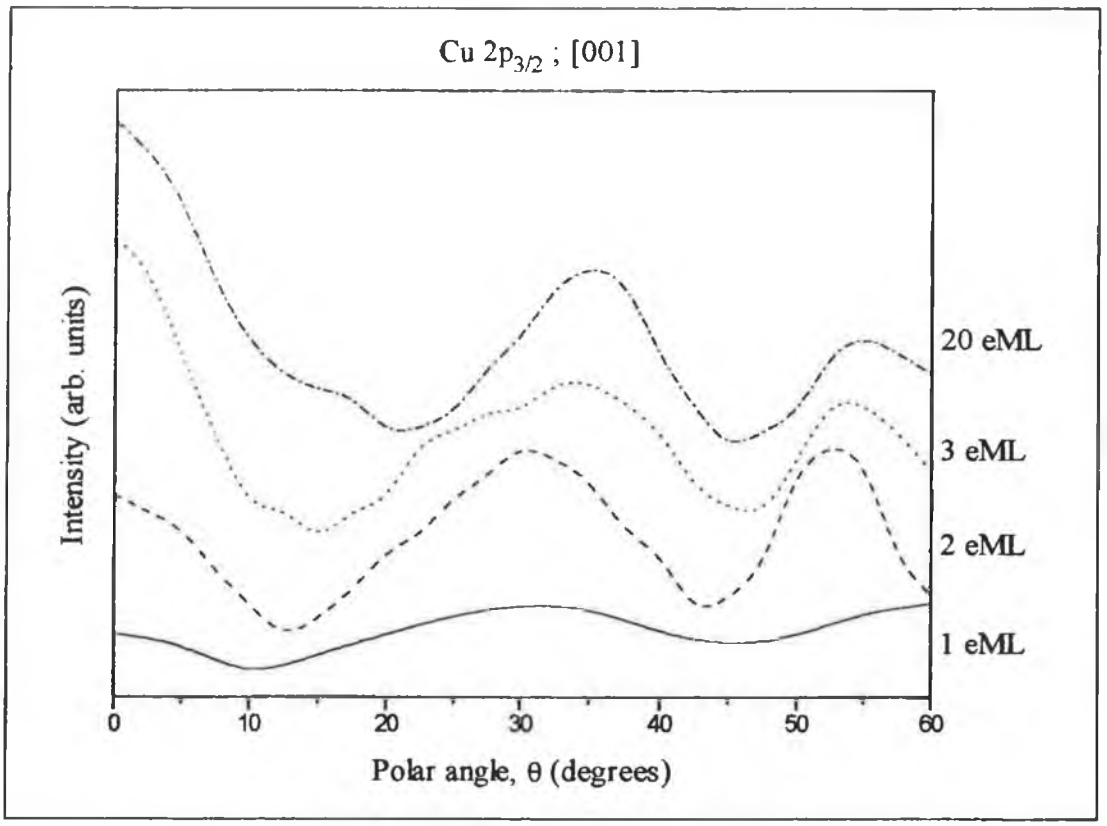

Figure 4: Polar XPD scans measured, using Cu 2p emission (~550 eV), from a range of Cu coverages on Pd {110}. The scans were measured along the [001] azimuth.

occur in this crystallographic direction. The polar angles shown are calculated on the basis of a bulk terminated structure with no surface refraction.

A series of polar XPD scans were measured along the [001] azimuth for a range of θ_{Cu} on Pd {110}. Emission was from the Cu 2p core levels using Al K_α excitation (KE~550 eV). The intensity at a given emission angle corresponds to the integrated area under the photo-emission peak after subtraction of a linear background. No attempt has been made to remove the effect of the variation in the core level photo-ionisation cross-section as a function of emission angle. The cross-section varies smoothly as a function of angle, and hence should introduce no new structure into the spectra, although the relative peak intensities will be affected [32]. The experimental scans are shown in figure 4. The curves were measured from estimated θ_{Cu} values of 1, 2, 3 and ~20 eML. For XPD scans from a bulk terminated fcc lattice structure along the [001] azimuth, forward scattering peaks are expected at polar angles of 0° and ~55° as shown on figure 3. These features are clearly present on the 20 eML XPD

curve. Similar forward focusing features are also clearly visible on the scans from the 2 eML and 3 eML θ_{Cu} curves. Since the forward focusing peaks originate from regions of θ_{Cu} of at least 3 layers thickness, the presence of these peaks on the 2 eML scan is direct evidence that the Cu growth is not perfect layer-by-layer.

The XPD scan from the 1 eML Cu overlayer is relatively flat and featureless, as would be expected from a flat monolayer. There are broad modulations visible on the scan, which may be due to small regions of clustering (or alloy formation in which Cu adatoms penetrate into the Pd substrate). These modulations are not sufficiently strong to allow concrete conclusions to be drawn, however they are suggestive of imperfections within the first Cu monolayer.

3.1.3. Single Scattering Cluster Calculations:

SSCC's were performed to model the electron emission intensity from the Cu $2p_{3/2}$ core level as a function of polar emission angle along the [001] surface azimuth. The outgoing electron wave was assumed to be s-like and a spherical wave correction was used. Non-relativistic phase shifts were calculated using Herman-Skillman wavefunctions [33]. A total of 20 phase shifts were used in the SSCC's for emission from Cu at a kinetic energy of 550 eV. The Debye temperatures (θ_D) of Cu and Pd were set at their bulk values (315 & 274 K respectively). The inner potential of the cluster was set at 10 eV. The inelastic-mean-free-path (IMFP) at KE=550 eV was calculated to be 10.5 Å using the formulism of Seah and Dench [27]. The clusters used in the SSCC's consisted of Cu layers on a Pd substrate. The substrate atoms were in a bulk fcc Pd {110} lattice structure with no relaxation of the surface layer. Different Cu thickness' were modelled using the corresponding number of complete Cu layers in the cluster.

Figure 5 shows SSCC's for a range of monolayer coverages of Cu on a Pd {110} substrate. The calculations correspond to Cu clusters of 1, 2, 3 and 5 ML thickness. The in-plane lattice parameters of the Cu overlayers were fixed at those of the Pd substrate (2.75 Å and 3.89 Å), while the inter-layer spacing was fixed at 1.1 Å (a contraction of the bulk Cu {110} value, 1.28 Å) in order to conserve bulk density. As expected, the SSCC's for the 1 & 2 ML clusters are essentially featureless since there are no forward focusing paths along the [001] azimuth of a 2 layer thick fcc {110} crystal structure. All XPD features must therefore arise from lateral- and back-scattering processes and from scattering by out-of-plane atoms, all of which are relatively weak at high outgoing KE's. The small modulations on the 2 ML SSCC are consistent with the modulations observed on the 1 eML experimental curve. This is a direct indicator of the formation of 2 layer thick Cu structures at sub-monolayer coverages. These structures may be due either to 2 ML thick clusters on the Pd substrate or substitution of Cu into the 1st & 2nd layers of the Pd selvedge. Once the

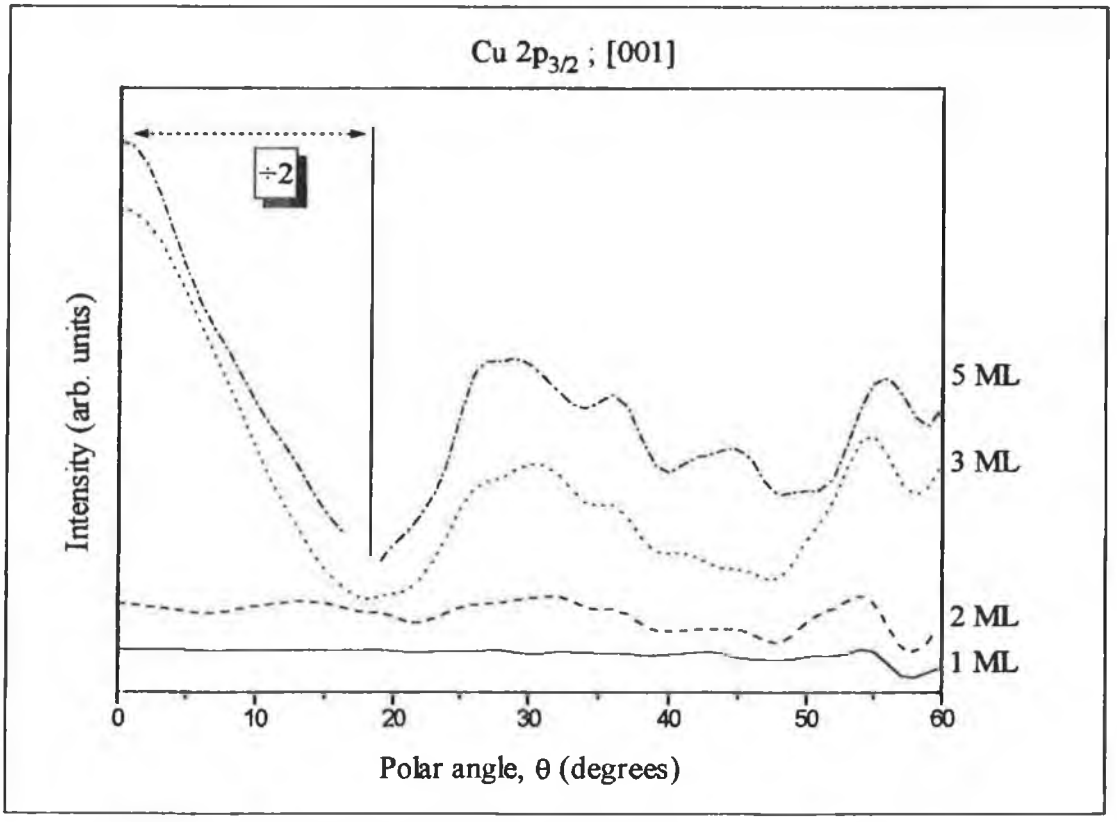

Figure 5: SSCC's for a series of Cu monolayers on a Pd {110} cluster substrate. The curves were calculated for emission from the Cu 2p levels along the [001] azimuth.

cluster size is increased to the critical 3 ML thickness the forward focusing feature at 0° and 55° appear as expected. Further increasing the cluster thickness (5 ML) maintains the same general features, although there are some changes in peak shape and position.

After deposition of 20 eML the Cu overlayers appear to have adopted a bulk fcc {110} structure. This conclusion is based on the position of the off-normal XPD forward focusing peak, which was located at θ~55°, the expected position for a normal fcc {110} lattice structure. LEED observations indicate that at low θ_{Cu} the overlayers grow commensurate with the Pd substrate. This requires an expansion of the in-plane lattice parameters from their bulk values by ~7.7% and raises the possibility of a corresponding contraction of the inter-layer spacing in order to compensate for the large reduction in two-dimensional density.

Figure 6 shows a comparison of SSCC's, calculated for a range of Cu inter-layer spacings, with the 3 eML experimental curve. All calculations were done for a 3 ML Cu cluster on a bulk Pd {110} substrate. The Cu inter-layer spacings used were 1.0, 1.1, 1.2, 1.3 (approximately bulk Cu {110} value) and 1.375 Å (bulk Pd {110} value). In all cases the in-plane parameters were fixed at those of the Pd substrate. The diffraction features are similar for all calculated curves. As the inter-layer spacing is increased there is a general shift of the off-normal forward focusing peak (and of the broad envelope containing the higher-order diffraction features) toward normal emission, as expected. It can be seen that the position of the off-normal forward focusing peak and the higher-order features on the experimental curve agree best with the SSCC's calculated for an inter-layer spacing of ~1.1-1.2 Å. This represents a contraction of the inter-layer spacing, which can be regarded as a mechanism for relieving the in-plane strain on the Cu lattice, and as an attempt to conserve the Cu bulk density. A contraction of the Cu inter-layer spacing to a value of 1.1 Å would be required to exactly conserve the Cu density for in-plane parameters expanded to those of Pd {110}. Hence, the data provides evidence of a tetragonal distortion within the thin Cu films. However, as the analysis is based only on a single XPD curve the suggestion of an inter-layer contraction must be considered tentative at present.

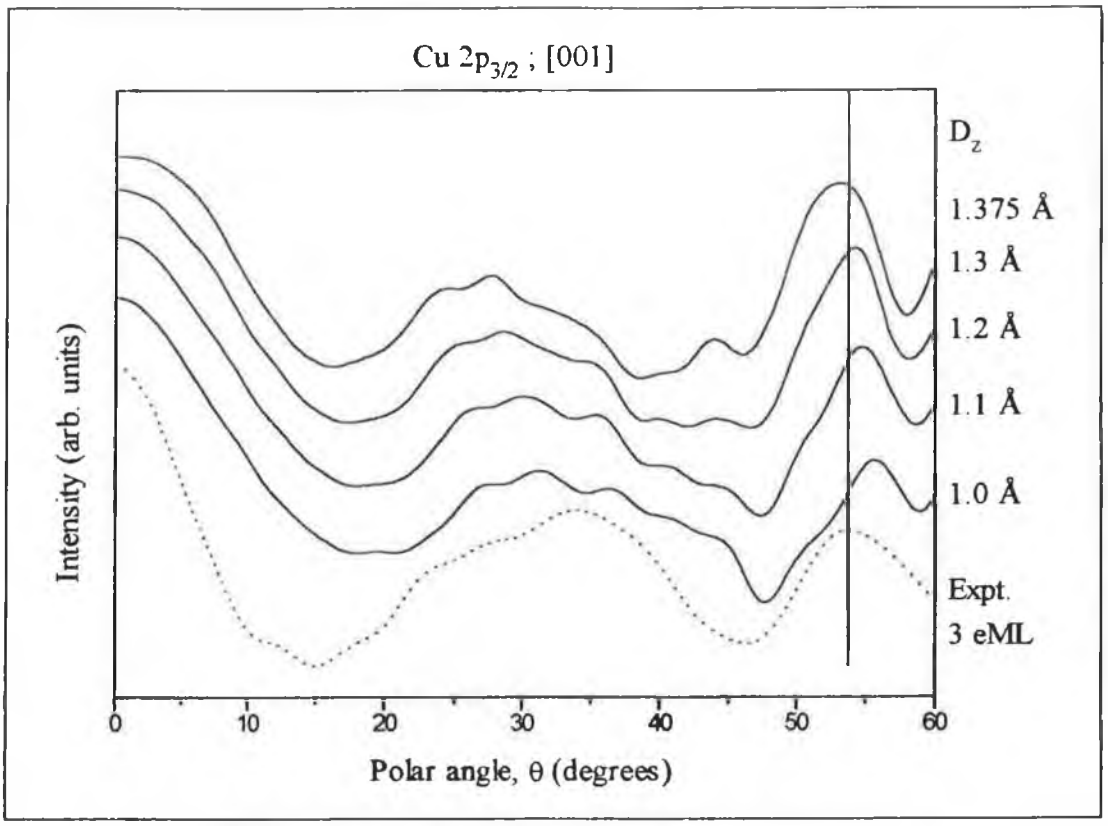

Figure 6: Comparison of SSCC's with the 3 eML experimental curve. The calculations are done for a range of Cu inter-layer spacings (D_z).

3.1.4. Cu/Pd Alloying:

The formation of Cu structures of at least 3 ML thickness is clearly evident from polar XPD curve for θ_{Cu}=2 eML. The possibility that these structures may arise due to alloy formation, either by Cu incorporation into the Pd selvedge or by Pd migration into the Cu overlayers, cannot be conclusively ruled out on the basis of the As-*t* and XPD data. If Cu adatoms are incorporated within the Pd selvedge it is possible that they will give rise to forward focusing features which are indistinguishable from 3 ML thick Cu clusters. The modulations observed in the θ_{Cu}=1 eML experimental curve may also arise due to such alloying.

Auger studies were performed in order to determine the temperature at which rapid alloying takes place on an experimental time-scale. A Cu overlayer (θ_{Cu}~12 eML) maintained at room temperature for a 12 hour period demonstrated no change in the Pd or Cu Auger intensities with time, indicating that alloying of the Cu overlayer with

a Pd {110} substrate does not occur to an appreciable degree on this time-scale. Deliberate alloying of an ~12 eML Cu overlayer with the Pd {110} single crystal was then investigated by step-wise annealing of the sample. The annealing experiment was done by heating the sample to the required temperature, holding at that temperature for 2 minutes and allowing it to cool to room temperature prior to measurement of the Pd MNN and Cu LMM Auger emission intensities. The annealing temperatures ranged between 325 K (~50° C) and 725 K (~450° C) in 50 K steps. Figure 7 shows a plot of the resultant Pd and Cu Auger intensities. Detectable alloying does not occur on the time-scale of annealing until sample temperatures of 485-525 K. Clearly, significant alloying of a Cu overlayer with Pd {110} will not occur on a fast time-scale at room temperature.

What cannot be ruled out is the possibility of alloying occurring during the deposition of the Cu overlayer. The 'hot' Cu atoms arrive at the Pd surface with a large excess of translational kinetic energy, which must be dissipated before they can equilibrate at

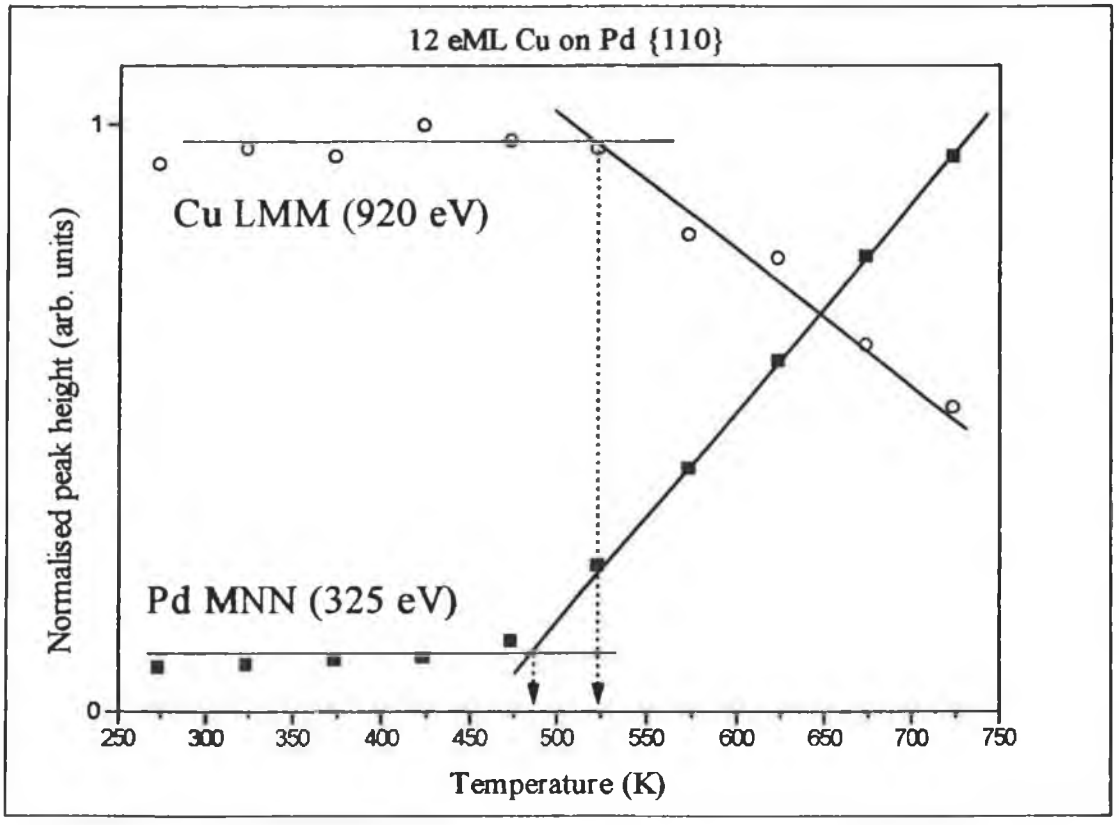

Figure 7: Variation of Pd and Cu Auger intensities as a function of sample annealing temperature.

the surface. In addition, the chemisorption energy must be locally dissipated upon adsorption. This excess energy may be sufficient to cause ejection of a Pd atom from the surface and incorporation of Cu within the crystal selvedge.

The results of the annealing experiment outlined above are in agreement with studies on the alloying/inter-diffusion of Cu/Pd overlayer systems on other low index Pd surfaces. A work function study of the growth and stability of thin Cu films (10 Å) on 1500 Å thick Pd {111} films grown on mica (coverages monitored by quartz crystal oscillator) found that Pd readily diffuses into the Cu film only at temperatures >500 K [19]. Depth profiling of the inter-diffused layers demonstrated that the annealing caused the Pd to diffuse rapidly through the Cu overlayer, whereas the Cu diffused only relatively slowly through the Pd substrate. Similarly, a 30 Å Pd film was found to diffuse rapidly through a 1200 Å thick Cu {111} substrate at ~500 K whereas the Cu diffused relatively slowly into the Pd [34].

Studies on the growth of Cu overlayers (0-12 ML) on Pd {110} by STM, and reflection absorption infra-red spectroscopy (RAIRS) for CO adsorption on Cu covered Pd {110}, found no evidence of Cu-Pd surface alloying either by annealing or direct growth of Cu (up to 12 eML) at temperatures <700 K [21, 22]. In agreement with these results, embedded atom method calculations find that Cu adatoms on the Pd {110} surface are more stable than Pd atoms promoted on-top and replaced in the first layer by Cu atoms [25].

Our results show that for films of θ_{Cu}~12 eML thickness, inter-mixing will commence at ~550 K. This is substantially lower than the >700 K quoted by Hahn *et al* in the STM/RAIRS studies [21, 22]. The discrepancy may be due to the surface localised nature of both the STM and the CO RAIRS measurements. Changes in the Auger signal intensity allows detection of intermixing at the Cu/Pd interface even though the outermost layers may remain pure Cu and hence unchanged with regard to measurement by STM or CO RAIRS. The work function measurements of the 10 Å Cu film with Pd {111} (1500 Å) indicated that the composition of the inter-mixed layers was critically dependent on the annealing temperature, i.e. holding a sample at a constant temperature did not result in progressive alloying [19]. Consequently, the

>700 K quoted by Hahn *et al* might be more correctly interpreted as the temperature required for the appearance of a Cu/Pd surface alloy rather than the temperature required to activate Cu/Pd inter-diffusion.

3.2. Electronic Structure of Cu films on Pd {110}:

Figure 8 shows a series of normal emission ARUPS spectra measured from clean Pd {110} using photon energies between 18 eV and 40 eV. The photon beam was incident at 25° to the surface normal along the [1$\bar{1}$0] surface azimuth, i.e. the E-vector of the light was mainly within the surface plane. These spectra compare well with similar measurements by Yagi *et al* [35], providing a useful independent check on the measurement technique and yielding information of the dispersion of substrate emission..

Figures 9 & 10 show normal emission ARUPS spectra measured as a function of θ_{Cu} for photon incidence angles of 25° and 60° respectively at 22 eV. By comparison with the ARUPS spectra measured from clean Pd, the peak at the Fermi level (E_f) can be assigned to emission from the Pd d-band, which is damped as θ_{Cu} increases This feature is never completely eliminated for curves up to 60 eML, indicating either that alloy formation occurs with Pd diffusing through the growing Cu film and residing in the surface region probed, or that island growth occurs resulting in regions of low local Cu coverage on the surface even at high θ_{Cu}. Hence, emission from the Pd substrate would still be detected due to "pin-holes" of low copper coverage. The existence of regions of the Cu overlayer with a low local θ_{Cu} is possible since the growth mechanism of Cu on Pd {110} at room temperature has been demonstrated to be island-like upon completion of the first monolayer [22]. At 300 K the film may not have sufficient activation energy to coalesce to a continuous film even for high θ_{Cu}.

A FM growth mechanism usually allows the electronic bands of overlayers to rapidly converge to their bulk character [36, 37]. Theoretical work indicates that film thickness' between 3-to-5 ML are sufficient for convergence to be essentially complete. VW growth requires much higher thickness' for the bulk-like bands to

develop [38]. For example, growth of Cu on Pd {100}, which has been reported as SK, does not show convergence of the ARUPS bands until θ~65 eML [20]. The fact that the ARUPS shown in figures 9 & 10 do not converge to "bulk-like" until high θ_{Cu} is indicative of island growth in full agreement with the AES/XPS results. This is demonstrated particularly well by the emission feature between 4-5 eV, whose binding energy position does not stabilise even at very high Cu film thickness'.

There is a non-dispersive peak at ~1.75 eV below E_f on the ARUPS spectra of the Cu covered surface. This peak does not show any marked polarisation dependence, in-keeping with the mixture of Pd d-states expected for a Pd "impurity" in a Cu lattice. This peak persists to θ_{Cu}=60 eML but is absent from the spectrum due to "bulk" Cu. Normal emission ARUPS spectra measured from Cu-rich CuPd bulk alloys using He I and Ne I excitation also showed a non-dispersive feature 1-2 eV below E_f, which was assigned to a Pd impurity state in a Cu lattice for dilute CuPd alloys. [39]. However, as outlined earlier, large-scale alloying of Cu overlayers with Pd substrates has not been reported at room temperature, backed up by our own Auger measurements from a 12 eML film. Any inter-mixing of Cu and Pd occurring during growth is almost certainly localised at the CuPd interface. The observed inter-mixed region cannot be covered by a thick Cu overlayer since the feature is still easily visible at 38 eV (figures 11 & 12), when the inelastic mean free path is small (5-10 Å).

An alternative explanation is that this feature may arise due to strain in the Cu overlayers. Changes in the lattice constant (i.e. pseudomorphic growth), or the crystal structure of the overlayers, may give rise to electronic states not observed in bulk fcc Cu [40]. Hence, the peak at ~1.75 eV may be a Cu derived bulk state, arising from strained, pseudomorphic Cu layers at the CuPd interface. Because of the growth mechanism, these strained layers may be observed in ARUPS even at high coverages, due to the existence of regions with low local θ_{Cu}. A possible source of this state stems from the observation that Cu grows in a meta-stable bct phase on Pd {100} [8, 9]. ARUPS measurements from these Cu overlayers show a new feature between 4 & 5 eV (θ_{Cu}<10 ML), which is not observed in bulk Cu {100} [8]. A theoretically calculated normal photo-emission spectrum for a Cu {100} bct structure reproduced

this feature, and also an additional shoulder to the Cu d-band at ~1-2 eV that is not present in the fcc calculation [41], although this feature was not remarked upon by the authors.

Given that a bct phase of Cu can be stabilised on Pd {100}, it is possible that a similar phase might exist on Pd {110}. The fact that the off-normal forward focusing peak in figure 4 quickly reverts to the bulk fcc position with θ_{Cu} means that the overlayer cannot be a pure bct phase, since the off-normal forward focusing peak would show a strong shift toward normal emission that would persist to high θ_{Cu}. It is unlikely that a fcc {110} crystal would be capable of efficiently stabilising such a highly distorted fcc structure as reported for Cu on Pd {100} since the 'ease-of-relaxation' is considerably different along the two high-symmetry surface azimuths on a {110} surface (see discussion). However, minority bct regions may exist on the surface, perhaps localised near the Cu/Pd interface. Provided these regions comprise only a minority of the overlayer structure, their off-normal XPD forward focusing peak may be masked by the strong emission from the fcc regions.

The main Cu d-band emission is centred at ~2.5 eV below E_f in figures 9 & 10. For θ_{Cu}>4.5 eML, the binding energy of this peak remains constant as a function of $h\nu$. At lower θ_{Cu} there is a slight shift in the peak maximum toward E_f.. This shift may be due to strain in the low θ_{Cu} overlayers or it may simply be due to a changing background as the signal from the Pd is damped with increasing coverage. The d-band peak intensity varies in a similar fashion as a function of θ_{Cu} both for Ψ_i=25° and for Ψ_i=60° (i.e. there is no obvious polarisation dependence of this peak).

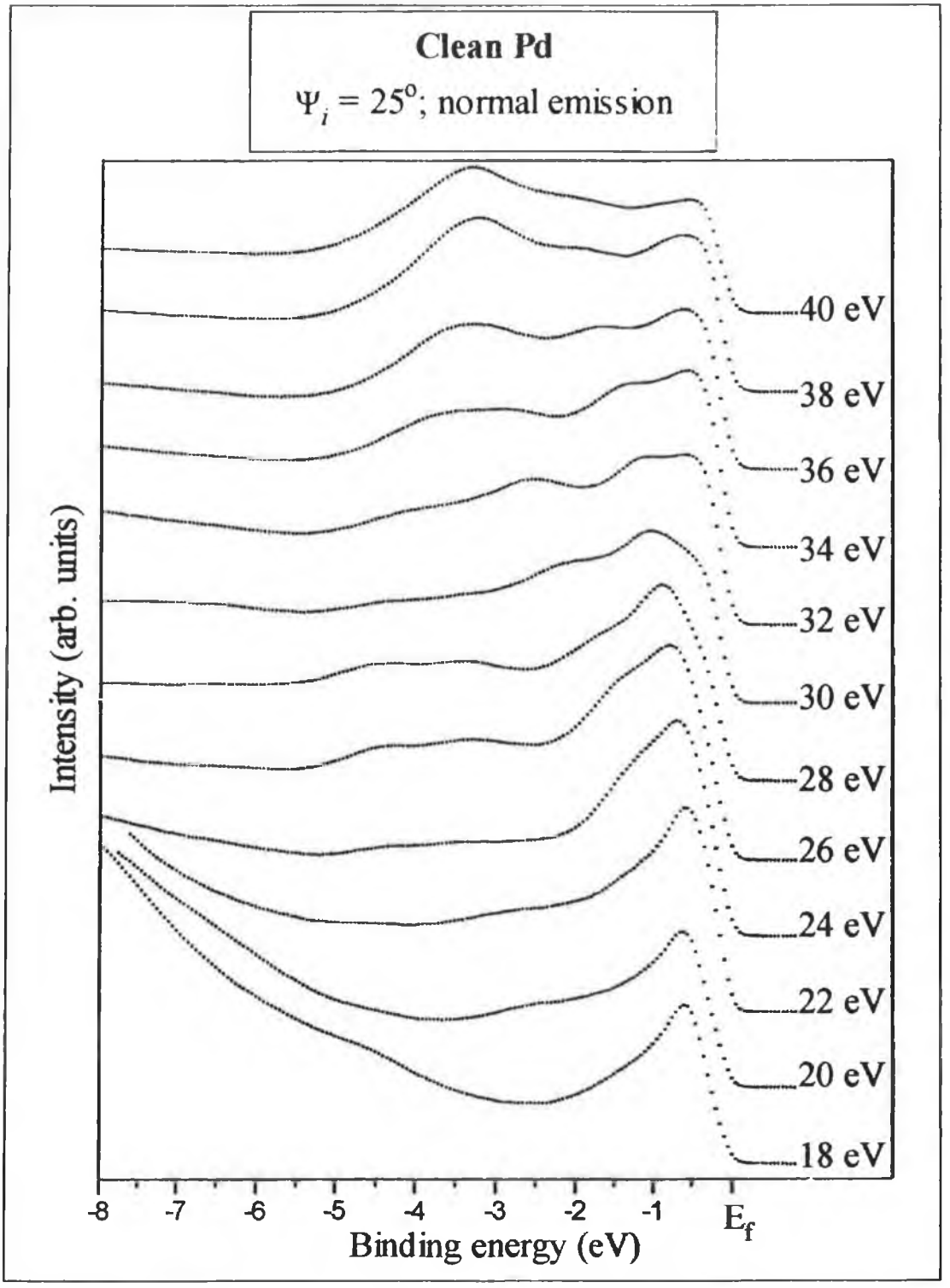

Figure 8: Normal emission ARUPS spectra measured as a function of photon energy from clean Pd {110} using a photon beam incident at 25° to the surface normal

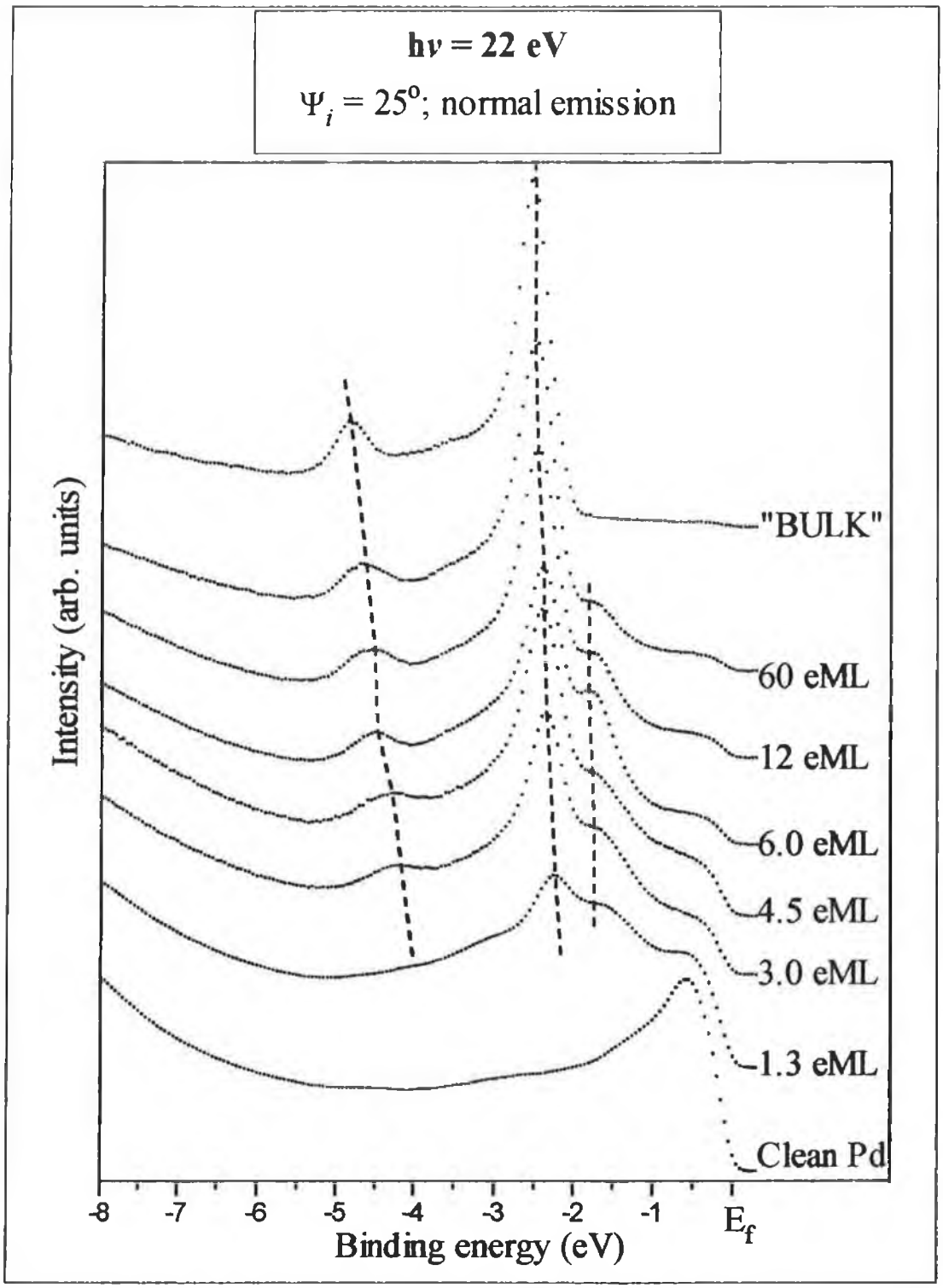

Figure 9: Normal emission ARUPS spectra measured as a function of θ_{Cu} on Pd {110} at 22 eV.

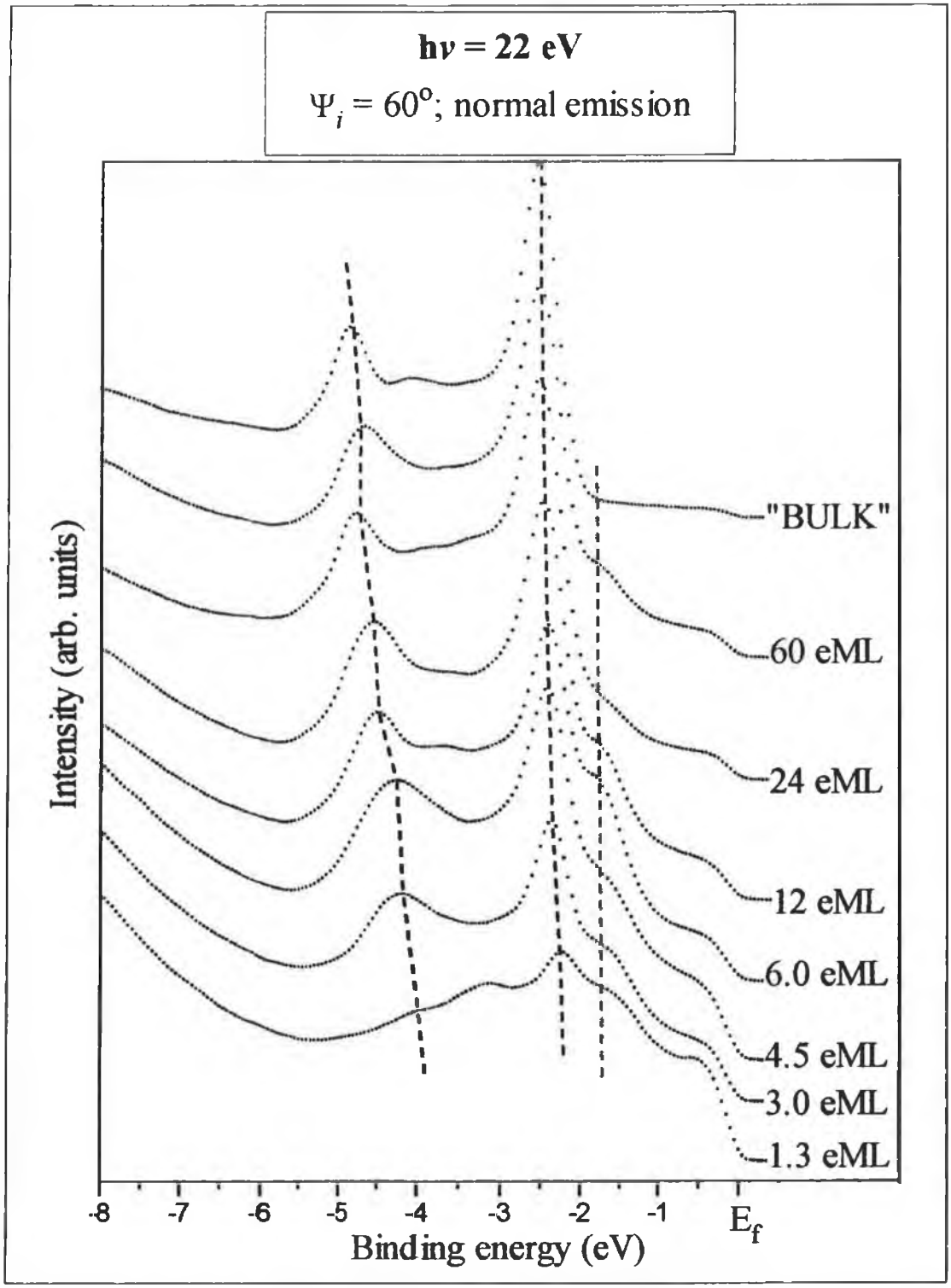

Figure 10: Normal emission ARUPS spectra measured as a function of θ_{Cu} on Pd {110} at 22 eV.

There is an band between 4-5 eV below E_f on the ARUPS spectra, which moves from ~4.0 eV below E_f at θ_{Cu}=1.3 eML to ~4.8 eV below E_f for bulk θ_{Cu}. The intensity of the ~4.6 eV emission is significantly greater at Ψ_i=60° than at Ψ_i=25°. At Ψ_i=60° a greater component of the incident light's E-vector is oriented perpendicular to the surface than at Ψ_i=25°. Such a polarisation is typical of a totally symmetric, initial state, and may be assigned to the Cu sp-band [20]. The fact that the binding energy of this peak varies with film thickness even at high θ_{Cu} is interesting. For un-strained Cu overlayers, a thickness of ~5 ML should be sufficient to allow the sp-band peak to adopt its bulk position. Hence, the dispersion seen on the spectra measured is indicative of coverage dependent changes in the film structure.

Figures 11 & 12 show ARUPS data measured as a function of θ_{Cu} at 38 eV photon energy, for photon incidence angles of 25° and 60° respectively. This energy is much closer to the minimum of the inelastic mean-free-path [27]. Consequently, the emission intensity measured in these curves should be significantly more 'surface localised'. Despite the shorter IMFP, the Pd d-band at E_f is still observable even for thick Cu films in agreement with the suggestion of a granular type film with 'pinholes'.

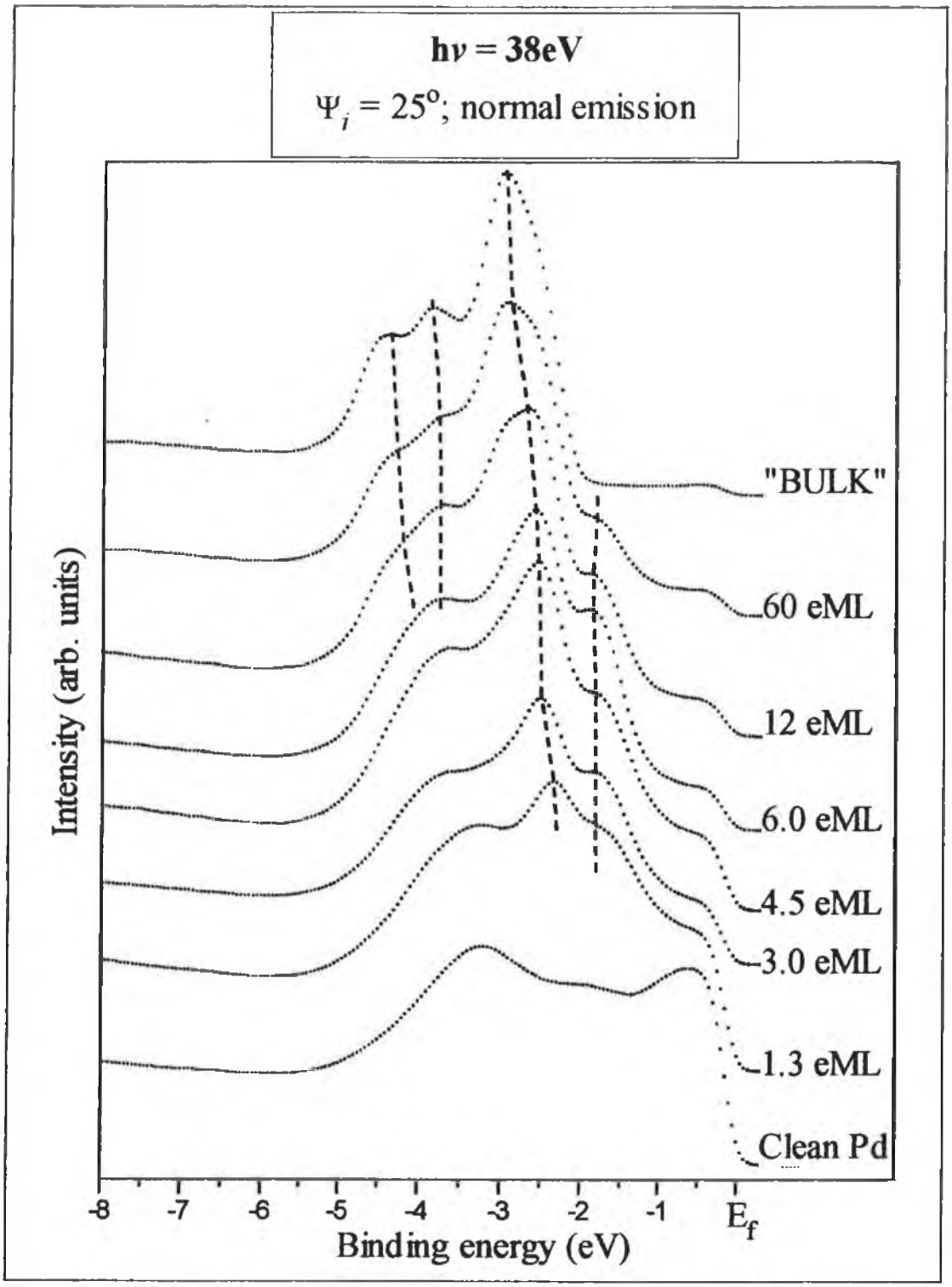

Figure 11: Normal emission ARUPS spectra measured as a function of θ_{Cu} on Pd {110} at 38 eV.

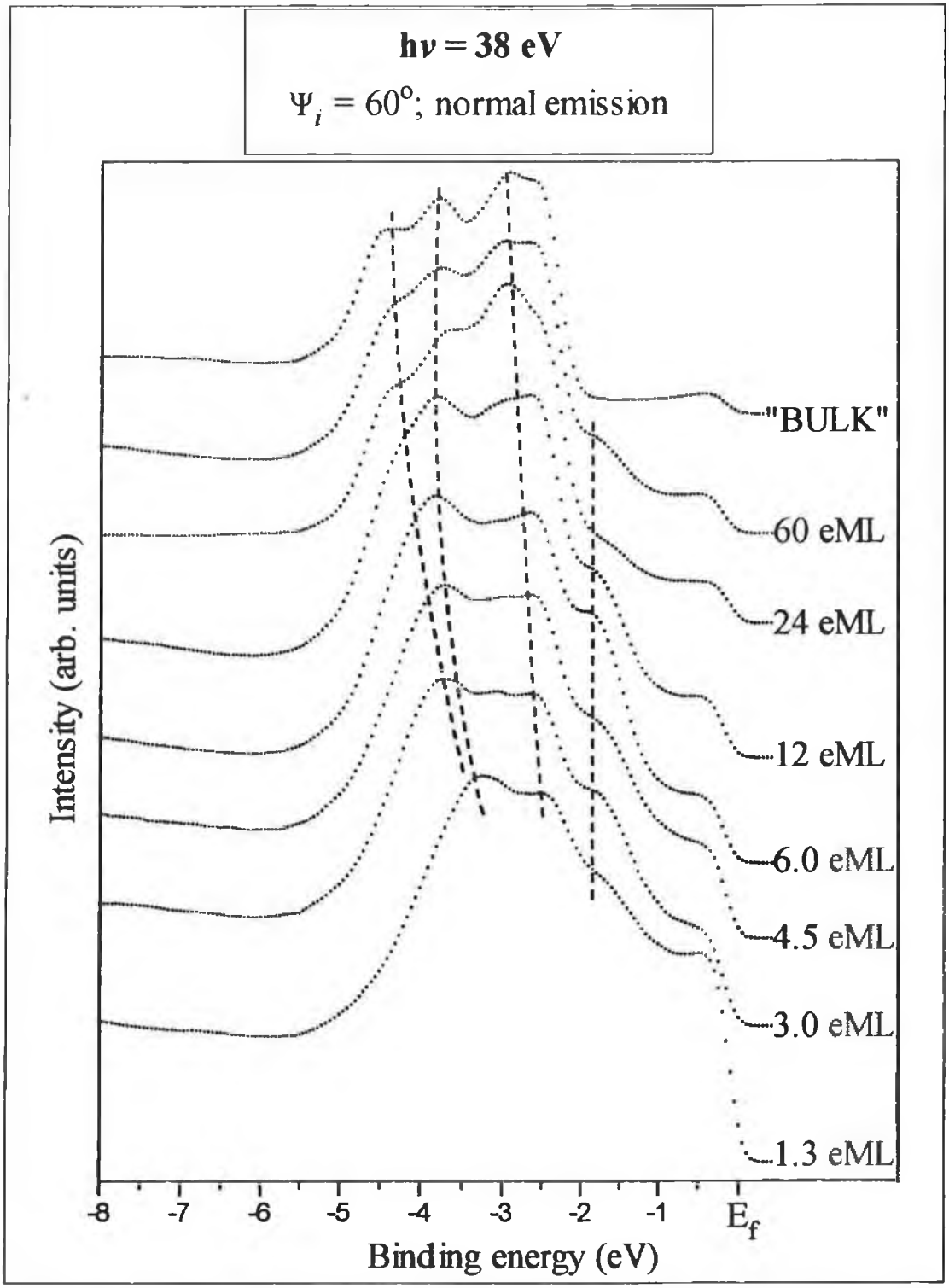

Figure 12: Normal emission ARUPS spectra measured as a function of θ_{Cu} on Pd {110} at 38 eV.

There is evidence of a structural transition occurring for θ_{Cu}>12 eML. This can be seen by comparison of the 12 & 60 eML curves at Ψ_i=25° and the 12 & 24 eML curves at Ψ_i=60°. This transition is indicated by the emergence of a peak at BE~3.8 eV preferentially excited by light at grazing angles of incidence. There is also evidence of the emergence of this peak at BE~4.0 eV on the bulk Cu ARUPS curve shown in figure 10 ($h\nu$=22 eV; Ψ_i=60°), although it is weak. Again, the absence of an equivalent feature for light incident at close to the surface normal is indicative of emission from a totally symmetric initial state. The fact that this new peak is stronger, relative to the emission from "bulk" Cu ARUPS bands, at $h\nu$=38 eV than at $h\nu$=22 eV indicates that it may arise from a surface localised effect (i.e. due to relaxations in the selvedge region of the Cu overlayers).

Figures 13 & 14 show a similar series to curves to those shown in figures 9 & 10, at $h\nu$=30 eV. All curves shown on figures 9-14 are taken from a series of ARUPS curves measured from Cu overlayers of different thickness' using photon energies from $h\nu$=18 eV to 100 eV in 2 to 5 eV steps in an attempt to experimentally band map the evolution of the Cu electronic structure. Some of these curves (for $h\nu$=18-40 eV) are plotted in an appendix to this chapter.

Figure 15 shows ARUPS spectra measured before and after annealing of θ_{Cu}~14 eML on Pd {110} to ~750 K for 5 minutes. The annealing temperature is above that required for large-scale alloying as discussed earlier. Alloying is demonstrated by the substantial changes observed in the ARUPS spectra after annealing. Comparison of the ARUPS spectra measured from the annealed surface with those measured from the clean Pd surface clearly demonstrates that the features present after annealing do not arise solely from Pd, but from a CuPd alloy mixture. The increased intensity at E_f after annealing is due to the re-emergence of the Pd d-band, and indicates a high Pd concentration in the surface region.

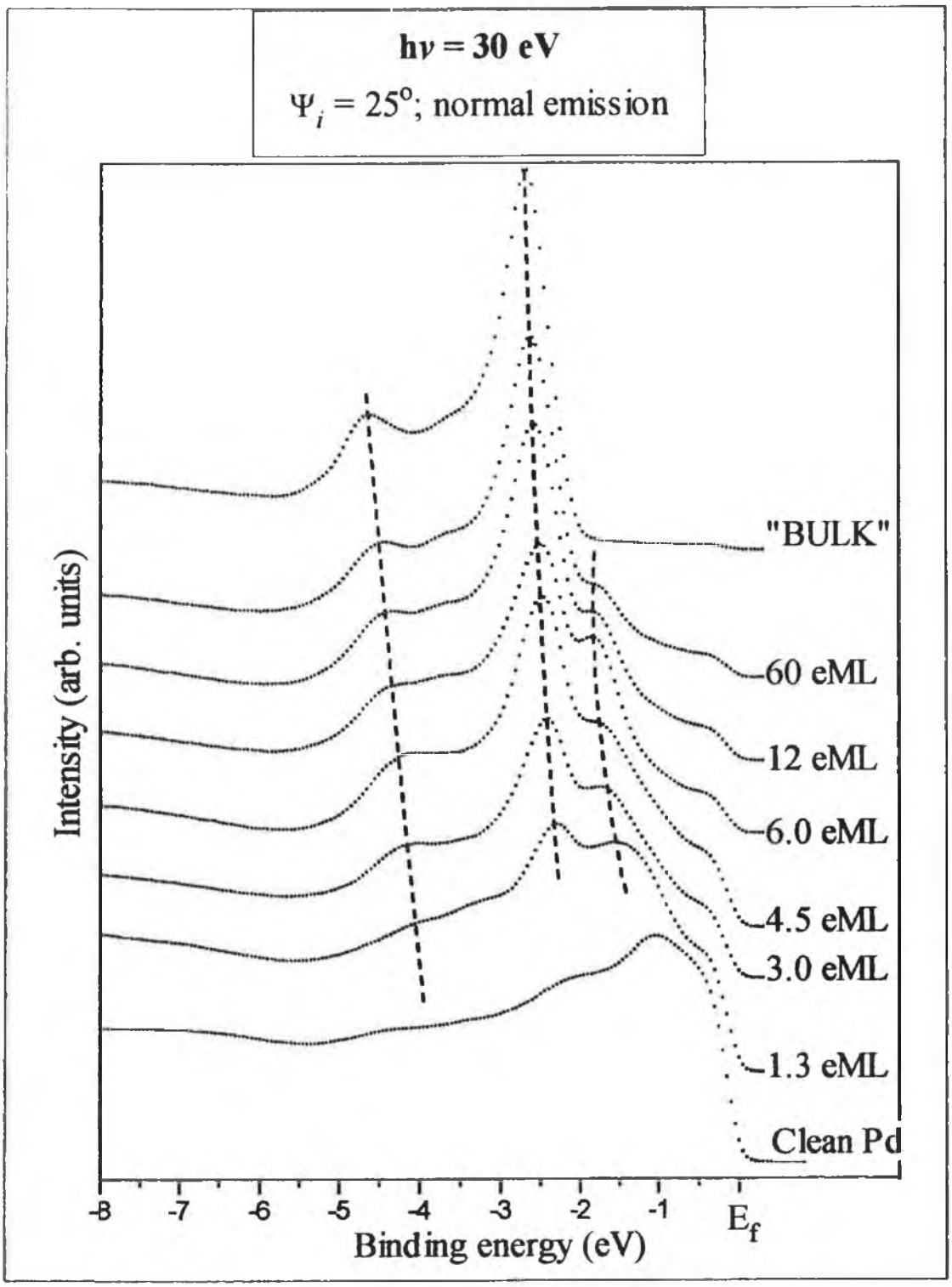

Figure 13: Normal emission ARUPS spectra measured as a function of θ_{Cu} on Pd {110} at 30 eV.

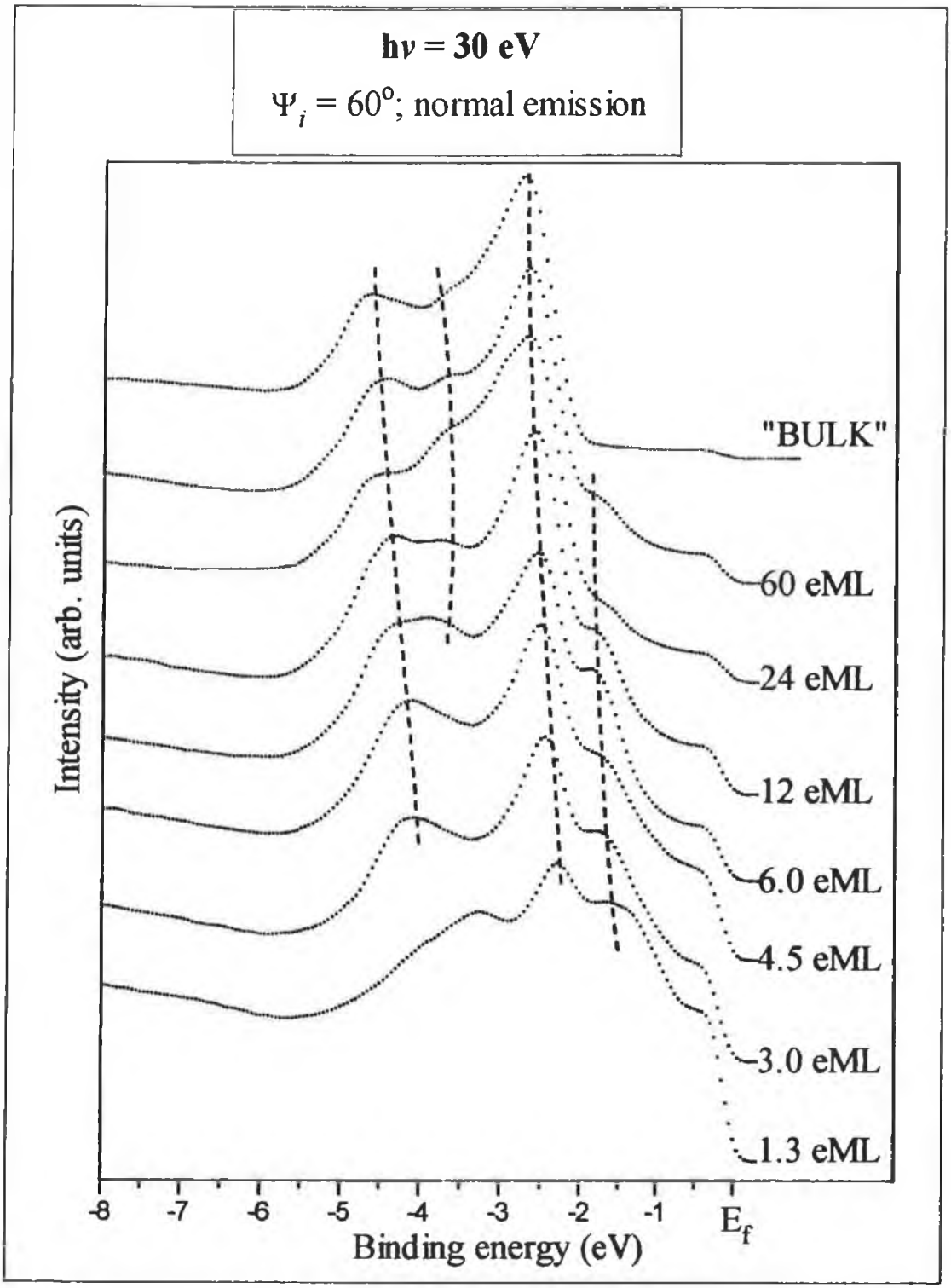

Figure 14: Normal emission ARUPS spectra measured as a function of θ_{Cu} on Pd {110} at 30 eV.

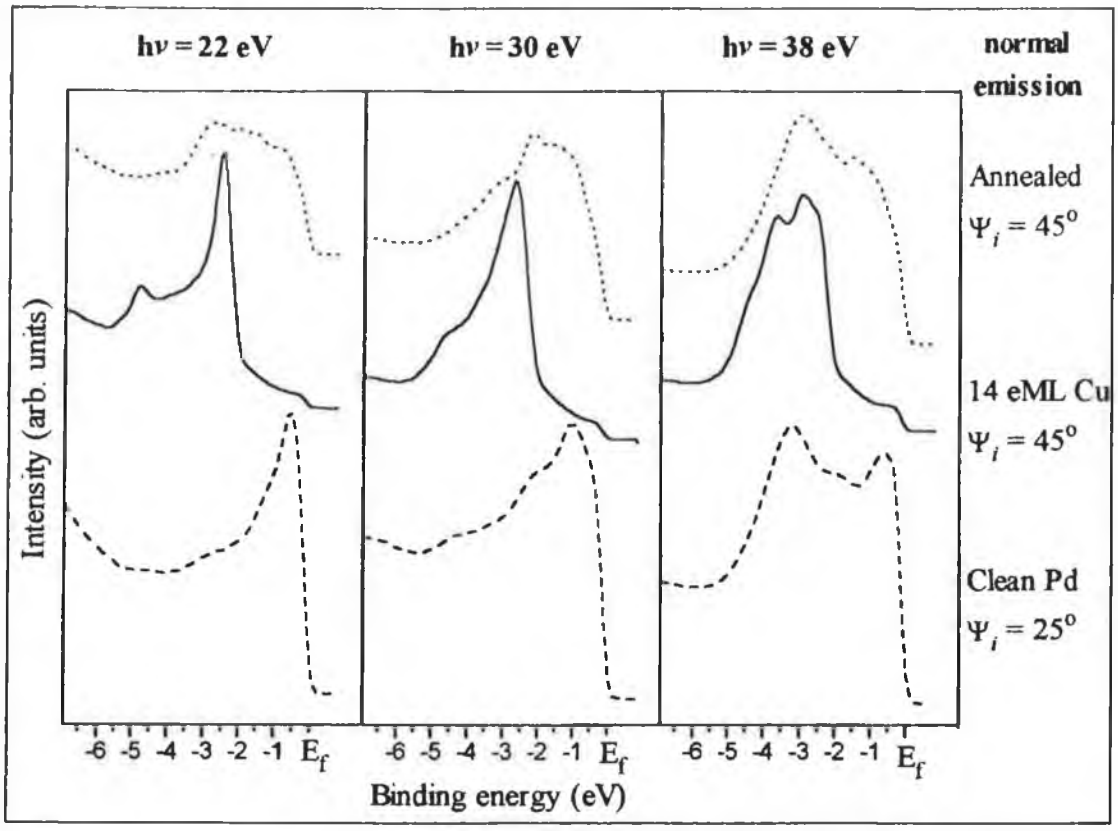

Figure 15: Normal emission ARUPS spectra, measured before and after annealing θ_{Cu}=14 eML on Pd {110} to 750 K, at 22 eV, 30 eV and 38 eV. The ARUPS spectra from clean Pd measured at 25° incidence is also shown for comparison.

Clearly the emission from the 14 eML film before annealing lacks the emission at ~1.8 eV binding energy. The Cu film was grown via a single evaporation on a clean Pd {110} surface (i.e. it is not directly comparable to the spectra shown in figures 9-14, which were grown by sequential evaporation.) The ~1.8 eV emission was present on all ARUPS spectra measured for Cu overlayers shown in figures 9-14, with the exception of the "BULK" overlayer, which was also formed in a "one-off" deposition (as opposed to sequential evaporation). If this shoulder were due to structural effects, such as strain or the existence of a bct structure, then it should also be readily apparent in the 14 eML curve. The fact that this peak is not present on the 14 eML curve is consistent with slow alloying occurring at 300 K and the assignment of the 1.8 eV feature to emission from Pd atoms incorporated as impurities in a Cu-rich lattice.

4. DISCUSSION:

For Cu growth on Pd {110} at or just above room temperature a SK growth mode for Cu on Pd {110} has been deduced, with a single flat Cu monolayer being formed prior to island growth. The fact that significant island growth occurs during the deposition of the second Cu eML is clearly apparent from the polar XPD curves. The results of this work agree with a recent STM study of Cu growth on Pd {110} [21-23], when the initial growth mode was classified as pseudo-SK. At room temperature the first ~0.7 ML of Cu forms 2-dimensional islands. At higher coverages island growth commences, although initially these islands are flat (only 2-3 ML thick). Deposition of Cu at ~400 K resulted in true SK growth [22]. Clearly the results of the present work show that As-*t* plots do not have sufficient sensitivity to detect the small deviations from perfect layer-by-layer growth, and in this case could easily be mistaken for layer-by-layer growth. However, the combination of XPD with a standard As-*t* plot clearly demonstrates that clustering occurs after deposition of the first Cu eML. In this case, the similarity of the As-*t* plot to that expected for layer-by-layer growth is a clear indicator that the cluster formed do not have a large height and cover a substantial fraction of the surface.

This work (along with the aforementioned STM study) represents the first attempt to study Cu on the anisotropic Pd {110} surface and completes a set of studies of Cu growth on all low index Pd surfaces. The growth mode of Cu on Pd {100} was first reported as SK, with the deposition of two flat Cu monolayers, which were epitaxial and pseudomorphic, prior to island growth [20]. The determination of formation of an initial 2 ML pseudomorphic slab is based on LEED, AES and work function measurements. The determination of subsequent island growth was based on AES measurements and the fact that Pd UPS signal could be observed even at θ_{Cu}~65 eML when using Ne I incident photons. In contrast, an STM study of Cu on Pd {100} found that layer-by-layer growth continues up to θ_{Cu}~7 ML [9]. This is attributed to the Cu growing in a meta-stable bct phase (in-plane lattice parameter equal to that of Pd {100}; a=2.75 Å, c=3.24 Å) [7-9], which allows the growth of Cu overlayers with little strain. The slow transformation of the ARUPS features to those of bulk Cu (at

θ_{Cu} between 20-65 eML) observed by Asonen *et al* [20] can be attributed to the existence of this phase [41, 42].

A similar SK (2 ML and islands) growth mechanism was reported for Cu on a 1500 Å thick Pd {111} slab supported on mica by Vook *et al* [19] on the basis of work function measurements. However, it is difficult to see how work function data alone is able to definitively classify the growth mechanism as the authors have claimed. The growth of Cu on a Pd {111} crystal was reported to be epitaxial, but not pseudomorphic by LEED [18]. LEED-(IV) analysis favoured a VW mechanism, i.e. substantially different from that suggested by Vook *et al*.

The difference between the growth of Cu on the Pd {111} and {100} crystal faces may be attributed to differences in the magnitude of adatom-substrate interactions relative to adatom-adatom interactions. The fcc {111} crystal face is quite smooth, and hence provides relatively little hindrance to lateral relaxations of adlayer structures. In contrast, the fcc {100} face is 2-dimensionally rough, with the surface four-fold-hollow (FFH) sites providing 'deep' energy-wells suitable for 'trapping' adatoms at an expanded in-plane lattice parameter.

However, a perhaps more cogent argument for the different growth mechanisms centres around the bct phase. This phase is obtained by a uniform expansion of two sides of the fcc unit cell, coupled with a contraction of the third side. The bct phase is stable on Pd {100} because the bi-axial expansion is achieved by pinning the Cu adatoms in the FFH sites, with the contraction occurring in the z-direction. Consequently, the Cu adlayers grow with little inherent strain, and little tendency to deviate from pseudomorphic growth. In contrast to the fcc {100} face, the bct structure has no lattice plane that is equivalent to the fcc {111} face. Hence, there is no mechanism by which the in-plane strain, which would be introduced by pseudomorphic growth, can be released on the {111} surface other than through in-plane relaxation and incommensurate growth. It is likely that on the {111} surface the growing Cu film is a largely undistorted fcc structure.

The fcc {110} face provides an interesting situation in that it is 1-dimensionally rough along the [001] azimuth. In this direction there is a large hindrance to lateral relaxation, similar to the {100} face. In contrast, along the orthogonal, $[1\bar{1}0]$ azimuth the surface is smooth, i.e. little hindrance to lateral relaxations. A bct plane equivalent to the fcc {110} face does exist. It involves contraction of the normal fcc lattice structure along the [001] direction, and a uniform expansion along both the $[1\bar{1}0]$ azimuth & the z-direction. Clearly it is difficult to envisage such a Cu structure being stabilised on a Pd {110} single crystal, since it requires a contraction along the azimuth where relaxation is most hindered, and an expansion along the azimuth where relaxation is most probable. Consequently, Cu adlayers on Pd {110} are most probably strained in the [001] azimuth during the initial stages of growth, while relaxation along the $[1\bar{1}0]$ azimuth is possible. This corresponds to a distortion of the normal fcc lattice structure, but it is not bct. The Cu-Pd interaction ensures that the first Cu adlayer is pinned in the FFH sites resulting in the growth of 2-D islands during deposition of sub-monolayer Cu coverages. As the film thickness increases, relaxation begins anisotropically, occurring more rapidly along the $[1\bar{1}0]$ azimuth.

The lack of convergence of the ARUPS spectra until high θ_{Cu} is indicative of island growth. There appears to be regions of low local θ_{Cu} even on the high coverage overlayers. These regions would explain the persistence of the Pd UPS signal at the Fermi edge, and also the alloy state at ~1.75 eV, due to CuPd intermixing at the substrate/adlayer interface. Based on the work of Hahn *et al* [21], Pd will not diffuse to the surface of a Cu overlayer on an experimental time-scale until the sample temperature is >700 K. However, the work of Vook *et al* [19, 34] indicates that, when activated, Pd diffuses rapidly into Cu at <550 K. This work suggests that, for a given temperature, the inter-diffusion reaches a saturation point beyond which prolonged annealing at that fixed temperature does not significantly alter the alloy composition. Hence, at room temperature there may be a tendency for Pd to diffuse into the lower layers of Cu multi-layer structures. If the extent of Pd diffusion is governed by the overlayer thickness, then the thick Cu overlayers may consist of several layer of pure Cu covering a CuPd alloy. Such CuPd inter-diffusion might be activated as a strain release mechanism for the deeper Cu adlayers. If this is the case,

the absence of an alloy state on the ARUPS spectra measured from Cu on Pd {100} [42] may be attributable to the lack of strain in the bct phase of these overlayers.

5 CONCLUSIONS:

For growth at or just above 300 K, the favoured sub-monolayer growth mechanism of Cu on Pd {110} is in 2D pseudomorphic islands. Three-dimensional growth commences before the completion of the first monolayer in the form of clusters of relatively small height. The As-*t* and polar XPD plots provide direct evidence that clustering occurs for Cu growth in the range 1-4 ML. Substantial alloying of the Cu and Pd, other than place exchange during deposition, has been ruled out by annealing experiments, in agreement with the studies of Vook *et al* [19] and Hahn *et al* [22], although alloying in the deeper layers of thick Cu overlayers is indicated by the ARUPS study.

The As-*t* plot covers only the θ_{Cu} range of 0-4 eML and, once substantial multi-layer structures have formed, XPD is also insensitive to the growth mechanism. Hence, the exact growth mode at θ_{Cu}>4 ML is uncertain. Continued island growth is the most probable mechanism. The increased background and diffuse nature of the LEED spots observed with increasing θ_{Cu} may be indicative of continued island growth with a loss of long-range order as the strain imposed on the initial Cu monolayers is relaxed.

There is evidence of a contraction of the Cu inter-layer spacing during the initial stages of overlayer growth. This can be attributes to Cu initially growing at an expanded in-plane lattice parameter as determined from our LEED observations and by STM [23]. As θ_{Cu} increases the overlayer structure reverts to the lattice parameters of bulk fcc Cu (demonstrated by the position of the off-normal forward focusing XPD peak along the [001] azimuth). The fact that the shift in the LEED spots was most evident along the [1$\bar{1}$0] azimuth is indicative of a greater 'ease-of-relaxation' along this direction. Clearly there is no mechanism of stabilising thick distorted fcc Cu overlayers on the Pd {110} surface as the relaxation occurs over a relatively small coverage range. The LEED spots at θ_{Cu}~20 eML were broad and diffuse, which is consistent with island growth with a range of lattice parameters depending on the layer thickness of the islands.

The absence of the (1×1)→(1×2)-MR transformation as predicted by Guillopé and Legrand [13] may be due to the inability to grow pseudomorphic Cu films of sufficient quality. Schmitz *et al* [43] observed the reconstruction for Au on Pd {110} at a critical coverage of ~1.5 ML (i.e. the 1st layer grows flat and the second layer adopts the (1x2)-MR structure). Based on the initial pseudo-FM growth of Cu on Pd {110} (for θ_{Cu}<0.7 ML) the reconstruction might reasonably be expected for θ_{Cu} of 1-2 eML. Clearly the strain of ~7.7% imposed by the underlying Pd substrate is not sufficient to drive the (1x1)→(1x2) transition. However, it should be noted that the calculations were performed for artificially expanded/contracted bulk metal phases, i.e. no Pd/Cu interface present.

The ARUPS measurements of the Cu overlayers show features that are not present for "bulk" Cu {110}. The high θ_{Cu} required to converge these features to the bulk structure, and the persistence of the Pd d-band emission to high θ_{Cu}, are both indicative of island growth in a crystal structure other than pure fcc even at high coverages. The changes in the Cu ARUPS with coverage can be attributed to strain in the Cu overlayers. The appearance of a Pd-like impurity state at a binding energy of ~1.8 eV may be due to inter-mixing at the CuPd interface, strain in the initial Cu adlayers or stabilisation of a minority bct phase on the Pd {110} surface. Band structure calculations are required to fully interpret the features in the ARUPS spectra.

6. REFERENCES:

[1] J.A. Venables, G.D.T. Spiller and M. Hanbücken, Rep. Prog. Phys., 47 (1984) 399.

[2] C.T. Campbell, Annu. Rev. Phys. Chem., 41 (1990) 775.

[3] G.A. Prinz, J. Magn. Magn. Mater., 100 (1991) 4690.

[4] R. Courths and S. Hufner, Phys. Rep., 112 (1984) 53.

[5] Z.Q. Wang, S.H. Lu, Y.S. Li, F. Jona and P.M. Marcus, Phys. Rev. B, 35 (1987) 9322.

[6] C.J. Barnes, M. Valden and A. Vuoristo, Solid State Commun., 74 (1990) 811.

[7] I.A. Morrison, M.H. Kang and E.J. Mele, Phys. Rev. B, 39 (1989) 1575.

[8] H. Li, S.C. Wu, D. Tian, J. Quinn, Y.S. Li, F. Jona and P.M. Marcus, Phys. Rev. B, 40 (1989) 5841.

[9] E. Hahn, E. Kampshoff, N. Wälchli and K. Kern, Phys. Rev. Lett., 74 (1995) 1803.

[10] W. Duam, C. Stuhlmann and H. Ibach, Phys. Rev. Lett., 60 (1988) 2741.

[11] W. Moritz and D. Wolf, Surf. Sci., 163 (1985) L655.

[12] T. Gustafsson, M. Copel and G. Fenter in: The Structure of Surfaces II,, Springer, Berlin, (1988) p. 110.

[13] M. Guillopé and B. Legrand, Surf. Sci., 215 (1989) 577.

[14] J.H. Sinfelt, Bimetallic Catalysts, Wiley, New York, (1983).

[15] J.H. Sinfelt and J.A. Cusumano in: Advanced Materials in Catalysis, Eds. J.J. Burton and R.L. Garten, Academic Press, London, (1977) pp. 1-31.

[16] V. Ponec, Surf. Sci., 272 (1992) 111.

[17] K.I. Choi and M.A. Vannice, J. Catal., 131 (1991) 36.

[18] H. Li, D. Tian, F. Jona and P.M. Marcus, Solid State Commun., 77 (1991) 651.

[19] R.W. Vook, J.V. Bucci and S.S. Chao, Thin Solid Films, 163 (1988) 447.

[20] H. Asonen, C.J. Barnes, A. Salokatve and A. Vuoristo, Applicat. Surf. Sci., 22/23 (1985) 556.

[21] E. Hahn, E. Kampshoff and K. Kern, Chem. Phys. Lett., 223 (1994) 347.

[22] E. Hahn, E. Kampshoff, A. Fricke, J.-P. Bucher and K. Kern, Surf. Sci., 319 (1994) 277.

[23] E. Kampshoff, E. Hahn and K. Kern, Phys. Rev. Lett., 73 (1994) 704.

[24] J.-P. Bucher, E. Hahn, P. Fernandez, C. Massobrio and K. Kern, Europhys. Lett., 27 (1994) 473.

[25] P. Fernandez, C. Massobrio, P. Blandin and J. Buttet, Surf. Sci., 307/309 (1994) 608.

[26] C.J. Barnes and M. Gleeson, Surf. Sci., 319 (1994) 157.

[27] D. Briggs and M.P. Seah, Practical Surface Analysis, John Wiley & Sons, New York, (1990).

[28] E. Bauer, Applicat. Surf. Sci., 11/12 (1982) 479.

[29] C. Argile and G.E. Rhead, Surf. Sci. Rep., 10 (1989) 277.

[30] L.Z. Mezey and J. Giber, Jap. J. Appl. Phys., 21 (1982) 1569.

[31] G.E. Rhead, M.G. Barthès and C. Argile, Thin Solid Films, 82 (1981) 201.

[32] C.S. Fadley, Prog. Surf. Sci., 16 (1984) 275.

[33] F. Herman and S. Skillman, Atomic Structure Calculations, Englewood Cliffs, N.J. Prentice Hall Inc., New York, (1963).

[34] R.W. Vook, T.J. Swirbel and S.S. Chao, Appl. Surf. Sci., 33/34 (1988) 220.

[35] K. Yagi, K. Higashiyama, S. Yamazaki, H. Yanashima, H. Ohnuki, H. Fukutani and H. Hato, Surf. Sci., 231 (1990) 397.

[36] J.G. Tobin, S.W. Robey, L.E. Klebanov and D.A. Shirley, Phys. Rev. B, 28 (1983) 6169.

[37] M. Pessa and O. Jylhä, Solid State Commun., 46 (1983) 419.

[38] W.F.J. Egelhoff, J. Vac. Sci. Technol., 20 (1982) 668.

[39] R.S. Rao, A. Bansil, H. Asonen and M. Pessa, Phys. Rev. B, 29 (1984) 1713.

[40] J.-H. Xu, A.J. Freeman, T. Jarlborg and M.B. Brodsky, Phys. Rev. B, 29 (1984) 1250.

[41] F. Máca and J. Koukal, Surf. Sci., 260 (1992) 323.

[42] H. Li, S.C. Wu, J. Quinn, Y.S. Li, D. Tian and F. Jona, J. Phys.:Condens. Matter, 3 (1991) 7193.

[43] P.J. Schmitz, H.C. Kang, W.-Y. Leung and P.A. Thiel, Surf. Sci., 248 (1991) 287.

7. APPENDIX:

The following are ARUPS measurements as a function of photon energy between 18 eV and 40 eV. They were measured for a range of θ_{Cu} from ~1.3 eML to a "bulk" Cu overlayer at normal emission. Figures 16-22 are measured using a photon incidence angle of 25° (E-vector predominantly in the surface plane), while figures 23-30 are measured at an incidence angle of 60° (larger E-vector component perpendicular to the surface plane).

This data was collected with a view to making quantitative comparison with band structures, calculated for strained and tetragonally distorted Cu {110} films, in order to better understand the spectral features. These calculations are currently in progress, in collaboration with Dr. Matti Lindroos (Dept. of Physics, Tampere University of Technology).

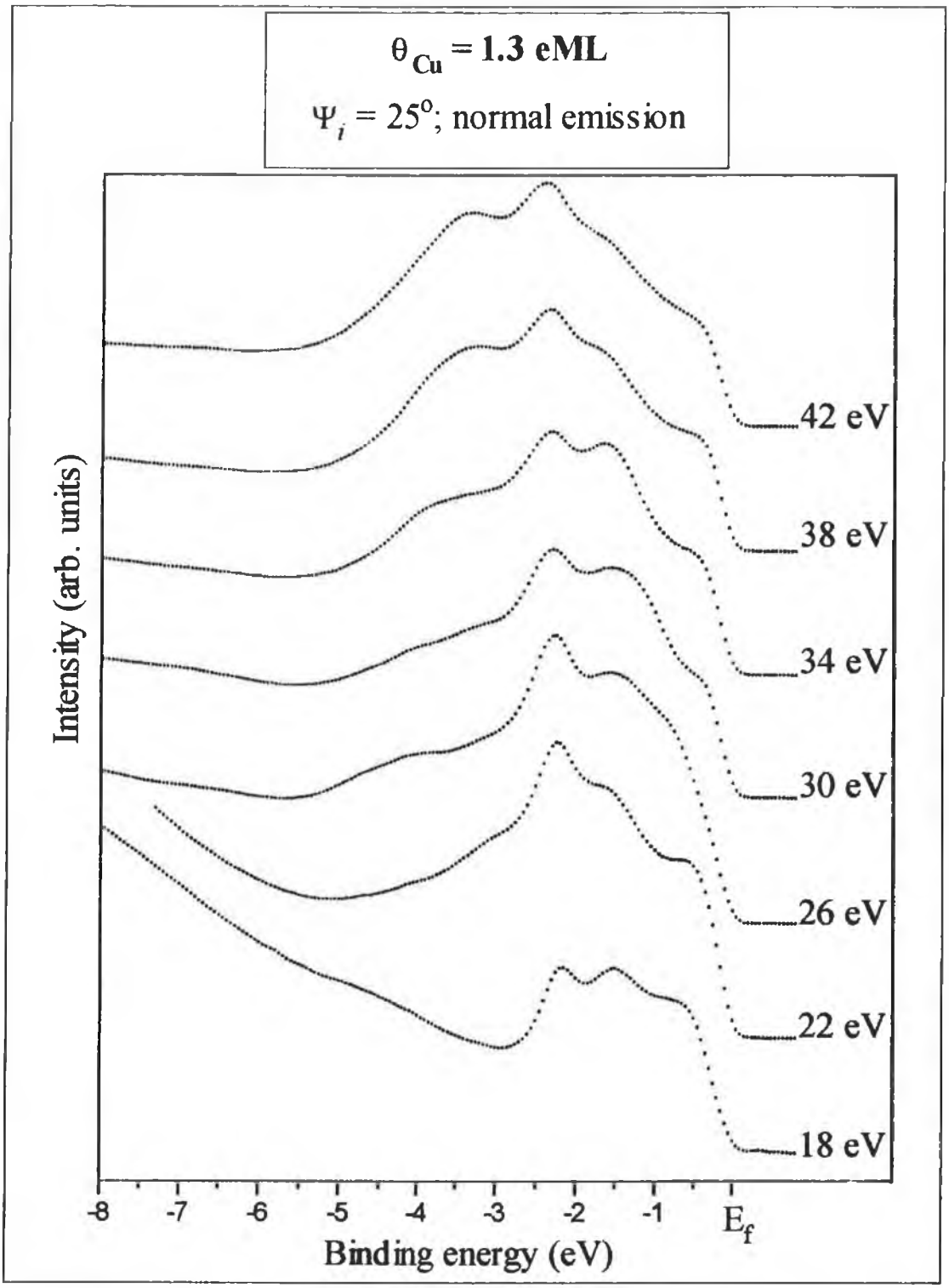

Figure 16: Normal emission ARUPS spectra measured as a function of photon energy for θ_{Cu}=1.3 eML on Pd {110}.

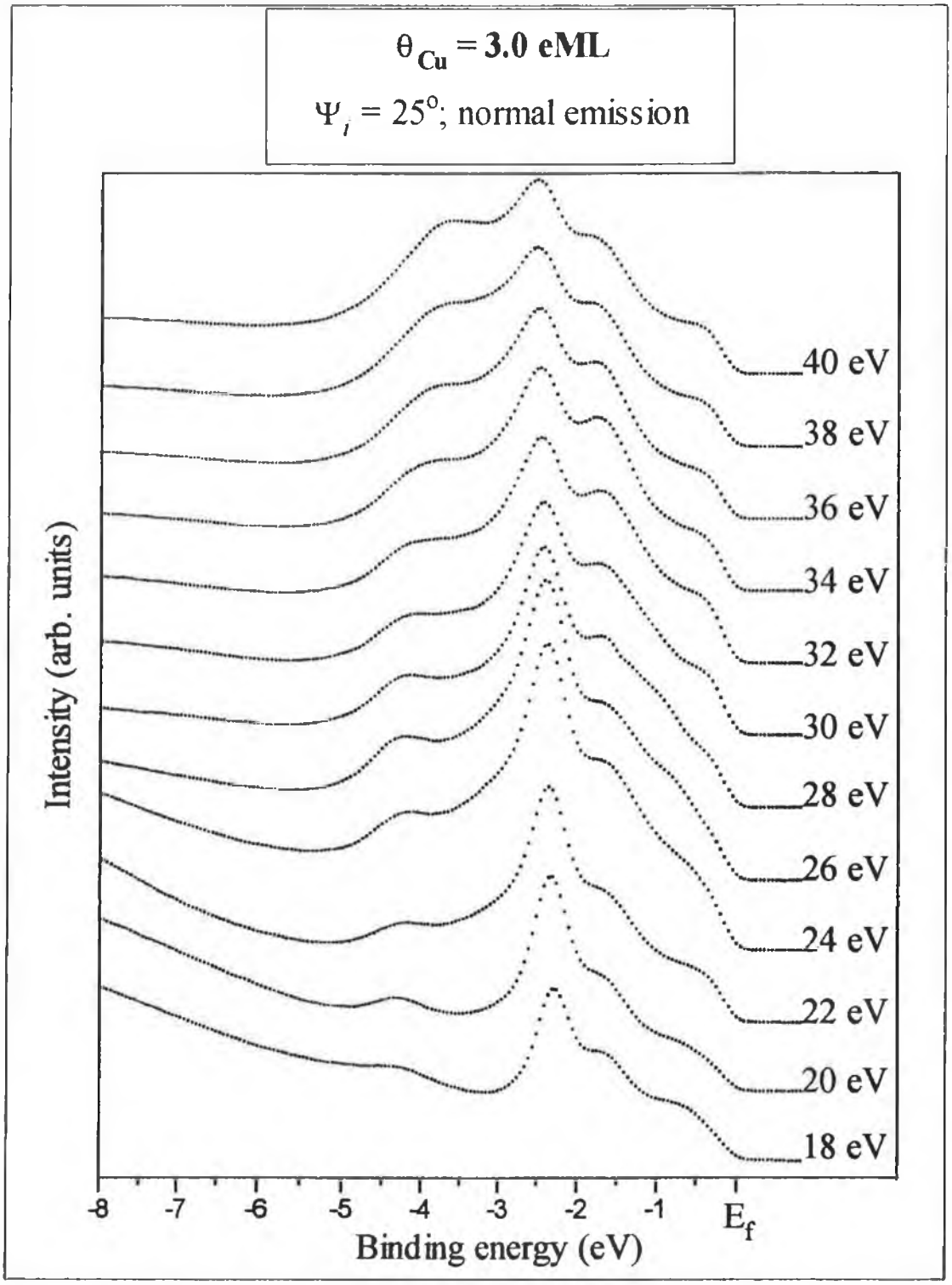

Figure 17: Normal emission ARUPS spectra measured as a function of photon energy for θ_{Cu}=3.0 eML on Pd {110}.

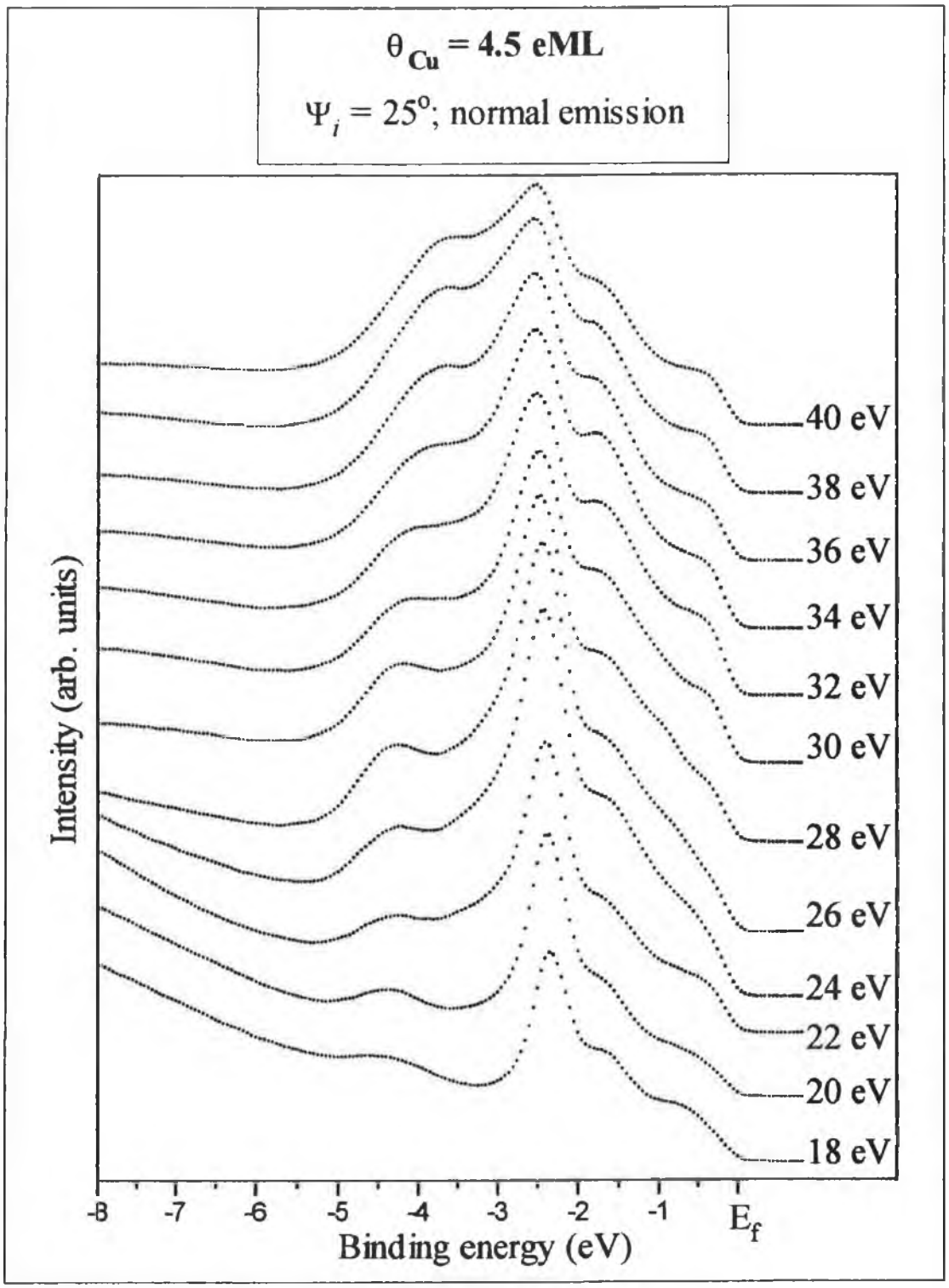

Figure 18: Normal emission ARUPS spectra measured as a function of photon energy for θ_{Cu}=4.5 eML on Pd {110}.

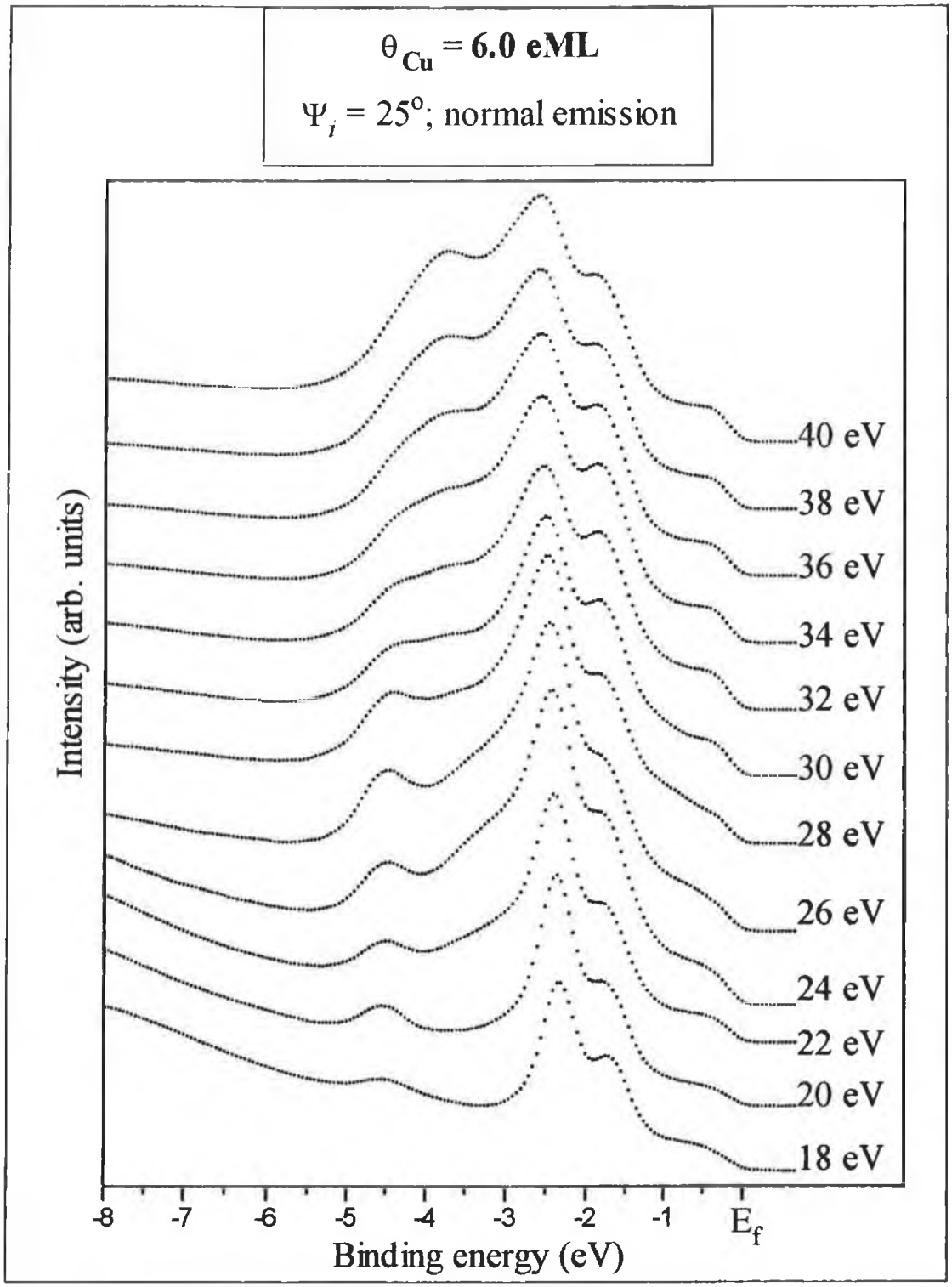

Figure 19: Normal emission ARUPS spectra measured as a function of photon energy for θ_{Cu}=6.0 eML on Pd {110}.

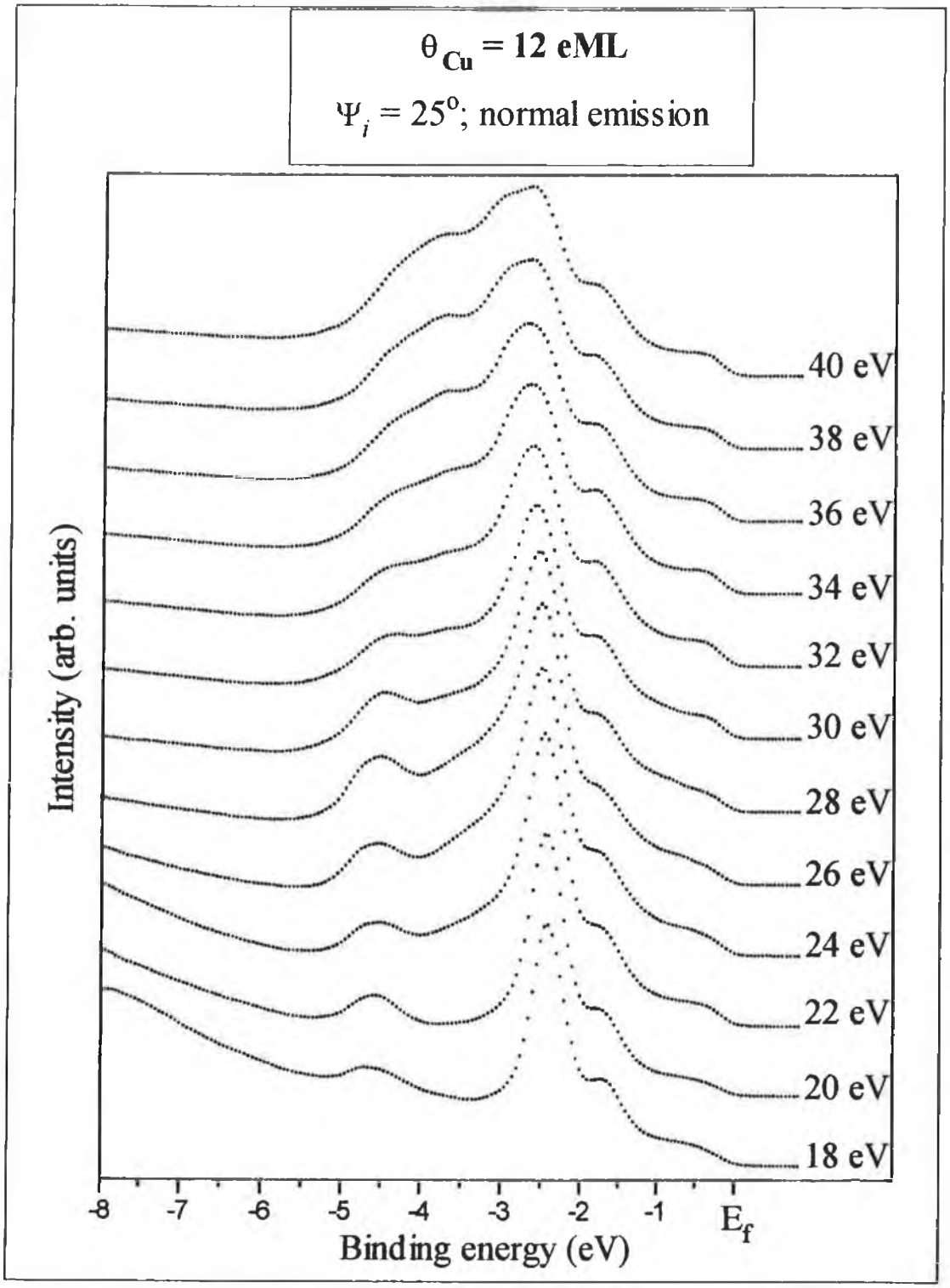

Figure 20: Normal emission ARUPS spectra measured as a function of photon energy for θ_{Cu}=12 eML on Pd {110}.

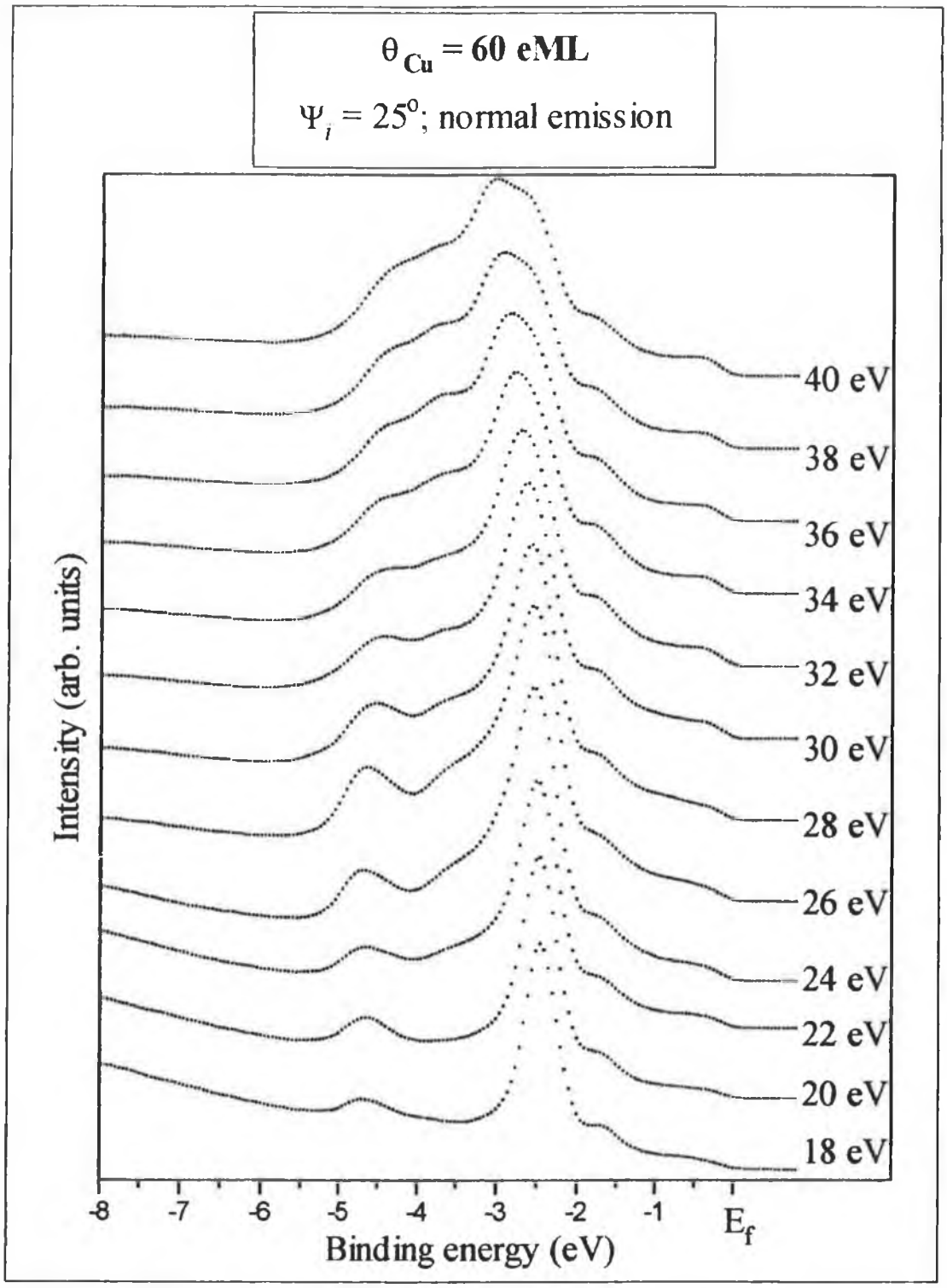

Figure 21: Normal emission ARUPS spectra measured as a function of photon energy for θ_{Cu}=60 eML on Pd {110}.

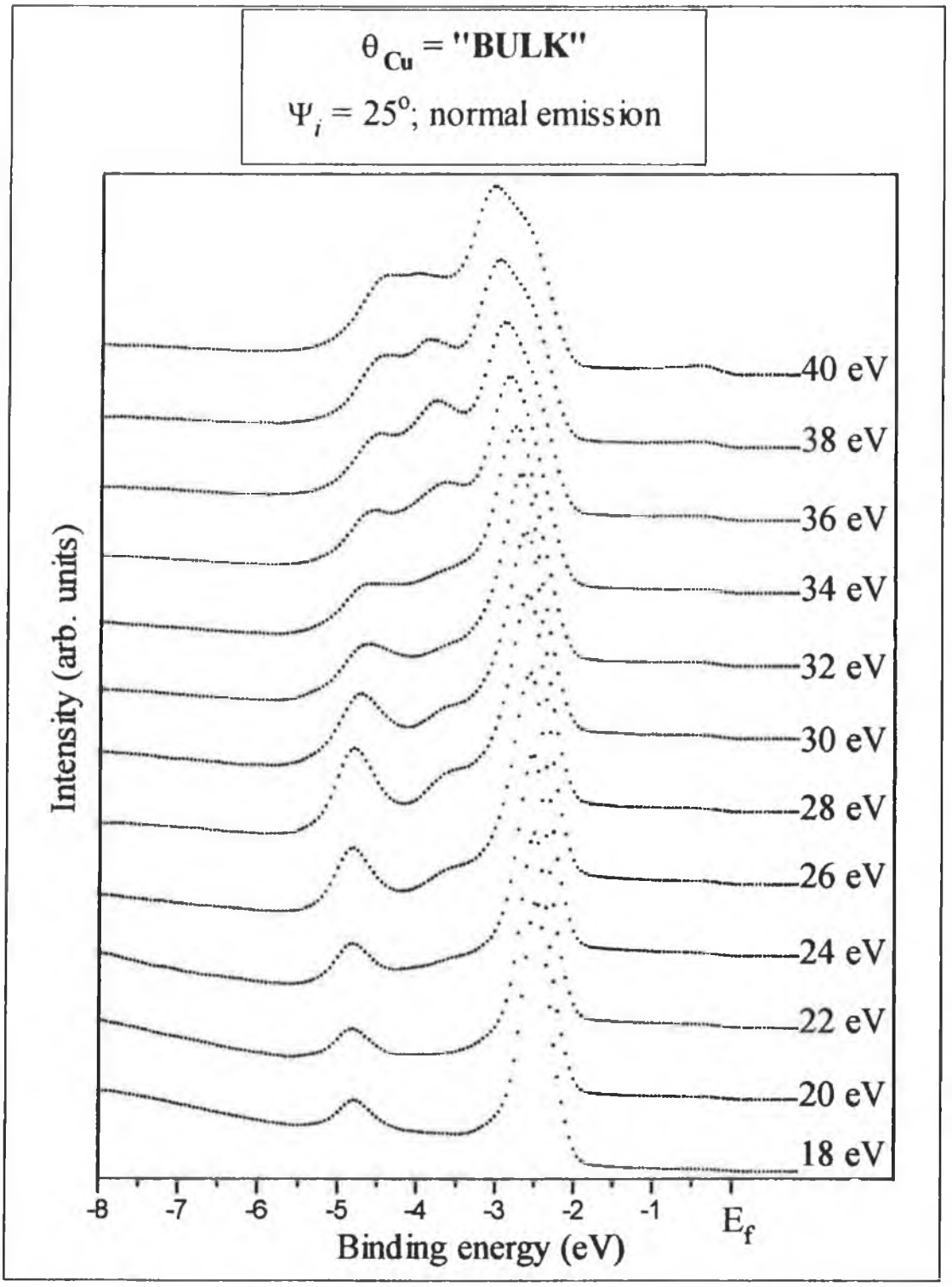

Figure 22: Normal emission ARUPS spectra measured as a function of photon energy for "bulk" θ_{Cu} on Pd {110}.

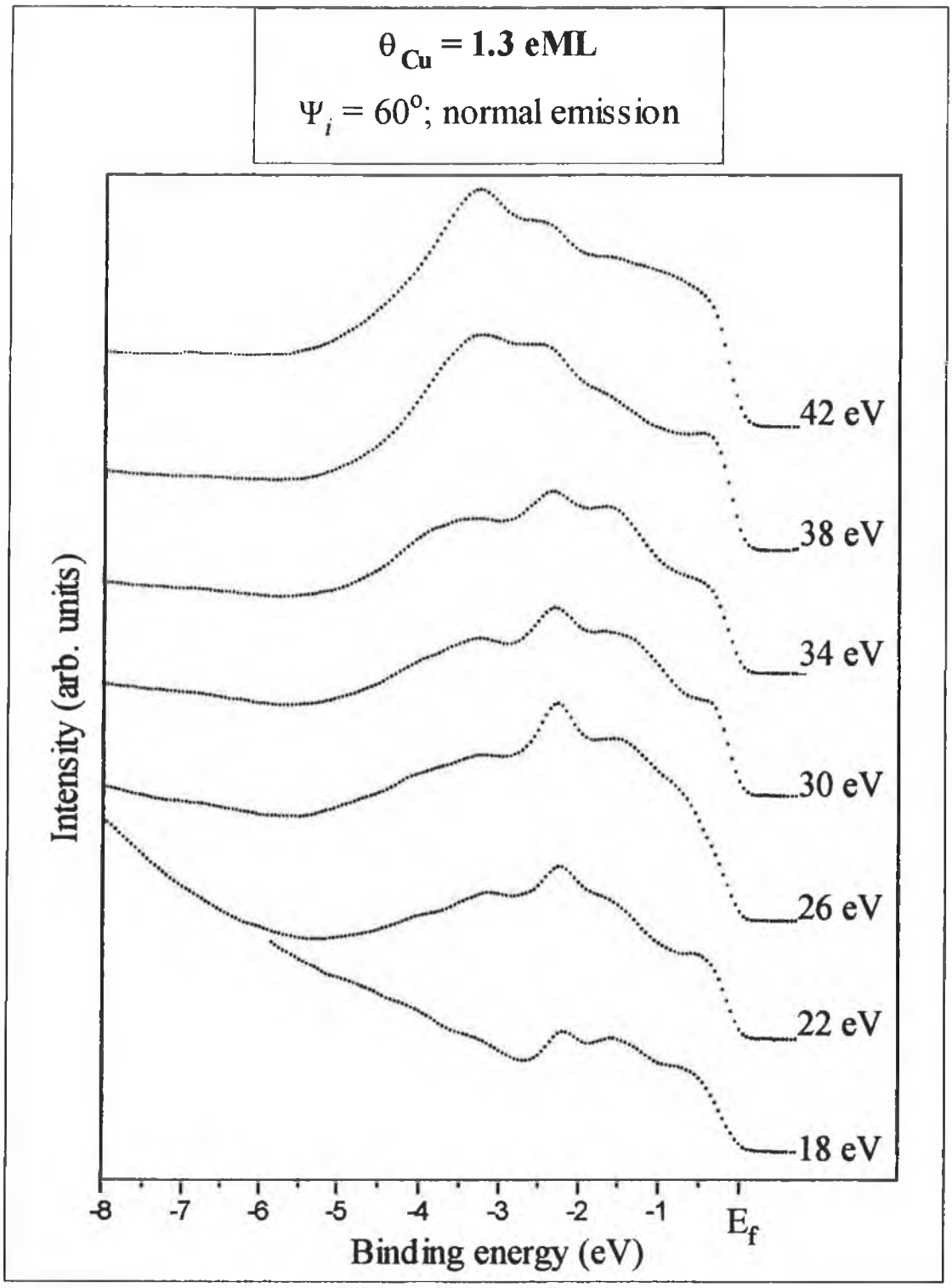

Figure 23: Normal emission ARUPS spectra measured as a function of photon energy for θ_{Cu}=1.3 eML.

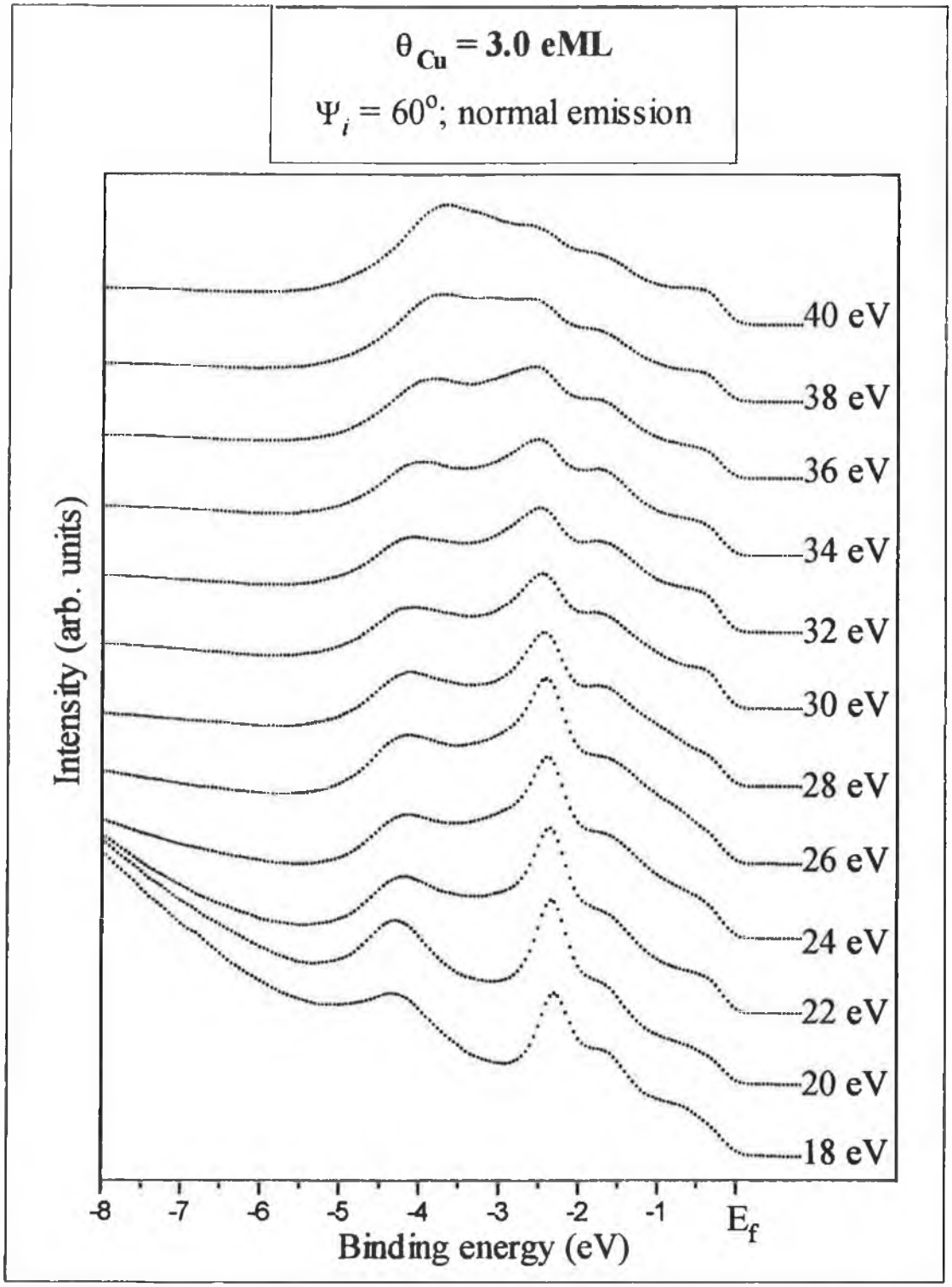

Figure 24: Normal emission ARUPS spectra measured as a function of photon energy for θ_{Cu}=3.0 eML on Pd {110}.

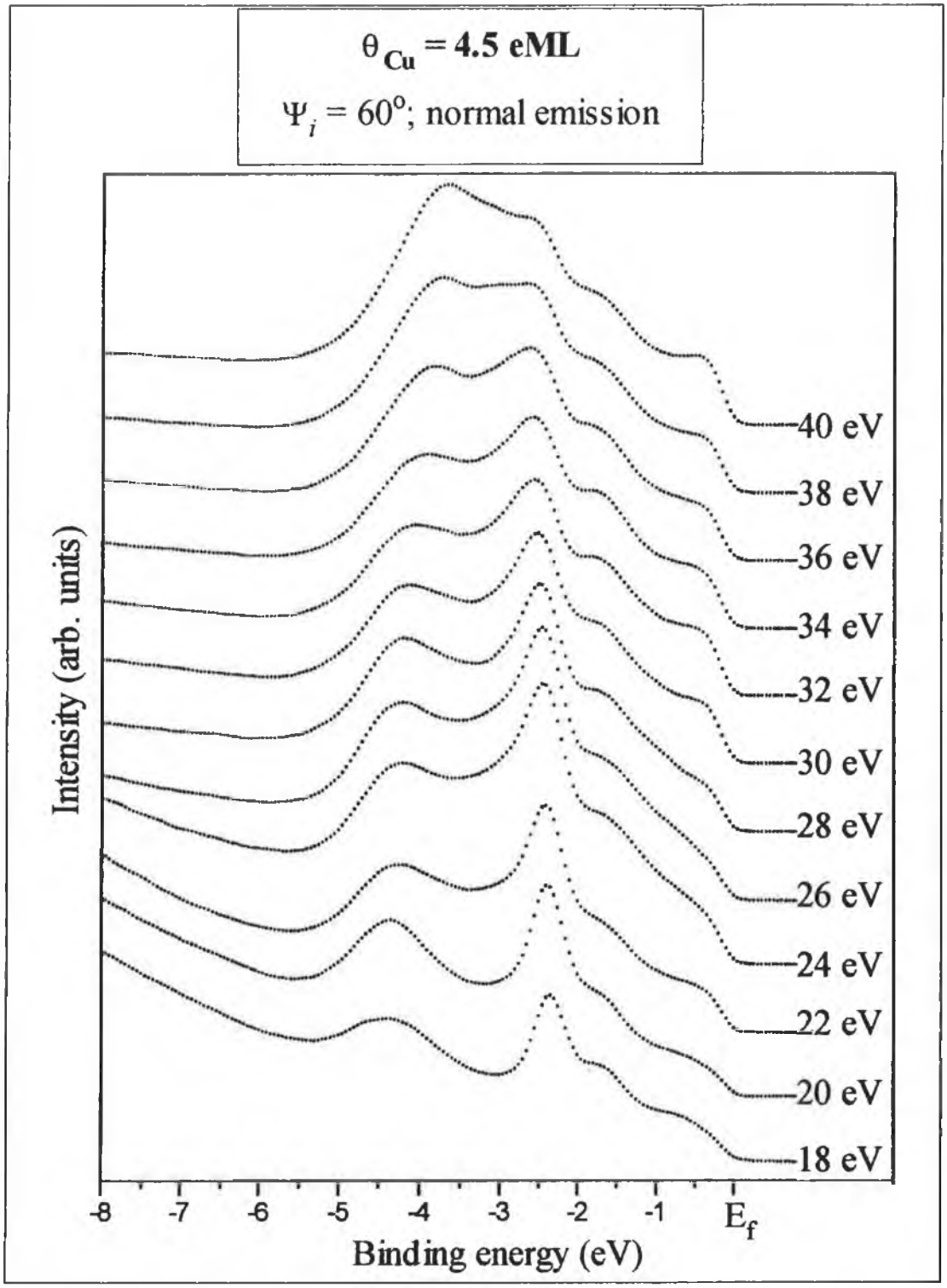

Figure 25: Normal emission ARUPS spectra measured as a function of photon energy for θ_{Cu}=4.5 eML on Pd {110}.

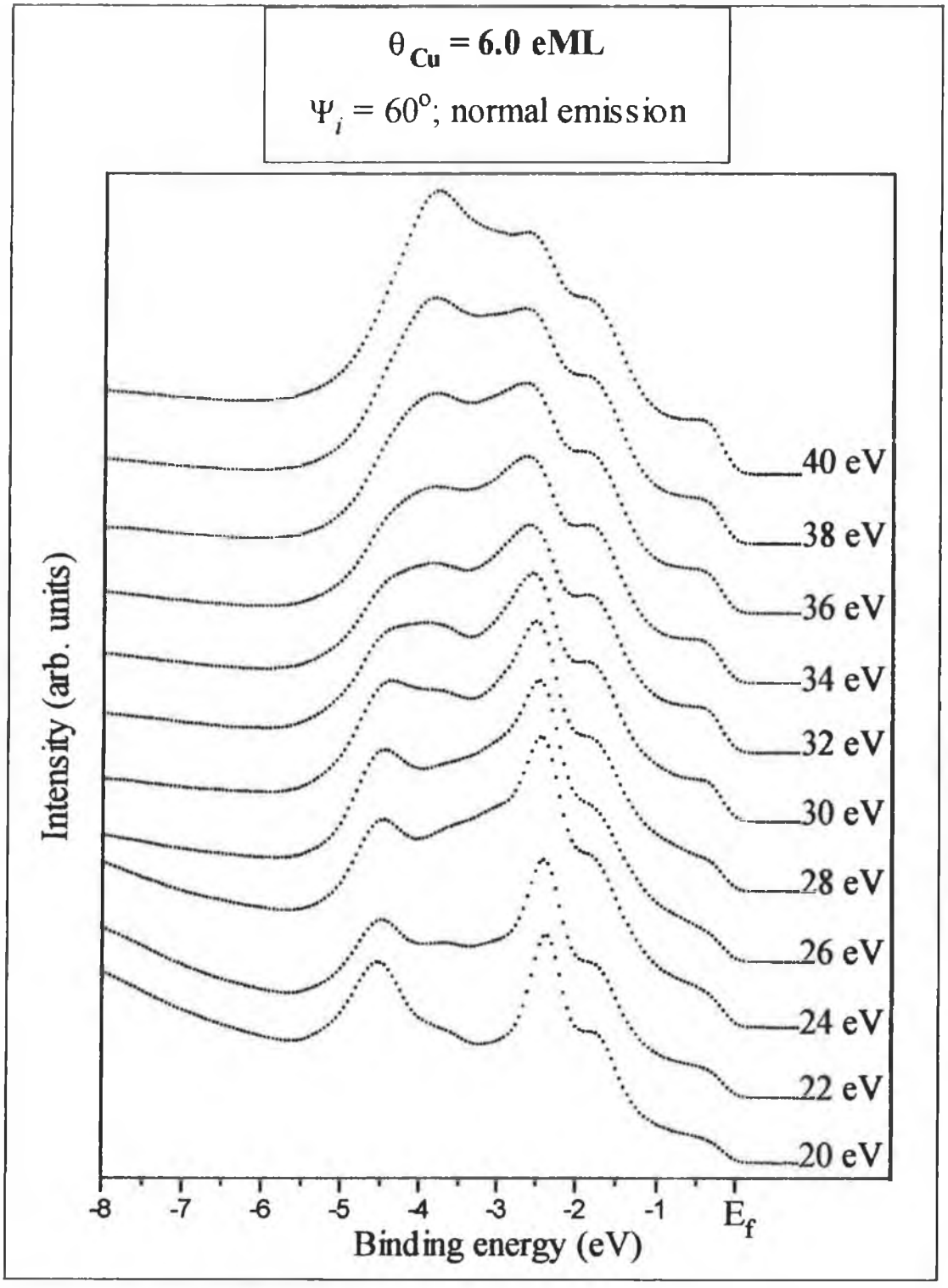

Figure 26: Normal emission ARUPS spectra measured as a function of photon energy for θ_{Cu}=6.0 eML on Pd {110}.

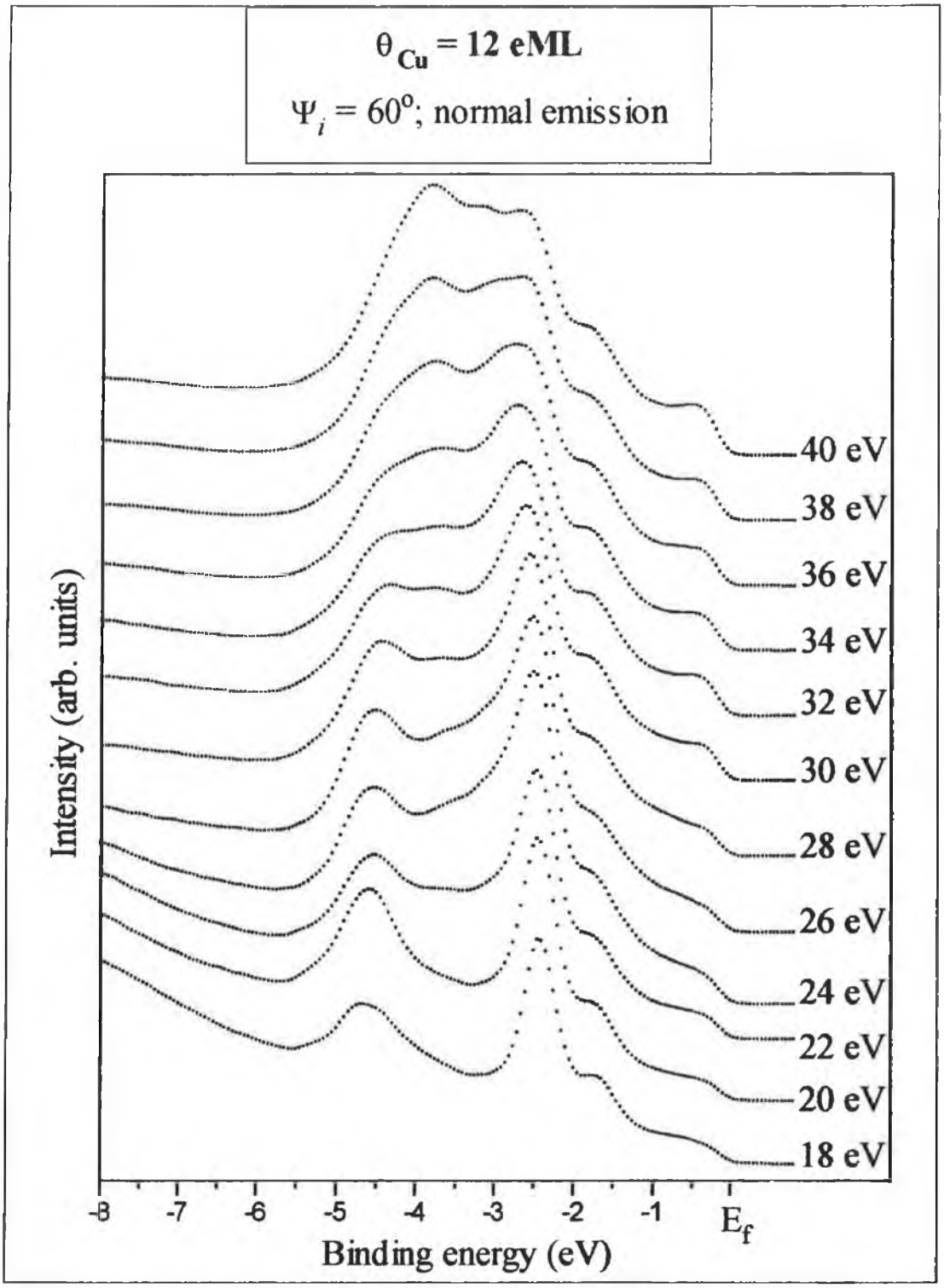

Figure 27: Normal emission ARUPS spectra measured as a function of photon energy for θ_{Cu}=12 eML on Pd {110}.

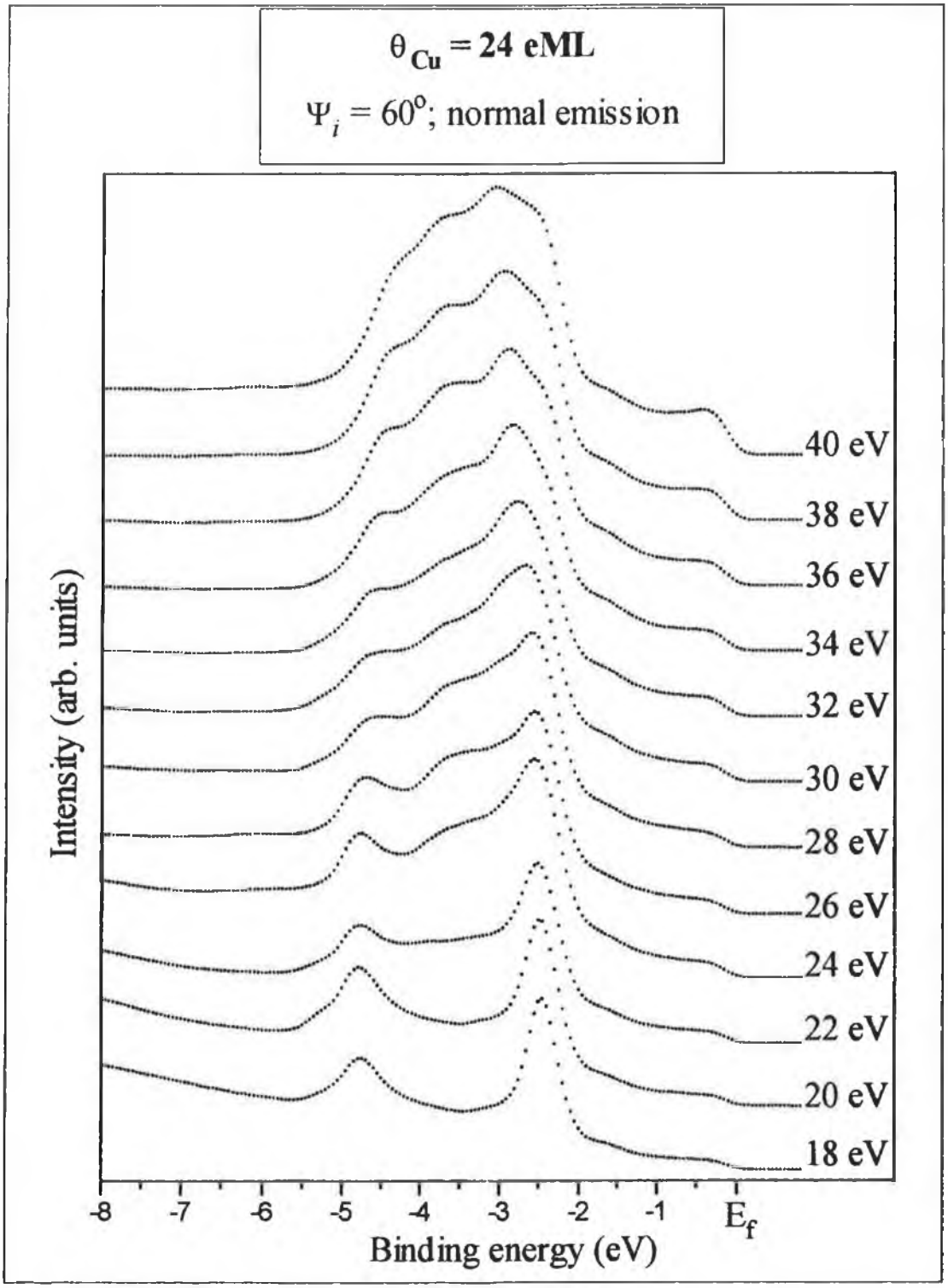

Figure 28: Normal emission ARUPS spectra measured as a function of photon energy for θ_{Cu}=24 eML on Pd {110}.

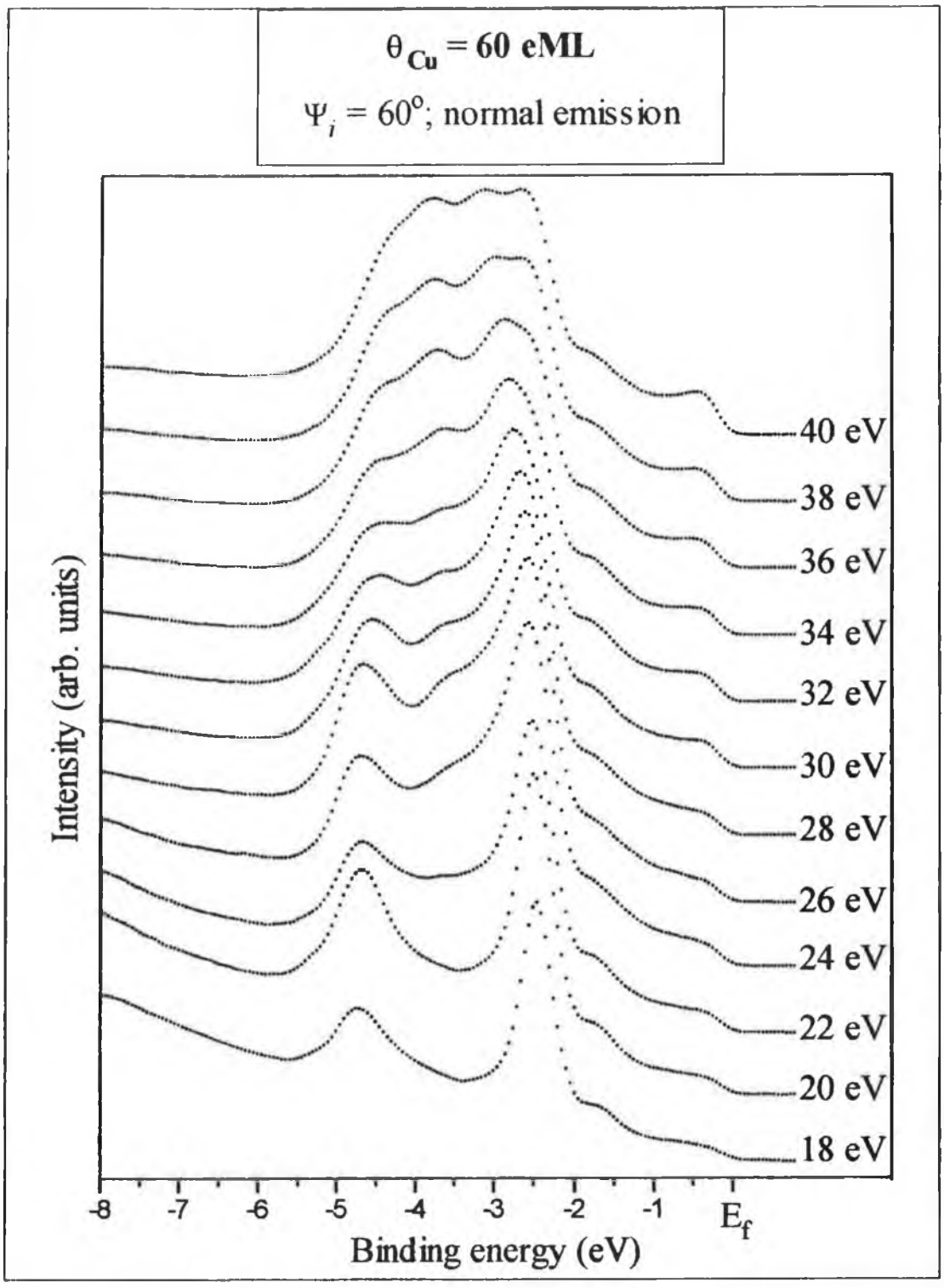

Figure 29: Normal emission ARUPS spectra measured as a function of photon energy for θ_{Cu}=60 eML on Pd {110}.

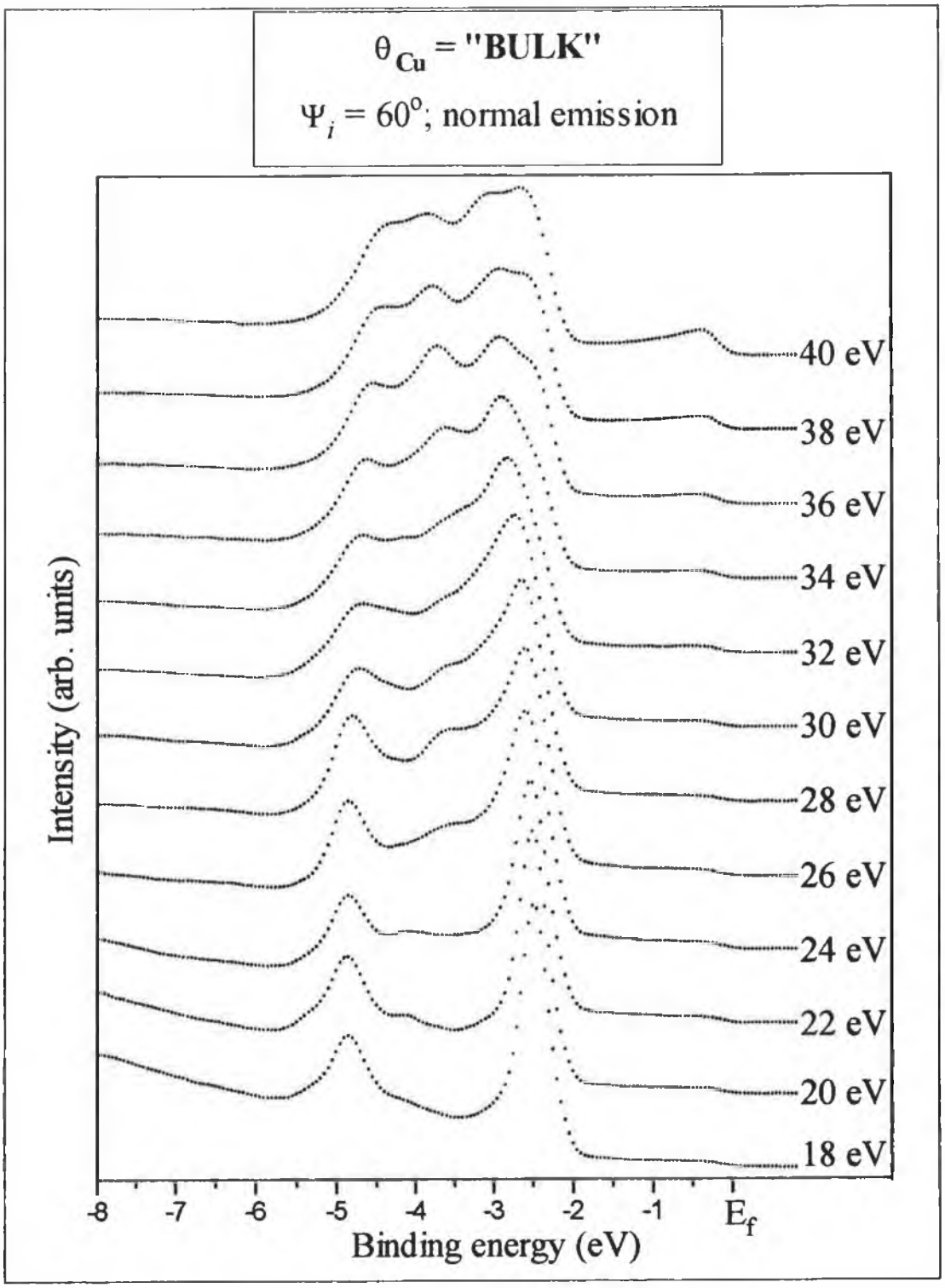

Figure 30: Normal emission ARUPS spectra measured as a function of photon energy for "bulk" θ_u on Pd {110}.

Chapter V

A NEXAFS/XPD study of the co-adsorption of K and CO on Co $\{10\bar{1}0\}$.

1. INTRODUCTION:

1.1. Alkali Metal/CO Co-adsorption:

Co-adsorption systems involving alkali metals (AM's) and carbon monoxide (CO) are of interest because of the important role that AM's play as promoters in transition metal catalysts [1]. Many catalysts are promoted by the addition of small amounts of alkali compounds. A typical example is the Fischer-Tropsch synthesis of hydrocarbons from CO/H_2 [2-6]. Iron or cobalt catalysts for this reaction are promoted with potassium salts in order to increase the relative production of high molecular weight hydrocarbons [7]. Potassium is also used to promote ammonia synthesis from N_2 and H_2 on iron catalysts [8-10] and in the synthesis of higher alcohols on ZnO [11].

Overlayers of AM's co-adsorbed with simple molecules (e.g. CO) on single crystal transition metal surfaces in a well controlled UHV environment are used as model systems. They are studied in order to gain a more fundamental understanding of how AM's act as promoters. Co-adsorbed AM/CO layers on different transition metal substrates often have a number of features in common. These include a lowering of the work function [12, 13], a lowering of the C-O stretching frequency [14, 15] and an increase in the desorption energy of both adsorbates, often coupled with coincident desorption [15-22]. In addition to the large number of experimental studies, the AM/CO interaction on transition metal surfaces has also been the subject of theoretically modelling in an attempt to elucidate the origin of these effects [23-26]. However, despite the large body of work that has been assembled, there is no unified description of AM/CO co-adsorption systems. Given the number of combinations of substrate and AM, and the range different relative coverages of co-adsorbate that may be studied, it is unlikely that any one model would be capable of describing all experimentally observed features. However, several general models of the AM/CO interaction have been proposed, and are outlined below [1]. A common feature of all these models is the assumption of a short-range AM-CO interaction within the adlayer and increased occupation of the CO $2\pi^*$ orbital in the sense of the Blyholder model [27].

Model A: The AM gives up electronic charge to the substrate, some of which is back-donated into the CO $2\pi^*$ orbital. There is also a direct interaction between the AM and the CO 1π orbital, which leads to back-donation of charge from the substrate to the AM and to overlap of the AM s-resonance and the CO 1π orbital. This introduces some anti-bonding character to the 1π orbital and weakens the C-O bond [28-32].

Model B: Weimer *et al* [19, 20, 33, 34] have suggested that the substrate-CO bond re-hybridises to sp^2 under the influence of a direct interaction with the AM and charge back-donation from the substrate. New σ and π bonds detected in the valence band are attributed to this re-hybridisation.

Model C: A direct interaction (either ionic or covalent) between the CO 2π orbital and the AM s-resonance occurs, in addition to 5σ donation/2π back-donation by the CO to the substrate [35-39]. Overlap of the CO 2π orbital with the substrate results in a filled $2\pi_b$ and an unfilled $2\pi_a$ level. Both of these levels are further split into bonding and anti-bonding levels through overlap with the K 4s-resonance [37]. In this model back-donation from the substrate has only a minor role, hence the substrate-CO bond may be weaker than for CO the clean surface.

Model D A direct, ionic interaction between K and CO resulting in the formation of a complex or "salt" on the Cu {110} surface, where the anion can be a polymeric species of the $C_qO_q^{2-}$ kind (q=2 or 4), has been proposed by Lackey *et al* [22]. The co-adsorbed AM ions and CO anions are proposed to form complexes that are similar to bulk compounds.

Models (A) and (C) are similar, except that different CO molecular orbitals are involved in the direct interaction with the alkali valence resonance. If such a direct interaction occurs, then it is conceivable that the AM s-resonance might overlap with both the CO 1π and 2π orbitals so these models are not mutually exclusive, although overlap is more energetically favourable for the $1s/2\pi$ combination. Furthermore, any direct interaction as proposed in models (A) & (C) might lead to re-hybridisation of the CO along the lines of model (B). Molecular orbital calculations would be required to properly quantify this. The "salt" formation proposed by model (D) is not

considered to be applicable in most co-adsorption systems, although it may occur in specific cases, especially in the high co-adsorbate coverage region.

A pre-requisite for detailed understanding of the interactions within an AM/CO co-adsorption system is a good understanding of the overlayer geometry. From a structural point of view, it is preferable that the co-adsorbed species form well-ordered, single-phase overlayers on the metal surface. However, due to the structural complexity of co-adsorption systems, it is only recently that full structural analyses of such systems have begun to appear. To date, three different AM/CO co-adsorption systems have been the subject of full structural studies. These are a p(2x2)-(K+CO) phase (K:CO=1:2) on Ni {111} studied by scanned-energy XPD [40], two p(2x2)-(Cs+CO) phases (K:CO=1:1 & 1:2) on Ru {0001} studied by quantitative LEED [41] and a c(2x2)-(K+CO) phase (K:CO=1:1) on Co $\{10\bar{1}0\}$ studied by quantitative LEED [42].

The co-adsorption of (K+CO) on Co $\{10\bar{1}0\}$ is a particularly interesting system because it forms a number of ordered, stoichiometric phases at different K coverages (θ_K). These include a c(2x4), a c(2x2) and a mixed phase p(3x1)/c(2x2) overlayer [43]. The c(2x4) phase is formed by saturating a 0.25 ML K adlayer with CO, while the c(2x2) is formed by saturating a 0.5 ML c(2x2)-K adlayer with CO. The p(3x1)/c(2x2) is formed by dosing a θ_K~0.6 ML adlayer with CO while monitoring the LEED pattern until a well-ordered, bright, sharp p(3x1) phase, which co-exists with the original c(2x2) phase, is observed. Using these phases the K-CO interaction on Co $\{10\bar{1}0\}$ can be studied systematically as a function of θ_K. To date only the c(2x2)-(K+CO) phase has received a full surface structural analysis [42].

1.2. (K+CO) co-adsorbed on Cobalt:

The model proposed for the c(2x2)-(K+CO) on Co $\{10\bar{1}0\}$ overlayer on the basis of a LEED-I(V) structural study [42] is illustrated in figure 1. The main points are:

- The K adatoms are located in the four-fold-hollow (FFH) sites, above the 2nd layer Co atoms.

- The CO molecules are displaced by ~0.5±0.2 Å (along the [0001] azimuth) from the Co short-bridge site and are located near the centre of gravity of the 3 neighbouring K atoms.
- There is a substantial increase (~0.4 Å) in the K-Co nearest neighbour distance compared to the c(2x2) K overlayer on Co $\{10\bar{1}0\}$.
- The centre of mass of K adatoms is located above that of oxygen atoms (by ~0.23±0.11 Å).

A RAIRS and temperature programmed desorption (TPD) study has been performed on the three (K+CO) co-adsorption phases and also on a fourth ordered phase, p(2x3)-(K+CO), [43]. The RAIRS spectra show that there is only one chemically distinct type of CO within the c(2x4)- and the c(2x2)- overlayers. In the case of the p(3x1)/c(2x2) overlayer there is also a single CO band for θ_{CO}<400 L. However, above this coverage two RAIRS bands (i.e. two chemically distinct type of CO) co-exist on the overlayer. In common with other (K+CO) co-adsorption systems, the stretching frequency of CO is strongly shifted to lower wave numbers when it is co-adsorbed with K, and this shift increases with θ_K. For the c(2x4)-(K+CO) overlayer the CO stretching frequency was located at ~1852 cm^{-1}, while on the c(2x2) overlayer it was ~1732 cm^{-1}. For CO on the clean surface the stretching frequency lies in the

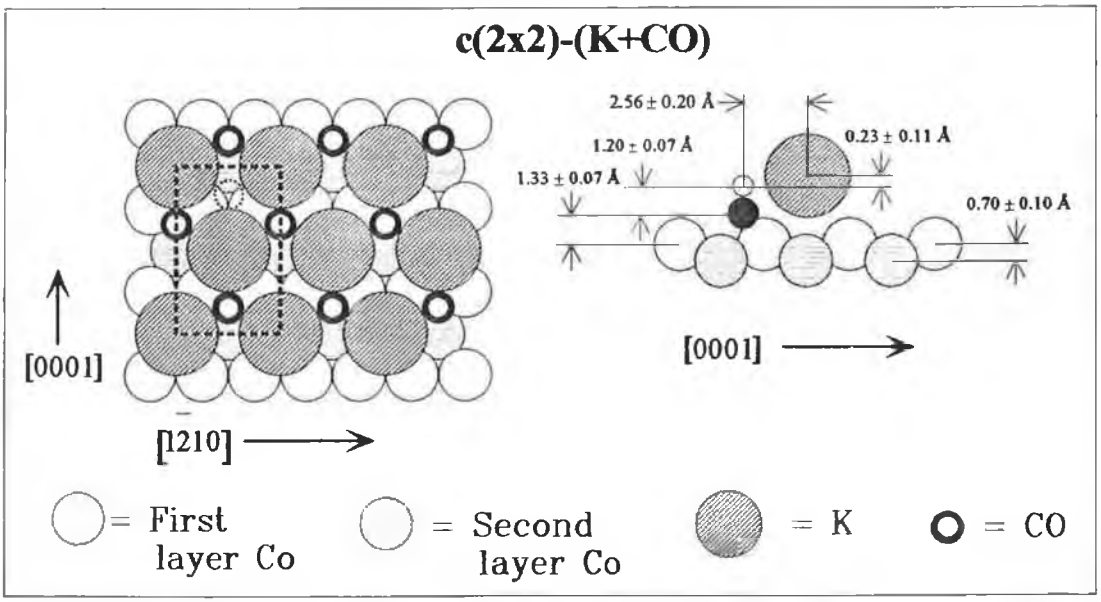

Figure 1: Structural model of the c(2x2)-(K+CO) overlayer as proposed in [42].

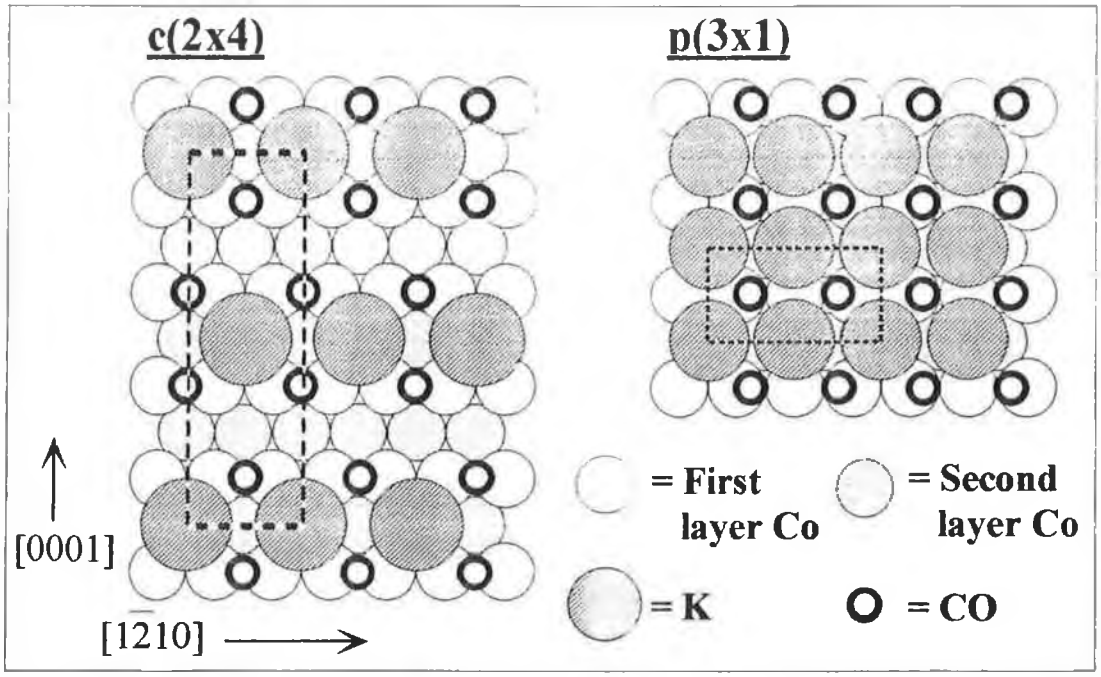

Figure 2: Structural models for the c(2x4)- and p(3x1)-(K+CO) domains as proposed in [43].

range 1972 cm^{-1} (low coverage) and 2021 cm^{-1} (saturation).

The stretching frequency was lowest on the p(3x1)/c(2x2) overlayer at ~1459 cm^{-1}, which corresponds to a red shift of ~513-562 cm^{-1}. In the case of this overlayer, progressive dosing with CO (θ_{CO}>400 L) led to the emergence of a second RAIRS band (1704-1733 cm^{-1}), which was attributed to CO in domains of c(2x2)-(K+CO). This band grew at the expense of the low frequency p(3x1) band. The authors proposed a model whereby initial CO adsorption induces the formation of the p(3x1) domains (which have an increased local θ_K). Once the p(3x1) sites are filled, CO begins to adsorb in c(2x2)-K domains resulting in a uniform redistribution of the K atoms across the surface and the consequent loss of the p(3x1) domains. The RAIRS/TPD data for the c(2x2)-(K+CO) overlayer was considered consistent with the LEED structural model as shown in figure 1. In addition, models were proposed for the c(2x4) and p(3x1) structures with a CO:K ratio of 2:1 and 1:1 respectively. These models are reproduced in figure 2.

We have utilised near-edge X-ray absorption fine structure (NEXAFS) to systematically study the orientation and intra-molecular bondlength of CO adsorbed

on clean Co $\{10\bar{1}0\}$ and on the three co-adsorption systems outlined above. In addition, XPS measurements were used to monitor the relative coverages of the co-adsorbed species on each of the overlayers and polar XPD measurements in conjunction with SSCC's have been utilised to determine the main structural parameters of the c(2x2)-(K+CO) overlayer. The intensity variation of the NEXAFS resonance features with photon incidence angle allows the orientation of the CO molecule to be determined. Shifts in the position of the characteristic CO "shape resonance" on the NEXAFS spectra measured from different overlayer systems allow us to estimate changes in the CO bondlength between the different phases. The azimuthal dependence of the CO π-resonance on the c(2x2) overlayer was also investigated.

Before discussing the experimental results, the theoretical basis of NEXAFS will be outlined along with the major structural parameters that may be extracted for simple (diatomic) molecules chemisorbed at a metal surface.

1.3. Near edge X-ray absorption fine structure (NEXAFS):

When the energy of X-ray radiation incident on a sample exceeds the excitation threshold of an atom's core electron a photo-electron may be generated leaving behind a core hole. The probability of excitation out of the core level is defined as the *absorption coefficient* of the shell from which the electron originates. NEXAFS is based on the measurement of the absorption coefficient of a surface atom near or above its characteristic excitation threshold ("absorption edge"). This may be achieved by measuring an Auger emission arising from relaxation of the core hole, and NEXAFS spectra may be obtained by monitoring the Auger emission intensity as the photon energy is swept across the absorption edge. Increased Auger intensity correlates with an increased absorption coefficient (core hole creation). Alternative measurement techniques involve monitoring either the X-ray fluorescence caused by core hole relaxation, or the 'total-electron-yield', as a function of photon energy.

For chemisorbed diatomic molecules, NEXAFS spectra are dominated by two characteristic resonances. One corresponds to electron transitions into an empty or partially filled molecular orbital with a transition energy less than the core ionisation energy (bound state transition). The other corresponds to a transition into a quasi-bound state in the continuum, termed a "shape resonance". An increase in the absorption coefficient (i.e. a resonance) is observed when the photon energy matches the energy required to excite these transitions. Figure 3 shows schematically the potential wells for a chemisorbed diatomic molecule (e.g. CO) and the location of the characteristic resonances.

For oxygen K-edge NEXAFS spectra (O 1s BE~531 eV) measured from CO adsorbed on a metal surfaces, the first transition occurs at photon energies just above the O 1s XPS binding energy (measured with respect to the Fermi level, E_f). This corresponds to excitation of an O 1s electron into the $2\pi^*$ CO molecular anti-bonding orbital and is referred to as a π-resonance. It is only present in molecules which have π bonding such as CO. In the case of CO, which has a triple bond (in the gas phase), there are two orthogonal $2\pi^*$ orbitals into which the electron transition can occur. Because the final state is bound, it has a long lifetime on the molecule. Consequently, it is a sharp resonance with a reasonably well-defined energy.

The second CO resonance is due to the transition of a 1s electron into a quasi-bound state above the vacuum level (E_v). This resonance appears as a broad feature typically >10 eV above the XPS binding energy [44, 45] and is present for all molecules. It was first associated, by Nefedov [46] and Dehmer [47], with final states trapped within the molecule by an effective potential barrier (the centrifugal barrier) as shown in figure 3. Such quasi-bound states decay away with a lifetime determined by the tunnelling probability through this barrier. The term "shape resonance" was introduced by Dill and Dehmer who used multiple-scattering theory to give a more general and quantitative description of these resonances [48]. The shape resonance can be thought of as resulting from electrons undergoing multiple scattering back-and-forth between the absorbing atom and its neighbours (i.e. between carbon and oxygen in the case of CO). NEXAFS is dominated by intra-molecular scattering processes and, in the first

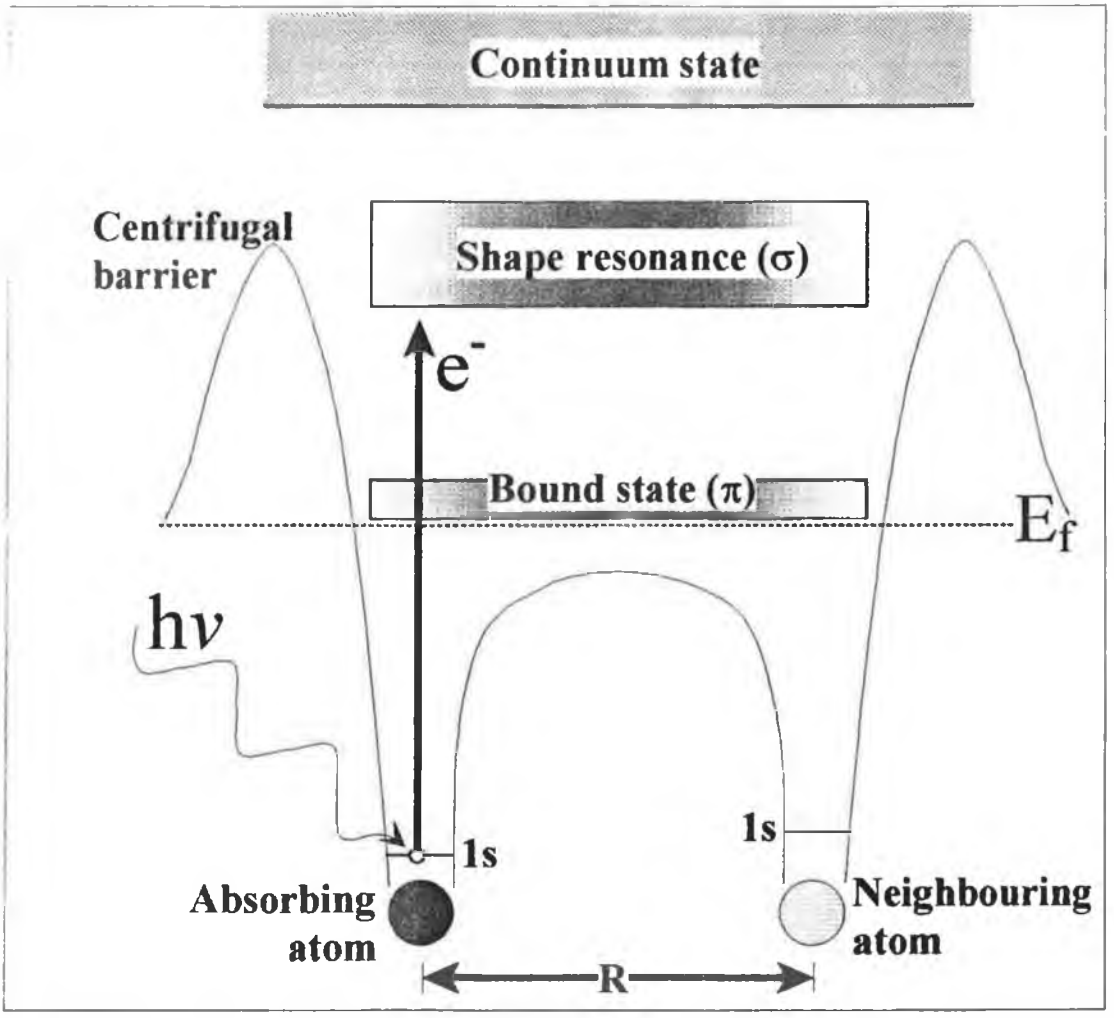

Figure 3: Schematic illustrating the positions of the characteristic π- and σ-resonances for a chemisorbed diatomic molecule. Energies are referenced to the Fermi level (E_f). For a gas phase molecule, the energies would be reference to the vacuum level (E_v), which lies above the π-resonance.

order, the effect of the substrate is merely to bind and orient the molecule. Hence, the simple inter-atomic scattering picture indicates that the resonance position should correlate closely with the molecular bondlength, R [44, 49, 50].

The extent to which either of these resonances is excited by incident photons is strongly dependent on the electric (E-) vector of the light (i.e. the polarisation), and this polarisation dependence can be used to determine molecular orientation. The shape resonance is symmetric with respect to a reflection plane containing the CO molecular bond axis (σ-symmetry) and is often referred to as a "σ-resonance". The π-resonance is anti-symmetric with respect to the same plane. Consequently, the π-

resonance intensity is maximised when the E-vector is perpendicular to the molecular bond axis (anti-symmetric to the reflection plane) while the σ-resonance intensity is totally quenched in this orientation (assuming there are no molecular vibrations). Conversely, when the E-vector is parallel to the bond axis the σ-resonance intensity is maximised and the π-resonance intensity is minimised. However, due to the fact that experimentally the incident photons are never perfectly polarised, the intensity of the π-resonance can never be completely eliminated, and some excitation of the $1s \rightarrow 2\pi^*$ transition will be possible at all incident angles. Even when the major E-vector component of the incident light is parallel to the CO bond axis, there is a minor E-vector component perpendicular to the axis, which will excite the transition to a $2\pi^*$ orbital. Unless specifically stated otherwise, the term 'E-vector' refers to the *major* E-vector component of the incident light (i.e. the polarisation vector).

1.3.1. Molecular orientation:

Because the final states associated with the π- and σ-resonances have well defined symmetries, the orientation of CO molecules adsorbed on a substrate can be determined by monitoring the intensity variation of the resonances as a function of the angle of incidence of the photon beam. For a given molecular tilt angle (α), the expected intensity of the π- and σ-resonances are given by the equations of Stöhr and Outka [45]:

$$I_\pi = C_\pi B\left\{2 - P\left[\cos^2(\Psi+\alpha) + \cos^2(\Psi-\alpha)\right]\right\}$$

$$I_\sigma = C_\sigma AP\left[\cos^2(\Psi+\alpha) + \cos^2(\Psi-\alpha)\right]$$

where:

C_π, C_σ, A and B are normalisation constants.

P is the degree of linear polarisation of the synchrotron radiation.

Ψ is the angle between the E-vector of the incident light and the surface normal (i.e. $\Psi=90^\circ$ for light at normal incidence, $\Psi=0^\circ$ for light incident parallel to the crystal surface).

I_π and I_σ are the intensities of the π- and σ-resonance peaks respectively, for given values of Ψ and α.

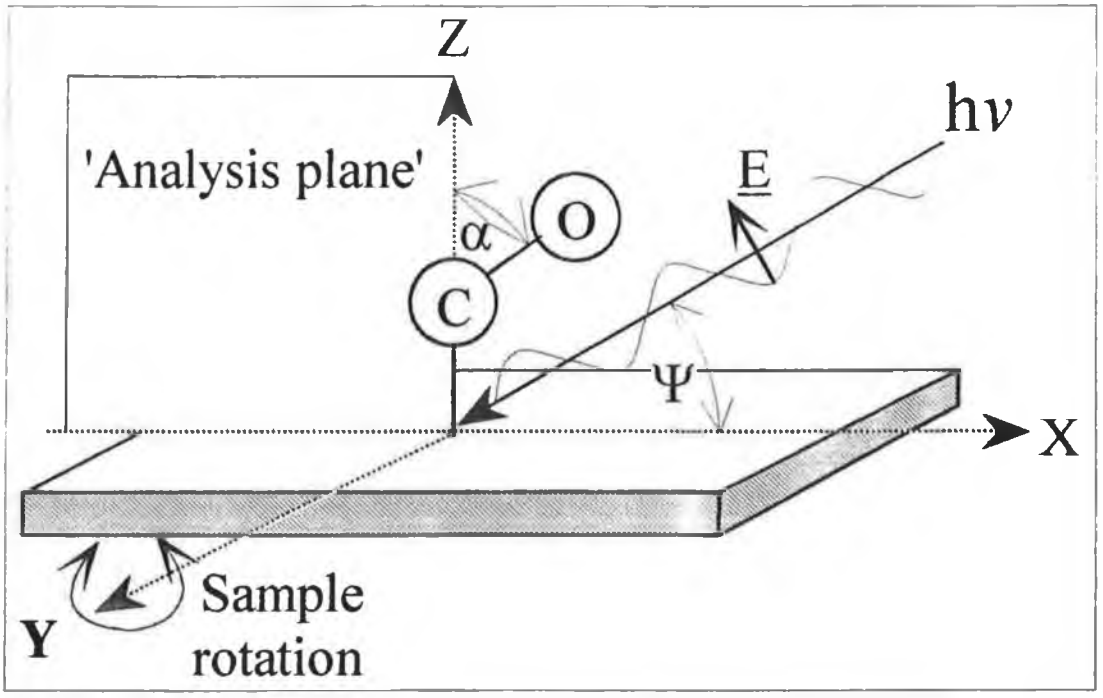

Figure 4: Definition of angles used in the molecular orientation equations.

α is the molecular tilt angle measured w.r.t. the surface normal (i.e. α=0° is an upright molecule, α=90° is a molecule lying flat on the substrate surface).

Figure 4 illustrates the angles used in the above equations. All angles are defined in the XZ plane as shown in the figure. α is the tilt of the C-O axis from the surface normal along this plane. Ψ is shown as the polar angle between the direction of incidence of the photon beam and the X azimuth of the surface. This is the same as the angle between the E-vector and the surface normal because the E-vector is in the XZ plane(the 'analysis plane'), and it is orthogonal to the incidence direction. Note that the equations, as shown, take no account of possible molecular tilts out of the analysis plane. The consequences of this will be discussed later.

The degree of linear polarisation of the synchrotron radiation, P, is defined as:

$$P = \frac{\left(E^{||}\right)^2}{\left[\left(E^{||}\right)^2 + \left(E^{\perp}\right)^2\right]}$$

where:

$E^{\parallel}$ and $E^{\perp}$ are the parallel and perpendicular components of the E-vector relative to the plane of polarisation (XZ plane) respectively.

For beamline 1.1, P has been determined to be in the range 0.8-0.9 [51]. The normalisation constants (A, B, $C_{\pi,\sigma}$) are not accurately known. However, they act merely as constant multiplication factors. Hence, by measuring the intensity variation of a resonance peak as a function of Ψ, we can determine a value for the molecular tilt angle (α) that fits the above equations. The equations contain the assumption that there are equal domains of CO, tilted in opposite directions along the XZ plane (i.e. rotated by 180° with respect to each other), on the crystal surface. Experimentally, Ψ is varied by rotating the crystal about the axis normal to the XZ plane as shown in figure 4.

Any given tilt direction of a diatomic molecule on the substrate can be split into 2 components. One is the component of the tilt that lies in the plane of crystal rotation (i.e. the XZ plane) and the other is the component of tilt perpendicular to this plane (i.e. the YZ plane). As stated above the NEXAFS resonance intensity variation analysis is primarily sensitive to the tilt component in the XZ plane. Hence, a comprehensive tilt determination requires the analysis to be done twice, along two orthogonal azimuths of the substrate surface.

CO NEXAFS analysis can be complicated by molecular vibrations [52, 53]. The equations above are based upon the assumption that the molecule has a rigid molecular tilt angle. However, at room temperatures adsorbed molecules are constantly vibrating about a 'mean' position on the surface. High frequency, low amplitude vibrations have a negligible effect on NEXAFS spectra, but low frequency, large amplitude vibrations can affect the molecular orientation determined significantly. The most obvious consequence of large amplitude vibrations is for an *upright* molecule. In this case, the σ-resonance intensity is never completely eliminated when the light is at normal incidence (as would be expected for a *frozen* molecule). This may result in the determination of a small "apparent" tilt for the upright molecule. For a tilted molecule, vibrations reduce the accuracy and precision with which the actual mean molecular tilt can be determined because they result in the

molecule being 'probed' at a range of different tilt angles (due to the relative time-scales of vibrational (10^{-13} to 10^{-15} sec.) and electronic (10^{-17} to 10^{-19} sec.) [54]). Measurements performed at low temperature (liquid N_2 or liquid He cooled) can help to eliminate this problem by 'freezing' out the large amplitude vibrations.

1.3.2. Molecular bondlength:

Shifts in the position of the σ-resonance peak have been correlated to changes in the intra-molecular bondlengths of small molecules both in the gas phase and upon chemisorption on a substrate [44, 49, 50]. Because this resonance originates from multiple scattering between atom cores, and is largely isolated on the molecule itself, it is sensitive to changes in the inter-atomic separation of the scattering atoms (i.e. the bondlength). Shifts of the σ-resonance peak to lower photon energy correspond to a lengthening of the molecular bondlength. Changes in the position of the CO σ-resonance peak upon co-adsorption with K, relative to that of CO on the clean metal surface, allow the determination of changes in the C-O bondlength, even though the absolute value of the bondlength may not be known.

Based on experimental measurements of gas phase diatomic molecules, a linear relationship has been proposed between the bondlength of molecules with the same sum of atomic numbers and the position of the NEXAFS σ-resonance peak (measured w.r.t. E_v) [44]. In the case of CO the relationship is given by:

$$\delta_g = 42.19 - 29.13R$$

where:

δ_g = gas phase molecule shape resonance position relative to E_v (eV).

R = inter-atomic bondlength (Å).

It was subsequently shown that for chemisorbed molecules the position of the shape resonances could be approximated by [50]:

$$\delta_s = \delta_g + C$$

where:

δ_s = chemisorbed molecule shape resonance position relative to the E_f (eV).

C = the difference in the core level binding energies between the chemisorbed (measured w.r.t. E_f) and gas phase molecules (measured w.r.t. the E_v) (eV).

C includes the effect of the sample work function, a possible initial state shift and a screening contribution from the metal substrate. It is effectively a constant for a given substrate so the linear relationship observed for gas phase molecules holds upon adsorption. Hence, changes in the intra-molecular bondlength of CO upon co-adsorption with K can be determined from the relative positions of the σ-resonance on the clean and K-dosed surfaces. The bondlength change can be approximately determined from:

$$\Delta R = 29.13(\delta_{Clean} - \delta_{Co\text{-}ad})$$

where:

ΔR = the bondlength difference between CO on the co-adsorbed overlayer and CO on the clean surface (Å).

δ_{Clean} = the σ-resonance peak position (w.r.t. E_f) for CO on clean Co (eV).

$\delta_{Co\text{-}ad}$ = The σ-resonance peak position (w.r.t. E_f) for CO co-adsorbed with K on Co (eV).

Although the results are purely empirical they have been found to give a good approximation of CO bondlength changes.

2. EXPERIMENTAL:

All experiments were carried out on beamline 1.1 at the CLRC Daresbury synchrotron radiation source in the UK. This beamline has a high-energy spherical grating monochromator which provides a high intensity beam of soft X-rays in the 250-1000 eV energy range [51]. The experimental chamber, pumped by a combination of turbo-molecular, ion and titanium sublimation pumps, had a base pressure of $\sim 1 \times 10^{-10}$ torr. It was equipped with Omicron rear view LEED optics, a multiplexed quadrupole mass spectrometer and a HA 100 hemispherical electron energy analyser. The angular acceptance of the analyser was $\sim 15^{\circ} \pm 3^{\circ}$.

The Co $\{10\bar{1}0\}$ crystal was rectangular in shape, with edges aligned along the high symmetry [0001] and $[1\bar{2}10]$ surface azimuths. The sample was cleaned in-situ using cycles of argon ion bombardment and annealing to ~600 K. After the bombard/anneal cycles a small but non-negligible amount of carbon contamination was still detectable by XPS. This was removed as CO_2 by adsorption of several Langmuirs of oxygen followed by annealing to 600 K. A short bombard/anneal cycle to remove residual chemisorbed oxygen resulted in a well-ordered surface with no contaminants detectable above XPS noise level. The crystal exhibited a sharp, bright p(1x1) LEED pattern.

Potassium was dosed from a well-out-gassed SAES getter source by resistive heating. The K coverages were monitored by XPS. The formation of a sharp, bright c(2x2) LEED pattern signified a θ_K of 0.5 monolayers (ML). Previous work has shown that slightly lower (0.47 ML) or higher (0.53 ML) coverages result in an observable splitting of the fractional order LEED beams [55]. Saturation coverages of CO on the clean Co and on the K-dosed surfaces was achieved by dosing with several hundred Langmuirs at room temperature. All overlayers except the p(3x1)/c(2x2) were formed using a saturation θ_{CO}. The p(3x1)/c(2x2) overlayer was created by monitoring the LEED pattern while gradually dosing CO and halting dosing when good quality p(3x1) spots were obtained.

XPS spectra in the region of the C 1s and O 1s core levels were measured using photon energies of 600 eV and 750 eV (KE~313 eV and ~219 eV respectively). At these energies the potassium $L_{2,3}M_{23}M_{23}$ Auger features (KE~250 eV) fall in close proximity to the respective core level peaks allowing simultaneous measurement of the K emission intensity. In addition, the K 2p photo-peaks (KE~307 eV at $h\nu$=600 eV) lie close to the C 1s peak. The photon beam was at normal incidence and the analyser subtended an angle of 30° to the surface normal for all XPS measurements. Peaks were normalised to the background on the low binding energy side of the core level peaks. Coverages were estimated from the integrated peak areas, after subtraction of a linear background.

Oxygen K-edge NEXAFS spectra were measured in constant final state (CFS) mode by monitoring the oxygen $KL_{23}L_{23}$ Auger yield at KE~510 eV. No interfering features from the monochromator were observed in NEXAFS scans of the oxygen K-edge region taken from the clean surface. All spectra were normalised to the same photo-absorption step-edge height (defined from a point before the onset of the oxygen adsorption edge (~532 eV) to a point after the shape resonance (~568 eV)). The photon incidence angle was varied by rotating the crystal. The bulk of the NEXAFS scans were measured along the [0001] azimuth of the crystal. In the case of the c(2x2)-(K+CO) overlayer, scans were also measured along the orthogonal $[1\bar{2}10]$ azimuth. The azimuths were aligned (±2°) using the clean surface LEED pattern.

All polar XPD scans were measured along the $[1\bar{2}10]$ surface azimuth from θ=-30° to 64° in 2° steps. The analyser aperture was rectangular in shape. It had an acceptance half-angle of ~2° in the plane of polar rotation, while in the orthogonal plane the acceptance half-angle was ~5°. The angle between the photon beam and the analyser was 30° in the plane of polar rotation and the E-vector of the incident light was parallel to this plane. Due to the absence of strong forward focusing features at θ=0° for the low kinetic energies used in many scans, and the relatively small source-analyser angle (see chapter 2), normal emission (±1°) was located using 180° reflection of the zero-order synchrotron light from the clean crystal surface. The

measured core level spectra were normalised to the background on the high KE side of the emission peaks. Polar XPD spectra were measured from the clean Co surface and the c(2x2)-(K+CO) surface. The core level emissions and kinetic energies monitored are cited in the relevant sections. Modelling of the XPD process was done by single scattering cluster calculations (SSCC's), which are detailed in the results section.

3. RESULTS:

3.1. XPS Analysis:

Figure 5 shows normalised XPS spectra measured in the carbon 1s and oxygen 1s photo-emission peak regions from the three co-adsorption systems studied, using photon energies of ~600 eV and ~750 eV respectively. The integrated areas under the various core level peaks was used to determined the CO:K coverage ratios on the different overlayers. In addition, if the absolute coverage of an adsorbate species is known for any one overlayer system it can be used as a reference point in determining the absolute coverages for each of the other overlayer systems. It has been demonstrated that K adsorbed on Co $\{10\bar{1}0\}$ forms a perfect c(2x2) LEED pattern at a coverage of 0.5 ML (±0.03 ML) [55].

Determining a reference point for CO is somewhat more complex. It is possible to

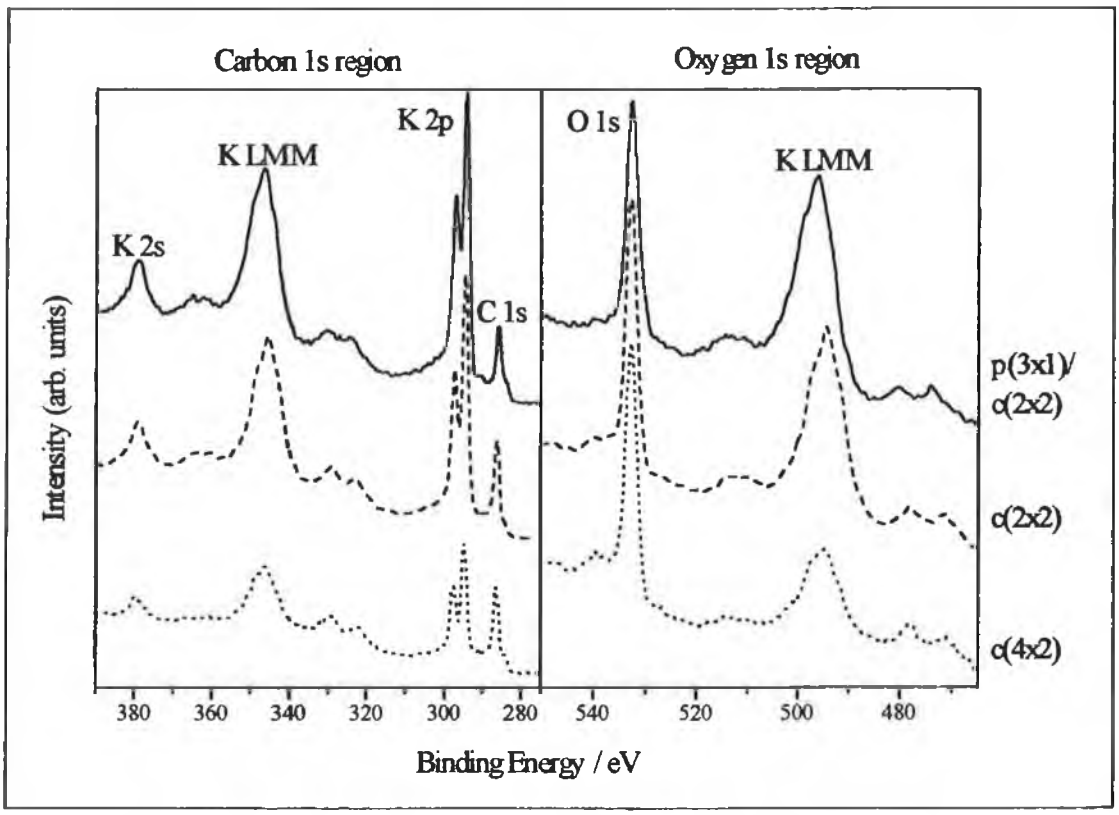

Figure 5: XPS spectra measured from the three (K+CO) co-adsorption systems.

	CO	c(2x4)	c(2x2)	p(3x1)/c(2x2)
θ_{CO} (ML)	0.5	0.92 ± 0.06	0.93 ± 0.06	0.82 ± 0.07
θ_K (ML)	-	0.25 ± 0.04	0.5	0.6 ± 0.03
θ_{CO}/θ_K	-	3.7 ± 0.8	1.9 ± 0.2	1.4 ± 0.2
~CO:K	-	4 : 1	2 : 1	4 : 3

Table 1: Absolute coverages and adsorbate ratios determined for the various co-adsorption systems on the basis of the XPS core level peak integrated areas.

obtain a saturation θ_{CO} of 1.0 ML at room temperature on clean Co $\{10\bar{1}0\}$ [56, 57]. For $\theta_{CO} \leq 0.5$ ML, TDS shows a single desorption peak (α_2) between 405-398 K. For $\theta_{CO} > 0.5$ ML, a second desorption peak (α_1) emerges at ~340 K. Estimation of the lifetime of CO in the two states, on the basis of the heats of adsorption calculated by Papp (145 KJmol^{-1} & 120 KJmol^{-1} respectively) [56], indicates that there should be negligible desorption from either state at room temperature over the experimental time-scale (i.e. the room temperature saturation coverage is ~1.0 ML). In contrasts, using the desorption energy calculated for the α_2 state by Toomes and King (110.7 KJmol^{-1}) [57], and assuming the desorption energy for the α_1 scales identically to the energies calculated by Papp, then the average lifetime of CO in the α_1 state is only ~11 minutes. There should be effectively no room temperature desorption from the α_2 state. Hence, at room temperature, saturation θ_{CO} may be as low as 0.5 ML. In this study a saturation coverage of θ_{CO}=0.5 ML on the clean surface has been chosen as the reference point for estimating the θ_{CO}'s on the co-adsorbed overlayer. This coverage is chosen on the basis that it is the lower limit of the range of θ_{CO} that may exist on the clean surface at room temperature. If θ_{CO} is higher on the clean surface, then the θ_{CO}'s determined for the co-adsorption layers will scale linearly with the clean surface value.

Table 1 summarises the results of the coverage determination based on the XPS analysis. It shows the absolute coverages determined based on the assumptions of θ_K=0.5 ML on the c(2x2)-(K+CO) co-adsorption layer and θ_{CO}=0.5 ML on the clean Co surface at room temperature. The corresponding CO/K ratios and the most probable CO:K stoichiometries on the different overlayers are also shown. The CO

coverages are based on the O 1s core level peak intensities, since these should be the least affected by processes such as photoelectron diffraction and inelastic scattering.

The θ_K values determined by XPS are in good agreement with their respective K evaporation times (assuming a coverage-independent sticking probability). However, the results show a significant increase in θ_{CO} on each of the three co-adsorption layers relative to the saturation coverage on clean Co. On all co-adsorption layers θ_{CO} is nearly doubled. A number of studies have observed increases in the saturation θ_{CO} upon co-adsorption with K [12, 58, 59]. Some studies have reported a drop in the saturation coverage upon co-adsorption [19, 21], however this may due to insufficient dosing times resulting in true saturation not being achieved [58]. This problem arises due to a decrease in the sticking probability of CO on alkali-dosed surfaces. For instance, when K is adsorbed on Fe {110} the CO dose must be increased by a factor of 100 in order to achieve saturation [59]. However, the saturation θ_{CO} on the alkali covered Fe surface is greater than that of the clean surface.

The CO:K ratios determined for the c(2x4) and c(2x2) overlayers are straight forward since those overlayers consist of a single phase (all domains on the surface have the same local CO:K ratio) as demonstrated by a reflection absorption infra-red spectroscopy (RAIRS) study [43]. The mixed phase p(3x1)/c(2x2) overlayer requires closer scrutiny. Upon deposition of ~0.6 ML of K but prior to CO dosing the adlayer gives a split c(2x2) LEED pattern. The p(3x1) spots only emerge upon dosing with CO. However, overdosing with CO results in a c(2x2) LEED pattern with a high background. Formation of the mixed phase requires monitoring of the LEED pattern while gradually dosing with CO until an optimum quality p(3x1)/c(2x2) pattern is obtained. The coverage density of potassium in the c(2x2) domains is 1 K atom to every 2 Co top-layer atoms. Thus, the most probable coverage density in the p(3x1) domains is 2 K atoms to every 3 Co top-layer atoms (i.e. 0.67 ML local coverage). Using these coverages, the ~0.6 ML of K deposited to form the p(3x1)/c(2x2) overlayer can be accounted for by a 40% coverage of c(2x2) and a 60% coverage of p(3x1) domains.

The fact that the p(3x1) phase appears upon CO dosing suggests that, during the initial stages of dosing, the adsorbed CO induces the p(3x1) ordering. The c(2x2) LEED spots can arise from regions of c(2x2)-K on the surface, since RAIRS spectra from low θ_{CO} overlayers show a single band corresponding to CO in the p(3x1) domains at ~1459 cm^{-1} [43]. However, as θ_{CO} increases RAIRS spectra containing 2 stretching bands (corresponding to CO molecules in both the c(2x2) and the p(3x1) domains) are observed. These overlayers still yielded the mixed phase LEED pattern. Since we did not have any experimental means of distinguishing between CO in the c(2x2) and the p(3x1) domains, the possibility that some domains of c(2x2)-(K+CO) existed on the p(3x1)/c(2x2) overlayer studied in this chapter cannot be ruled out.

Assuming the CO dose was sufficient to saturated the p(3x1) domains but resulted in little or no adsorption in the c(2x2) domains, then the CO:K ratio in the p(3x1) domains would be 2:1, i.e. the p(3x1) unit cell would consist of two K adatoms and 4 CO molecules. This is an extremely high coverage density for a monolayer structure. It is possible that the p(3x1) domains might consist of a 2-layer structure, thereby allowing this high coverage. Alternatively, partial adsorption of CO in the c(2x2) domains would reduce the CO:K ratio in the p(3x1) regions and make a single layer structure more feasible.

A model recently proposed for the p(3x1) domain has a CO:K ratio of 1:1 [43]. In this model the CO molecules induce the formation of domains with a p(3x1) structure, leading to a local increase in θ_K. The resultant depletion of K from the surrounding surface leads to the formation of c(2x2)-K domains. Excess CO dosing results in adsorption in the c(2x2)-K domains. Saturation with CO causes K redistribution and the loss of the p(3x1) spots [43]. It is clear that some CO adsorption in the c(2x2) domains can occur without severely disrupting the p(3x1) domains. Based on this model (1:1 ratio) and the assumption of a 60% coverage of the surface by domains of p(3x1), then 0.4 ML of CO would be accommodated within the p(3x1) domains on the overlayer studied in these experiments. The remaining ~0.4 ML determined by our XPS measurements would adsorb in domains of c(2x2) also with a CO:K ratio of 1:1.

	c(2x4)	c(2x2)	p(3x1)/c(2x2)
Δ C 1s (eV) (± 0.6 eV)	-0.35	-0.4	-0.65
Δ O 1s (eV) (± 0.6 eV)	-0.55	-0 55	-0.7

Table 2: Shifts in the C 1s and O 1s binding energies on the co-adsorption phases relative to the binding energies of CO on clean Co.

Although beamline 1.1 does not have a high resolution (±0.6 eV), small shifts in the CO core level binding energies were detected for the co-adsorption phases. These are summarised in table 2. There is a general shift of the carbon and oxygen core electrons to lower binding energy when CO is co-adsorbed with K. The magnitude of the shift increases with increasing θ_K. These results follow the general trend, seen on other AM/CO co-adsorption systems, of shifts in the C & O core levels to lower binding energies [30, 38].

3.2. NEXAFS results:

3.2.1. CO on Clean Cobalt:

Figure 6(a) shows a series of O K-edge NEXAFS spectra measured as a function of the photon incidence angle (Ψ) from a CO saturated Co $\{10\bar{1}0\}$ surface, with the E-vector parallel to the [0001] azimuth of the crystal surface. Also shown (figure 6(b)) is a plot of the variation of the π-resonance intensity (I_π) as a function of Ψ. I_π is the integrated area under the π-resonance peak on the normalised NEXAFS spectra after subtraction of a linear background.

The two characteristic NEXAFS resonances for an adsorbed CO molecule are obvious in figure 6(a). The π-resonance peak occurs at ~537 eV, just above the oxygen absorption threshold. The σ-resonance peak is much broader and is located >15 eV above the absorption threshold. The variation of the resonance peak intensities with Ψ (and hence with E-vector orientation) is clear. The fact that the π-resonance intensity is maximised at Ψ=90° (normal incidence) while the σ-resonance intensity increases as $\Psi \rightarrow 0°$ is a qualitative indication that the molecular orientation is upright or close to upright.

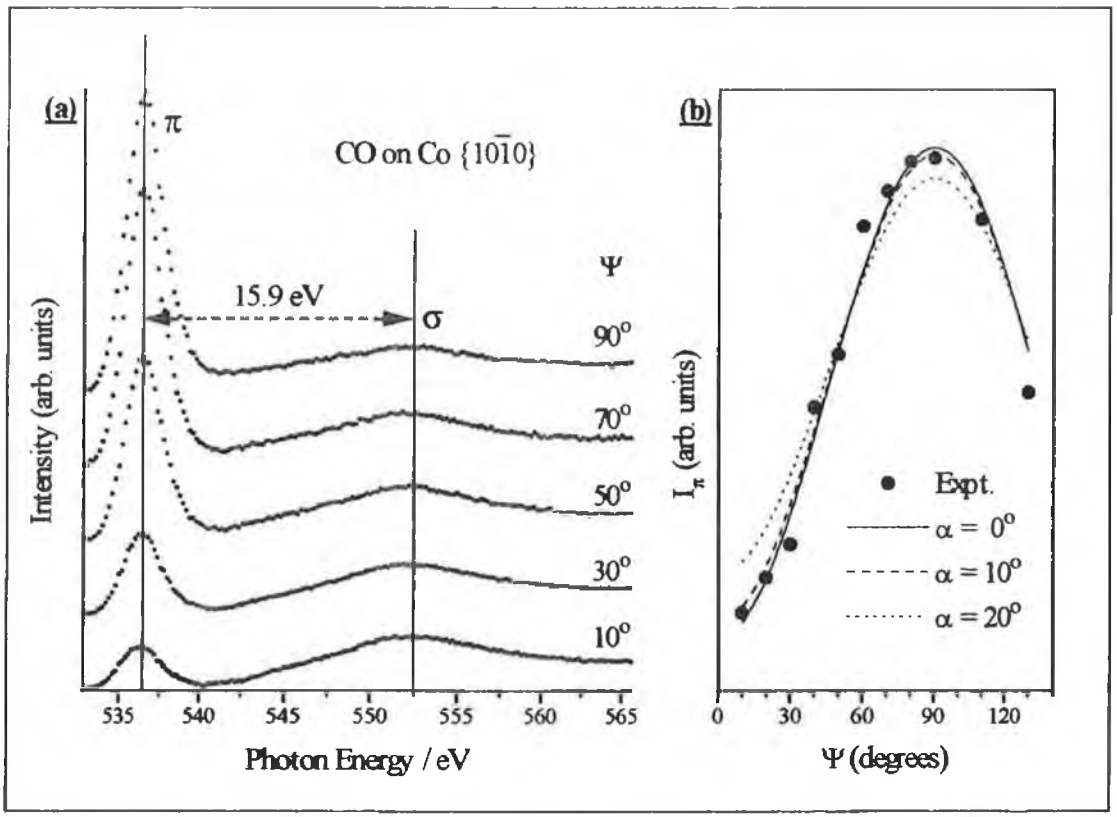

Figure 6: **(a)** O K-edge NEXAFS scans measured for CO on Co $\{10\bar{1}0\}$ as a function of Ψ along the [0001] azimuth.
(b) Experimental variation of I_π as a function of Ψ and the calculated variation for a range of tilt angles along the [0001] azimuth.

The variation of I_π with Ψ is shown as data points in figure 6(b). The line curves fitted to these points are the calculated intensity variations for molecular tilt angles of 0°, 10° and 20°. The normalisation constants, C_π and B were allows to vary freely during the calculations, while P was allowed to vary between 0.8-0.9, in order to obtain the best fit for each given value of α. The best agreement was obtained for α=0° although the tilt angle cannot be determined to an accuracy of better than ±10°.

The position of the σ-resonance on the CO saturated surface will be used as the reference for the determination of CO bondlength changes on the (K+CO) co-adsorption overlayers. The position of this peak maximum was measured relative to the π-resonance maximum for each overlayer system as a standard reference point for the measurement of σ-resonance position. For CO on Co $\{10\bar{1}0\}$ the π-σ separation is ~15.9 eV.

3.2.2. The c(2x4)-(K+CO) Phase:

Figure 7(a) shows a similar series of NEXAFS scans to those shown in figure 6(a), measured from the c(2x4)-(K+CO) phase. The O K-edge NEXAFS spectra measured from the c(2x2)-(K+CO) overlayer also show the characteristic π- and σ-resonances of the adsorbed CO molecule. However, a new feature (labelled χ) has emerged in the spectra at ~544 eV. This feature is evident on NEXAFS spectra measured for $\Psi>70^{\circ}$. At more grazing incidence angles it becomes masked by the emerging σ-resonance. There is no evidence of the χ-feature present on O K-edge NEXAFS scans taken from CO on Co or from K on Co. This feature is only apparent on co-adsorption overlayers and is located at ~7.8 eV above the π-resonance maximum.

Figure 7(b) shows the tilt analysis based on the variation of the π-resonance peak

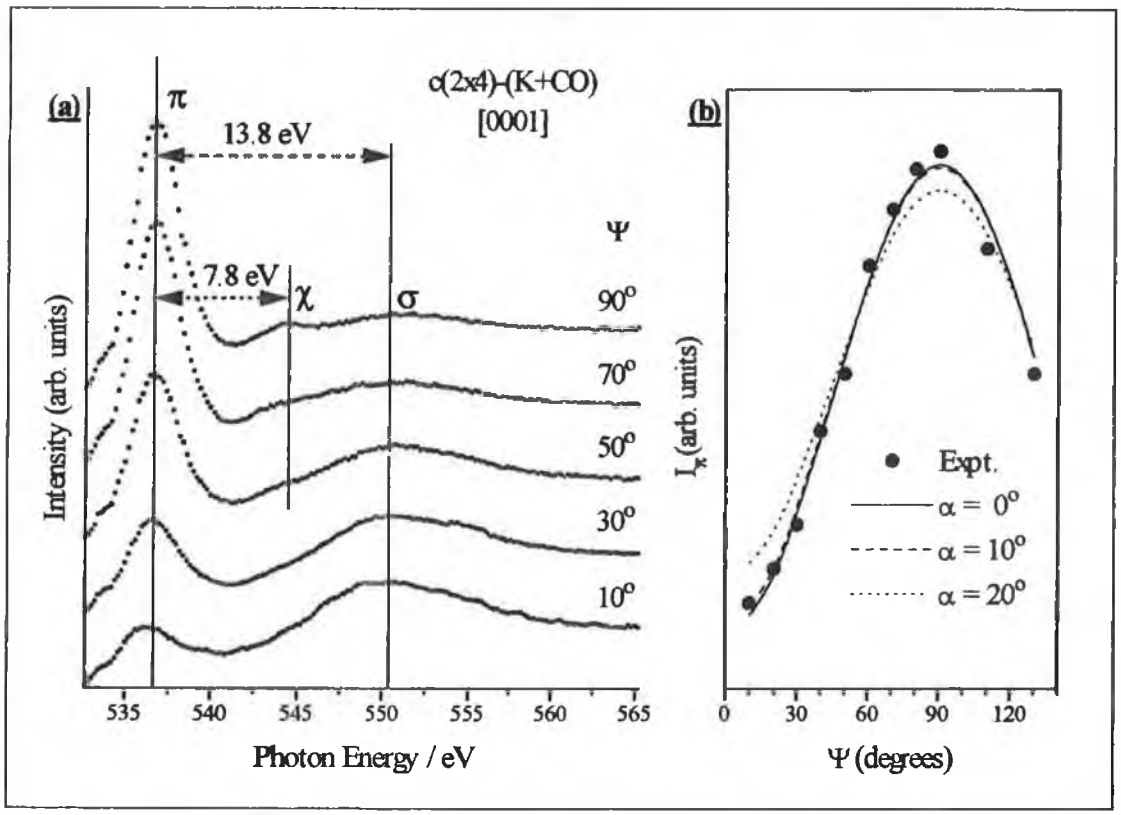

Figure 7: **(a)** O K-edge NEXAFS scans measured for the c(2x4)-(K+CO) overlayer on Co $\{10\bar{1}0\}$ as a function of Ψ along the [0001] azimuth. **(b)** Experimental variation of I_π as a function of Ψ and the calculated variation for a range of tilt angles along the [0001] azimuth.

intensity with Ψ. The expected variation of I_π with Ψ for a range of values of α was calculated as before. Again, the results favour an upright orientation of the molecule (±10°) along the [0001] azimuth. The σ-resonance peak maximum is ~13.8 eV above the π-resonance peak maximum, a shift of ~2.1 eV relative to CO on clean Co. Based on the empirical "bondlength with a ruler" method [50], this constitutes an increase in bond length of ~0.07 Å (±0.06 Å) compared with CO on Co. The large error is due to the broad nature of the σ-resonance on the spectra measured from both overlayers, which makes the position of the σ-resonance peak maximum difficult to precisely locate.

3.2.3. The c(2x2)-(K+CO) Phase:

Figure 8 shows a series of NEXAFS scans and the corresponding tilt analysis for a c(2x2)-(K+CO) overlayer along the [0001] azimuth. The χ-feature seen in figure 7 is

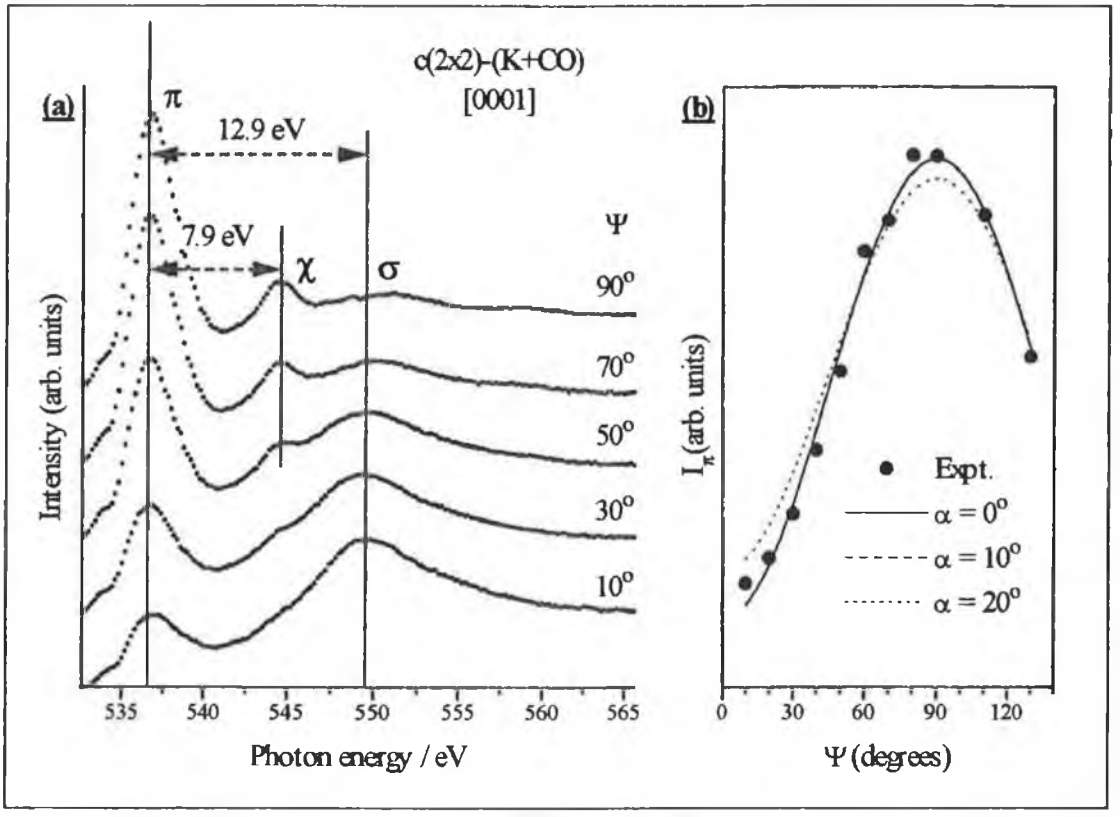

Figure 8: **(a)** O K-edge NEXAFS scans measured from a c(2x2)-(K+CO) overlayer on Co $\{10\bar{1}0\}$ as a function of Ψ, along the [0001] azimuth. **(b)** Experimental variation of I_π as a function of Ψ and the calculated variation for a range of tilt angles along the [0001] azimuth.

also present on the NEXAFS scans of the c(2x2)-(K+CO) overlayer. However, it is now clearly more prominent. Based on the XPS analysis, saturation θ_{CO} on the c(2x4) and c(2x2) overlayers are approximately equal, while θ_K is doubled. Thus, the increased intensity of the χ-feature appears to directly correlate with the increased θ_K. Although masked by to the emergence of the σ-resonance as $\Psi \rightarrow 0^\circ$, this feature seems to demonstrate 'π-like' symmetry (i.e. it is maximised when the E-vector of the incident light is perpendicular to the CO bond axis).

The molecular tilt analysis again favours an upright orientation ($\pm 10^\circ$). The calculated curve for a tilt of $\alpha=10^\circ$ cannot be seen in figure 8(b) as it is masked by the curve for $\alpha=0^\circ$. This is a consequence of the fact that C_π, B and P are allowed to vary independently during the fitting of the various curves. If these parameters were know exactly (i.e. fixed for all tilt angles) then the calculated curves would show greater differences. However, even for constant values of C_π, B and P, the NEXAFS analysis is not very sensitive to small tilt angles.

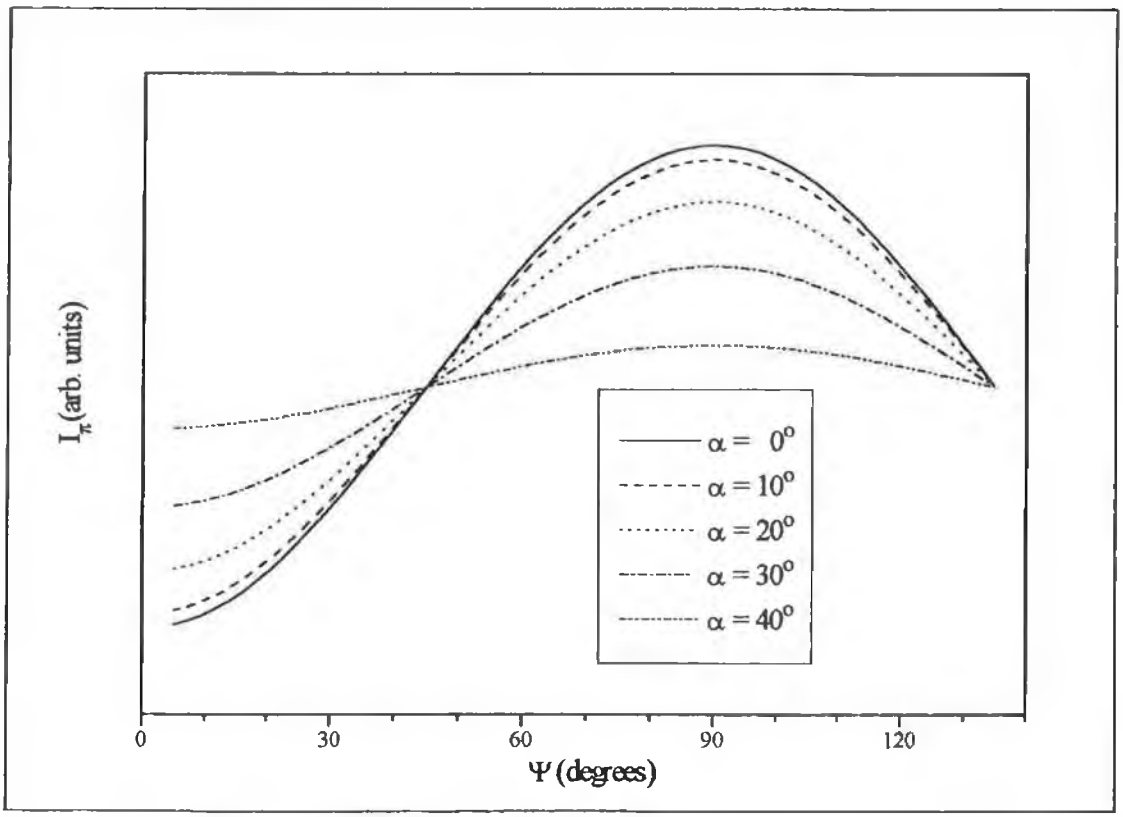

Figure 9: Calculated variation of I_π with Ψ for given values of α.

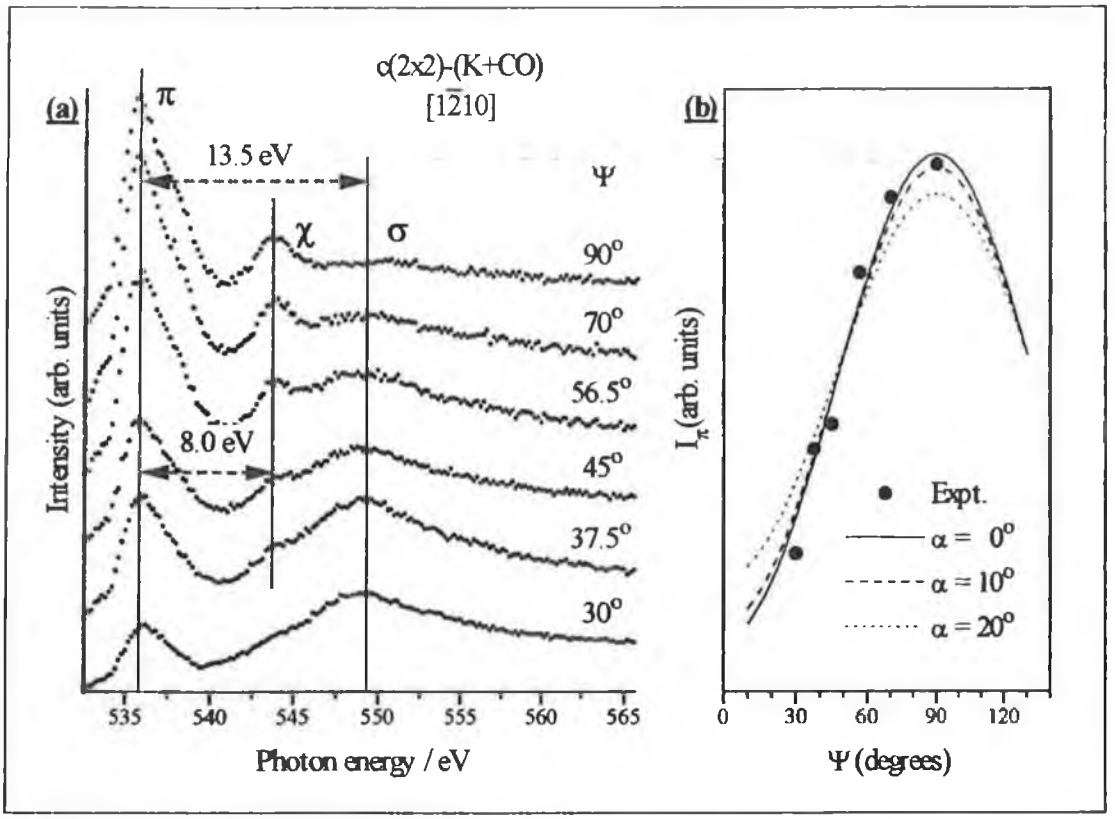

Figure 10: **(a)** O K-edge NEXAFS spectra measured from a c(2x2)-(K+CO) overlayer on Co $\{10\bar{1}0\}$ as a function of Ψ, along the [1$\bar{2}$10] azimuth. **(b)** Experimental variation of I_π as a function of Ψ and the calculated variation for a range of tilt angles along the [1$\bar{2}$10] azimuth.

Figure 9 shows the expected variation of I_π with the photon incidence angle for a series of α calculated at constant values of C_π, B and P. Clearly, the analysis is rather insensitive to differences in the tilt angles around α=0°. Hence, when the constants are allowed to vary in order to obtain a best fit of a given tilt angle to a set of data points the analysis becomes even less sensitive to these small tilt angles. It is evident from figure 9 that the NEXAFS analysis is much more reliable in determining tilt angles >20°. It should be noted that the tilt analysis is also relatively insensitive to the exact tilt value at large tilt angles (>70°).

As noted earlier, the equations used in the tilt analysis are based on the assumption that the CO molecules are only tilted off-normal along the azimuth of rotation (the [0001] azimuth). No account is taken of the possibility of a molecular tilt orthogonal

to this azimuth (i.e. along the $[1\bar{2}10]$ azimuth). The effect of such a tilt would be to reduce the overall I_π variation of the resonances as a function of Ψ along the [0001] azimuth. The greater the tilt along the orthogonal azimuth, the smaller the intensity variation as a function of Ψ observed along the [0001] azimuth. Such a reduction in the intensity variation would be perceived as a molecular tilt (albeit a smaller one) along the [0001] azimuth. If a tilted orientation had been obtained in the previous analyses it would have been uncertain whether it arose due to a tilting along the [0001] azimuth or along the $[1\bar{2}10]$ azimuth (or a mixture of both). However, the fact that an upright orientation was obtained is a strong indicator that the molecule has little tilt along any azimuth.

Figure 10 shows NEXAFS spectra and the corresponding tilt analysis for a c(2x2)-(K+CO) overlayer, measured with the E-vector orientated along the $[1\bar{2}10]$ azimuth. The tilt analysis confirms the qualitative conclusion, based on the upright orientation determined for the [0001] azimuth, that there is little or no tilt along this azimuth.

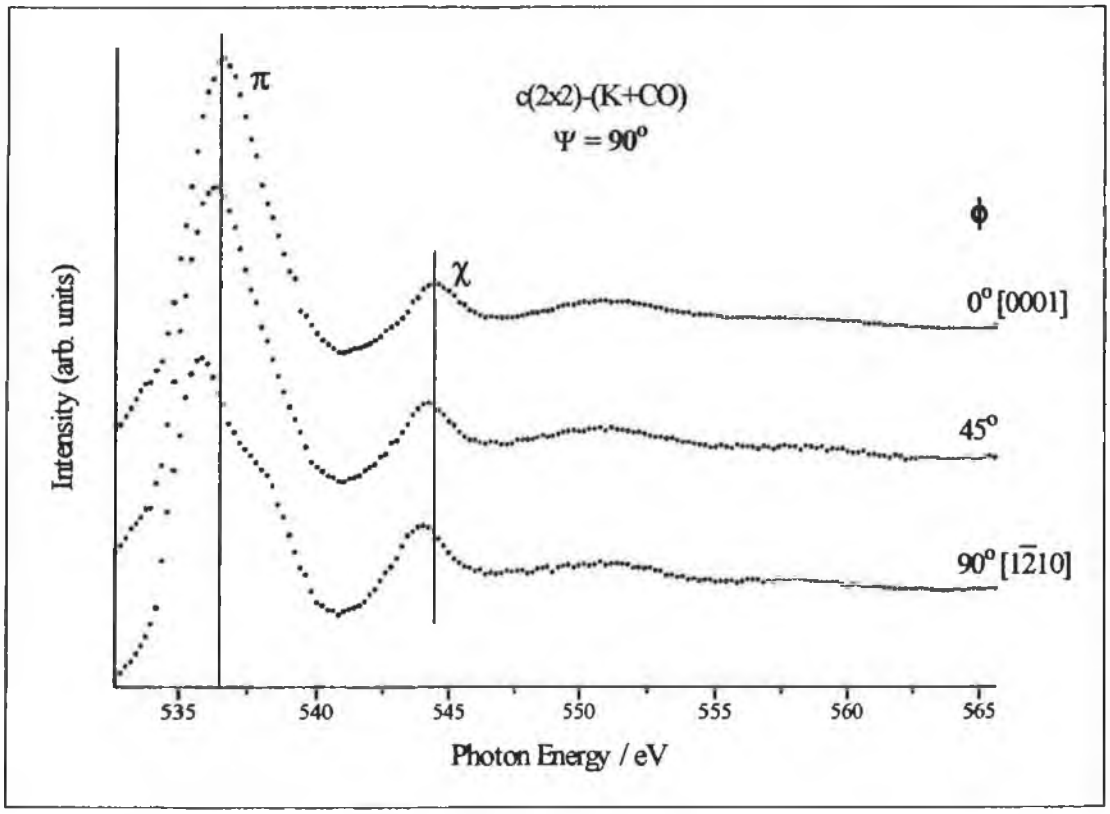

Figure 11: Normal incidence NEXAFS spectra measured as a function of azimuthal rotation.

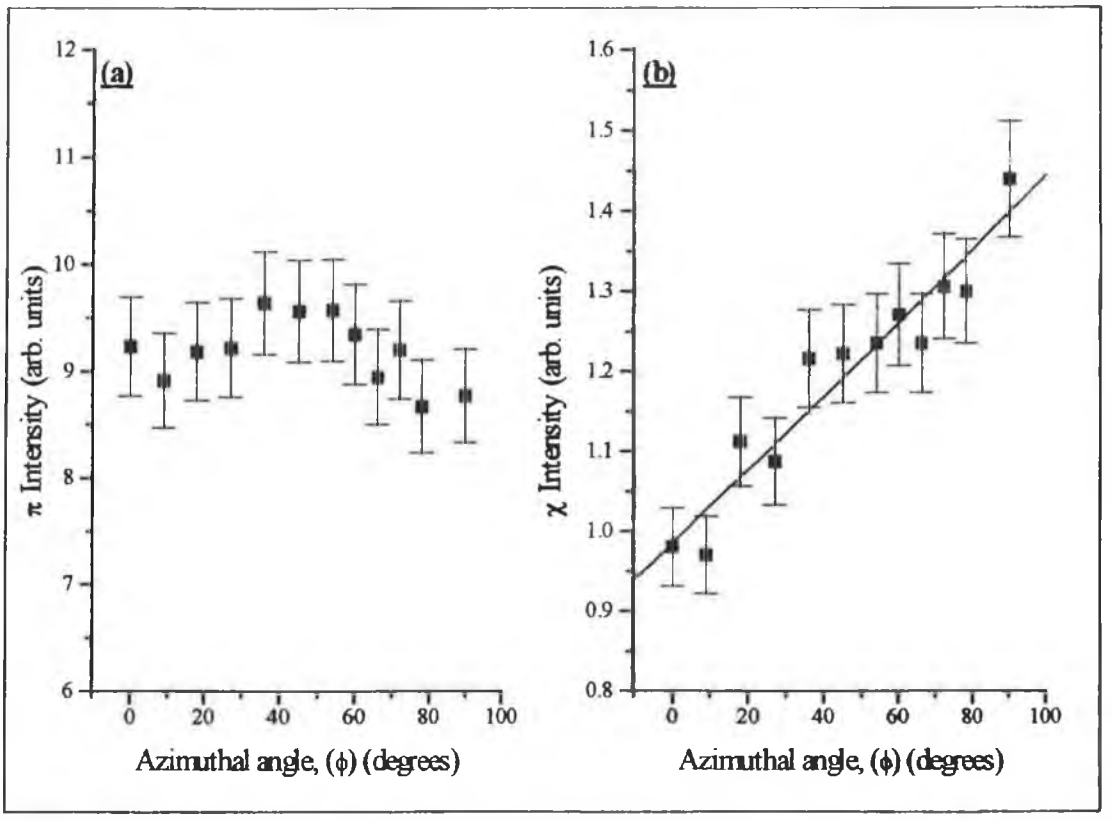

Figure 12: **(a)** Intensity variation of the π peak as a function of ϕ. The E-vector is oriented along the [0001] azimuth at ϕ=0°, and along the $[1\bar{2}10]$ azimuth at ϕ=90°.
(b) Intensity variation of the χ peak as a function of ϕ.

There is an increase in the π→σ separation along the $[1\bar{2}10]$ azimuth compared with the [0001] azimuth, while the π→χ separation is effectively unchanged. This results from a splitting of the π-resonance peak into two components. The low energy component is the most intense and so determines π-resonance maximum. The 2nd component appears as a shoulder on the high photon energy side of this peak.

The splitting of the π-resonance peak can be seen much more clearly by comparing normal incidence NEXAFS spectra measured as a function of azimuthal rotation (ϕ). Figure 11 shows such a comparison. In the spectra shown in figure 11 the azimuthal rotation of the crystal was varies between 0° and 90°. At ϕ=0° the E-vector of the incident light is orientated along the [0001] azimuth of the crystal surface, while at ϕ=90° it is orientated along the orthogonal azimuth. The splitting of the π-resonance peak gradually becomes more apparent as ϕ→90°. The maximum resonance intensity

shifts by ~0.7 eV to lower photon energy. There is a corresponding shift in the maximum of the χ-resonance to lower photon energy as a function of ϕ. This indicates that the π- and χ-resonances may be related

The integrated areas under the π and χ peaks were plotted as a function of ϕ and the data is shown in figure 12. The integrated areas were measured after subtraction of a linear background from the respective resonances on the normalised NEXAFS spectra. Error bars corresponding to ±5% of the intensity of each data point have been included on both plots to allow the scale of the intensity variation as a function of ϕ to be judged. It is evident from figure 12 that the π-resonance has only a weak intensity variation with ϕ. In contrast, there is a significant increase in the χ peak intensity when the E-vector is orientated along the $[1\bar{2}10]$ azimuth. The intensity of the χ feature peak at ϕ=90° is ~1.5 times that of the peak at ϕ=0°. The linear fit shown in figure 12(b) is intended as a guide for the eye. It cannot be determined with absolute certainty whether or not the intensity variation of χ with ϕ is purely linear.

3.2.4. The p(3x1)/c(2x2)-(K+CO) Phase:

Figure 13 shows the NEXAFS spectra and tilt analysis done for the p(3x1)/c(2x2) mixed phase overlayer. The χ-feature is even more prominent on this overlayer system in comparison to the previous (K+CO) systems, again indicating a direct relationship with θ_K. The π- to σ-resonance separation is now ~12.1 eV, corresponding to a bond length increase of ~0.13 Å. The maximum of the π-resonance peak appears to shift by ~1 eV to higher photon energy as $\Psi \rightarrow 0°$. This is due to the π-resonance peak consisting of two components, with the second component (at slightly higher photon energy) becoming more prominent at grazing incidence. This would indicate that the two components do not have the same angular intensity variations and hence that the symmetry (orientation) of the final states is different.

The second component may arise from an electron transition into the normally 'unexcited' CO $2\pi^*$ orbital. Because the CO molecule has two orthogonal $2\pi^*$ orbitals, one will always be orthogonal to the *major* E-vector of the incident light at any Ψ. The electron transition into this orbital is normally only excited by the *minor* E-vector of the incident light, which arises due to the imperfect polarisation (P≠1.0) of the photon beam. This component always remains parallel to the surface plane as a function of Ψ (i.e. its ability to excite the $1s \rightarrow 2\pi^*$ transition is unaffected by changes in the orientation of the *major* E-vector w.r.t. the surface normal). However, if the second component of the π-resonance peak seen in figure 13 were to arise purely from excitation by the *minor* E-vector of the incident light, then it should be apparent on the grazing incidence NEXAFS spectra measured from all overlayers, since the polarisation of the light is constant. The fact that this component is only apparent on the spectra of the p(3x1)/c(2x2) overlayer means that some factor must be making the

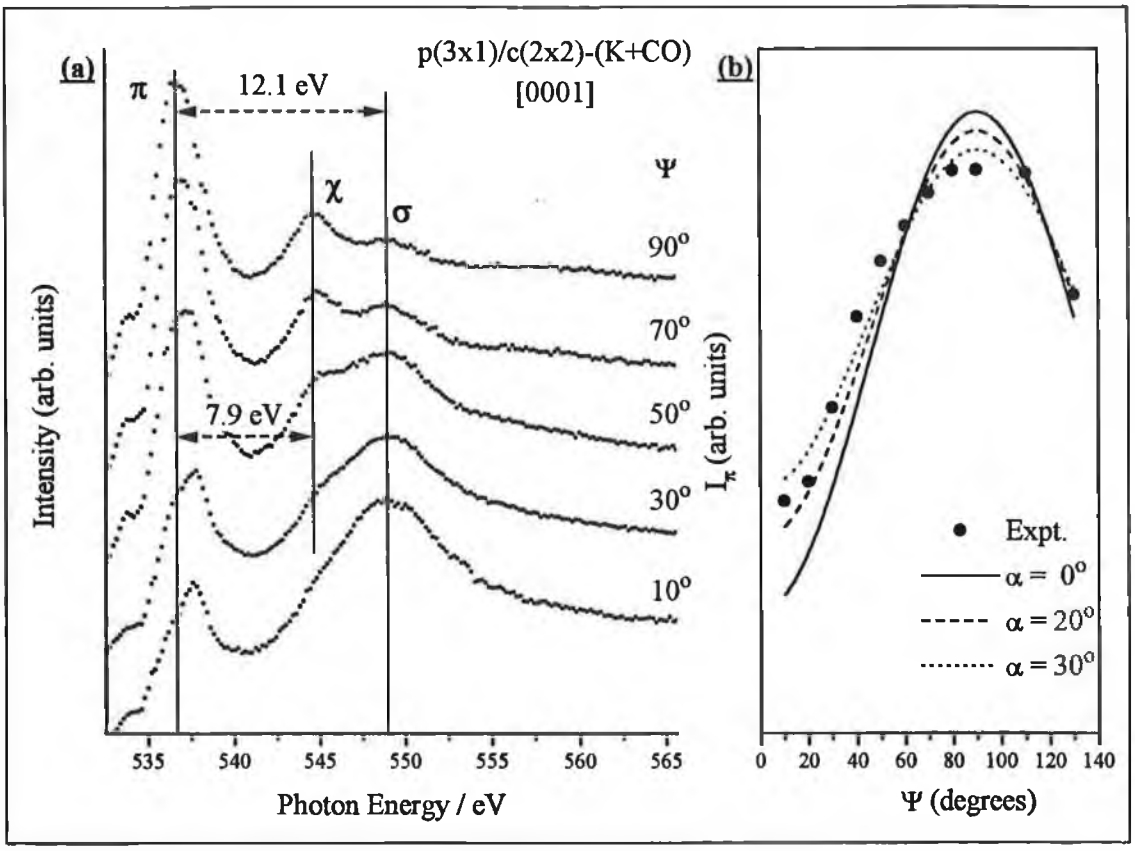

Figure 13: **(a)** O K-edge NEXAFS scans measured for the p(3x1)/c(2x2)-(K+CO) overlayer on Co $\{10\bar{1}0\}$ as a function of Ψ along the [0001] azimuth.
(b) Experimental variation of I_π as a function of Ψ and the calculated variation for a range of tilt angles along the [0001] azimuth.

'unexcited' transition more probable for grazing incidence measurements from this overlayer.

The transition into the second $2\pi^*$ orbital will also be excited by the *major* E-vector of the incident light *provided* the CO molecule has some degree of tilt along the $[1\bar{2}10]$ azimuth. In this case, the *major* E-vector component will not excite the transition at normal incidence ($\Psi=90°$). However, as $\Psi \rightarrow 0°$ it will be increasingly able to excite the transition (i.e. the intensity variation with Ψ of the two $2\pi^*$ orbitals will be opposite). The fact that the maximum of the π-resonance peak shifts may be due to a lifting of the $2\pi^*$ orbitals degeneracy as a result of the influence of the K adatoms and/or preferential tilting along a single azimuthal direction.

The tilt analysis shown in figure 13(b) indicates that the CO molecules on the p(3x1)/c(2x2) co-adsorption layer are indeed tilted. The data points fit best to a calculated tilt of ~25°±10° along the [0001] azimuth. However as discussed previously, the analysis neglects the possibility of any contribution due to a tilt along the orthogonal azimuth which would also contribute to the angular variation of I_π. Hence, the tilt may be partially (or wholly) along the $[1\bar{2}10]$ azimuth, thereby explaining the two-component nature of the π-resonance.

The tilted orientation determined on the p(3x1)/c(2x2) overlayer system must be treated with some caution as it may be a consequence of CO dissociation. This is due to the fact that the NEXAFS spectra shown in figure 13 were measured in the sequence $\Psi=10° \rightarrow 90°$ (i.e. from grazing incidence to normal incidence). If the CO on the p(3x1)/c(2x2) co-adsorption layer is subject to time dependent dissociation due to photon beam damage, then this may lead to a significant decrease in the amount of molecular CO on the overlayer during the time-scale of the measurements (several hours). The effect of such a loss of molecular CO would be a reduction in the I_π variation as the incident light direction is changed from $\Psi=10°$ to $\Psi=90°$, effectively giving the appearance of a greater molecular tilt than may actually exist. The presence at ~534 eV of an absorption feature as a pre-edge to the π-resonance shown in figure 13(a) is evidence of CO dissociation. This feature is also present on the other co-

adsorption systems and we attribute it to atomic oxygen resulting from CO dissociation. It can be seen that the intensity of this feature increases strongly on the p(3x1)/c(2x2) overlayer as $\Psi \rightarrow 90^{\circ}$. Such a strong increase is not evident on the other co-adsorption systems, and it indicates that progressive dissociation of the CO on the time-scale of the measurements may be a significant factor in the spectra measured from the p(3x1)/c(2x2) overlayer.

In order to ensure that the increase observed for the ~534 eV feature was not merely due to Ψ-dependent variation in intensity of the pre-edge, normal incidence NEXAFS spectra were measured from the p(3x1)/c(2x2) overlayer at different times after its formation. Figure 14 shows the series of NEXAFS scans collected. The spectra were measured immediately after formation of the co-adsorption overlayer, and again after it had been exposed to the photon beam for 6 & 10 hours. Clearly there is only a small

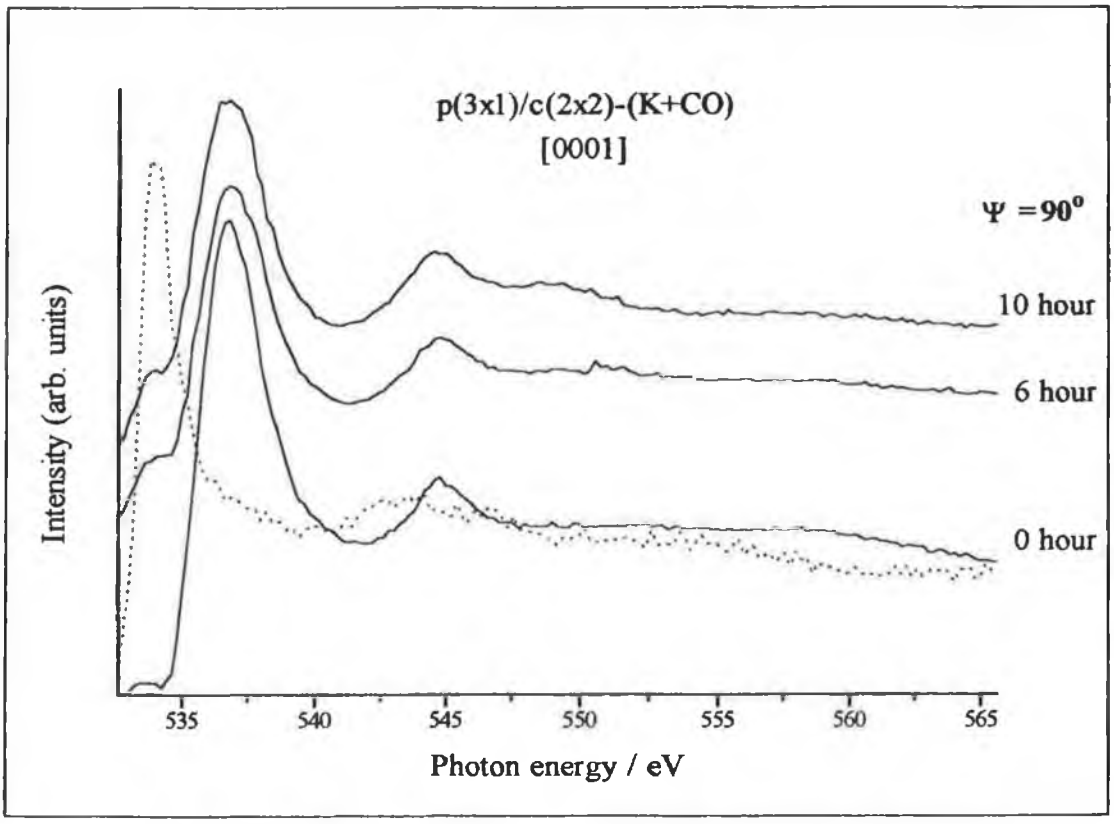

Figure 14: O K-edge NEXAFS scans measured, from a p(3x1)/c(2x2)-(K+CO) overlayer on Co $\{10\bar{1}0\}$ at Ψ=90°, after exposure to the photon beam for various time periods. The dotted curve is an O K-edge NEXAFS spectrum measured from atomic oxygen on the clean surface.

feature present at 534 eV on the freshly prepared overlayer. However, after 6 hours exposure it has emerged strongly, accompanied by a decrease in the intensity of the π-resonance peak to ~80% of its original value. After a further 4 hours exposure there is a further slight increase in the feature at ~534 eV although the π-resonance peak intensity is effectively unchanged. Clearly, the increase in the pre-edge feature as $\Psi \rightarrow 90^{\circ}$ seen in figure 13(a) is not solely an angular effect, although this may account for some of the increase observed. The angular measurements in figure 13 were taken over the same 10 hour period in which the three normal incidence spectra were collected. Hence, this dissociation of CO will influence the measured I_{π}.

The dotted curve shown in figure 14 is an O K-edge NEXAFS spectrum measured from atomic oxygen on the clean Co surface produced by exposure to O_2 to form a p(2x1) overlayer. It can be seen that the position of the sharp atomic oxygen absorption feature corresponds well with the pre-edge at ~534 eV on the co-adsorption spectra, in agreement with the assignment of this feature to atomic oxygen. Clearly, given the similarity of the normal incidence NEXAFS scans measured after 6 and 10 hours, the dissociation of CO on the p(3x1)/c(2x2) overlayer does not have a constant rate. The bulk of the dissociation appears to occur within the first few hours after formation of the adlayer. Constant geometry ($\Psi=90^{\circ}$) NEXAFS spectra measured from the other co-adsorption overlayers showed no significant increase in the atomic oxygen feature and no decrease in the π-resonance with time.

In the case of the p(3x1)/c(2x2) overlayer, the height of the pre-edge after 10 hours beam exposure is ~15% of the height of the absorbance resonance due to atomic oxygen. The absolute θ_O on the clean surface is uncertain, but it may be as high as 1 ML [60]. On this basis, the pre-edge observed after 10 hours should correspond to, at most, ~0.15 ML of atomic oxygen. This is in-keeping with the estimated 20% reduction in the intensity of the normal incidence π-resonance.

Clearly, in order to properly quantify the molecular tilt on the p(3x1)/c(2x2) overlayer, the effect of CO dissociation must be minimised. Comparing the ratio of the π-resonance intensities at $\Psi=30^{\circ}$ and $\Psi=90^{\circ}$ for a freshly prepared p(3x1)/c(2x2)

overlayer with those of the c(2x4) and c(2x2) overlayers should give an indication of the reliability of the tilt analysis. These two NEXAFS scans were obtained from a freshly prepared p(3x1)/c(2x2) overlayer (i.e. before substantial dissociation could occur). The ratios (I_{30}/I_{90}) determined were 0.31, 0.33 and 0.39 for the c(2x4), c(2x2) and p(3x1)/c(2x2) overlayers respectively. This result supports the conclusion that CO adopts a tilted configuration in the p(3x1)/c(2x2) overlayer. The c(2x4) and c(2x2) overlayers compare well and indicate that the degree of polarisation is close to 0.9 (for an upright molecule I_{30}/I_{90}=0.325 at P=0.9). The tilt angle of CO on the p(3x1)/c(2x2) adlayer, based solely on values of I_{30}/I_{90}=0.39 and P=0.9, would be ~17°.

A totally unambiguous determination of the molecular tilt angle requires a negligible rate of CO dissociation on the time-scale of the measurements. This may not be possible if the dissociation is an intrinsic property of the overlayer due to alkali induced weakening of the molecular bond. One alternative is to measure the NEXAFS spectra in the opposite sequence (i.e. Ψ=90° first and subsequent scans in order of descending Ψ). Although not ideal, this would reverse the effect, making a tilted molecule appear more upright. Hence, a tilted orientation obtained under these circumstances would be more conclusive. Despite the uncertainty due to CO dissociation, it appears probable that there is a tilted CO species on the p(3x1)/c(2x2) overlayer.

Unfortunately, additional NEXAFS spectra, varying Ψ along the $[1\bar{2}10]$ azimuth, were not measured from the p(3x1)/c(2x2) overlayer. This would have allowed determination of the directionality (i.e. azimuthal preference) of the CO tilt. In addition, the assignment of the second (high photon energy) component of the π-resonance to the normally forbidden $1s \rightarrow 2\pi^*$ transition might be confirmed by such measurements. If this assignment is correct, then the appearance of this component at grazing incidence is proof that the CO in the p(3x1)/c(2x2) overlayer has some component of tilt along the $[1\bar{2}10]$ azimuth.

3.2.5. θ_K Effects:

The effect of dosing additional K onto a c(2x2)-(K+CO) overlayer was studied. Potassium was dosed onto the overlayer layer for a period equal to that required to produce the initial c(2x2) pattern (i.e. an additional 0.5 ML of K was dosed). After dosing θ_K was ~0.8±0.05 ML, based on the integrated peak areas, while θ_{CO} was unchanged. After dosing the K $2p_{1/2}$ and $2p_{3/2}$ core levels were no longer clearly resolved as had been the case for the original c(2x2)-(K–CO) overlayer. Emission from the K $2p_{1/2}$ level now appeared as a shoulder on the high binding energy side of the photo-emission peak. This is indicative of the excess K adatoms being adsorbed in a different chemical environment from those in the original c(2x2) adlayer. The fact that θ_K is lower than would be expected on the basis of simple dose-time considerations may be due to a limited residence time/lower sticking probability of the K atoms on the c(2x2) overlayer. However, some intensity may be lost as a result of attenuation of the signal from the potassium in the c(2x2)-(K+CO) monolayer by

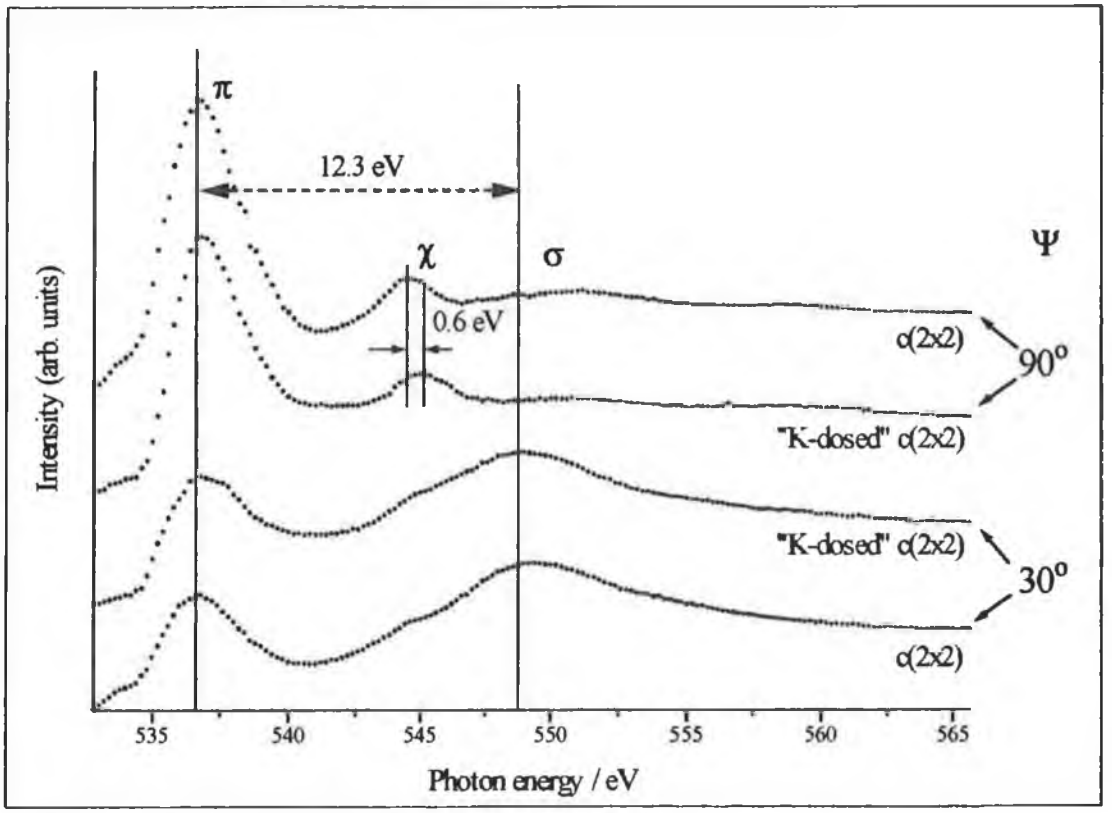

Figure 15: O K-edge NEXAFS scans measured for the c(2x2)-(K+CO) overlayer on Co $\{10\bar{1}0\}$ and for a 'K-dosed' c(2x2)-(K+CO) overlayer at Ψ=90° and 30° along the [0001] azimuth.

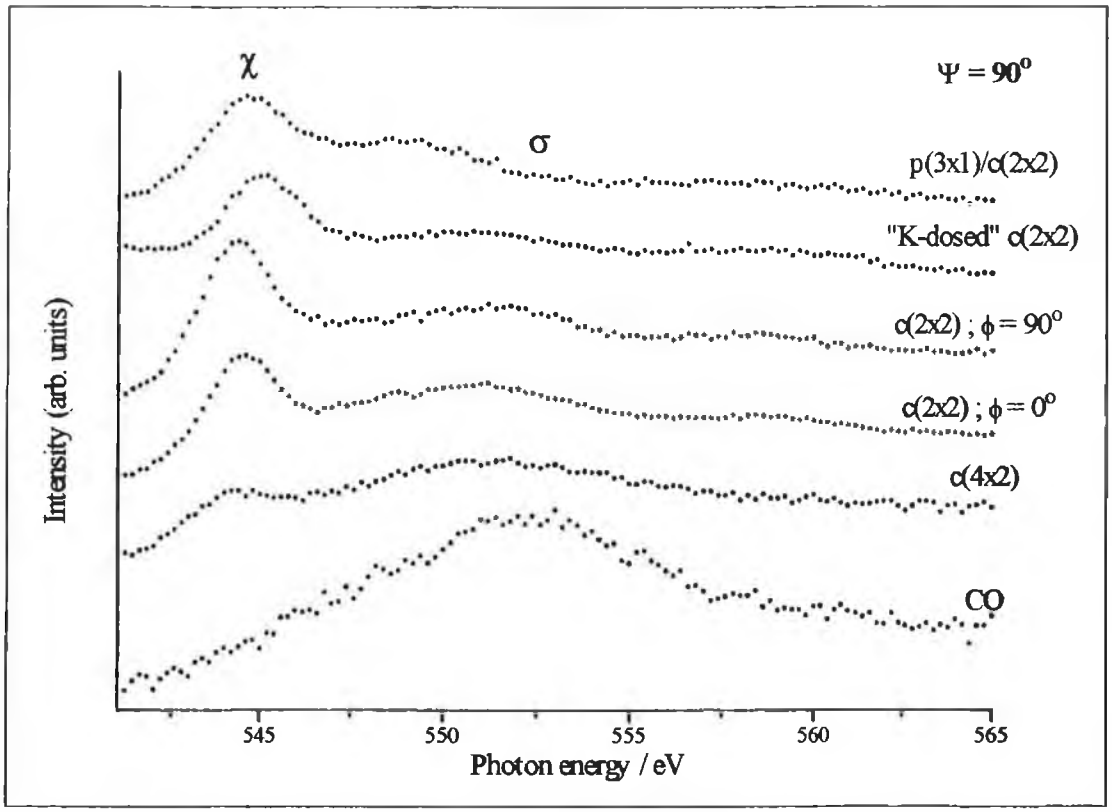

Figure 16: σ-resonance region of normal incidence O K-edge NEXAFS spectra measured from CO on Co $\{10\bar{1}0\}$ and from various (K+CO) co-adsorption systems.

overlying potassium.

Figure 15 shows the NEXAFS spectra, measured at normal (Ψ=90°) and grazing (Ψ=30°) incidence, before and after the additional K dosing. The NEXAFS spectra do not undergo extreme changes as a result of the dosing. The position of the σ-resonance shifts by ~0.6 eV to lower photon energy, corresponding to a CO bondlength increase of 0.12±0.06 Å. There is also a shift of the χ-feature to higher photon energy. This shift can be attributed mainly to changes in the background shape at normal incidence and to a loss of residual σ-resonance intensity (due to quenching of molecular vibrations) as a result of K dosing. Such quenching can be regarded as merely a steric hindrance effect caused by the additional K adatoms.

Figure 16 shows the σ-resonance region of the normal incidence O K-edge NEXAFS spectra from the different overlayers shown in the previous figures. All spectra are

measured with the E-vector oriented along the [0001] azimuth (ϕ=0°), with the exception of one of the c(2x2)-(K+CO) overlayer scans, when it is oriented along the $[1\bar{2}10]$ azimuth (ϕ=90°). The spectra have been normalised to a constant step edge high as described earlier. With the possible exception of the p(3x1)/c(2x2) overlayer, the residual σ-resonance intensity at normal incidence should arise solely from vibrations of the CO molecule about an upright orientation.

It can be seen from figure 16 that co-adsorption with K results in a significant drop in the σ-resonance intensity. We attribute this to hindrance of the molecular vibrations by the K adatoms. The magnitude of this drop increases with θ_K. It should be noted that the normalisation of the spectra is not ideal since effects due to coverage changes between the different overlayers cannot be properly accounted for. However, there does appear to be a reduction in the σ-resonance at normal incidence when K is co-adsorbed, which is consistent with a 'freezing'/hindrance of the CO molecule.

3.3. XPD Results:

3.3.1. Clean Cobalt Surface:

Figure 17 illustrates the crystal structure of the Co $\{10\bar{1}0\}$ surface. It has an open '{110}-fcc-like' atomic arrangement. However, the layer stacking is significantly different, consisting of alternating long (1.46 Å) and short (0.73 Å) inter-layer spacings. The short spacing occurs when the atoms of adjacent layers occupy FFH sites with respect to each other, while the long spacing occurs when the atoms of adjacent layers occupy long-bridge sites. The alternating inter-layer spacing gives rise to the possibility of two surface terminations as shown in figure 17. Experimentally, the Co $\{10\bar{1}0\}$ surface has been found to terminate exclusively with a short inter-layer separation by LEED-I(V) analysis [61, 62].

The cross-sectional cuts shown in figure 17 illustrate the angles at which XPD forward focusing peaks would be expected to occur for polar scans along the high symmetry $[1\bar{2}10]$ and [0001] surface azimuths. Along the $[1\bar{2}10]$ azimuth, forward

focusing only occurs between atoms in the 1st and 3rd layers (also, 2nd and 4th, etc.) not between atoms in adjacent layers. The out-of-plane atoms have a different stacking position for the long and short termination, but these will only have a minor effect on the overall XPD pattern (especially at high outgoing kinetic energy) due to the concentration of scattering intensity in the forward focusing peak of half-width ~20° (see chapter 2). In the case of the [0001] azimuth, forward focusing can occur between the atoms of adjacent layers. Hence, this azimuth has greater potential for determination of the crystal termination than the orthogonal azimuth. Figure 17 shows the origin of the two main off-normal forward focusing peaks along the [0001] azimuth. The peak at ~35° should be stronger, relative to the peak at ~54°, for a short termination than for a long termination. In theory this would allow determination of the crystal termination from polar XPD scans along this azimuth, although signal from the crystal bulk would make unambiguous determination difficult.

Figure 18 shows SSCC's done for Co $2p_{3/2}$ emission from a bulk Co crystal at KE=120 & 250 eV. The calculations are done for azimuthal scans along both the $[1\bar{2}10]$ and the [0001] azimuths using the SSCC program of Dr. Peijun Hu [63]. The initial state of the outgoing electron (p) and the transition into two outgoing waves (s and d) were accounted for in the calculations [64]. The first point to note is the general similarity between the 'short' and 'long' calculations at a given kinetic energy and azimuthal scan direction. In particular, at KE=250 eV the two terminations are virtually identical and the level of similarity between them increases with increasing KE. At 120 eV there are differences between the terminations. The most obvious changes occur between θ=20°-40°. For the SSCC's along the $[1\bar{2}10]$ azimuth the short termination calculation has a single peak in this region whereas the long termination calculation has a clear doublet. For the [0001] azimuth the situation is reversed, with two peaks occurring for the short termination and one peak for the long termination.

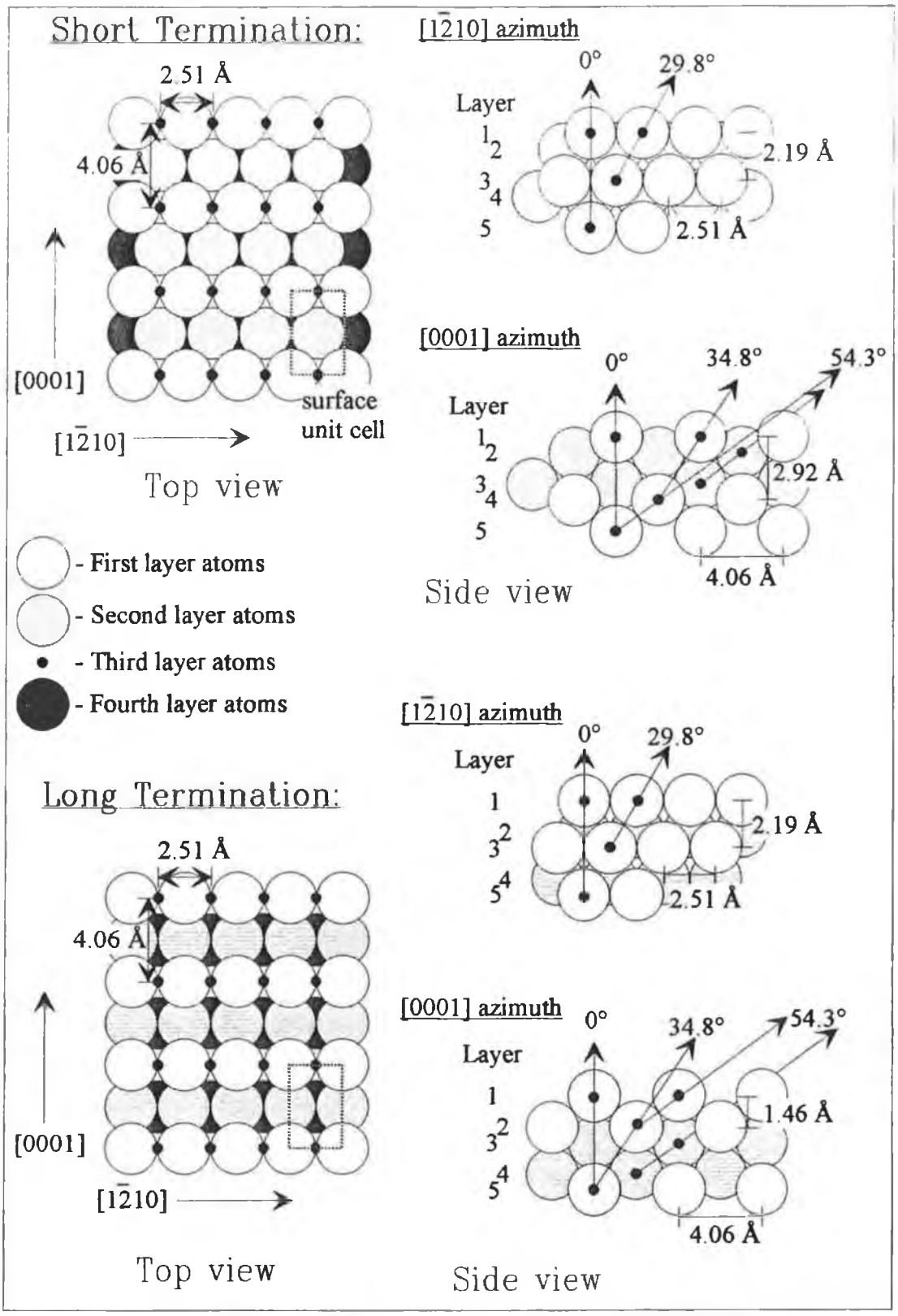

Figure 17: Structure of Co $\{10\bar{1}0\}$ illustrating a short (top) and long (bottom) bulk lattice structure termination. The forward scattering angles are calculated purely on the geometric arrangement of the atoms with no account being taken of refraction at the surface.

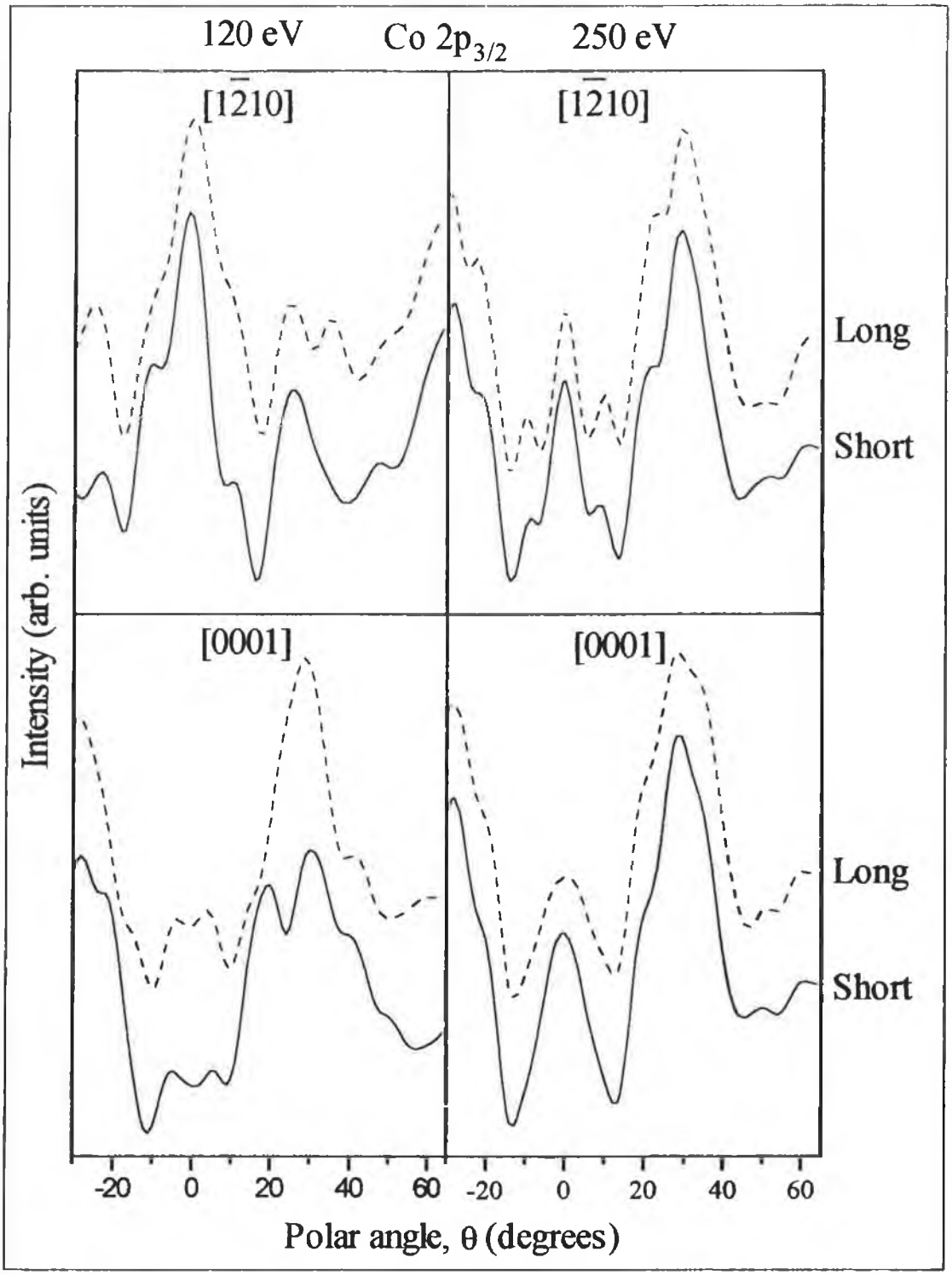

Figure 18: SSCC's for a 'short' and 'long' terminated Co bulk cluster along the two high symmetry surface azimuths at outgoing kinetic energies of 120 &250 eV.

Use of double scattering calculations yielded no significant change in the calculated diffraction pattern even at the lowest KE (120 eV) used. This is illustrated in figure 19 where single- and double-SCC's (scattering cluster calculations) are shown for polar

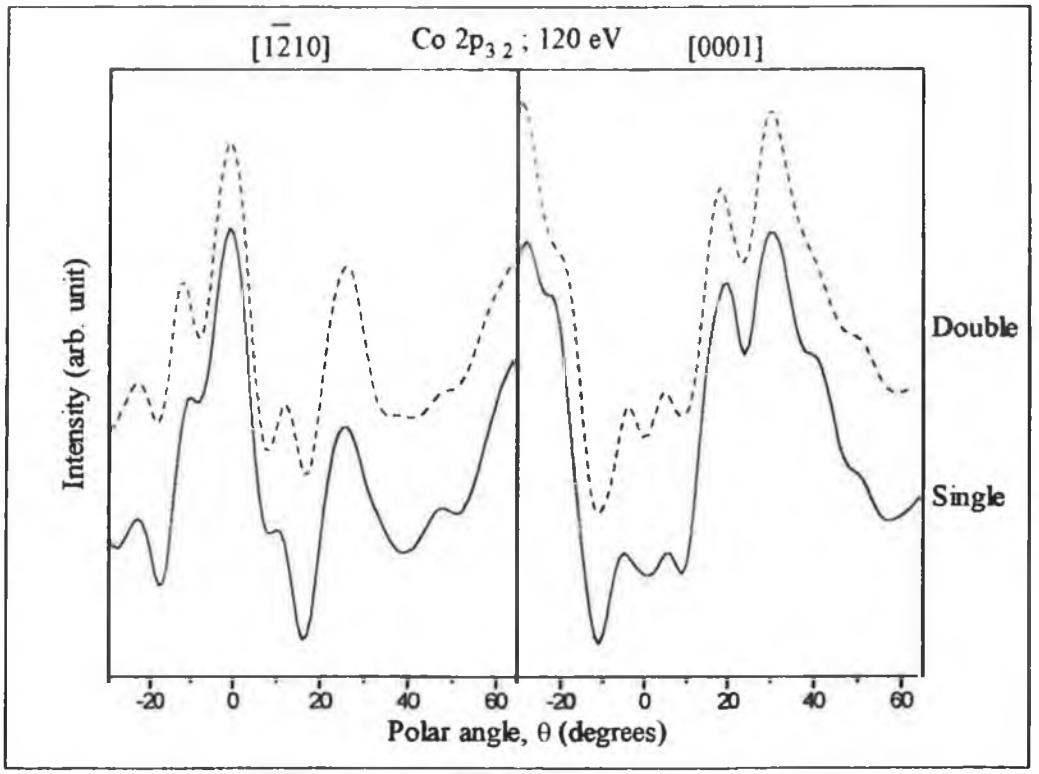

Figure 19: Single- versus double-SCC's for a short-terminated bulk Co $\{10\bar{1}0\}$ cluster along the two high symmetry surface azimuths.

XPD scans along the two high symmetry surface azimuths of Co $\{10\bar{1}0\}$. The electron kinetic energy was 120 eV and the cluster had a short, bulk termination. There are some changes in the curve features between single- and double-scattering. The most noticeable changes are around $\theta=0^{\circ}$ on the SCC's along the $[1\bar{2}10]$ azimuth. However, there are no major changes in the calculated curves when double scattering is used. Consequently, SSCC's should be adequate even for modelling low energy XPD processes.

Figure 20 shows a series of experimental polar XPD scans measured from a clean Co $\{10\bar{1}0\}$ single crystal surface along the $[1\bar{2}10]$ azimuth at a number of different photo-emission energies. Emission from the Co 2p core levels was monitored at outgoing KE's of 120, 170 & 250 eV, from the 3p core levels at 640 eV and from the Cu LMM Auger process at 770 eV. The dashed curves shown in figure 20 are SSCC's corresponding to the experimental curves. The Co cluster was bulk terminated, with a short inter-layer spacing outermost. In the case of the low kinetic energy SSCC's

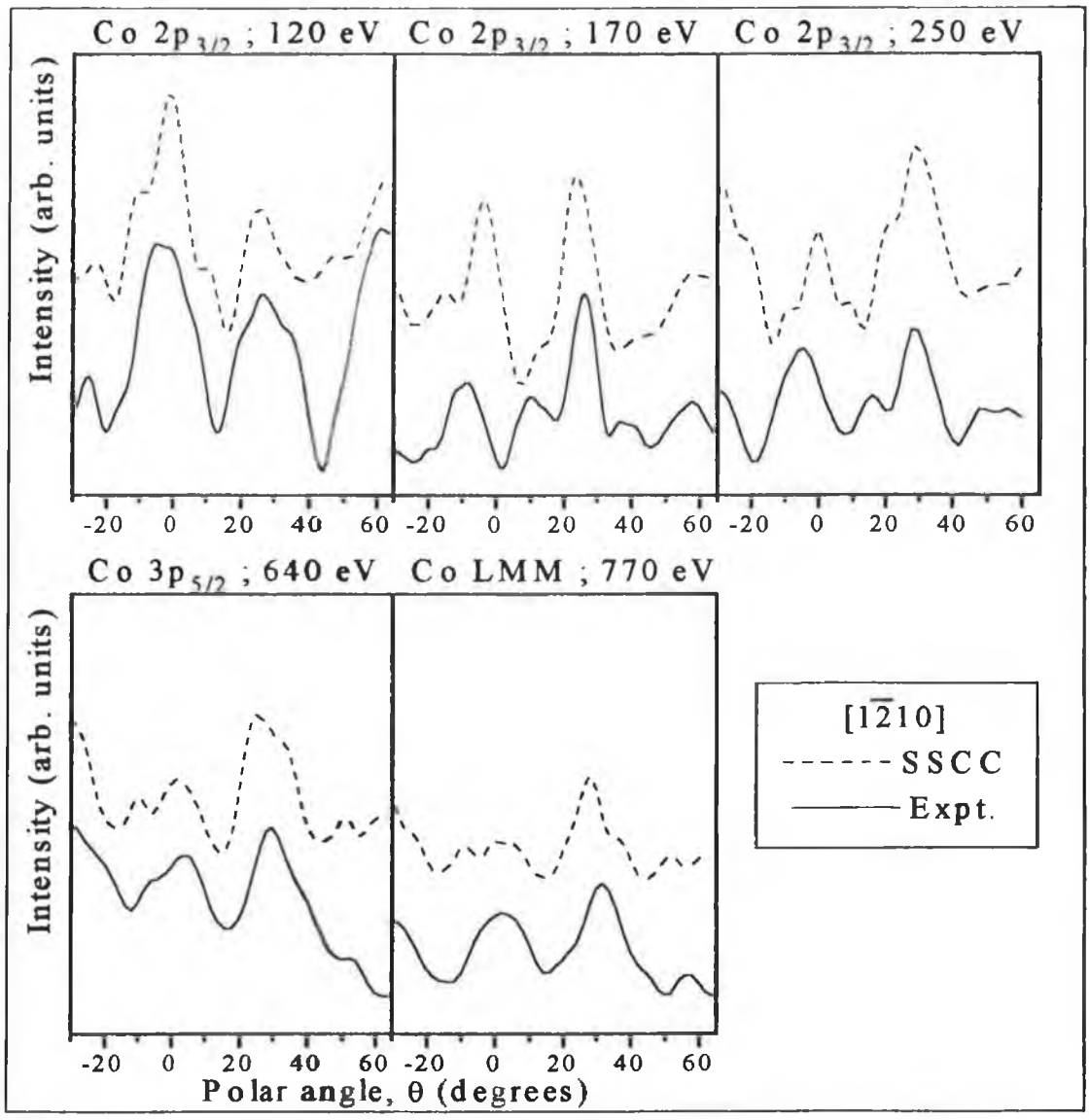

Figure 20: Polar XPD curves measured along the [1$\bar{2}$10] azimuth of a clean Co {10$\bar{1}$0} single crystal for a series of emission energies.

(120, 170 and 250 eV) the initial state of the outgoing electron (p) and the transition into two outgoing waves (s and d) were accounted for in the calculations [64]. For the high photo-emission energy (640 eV) and the Auger emission the outgoing electron wave was treated as an s-wave. It can be seen from figure 20 that there is good agreement between theory and experiment. This indicates that SSCC's are satisfactory for modelling low KE XPD processes, at least for emission from bulk crystal structures.

There is a single peak in the θ=20°-40° region of the polar XPD scan at KE=120 eV. This is in-keeping with a short termination as shown by the SSCC's in figure 18.

However, one scan is not sufficient to irrefutably confirm the crystal termination. Polar XPD scans measured along the [0001] would have provided an independent determination of the crystal structure. The results indicate that low energy polar XPD scans should be capable of determining the bulk crystal termination provided that SSCC's are performed prior to obtaining the experimental data in order to isolate the azimuths most sensitive to the change in surface termination.

3.3.2. The c(2x2)-(K+CO) Phase:

The NEXAFS results have already confirmed the essentially upright nature of the CO molecule on the c(2x2) overlayer. Polar XPD scans coupled with SSCC's can be used to independently confirm the other main structural parameters of the model proposed for the c(2x2) overlayer on the basis of the LEED-I(V) study [42], which are summarised in the introduction. This study also serves to examine the potential of polar XPD at low outgoing kinetic energies for the study of co-adsorption systems.

The cross-section model shown in figure 21 is for the c(2x2)-(K+CO) overlayer with a CO:K ratio of 2:1 as determined by the XPS results shown previously. All experimental polar XPD scans were measured along the $[1\bar{2}10]$ azimuth. Along this scan direction the emission from all CO molecules appears identical to the electron energy analyser. If polar XPD measurements were take along the [0001] azimuth,

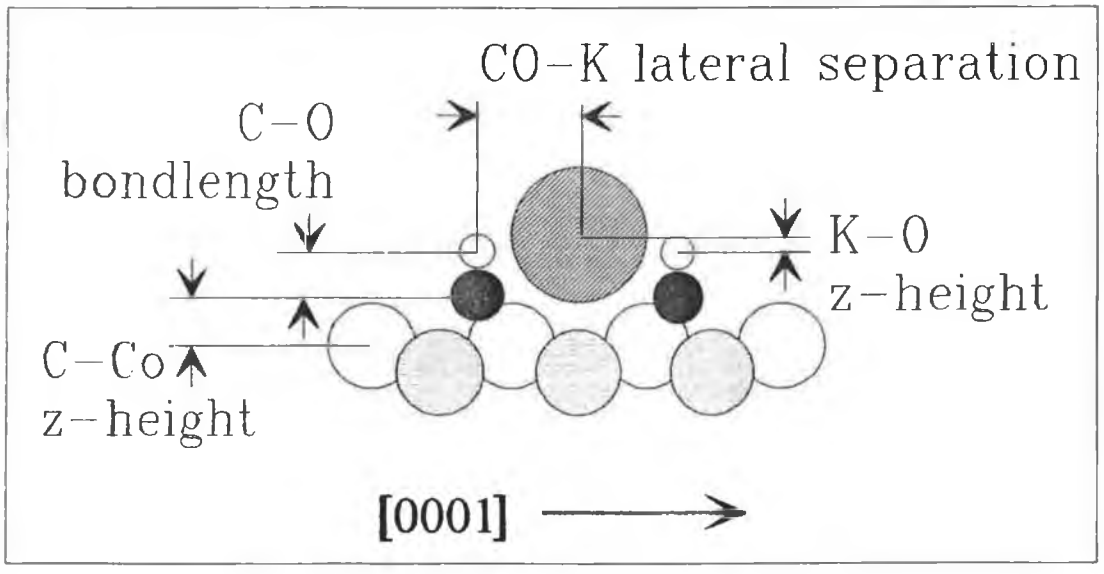

Figure 21: Structural parameters varied during the initial SSCC's.

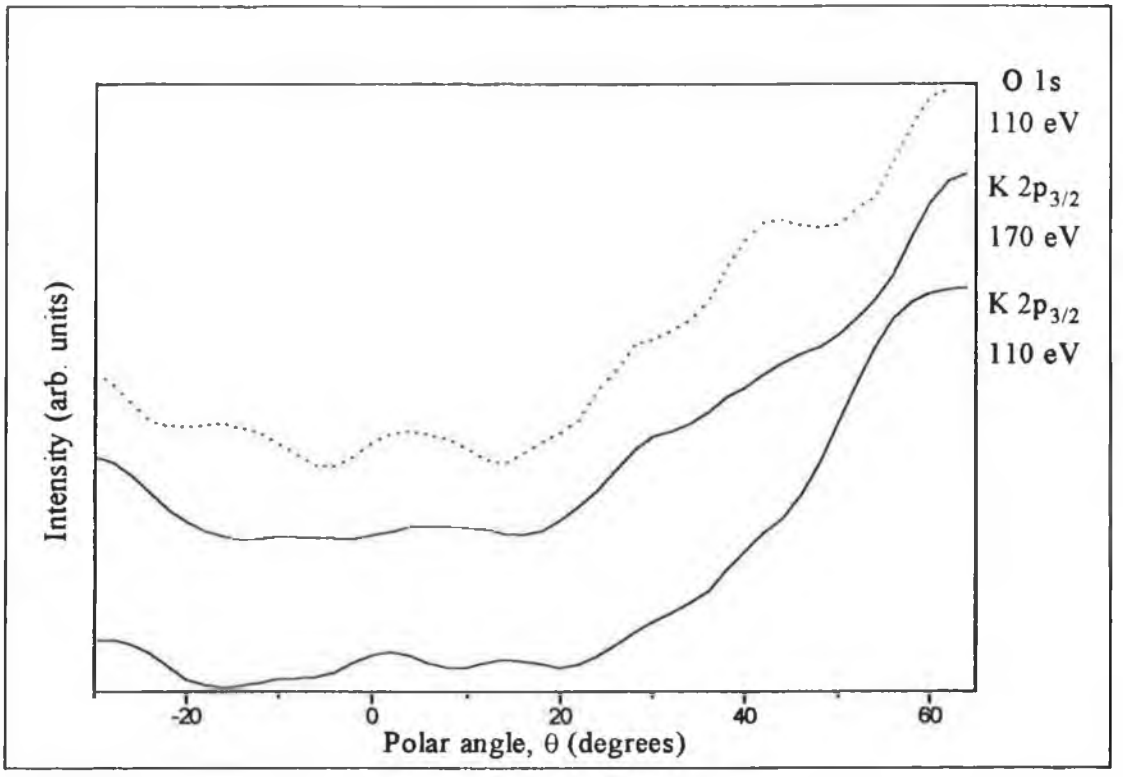

Figure 22: Polar XPD curves measured from the c(2x2)-(K+CO) overlayer along the [$1\bar{2}10$] azimuth using K 2p emission at 110 & 170 eV. Also shown is a polar XPD curve measured from CO on the clean Co surface along the same azimuth using O 1s emission at 110 eV.

then the analyser would 'see' 2 types of CO depending on the adsorption site relative to the K adatoms (i.e. the 2 CO molecules in figure 21). This would also be the case for a CO:K ratio of 1:1 as the overlayer structure would consist of two domains. A surface model of the c(2x2)-(K+CO) overlayer structure used in the SSCC's can be seen in the discussion section (figure 27).

Polar XPD scans were measured using K 2p emission at 110 & and 170 eV. These are shown in figure 22. Also shown in this figure is a polar XPD curves measured using O 1s emission at 110 eV from CO on clean Co. Clearly the shape of all three curves is similar. They are all relatively featureless, with an exponential rise in intensity as the polar angle becomes more grazing. In the case of the O 1s emission, the CO molecule is upright on the surface and the oxygen is proud of all other atoms. The fact that the K atoms yield a similar curve to the O is direct evidence that the K adatoms in the c(2x2) overlayer are also proud of the surface. Any structural models of the c(2x2)-(K+CO) adlayer involving substitution of K into the Co substrate can be immediately

ruled out on the basis of figure 22. If substitution did occur, then strong diffraction features would be seen on the K XPD scans at these low energies.

Figure 23 shows a polar XPD curve measured from the c(2x2)-(K+CO) overlayer using C 1s emission. The kinetic energy used was ~410 eV. Also shown on this figure is a polar XPD curves measured using K $2p_{3/2}$ emission at ~400 eV. These curves were measured simultaneously, since the C 1s and K $2p_{3/2}$ core level peaks are separated by only ~10 eV. The first point to note is the strong forward focusing peak at $\theta=0^{\circ}$ on the C 1s polar scan. This is a direct indicator of an upright molecular orientation, which confirms the NEXAFS results for this overlayer system. Large molecular tilts can be immediately ruled out since a tilt of ~20° should produce a clear splitting of the forward focusing peak due to oxygen scattering [65]. The strong diffraction feature at off-normal polar angles can be attributed to scattering of the electron wavefront by K atoms. The fact that there feature are strong is an indication that the K atoms are above the C atoms co-adsorbed layer. If the K were below the C,

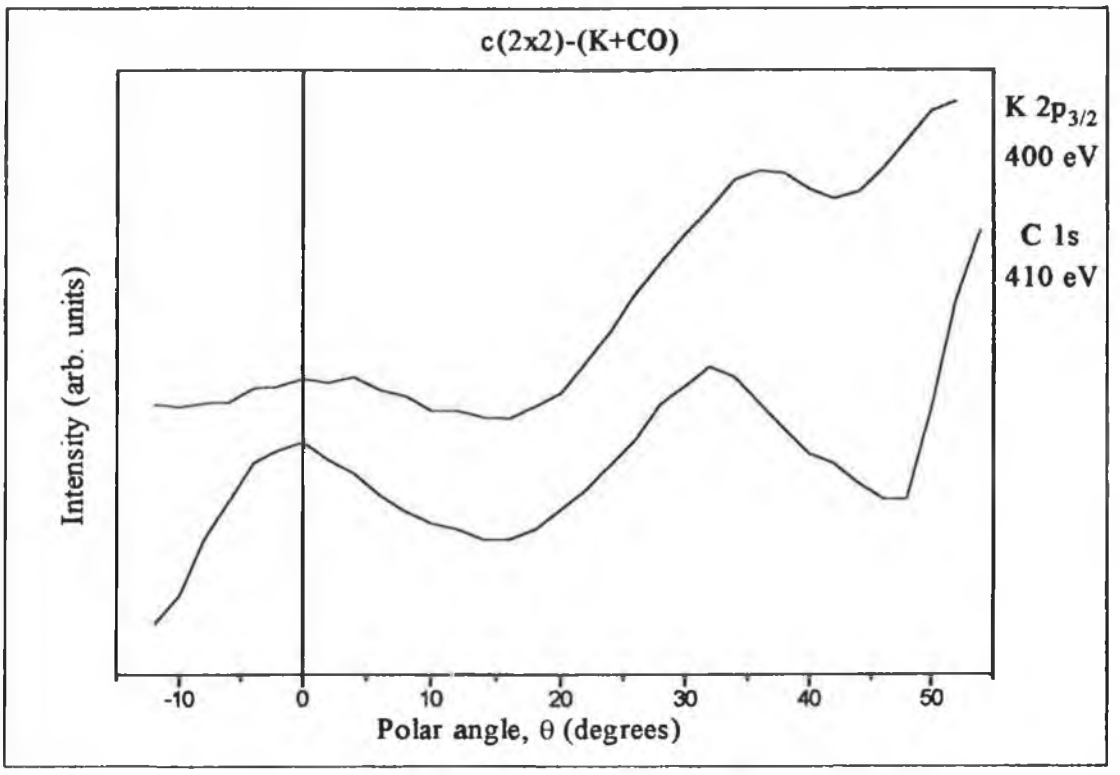

Figure 23: Polar XPD curves measured from the c(2x2)-(K+CO) overlayer along the $[1\bar{2}10]$ azimuth using C 1s emission at 410 eV and K 2p emission at 400 eV.

strong features would not be observed due to the weakness of back-scattering processes.

The polar XPD curve measured from the K atoms at ~400 eV shows an exponential rise similar to the low energy curves shown on figure 22. This is a further indication the these atoms are proud of the surface. The modulations on the curves at $\theta=0^{\circ}$ & 35° are unexpected, given the lack of features on the low energy XPD curves. The fact that these modulations coincide with the strong XPD feature on the C 1s polar scan at 410 eV indicates that they probably arise from imperfect background normalisation. Ideally, normalisation of the core level intensities to the background on the high kinetic energy side should remove all background effect. However, due to the close proximity of the K 2p and the C 1s core levels, this appears to be inadequate for normalisation of the K 2p core level peaks.

In order to determine the main structural parameters of the c(2x2)-(K+CO) overlayer three XPD polar scans were used. Two were measured using C 1s emission at kinetic energies of ~120 and ~180 eV. The third scan was measured using O 1s emission at ~110 eV. The structural parameters that were investigated (shown in figure 21) are:

-the CO lateral position with respect to the K adatoms along the [0001] azimuth.

-the C-top layer Co z-separation.

-the C-O bondlength.

-the K-O z-separation.

On the basis of the NEXAFS analysis the CO molecule was maintained upright throughout the analysis. The Co crystal was assumed to have a short outermost termination with all structural parameters fixed at their bulk values. The K adatoms were assumed to occupy the surface FFH sites, as determined by the LEED-I(V) analysis.

Because the 4 geometric parameters must be varied independently resulting in a large number of SSCC's, R-factor analysis has been used to determine which structures yield the best agreement between theory and experiment. As usual, the Pendry R-factor [66] is employed. As discussed in chapter 2, this compares the logarithmic derivatives of the experimental versus the calculated curves. The quality of agreement

is judged on the basis of the position of the diffraction peak maxima and minima. It is largely insensitive to relative peak heights and hence is ideally suited to single scattering theory where peak intensities cannot always be relied upon.

Rather than attempt to optimise all structural parameters simultaneously, certain parameters were initially fixed while others were varied. The CO-K lateral position and the C-Co z-separation were optimised first. The CO bondlength on transition metal surfaces is generally between 1.1-1.2 Å [67]. Including the increase in bondlength upon co-adsorption with K determined by NEXAFS, the C-O bondlength was initially fixed at 1.25 Å. The K adatoms were located co-planar with the O adatom (K-O z-separation of 0.0 Å).

The lateral separation of the CO molecules from the K adatoms along the [0001] azimuth was varied between 2.0 Å and 3.6 Å in 0.1 Å steps. For CO adsorbed in an on-top site on a transition metal surface, the C-metal bondlength is typically ~1.8 Å [67]. Treating the C and Co atoms as solid spheres and maintaining a C-Co nearest neighbour separation of 1.8 Å would result in a C-to-top layer Co z-separation of ~1.3 Å if the CO were adsorbed in the short-bridge site of the Co surface. Translating the CO molecule along the [0001] azimuth while still maintaining the C-Co nearest neighbour separation (1.8 Å) would result in a drop of the C-Co z-separation to a minimum of ~0.8 Å followed by a rise to ~1.1 Å as the CO approaches the FFH site (atop the 2nd layer Co atoms). Given these considerations, the C-Co z-height was varied between 0.9 and 1.6 Å in 0.05 Å steps at each of the CO lateral positions. Figure 24 shows the results of the R-factor analysis on the effect of varying the CO lateral position and the C-Co z-height. As well as showing the contour plots for the comparison of theory for each XPD scan independently, an averaged contour plot is also shown to aid the location of a global minimum.

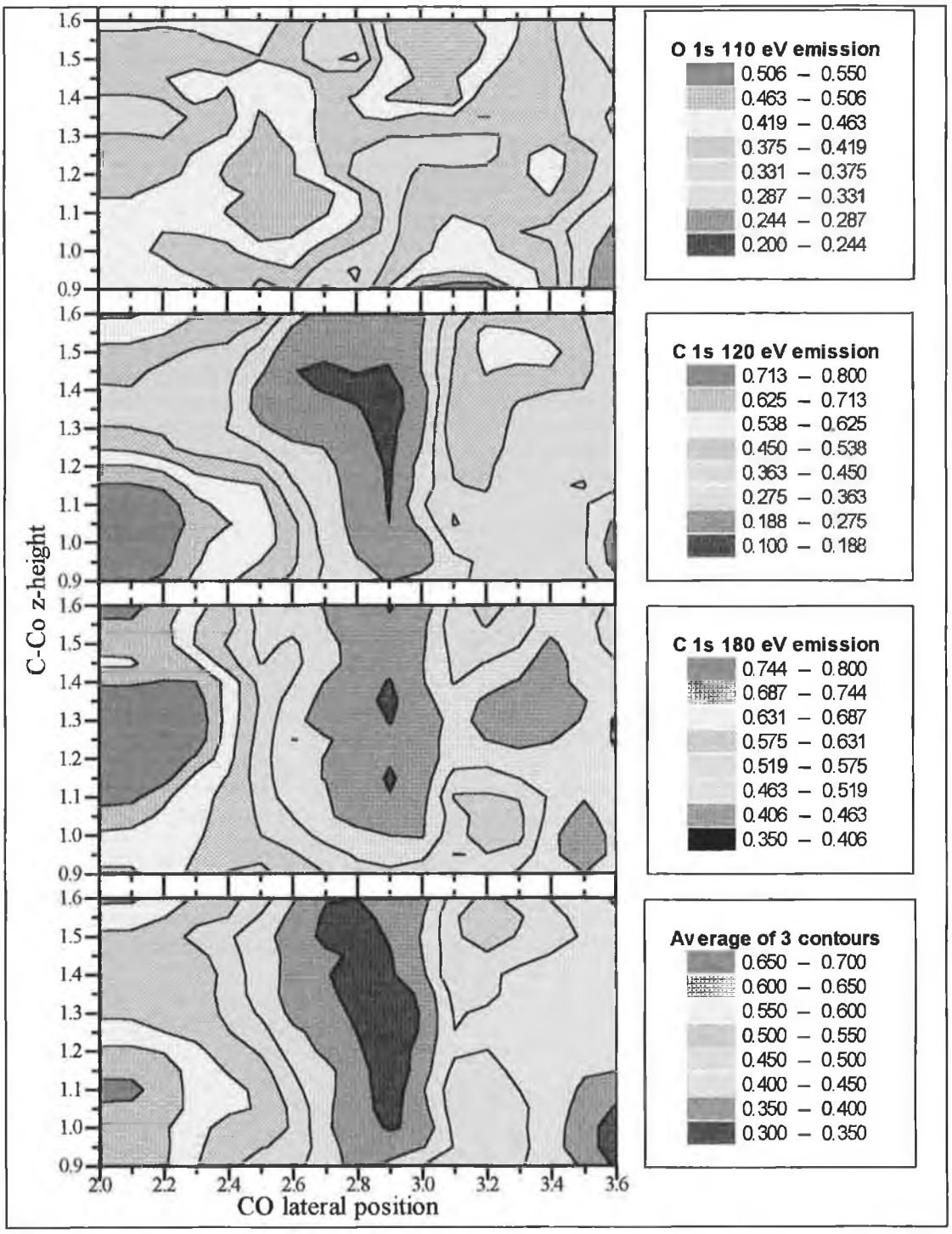

Figure 24: R-factor contour plots of the comparison of SSCC's with experimental curves for emission from O 1s at 110 eV and C 1s at 120 and 180 eV and the average of the three independent measurements.

A number of general observations can be made. There are clear similarities between the two C 1s emission contour plots. Both show a minimum centred around a K-CO lateral separation of 2.9 Å. In contrast, the C-Co z-height does not show as clear a minimum. This is unsurprising since this parameter is probed by back-scattering of the

	CO lateral position (Å)	*C-Co z-height (Å)*	R_p
Oxygen, 110 eV	2.8	1.5	0.32
Carbon, 120 eV	2.9	1.35	0.15
Carbon, 180 eV	2.9	1.35	0.39
Averaged plot	2.9	1.25	0.31

Table 3: R-factor minima and corresponding geometric parameters for the contour plots shown in figure 24.

emitted electron from the underlying substrate, which is intrinsically weaker than forward scattering. In the case of the O 1s contour plot the absolute minimum occurs at a CO lateral position of 3.6 Å and a C-Co z-height of 0.9 Å. This can be disregarded as a spurious minimum since, for a CO:K ratio of 2:1, a lateral K-CO separation of 3.6 Å would result in a separation of only ~0.9 Å between adjacent CO molecules along the [0001] azimuth. This separation is physically unreasonable considering the atomic radii of C and O are ~0.77 and ~0.6 Å respectively. The entire oxygen plot is quite 'flat' with the bulk of R-factors falling in the range 0.33-0.55, which, compared with ranges of 0.1-0.8 for C at 120 eV and 0.35-0.8 for C at 180 eV, indicates that the oxygen curve is largely insensitive to the parameters being varied. This can be attributed to the larger separation of the O atoms from the Co substrate and to the fact that they are proud of the majority of scattering atoms.

It is clear from the contour in figure 24 that the C emission XPD curves allow the CO lateral position to be well-defined (±0.1 Å) but that the curves are less sensitive to the C-Co z-separation. Table 3 summarises the geometric parameters corresponding to the minimum point for the 4 contour plots shown in figure 24. In the case of the oxygen plot, R-factors for CO lateral positions >3.4 Å are neglected. Based on table 3 we can fixed the CO lateral position with respect to the K adatom at 2.9 Å. The C-Co z-height can be fixed at a value of 1.35 Å. This value is chosen as the average of the two C 1s emission results because it is reasonable to assume that the oxygen XPD curve is not very sensitive to the value of this parameter. A minimum based on the averaging of the 3 plots (thereby treating each plot equally) could be skewed to an incorrect value by a plot that is insensitive to the parameters being investigated.

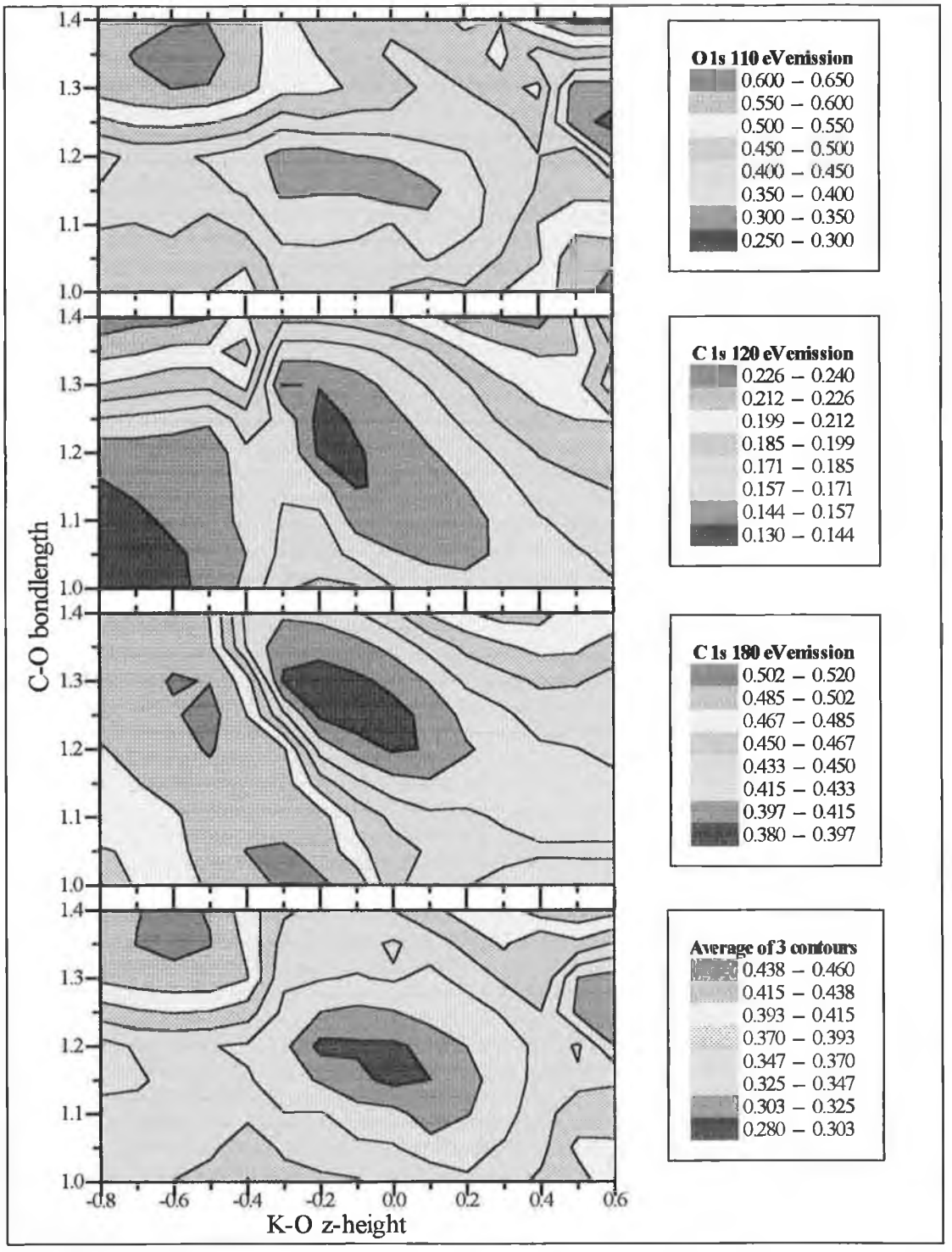

Figure 25: R-factor contour plots of the comparison of SSCC's with experimental curves for emission from O 1s at 110 eV and C 1s at 120 and 180 eV. The bottom plot is the average of the top three.

Fixing the CO lateral position at 2.9 Å and the C-Co z-height at 1.35 Å, the effect of varying the C-O bondlength and the K-O z-height was then examined. The resultant R-factor contour plots are shown in figure 25. When the K-O z-height is 0.0 the K

and O atoms are co-planar. Negative value of the K-O z-height indicate that the K atom is below that of the O atom while positive value indicate that it is above the O atom. The K-O z-height was varied between -0.8 and 0.6 Å in 0.1 Å steps. The CO bondlength was varied between 1.0 and 1.4 Å in 0.05 Å steps.In this case the three XPD curves are in good agreement on both structural parameters. Each of the contour plots in figure 25 show a local minimum around a K-O z-separation of -0.2 to 0.0 Å and a C-O bondlength of 1.2 to 1.25 Å. Secondary minima occur on the O 1s plot at K-O=0.6 Å/C-O=1.25 Å, and on the C 1s (120 eV) plot at K-O=-0.7 Å/C-O=1.0 Å. Both of these can be regarded as spurious since they do not appear on the other contour plots. Table 4 summarises the geometric parameters corresponding to the minima of the contour plots shown in figure 25 (excluding the spurious minima mentioned above). The results clearly favour a C-O bondlength of between 1.2 and 1.25 Å and a K atom with centre-of-mass slightly below that of the oxygen atom. The CO bondlength is in-keeping with the value expected on the basis of the NEXAFS results.

The overall results of this XPD analysis on the c(2x2)-(K+CO) structure are summarised in table 5 and compared with the structural parameters obtained in the LEED-I(V) analysis [42]. There is good agreement between the parameters

	K-O z-height (Å)	*C-O bondlength (Å)*	R_p
Oxygen, 110 eV	-0.2	1.2	0.32
Carbon, 120 eV	-0.2	1.25	0.14
Carbon, 120 eV	-0.2	1.25	0.39
Averaged plot	-0.2	1.2	0.30

Table 4: R-factor minima and corresponding geometric parameters for the contour plots shown in figure 25.

	Current analysis (Å)	*LEED analysis (Å)*
K-CO lateral position	2.9 ± 0.1	2.9
C-Co z-height	1.35 ± 0.1	1.33 ± 0.07
C-O bondlength	1.2 ± 0.05	1.2 ± 0.07
K-O z-height	-0.2 ± 0.1	0.23 ± 0.11

Table 5: Optimum structural parameters for the proposed model. Also included for comparison are the optimum parameters determined by LEED for the 1:1 CO:K model of the c(2x2) overlayer [42].

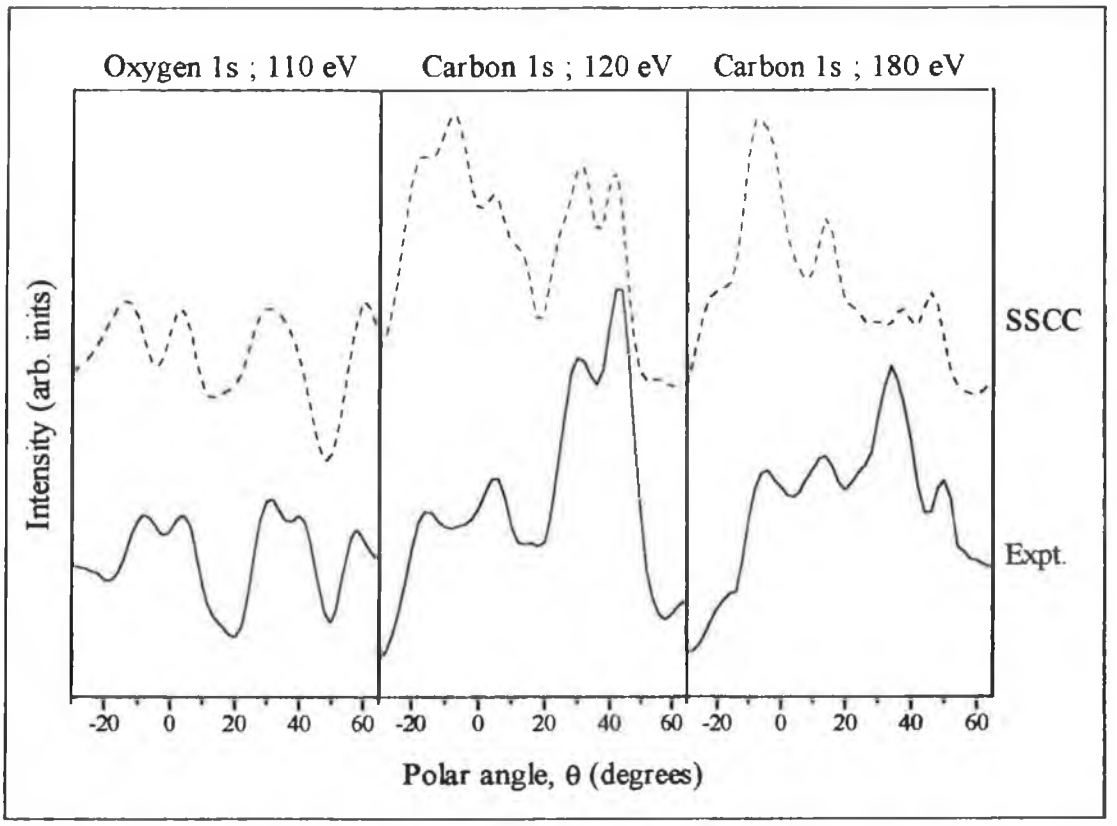

Figure 26: Polar XPD curves measured from a c(2x2)-(K+CO) overlayer on Co $\{10\bar{1}0\}$ along the $[1\bar{2}10]$ azimuth. The SSCC's are for the best fit structural parameters as determined by the R-factor analysis.

determined by the two techniques. The main exception is the position of the K atoms. The XPD analysis places this just below the oxygen atoms whereas the LEED analysis locates it just above. However both models agree that the K atoms are nearly co-planar with the oxygen.

Figure 26 shows the experimentally measured polar XPD curves and SSCC's done using the optimal structural parameters determined by the R-factor analysis (listed in table 5). There is a reasonable level of agreement, except for C 1s emission at 180 eV where there is a large discrepancy in relative peak intensities between theory and experiment.

4. DISCUSSION:

4.1. Overlayer Coverages:

A major disagreement between the results presented in this chapter and the LEED and RAIRS studies of the (K+CO) overlayer centres around the CO:K stoichiometry. The XPS coverage calibration suggests a CO:K ratio of 2:1 on the c(2x2) overlayer. Both the LEED [42] and the RAIRS/TPD [43] favour a 1:1 ratio. In addition, an earlier preliminary study of the coverage of the c(2x2) overlayer also favoured a 1:1 ratio [68]. This study estimated the coverage based on the core level peak intensities and the respective Scofield absorption cross-sections [69]. The CO:K ratio determined for the c(2x4) overlayer in this chapter (4:1) also disagrees with the RAIRS/TPD study, which finds a 2:1 ratio.

It is possible to place an additional CO molecule in the proposed c(2x2) overlayer structure while maintaining a single local bonding environment (as required by the RAIRS data). The additional CO adopts a site that is a mirror image of the CO molecule in the 1:1 ratio model. This site is shown as a broken circle in the surface unit cell shown in figure 1. It would be expected that, for LEED-I(V) spectra collected at normal incidence, the insertion of an extra CO molecule in an identical local bonding environment would not have a particularly great affect on the measured spectra. However, it should be noted that a LEED-I(V) R-factor analysis of the 2:1 versus the 1:1 structure still favoured the latter stoichiometry [70].

It is difficult to reconcile the results of the XPS analysis with the TPD measurements of Toomes and King [43] who reported no increase in the room temperature saturation θ_{CO} upon co-adsorption with K. A possible explanation of this discrepancy is that in the present study θ_{CO} on the clean Co surface (used as a calibration point) was less than 0.5 ML. Such a reduction in the saturation coverage might occur as a result of photon induced desorption. However, in order to account for the discrepancy, θ_{CO} on the clean surface would have to be *considerably* lower than 0.5 ML (i.e. ~0.25-0.3 ML). This is unlikely given that the desorption energy determined

by Toomes and King [43] indicates that at least 0.5 ML of CO on the clean surface should be stable at room temperature, while the adsorption energies determined by Papp [56] suggests that the saturation θ_{CO} may be as high as 1 ML. An alternative explanation is that during the TPD study some of the CO may have remained associated with the K within a K/CO complex. If this were the case, the differing ionisation cross-sections of molecular CO and the CO within the complex may help explain the disagreement.

It is possible that oxygen atoms, due to dissociated CO, are responsible for the high coverages ratios determined on the co-adsorbed overlayers by the XPS analysis. The pre-edge observed in the NEXAFS spectra is a clear indicator of CO dissociation on the co-adsorbed phases. However, it is unlikely that dissociation could account for such the large discrepancy. The intensity of the O K-edge feature from a p(2x1)-O overlayer (θ_O=0.5-1.0 ML) is significantly greater than the pre-edge feature on any of the co-adsorbed overlayer. Even in the case of the p(3x1) overlayer, which is the worst case, the pre-edge after 10 hours beam exposure corresponded to ~0.15 ML, based on the assumption that θ_O on the clean surface is 1 ML. Furthermore, the emergence of the pre-edge is a time-dependent effect, and it occurs, in the main, after CO dosing has ceased. Hence, even though dissociation may result in sites for CO adsorption becoming available, the absence of an large partial pressure of CO in the experimental chamber means that CO uptake cannot occur at an appreciable rate. Clearly the occurrence of CO does not reconcile the coverage results of the different studies.

It should be noted that the exact value of the CO:K ratio in no way affects the conclusions of this work regarding the molecular orientation and K-induced changes in geometry. It is also be worth noting that an increased CO:K stoichiometry may be more in-keeping with the unusually small K-induced shift of the CO stretching frequency for the c(2x4) and c(2x2) overlayers of 169 and 289 cm^{-1} as noted by Toomes and King [43].

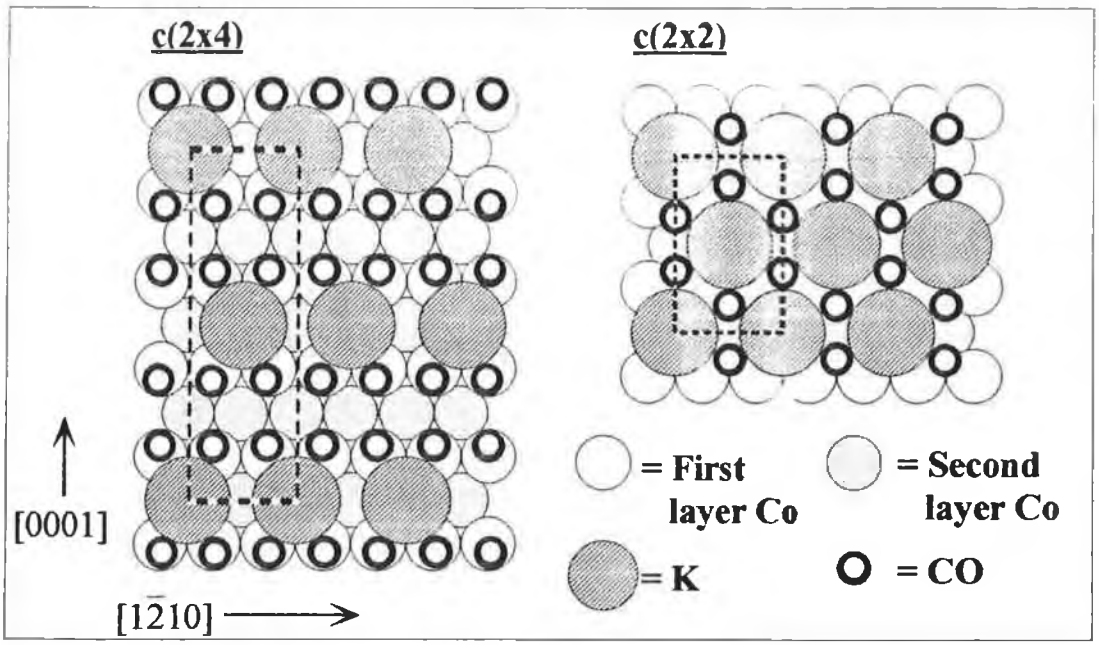

Figure 27: Models for the c(2x4) and c(2x2) structures using CO:K ratios of 4:1 and 2:1 respectively.

As was the case for the c(2x2) structural model, the c(2x4) model (figure 2) can also be modified to accommodate the higher CO:K ratio (4:2) determined by XPS. However, in this case the existing CO molecules must change their adsorption site from that proposed for the 2:1 c(2x4) model in order to maintain a single chemically distinct site for all CO molecules (as required by RAIRS). In the case of the 2:1 model shown in figure 2 the CO molecules are either in a short-bridge site or are displaced from the short bridge along the [0001] azimuth. For the 4:1 model, the CO molecules are displaced from an on-top site. Figure 27 shows the structural models on the c(2x4) and c(2x2) overlayers based on the XPS coverage analysis (with respective CO:K ratios of 4:1 and 2:1). As discussed in the results section, the local θ_{CO} in the different domains of the p(3x1)/c(2x2) overlayer is uncertain. Simple size considerations make a CO:K ratio of 1:1 in the p(3x1) domains most likely. Given the lack of structural information available from the techniques applied to the study of this overlayer system, the model proposed by Toomes and King [43] (see figure 2) seems as plausible as any other in the absence of quantitative structural analysis.

4.2. CO Bondlength Changes:

The position of the σ-resonance maxima relative to the π-resonance maxima as shown in figures 6, 7, 8 and 13, are summarised in table 6. The corresponding change in the CO bondlength, based on the empirical relationship [44, 49, 50] discussed earlier are also shown. Clearly the CO inter-nuclear bondlength shows a systematic increase with θ_K. Although doubts have been expressed about the validity of the "bond length with a ruler" method for determining bondlength changes in poly-atomic molecules [71, 72], it is generally accepted as being qualitatively correct for diatomic molecules such as CO.

Bondlength increases upon co-adsorption with AM's are usually explained in terms of the Blyholder model [27]. This focuses on two main orbital overlaps leading to a charge re-distribution. The first is charge donation from the CO 5σ states to the metal substrate resulting in a carbon-metal bond. This is accompanied by back donation of electron density from metal states into the CO $2\pi^*$ anti-bonding orbitals resulting in a weakening of the C-O bond. Due to the electropositive nature of the alkali atom, upon adsorption some of its valence electron density is readily donated to the substrate forming a polarised covalent bond. Thus, co-adsorption of CO with an AM results in an increased amount of back-donation from the substrate into the CO $2\pi^*$ orbitals (more electron density is available). The consequence is a stronger substrate-CO bond and a weaker C-O molecular bond. In addition, the electrostatic field of the δ(+) K atoms, which surrounds the CO molecules, results in a reduction in the energy of the $2\pi^*$ orbitals. This enhances their ability to interact with the substrate conduction band also resulting in increased back-donation.

Overlayer	π to σ separation (eV)	Bondlength increase (Å)
CO	15.9	-
c(2x4)	13.8	0.07 (± 0.06)
c(2x2)	12.9	0.10 (± 0.06)
p(3x1)/c(2x2)	12.1	0.13 (± 0.07)

Table 6: π- to σ-resonance peak maxima separation and the corresponding bondlength increase with respect to CO on clean Co.

It should be noted that recent *ab initio* total energy calculations have demonstrated that the Blyholder model is an over-simplistic representation of the CO bonding process [73], although the basic principle behind the model remains valid. Orbital mixing upon adsorption of CO at a metal surface results in the generation of new metal/CO derived bonding and anti-bonding orbitals. All orbitals below the Fermi level will be filled. If this constitutes a net increase in the number of anti-bonding electrons involved in the CO molecular bond the result is a weakening of the bond. Any additional increase in the electron density available (such as thought the adsorption of electropositive AM's) will increase the number of filled anti-bonding states and further weaken the CO bond. The systematic increase in the CO bondlength with K coverage can be viewed as simply reflecting the increase in electron density available to the K/CO/substrate states.

In addition to bond weakening through the substrate-mediated electron transfer mechanism outlined above, the CO bond may also be weaken via a direct K-CO interaction. If chemical bonds are formed between the K atoms and the CO molecules the result will be a reduction in the bond order between the C and O atoms (i.e. partial loss of the CO triple-bond nature).

4.3. Molecular Orientation:

Most studies of CO orientation on AM/CO co-adsorption systems favour an upright orientation [1, 40-42, 74-76]. This is in agreement with the NEXAFS results for the c(2x4) and c(2x2) overlayers studied in this chapter. However, the indication of a tilted orientation for the p(3x1)/c(2x2) overlayer is interesting. As stated in the results section some doubt remains about the accuracy of the tilt analysis and this overlayer merits further study in order to determine the CO tilt more accurately. Polar XPD utilising emission from the C 1s core level may be a suitable technique for this task [65, 77].

A number of factors, apart from the tilt analysis shown in figure 13, give credence to the existence of a tilted CO species on the p(3x1)/c(2x2) overlayer. The first is the comparison of the I_{30}/I_{90} π-resonance ratios shown in the results section, which was relatively free of dissociation effects. A second factor is the fact that the π-resonance on the NEXAFS spectra measured from the p(3x1)/c(2x2) overlayer appears to have two components. The higher photon energy component, which is not visible at normal incidence, becomes progressively more prominent as the incidence angle becomes more grazing. As discussed earlier, this feature is consistent with some degree of tilting of the CO along the $[1\bar{2}10]$ azimuth. The difference in the photon energy position of the two π-resonance components may imply a lifting of the degeneracy of the orthogonal $2\pi^*$ orbitals, which is a possible consequence of a tilted molecular orientation. It is worth noting that if some of the CO adsorbed on the p(3x1)/c(2x2) overlayer is occupying c(2x2) domains, then the CO molecules in the p(3x1) domains may have an even greater tilt than was determined in figure 13. This is because the presence of CO in the c(2x2) domains (where the CO is upright as indicated by the NEXAFS results) will skew the analysis toward an upright orientation.

4.4. Additional NEXAFS Features:

The feature labelled χ is clearly visible on the normal incidence NEXAFS scans taken from the different co-adsorption overlayers. It exhibits π-like symmetry and becomes more prominent with increasing θ_{CO}. Its photon energy position is effectively constant ($\pm$0.2 eV) on the three co-adsorption systems. On the c(2x2)-(K+CO) overlayer the peak intensity, I_χ, showed a significant variation with the azimuthal orientation of crystal at normal incidence. The intensity along the $[1\bar{2}10]$ azimuth was ~1.5 times greater than along the [0001] azimuth. In addition, a small azimuth-dependent shift is the photon energy position of the feature was apparent. There was no evidence of an equivalent feature on O K-edge NEXAFS scans measured from either CO covered or K covered Co $\{10\bar{1}0\}$.

A similar feature has been observed for (K+CO) co-adsorbed on Ni {111} [75, 78]. A number of other NEXAFS studies have observed additional peaks in a similar position for various molecular adsorbates, although these were not co-adsorption systems [79-81]. These features have generally been attributed by the authors to Rydberg states and/or multi-electron excitation processes. A theoretical study, using *ab initio* cluster calculations, has indicated that NEXAFS features may arise from transitions into new adsorbate-substrate anti-bonding orbitals formed upon adsorption [82].

In a study of higher excited states in NEXAFS spectra by Björneholm *et al* [81] features occurring below the ionisation threshold (IT) on NEXAFS spectra of chemisorbed systems are attributed to Rydberg derived states, while those above the IT are assigned to multi-electron excitations. Although the IT for the systems studied in this chapter were not determined, the distance of the χ feature above the absorption threshold coupled with the well-established lowering of the IT induced by AM adsorption [13, 83] clearly places this feature above the IT. Consequently, we attribute this feature to a multi-electron excitation process. The χ feature may arise due to electron transitions into a new state generated by the overlap of K and CO orbitals (resulting in new bonding/anti-bonding pairs). This would constitute a direct interaction between the K and the CO within the adlayer structure consistent with models (A) and (C) outlined in the introduction. The fact that the χ feature has increased intensity when the E-vector of the incident light is orientated along the $[1\bar{2}10]$ azimuth indicates that the second transition is preferentially excited in this geometry.

Various direct interaction models for the co-adsorption of CO and alkali atoms on transition metal surfaces have been proposed as outlined in the introduction. Indirect evidence for a direct interaction is provided by the recent structural studies done on (K+CO) co-adsorption systems [40, 42]. These studies observed a substantial increase in the K-substrate separation upon co-adsorption with CO. Such a change is consistent with a direct interaction between potassium and oxygen, where the weakening of the K-substrate bond is compensated for by a strong K-O interaction. It is hard to envisage a large increase in the K-substrate separation arising from purely

surface mediated effects. The extremely short K-O separation in the c(2x2) co-adsorption model which has been proposed (~2.90 Å, [42, 43]) is close to the O-K chemical bonding distances in bulk K/CO complexes (~2.78 Å [84]), also pointing to a direct chemical interaction.

Within a direct interaction model, the splitting of the π-resonance observed on the NEXAFS spectra measured from the c(2x2)-(K+CO) overlayer along the $[1\bar{2}10]$ azimuth may be attributed to the formation of new composite K-CO molecular orbitals. The π-resonance observed on the NEXAFS spectra measured from CO on clean Co arises from O 1s electron transitions into a CO $2\pi^*$ orbital (or substrate/$2\pi^*$ derived states). In the case of co-adsorbed overlayers, these $2\pi^*$ orbitals may be modified by overlap with the potassium 4s resonance. The c(2x2) structural models shown in figures 1 & 27 indicate that there should be a significant differences in the K/CO orbital overlap along the two high symmetry azimuths of the substrate. The observed splitting may result from transitions from the O 1s level into a new bonding/anti-bonding combination formed preferentially along the $[1\bar{2}10]$ azimuth by overlap of the K 4s and CO $2\pi^*$ orbitals (model (C), see introduction). Model (C) has the advantage that it allows for the degeneracy of the $2\pi^*$ orbitals to be lifted and a splitting of the $2\pi^*$ states into several different levels [37]. Hence, it provides a rational for the observed splitting of the π-resonance on the c(2x2) overlayer and the shift of the resonance maximum with azimuthal orientation. A first principles total energy calculation, based on the known c(2x2)-(K+CO) geometry may throw further light on this and other aspects of the NEXAFS spectra.

4.5. Polar XPD Analysis:

The analysis of the polar XPD curves indicates a C-O bondlength of 1.2±0.05 Å in the c(2x2)-(K+CO) phase. This is in agreement with the NEXAFS results, which indicate that the bondlength was increased by ~1.0 Å from that of CO on the clean surface, since CO on transition metal surfaces tends to have a bondlength of ~1.15±0.05 Å. The analysis indicates that the K adatoms are -0.2 Å below the oxygen, while the LEED-I(V) analysis places the CO ~0.2 Å above the oxygen. However, both analyses

are in agreement that the K & O are approximately co-planar, and both return a K-CO lateral separation of ~2.9 Å. This locates the K atoms in a good position to form a direct interaction with the CO $2\pi^*$ orbitals, with the possible formation of a K-O chemical bond.

In the c(2x2)-(K–CO) structural model the K atoms occupy the Co FFH sites. Given the C-O bondlength and the C-Co z-separation determined by the XPD analysis (1.2 Å & 1.35 Å respectively), then the K-nearest-neighbour-Co separation is ~3.1 Å. This is the same K-Co separation reported for the c(2x2)-K overlayer on Co $\{10\bar{1}0\}$ [85]. The LEED study found a K-Co separation of ~3.5 Å. The discrepancy between LEED and XPD arises solely from the location of the K atoms relative to the O atoms.

At the low KE's utilised for the XPD measurements, the question of the validity of single versus multiple scattering will always arise. However, comparison of the XPD results with those obtained by LEED indicates that single scattering is capable of obtaining reasonable results even at very low energies (120 eV). It may be the case that multiple scattering theory gives more well-defined R-factor minima and more precise results. In order to rigorously test the suitability of SSCC's at low KE's, a comparative study with full multiple scattering theory should be carried out on a set of experimental results. Ideally a more complete set of experimental measurements than was available in this analysis should be used (i.e. scans at several different energies along different azimuths).

While the SSCC analysis of the low energy polar XPD scans was capable of yielding similar structural parameters to the LEED-I(V) study, the analysis for such a complex structure was time-consuming and as such is probably inferior to more automated analysis techniques such as tensor-LEED. It is conceivable that, with a larger database of experimental scans, low energy XPD might rival LEED in terms of accuracy of structural determination. Unfortunately, one area in which low energy XPD cannot compete with LEED is that of cost since, in order to perform the range of scans required, a synchrotron radiation source is required. In addition, given the large

demand for synchrotron beam-time, experiments can usually only be performed for limited time periods. In contrast, LEED is cheap (beyond the initial start-up cost) and allows measurement to be taken from a given system over indefinite periods. The one drawback of LEED in terms of co-adsorption systems is e^--beam induced dissociation of the adsorbed molecules. Low energy polar XPD of co-adsorbed layers may be less prone to this effect. However, the NEXAFS results from the (K+CO) overlayers studied in this chapter do show the presence of atomic oxygen. Hence , the absence of CO dissociation in low energy XPD experiments cannot be taken for granted prior to performing the measurements.

5. CONCLUSIONS:

The co-adsorption of CO with K on Co $\{10\bar{1}0\}$ results in an increase in the room temperature saturation θ_{CO} relative to the saturation coverage on the clean Co surface. The C-O bondlength increases with increasing K due to the filling of CO anti-bonding states. The bondlength increases, determine relative to that of CO on the clean surface, were: 0.7 Å - c(2x4), 0.10 Å - c(2x2) and 0.13 Å - p(3x1)/c(2x2). As on the clean surface, the CO molecule maintains an upright (±10°) orientation on the c(2x4)- and c(2x2)-(K+CO) co-adsorption overlayers. However, on the high θ_K p(3x1)/c(2x2) overlayer there is evidence of a tilted CO species (~25°).

The π-resonance within the c(2x2)-(K+CO) overlayer is split into two components, most apparent when the E-vector of the incident light is oriented along the $[1\bar{2}10]$ crystal azimuth. This splitting may be due to a direct interaction of the K 4s resonance with the CO $2\pi^*$ orbital, resulting in the generation of a new bonding/anti-bonding pair.

In addition to the typical π- and σ- resonance features, an additional feature (χ) was observed on the co-adsorption overlayer, which was not present on NEXAFS scans of either CO or K adsorbed alone on the Co surface. The intensity of this feature increased with θ_K, and it showed a significant intensity variation with azimuthal orientation on the c(2x2)-(K+CO) overlayer. It was ~1.5 times more intense when the E-vector was oriented along the $[1\bar{2}10]$ surface azimuth than when the E-vector was oriented along the [0001] azimuth. In addition, the χ-resonance shifted, by ~0.5 eV, to lower photon energy on the NEXAFS spectra measured along the $[1\bar{2}10]$ azimuth. This correlates with a shift of the π-resonance as a result of the splitting outlined above, by ~0.7 eV, to lower photon energy along this azimuth. The χ-resonance was attributed to a multi-electron excitation process. Both this features and the π-resonance splitting point to a direct interaction between the K and the CO within the adlayer structure, resulting in the generation of new K/CO hybrid orbital states.

There was a second, high-energy component in the π-resonance of the p(3x1)/c(2x2) overlayer. This became more apparent as the photon incidence angle became more grazing. This feature can be attributed to a tilting of the CO molecule long the $[1\bar{2}10]$ azimuthal direction and a lifting of the degeneracy of the CO $2\pi^*$ orbitals.

The XPD analysis suggests that a SSCC approach may be sufficient even at low outgoing KE's to produce quantitative results from scanned-angle XPD measurements. Although, not extremely sensitive, it should be possible to distinguish between short and long terminations of a bulk Co $\{10\bar{1}0\}$ single crystal. The analysis yielded structural parameters for the c(2x2)-(K+CO) overlayer that agreed well with the results from a full quantitative LEED-I(V) study of this system. The best agreement was found for:

- A C-Co z-separation of 1.35±0.1 Å.
- A CO bondlength of 1.2±0.05 Å.
- The CO was laterally displaced along the [0001] azimuth by 2.9±0.1 Å from the K atoms, which were located in the Co FFH sites.
- K adatoms located 0.2±0.1 Å below the oxygen atoms.

Polar XPD scans measured using K 2p emission at various KE's were featureless, indicating that the K atoms are proud of the surface. This is in-keeping with the proposed structural model of the c(2x2)-(K+CO) overlayer. The presence of a prominent forward focusing peak at normal emission on a C 1s polar XPD curves measured at KE=410 eV from the c(2x2) overlayer is a direct indicator of an upright CO orientation. This is in agreement with the NEXAFS results from this overlayer.

6. REFERENCES:

[1] H.P. Bonzel, Surf. Sci. Rep., 8 (1987) 43.

[2] H. Pichler in: Advances in Catalysis and Related Subjects, Eds. W.G. Frankenburg, V.I. Komarewsky and E.K. Rideal, Academic Press, New York, (1952) p. 271.

[3] P. Biloen and W.M.H. Sachtler in: Advances in Catalysis and Related Subjects, Eds. W.G. Frankenburg, V.I. Komarewsky and E.K. Rideal, Academic Press, New York, (1981) p. 165.

[4] A.T. Bell, Catal. Rev.-Sci. Eng., 23 (1981) 203.

[5] V. Ponec, Catal. Rev.-Sci. Eng., 18 (1978) 151.

[6] H.P. Bonzel and H.J. Krebs, Surf. Sci., 117 (1982) 639.

[7] R.B. Anderson, Catalysis, Reinhold, New York, (1956).

[8] K. Aika, H. Hori and A. Ozaki, J. Catal., 27 (1972) 424.

[9] P.H. Emmett in: The Physical Basis for Heterogeneous Catalysis, Eds. E. Drauglis and R.I. Jaffee, Plenum, New York, (1975).

[10] G. Ertl, Catal. Rev.-Sci. Eng., 21 (1980) 201.

[11] G. Natta, U. Colombo and I. Pasquon, Catalysis, Rheinhold, New York, (1957).

[12] M. Kiskinova, G. Pirug and H.P. Bonzel, Surf. Sci., 133 (1983) 321.

[13] D. Heskett, D. Tang, X. Shi and K.-D. Tsuei, J. Phys.:Condens. Matter, 5 (1993) 4601.

[14] L. Walldén, Surf. Sci., 134 (1983) L513.

[15] J.E. Crowell, E.L. Garfunkel and G.A. Somorjai, Surf. Sci., 121 (1982) 303.

[16] H.P. Bonzel, J. Vac. Sci. Technol. A, 2 (1984) 866.

[17] F.M. Hoffmann, J. Hrbek and R.A. dePaola, Chem. Phys. Lett., 106 (1984) 83.

[18] R.A. dePaola, J. Hrbek and F.M. Hoffmann, J. Chem. Phys., 82 (1985) 2484.

[19] J.J. Weimer, E. Umbach and D. Menzel, Surf. Sci., 155 (1985) 132.

[20] J.J. Weimer, E. Umbach and D. Menzel, Surf. Sci., 159 (1985) 83.

[21] J. Lee, J. Arias, C.P. Hanrahan, R.M. Martin and H. Metiu, J. Chem. Phys., 82 (1985) 485.

[22] D. Lackey, M. Surman, S. Jacobs, D. Grinder and D.A. King, Surf. Sci., 152/153 (1985) 513.

[23] S.-I. Ishi, H. Asada and Y. Ohno, Surf. Sci., 17 (1986) L441.

[24] P.E.M. Siegbahn, Surf. Sci., 269/270 (1992) 276.

[25] A. Görling, L. Ackermann, J. Lauber, P. Knappe and N. Rösch, Surf. Sci., 286 (1993) 26.

[26] O.B. Christensen and J.K. Norskov, Chem. Phys. Lett., 214 (1993) 443.

[27] G. Blyholder, J. Phys. Chem., 68 (1964) 2772.

[28] D. Heskett, I. Strathy, E.W. Plummer and R.A. dePaola, Phys. Rev. B, 32 (1985) 6222.

[29] W. Eberhardt, F.M. Hoffmann, R.A. dePaola, D. Heskett, I. Strathy, E.W. Plummer and H.R. Moser, Phys. Rev. Lett., 54 (1985) 1856.

[30] D. Heskett and E.W. Plummer, Phys. Rev. B, 33 (1986) 2322.

[31] J.M. MacLaren, D.D. Vvedensky, J.B. Pendry and R.W. Joyner, J. Chem. Soc., Faraday Trans. 1, 83 (1987) 1945.

[32] E. Wimmer, C.L. Fu and A.J. Freeman, Phys. Rev. Lett., 55 (1985) 2618.

[33] J.J. Weimer and E. Umbach, Phys. Rev. B, 30 (1984) 4863.

[34] J.J. Weimer, W. Wurth, E. Hudeczek and E. Umbach, J. Vac. Sci. Technol. A, 4 (1986) 1347.

[35] J. Benziger and R.J. Madix, Surf. Sci., 94 (1980) 119.

[36] P.A. Schultz, C.H. Patterson and R.P. Messmer, J. Vac. Sci. Technol. A, 5 (1987) 1061.

[37] H.P. Bonzel, G. Pirug and R.P. Messmer, Surf. Sci., 184 (1987) L415.

[38] P.A. Schultz and R.P. Messmer, Surf. Sci., 209 (1989) 229.

[39] P.A. Schultz, J. Vac. Sci. Technol. A, 8 (1990) 2425.

[40] R. Davis, D.P. Woodruff, O. Schaff, V. Fernandez, K.-M. Schindler, P. Hofmann, K.-U. Weiss, R. Dippel, V. Fritzsche and A.M. Bradshaw, Phys. Rev. Lett., 74 (1995) 1621.

[41] H. Over, H. Bludau, R. Kose and G. Ertl, Phys. Rev. B, 51 (1995) 4661.

[42] P. Kaukasoina, M. Lindroos, P. Hu, D.A. King and C.J. Barnes, Phys. Rev. B, 51 (1995) 17063.

[43] R.L. Toomes and D.A. King, Surf. Sci., 349 (1996) 19.

[44] F. Sette, J. Stöhr and A.P. Hitchcock, J. Chem. Phys., 81 (1984) 4906.

[45] J. Stöhr and D.A. Outka, Phys. Rev. B, 36 (1987) 7891.

[46] V.I. Nefedov, J. Struct. Chem., 11 (1970) 277.

[47] J.L. Dehmer, J. Chem. Phys., 56 (1972) 4496.

[48] J.L. Dehmer and D. Dill, Phys. Rev. Lett., 35 (1975) 213.

[49] J. Stöhr, J.L. Gland, W. Eberhardt, D.A. Outka, R.J. Madix, F. Sette, R.J. Koestner and U. Doebler, Phys. Rev. Lett., 51 (1983) 2414.

[50] J. Stöhr, F. Sette and A.L. Johnson, Phys. Rev. Lett., 53 (1984) 1684.

[51] M. Surman, I. Cragg-Hine, J. Singh, B.J. Bowler, H.A. Padmore, D. Norman, A.L. Johnson, W.K. Walter, D.A. King, R. Davis, K.G. Purcell and G. Thornton, Rev. Sci. Instrum., 63 (1992) 4349.

[52] J. Singh, W.K. Walter, A. Atrei and D.A. King, Chem. Phys. Lett., 185 (1991) 426.

[53] M. Pérez Jigato, W.K. Walter and D.A. King, Surf. Sci., 301 (1994) 273.

[54] C.N. Banwell and E.M. McCash, Fundamentals of Molecular Spectroscopy, McGraw Hill Book Company, London, (1994).

[55] T. Masuda, C.J. Barnes, P. Hu and D.A. King, Surf. Sci., 276 (1992) 122.

[56] H. Papp, Ber. Bunsenges. Phys. Chem., 86 (1982) 555.

[57] R.L. Toomes and D.A. King, Surf. Sci., 349 (1996) 1.

[58] U. Seip, I.C. Bassignana, J. Küppers and G. Ertl, Surf. Sci., 160 (1985) 400.

[59] G. Brodén, G. Gafner and H.P. Bonzel, Surf. Sci., 84 (1979) 295.

[60] P.C. Görts, B.H.P. Dorren and F.H.P.M. Habraken, Surf. Sci., 287/288 (1993) 255.

[61] M. Lindroos, C.J. Barnes, P. Hu and D.A. King, Chem. Phys. Lett., 173 (1990) 92.

[62] H. Over, G. Kleinle, G. Ertl, W. Moritz, K.H. Ernst, H. Wohlgemuth, K. Christmann and E. Schwarz, Surf. Sci., 254 (1991) L469.

[63] P. Hu, Chemistry Dept., Queens University Belfast.

[64] S.M. Goldberg, C.S. Fadley and S. Kono, J. Elect. Spec. Relat. Phenom., 21 (1981) 285.

[65] D.A. Wesner, F.P. Coenen and H.P. Bonzel, Phys. Rev. B, 39 (1989) 10770.

[66] J.B. Pendry, J. Phys. C: Solid State Phys., 13 (1980) 937.

[67] G.A. Somorjai, Introduction to Surface Chemistry and Catalysis, Wiley interscience, New York, (1994).

[68] C.J. Barnes and M Valden, J. Phys. Condens. Matter, 1 (1989) SB185.

[69] J.H. Scofield, J. Elect. Spec Relat. Phenom., 8 (1976) 129.

[70] M. Lindroos, Private Communication, (1995).

[71] M.N. Piancastelli, D.W. Lindle, T.A. Ferrett and D.A. Shirley, J. Chem. Phys., 86 (1987) 2765.

[72] M.N. Piancastelli, D.W. Lindle, T.A. Ferrett and D.A. Shirley, J. Chem. Phys., 87 (1987) 3255.

[73] P. Hu, D.A. King, M.-H. Lee and M.C. Payne, Chem. Phys. Lett., 246 (1995) 73.

[74] J. Vaari, J. Lahtinen, T. Vaara and P. Hautojärvi, Surf. Sci., 346 (1995) 1.

[75] W. Wurth, C. Schneider, E. Umbach and D. Menzel, Phys. Rev. B, 34 (1986) 1336.

[76] F. Sette, J. Stöhr, E.B. Kollin, D.J. Dwyer, J.L. Gland, J.L. Robbins and A.L. Johnson, Phys. Rev. Lett., 54 (1985) 935.

[77] E. Holub-Krappe, K.C. Prince, K. Horn and D.P. Woodruff, Surf. Sci., 173 (1986) 176.

[78] W. Wurth, C. Schneider, R. Treichler, E. Umbach and D. Menzel, Phys. Rev. B, 35 (1987) 7741.

[79] J. Somers, M.E. Kordesch, T. Lindner, H. Conrad, A.M. Bradshaw and G.P. Williams, Surf. Sci., 188 (1987) L693.

[80] L. Wenzel, D. Arvanitis, R. Schlögl, M. Muhler, D. Norman, K. Baberschke and G. Ertl, Phys. Rev. B, 40 (1989) 6409.

[81] O. Björneholm, A. Nilsson, E.O.F. Zdansky, A. Sandell, H. Tillborg, J.N. Andersen and N. Mårtensson, Phys. Rev. B, 47 (1993) 2308.

[82] P.A. Stevens, T.H. Upton, J. Stöhr and R.J. Madix, Phys. Rev. Lett., 67 (1991) 1653.

[83] J. Hölzl and L. Fritsche, Surf. Sci., 247 (1991) 226.

[84] von E. Weiss and Büchner, Helvetica Chimica Acta, XLVI (1963) 1121.

[85] C.J. Barnes, P. Hu, M. Lindroos and D.A. King, Surf. Sci., 251/252 (1991) 561.

Chapter VI

The Surface Structure of Bulk and Surface CuPd Alloys Studied by Polar X-ray Photo-electron Diffraction.

1. INTRODUCTION:

Bi-metallic surface chemistry plays an important role in a range of technologically important areas such as catalysis, microelectronics fabrication and corrosion passivation. The intermixing of the two component elements (alloy formation) can be regarded as a special case in the study of bi-metallic chemistry. Such alloy surfaces are interesting because a large number of catalysts are bi- or multi-metallic. Synergistic effects due to the interaction of the metal species at an atomic level may play an important role in the effectiveness of the catalyst [1]. The catalytic properties of a given alloy mixture can be strongly dependent on its composition. For instance, Ni/Cu alloys show a decrease in hydrogenolysis activity with increasing Cu concentration [2]. In particular, there is a marked decrease in activity at low (5 *at.*%) Cu concentrations. This is due mainly to the fact that the surface composition of an alloy can be markedly different from that of the bulk. In the case of Cu/Ni, an alloy containing 5 *at.*% Cu can have a surface Cu composition of 50% or higher based on hydrogen chemisorption [2] and Auger spectroscopy [3] measurements. This fact illustrates the importance and need for careful study of the surface composition of bi-metallic alloys.

The ability to create well-defined single crystal alloy surfaces has resulted in a great deal of study on the structure and chemical reactivity of a range of single crystal bi-metallic alloy surfaces. By studying the reactivity and structure of such alloy surfaces, the possibility of acquiring basic knowledge of how to produce alloys with predictable and desirable reactive properties arises. A number of excellent recent reviews [4, 5] exist on the work performed on bi-metallic and alloy surfaces.

Two types of alloy surfaces can be distinguished. The first is the surface of a bulk single crystal alloy (either random substitutional alloys or ordered compounds of the Cu_3Au type). As is the case for CuNi mentioned above, the surface/selvedge of 'bulk alloys' may have a composition that is significantly different from that of the bulk, due to the well known phenomenon of "surface segregation" [6]. In addition, the possibility arises that the surface may adopt an ordered structure even though the bulk

is a random substitutional alloy. The second type is a so called "surface alloy". These are usually prepared by vapour deposition of a sub-monolayer coverage of one metal upon the surface of another metal. The resulting alloy may be ordered or substitutionally disordered and it may be two-dimensional (localised within a single layer, usually the top layer) or it may be distributed throughout the selvedge region.

Information about the surface structural properties and the selvedge composition of alloys can be obtained from polar XPD measurement in conjunction with SSCC's. The XPD forward focusing effect at medium and high outgoing kinetic energies can be particularly useful in identifying preferential localisation of a given atomic species within the selvedge of an alloy surface and is particularly suited to distinguishing between atomic localisation in the outermost, in the 2^{nd} or in the 3^{rd} (and deeper) layers of a crystal. In addition, XPD spectra measured from a species that is enriched in a crystal selvedge relative to its bulk concentration have an increased sensitivity to the surface structure of the crystal. This makes effects such as surface relaxations and reconstructions easier to identify and accurately quantify.

Copper and palladium can form bulk substitutional alloys across their entire compositional range [7]. Cu/Pd alloys are part of the range of alloys resulting from the combination of group VIII metals (e.g. Ni, Pd, Pt) with group IB metals (e.g. Cu, Ag, Au). These alloys are of interest mainly for hydrogenolysis, hydrogenation/dehydrogenation reactions and CO oxidation/NO_x reduction, which is related to automobile pollution control (catalytic converters) [8]. In this chapter the results of structural studies on two CuPd single crystal alloy systems, a CuPd [85:15] {110} bulk alloy and a Cu {100}-c(2x2)-Pd surface alloy, are presented. Polar XPD is used to study the selvedge structure of the CuPd [85:15] bulk alloy, while the c(2x2)-Pd surface alloy structure is probed by a combination of LEED, CO TPD and polar XPD [9]. The main structural information published on these two systems is briefly summarised below before progressing to the results of the current work.

1.1. CuPd [85:15] {110}:

The first system considered is a CuPd [85:15] {110} single crystal bulk alloy. The clean, annealed alloy gives a p(2x1) LEED pattern for which an ordered CuPd 2nd layer with an almost pure Cu top layer was proposed as the structural model based on LEED/TDS analysis [10]. This was confirmed by a quantitative LEED analysis [11] and low energy ion scattering (LEIS) [12]. This is the only reported case of an ordered layer being formed below the top layer of a random substitutional alloy. However, the pure Cu top layer is in keeping with another bulk substitutional alloy system, PtNi, where the outermost layer is strongly enriched in Ni and the 2nd layer is enriched with Pd [13]. This termination is an inversion of the normal situation for the {100} and {111} crystal faces of Pd/Ni alloy crystals, where Pt is enriched in the outermost layer. The inversion is characteristic of the {110} surface of random substitutional alloys [5].

The CuPd [85:15] {110} alloy surface has also been extensively studied by Newton *et al* [14-18], who have dealt with the surface structure, the equilibrium composition and reconstructions of the surface upon adsorption of oxygen. Of most relevance to the current XPD analysis is the compositional profile of the alloy selvedge. This has been determined from a simple surface segregation model [15]. The selvedge was determined to consist of a pure Cu outer layer and a 2nd layer enriched with Pd (~40%), which is in-keeping with the proposed LEED structural model. The Pd composition in deeper layers was determined as having a damped oscillation into the bulk (i.e. Pd depletion in layers 3 (~5%) and 5; enrichment in layers 4 (~25%) and 6). This damped oscillation into the alloy bulk is characteristic of bulk substitutional alloys [13].

1.2. Cu {100}-c(2x2)-Pd:

The second system is a Cu {100}-c(2x2)-Pd surface alloy, which is formed by vapour deposition of Pd on Cu {100}. The formation of a surface alloy was proposed by Graham [19] on the basis of LEED. A subsequent quantitative LEED-I(V) analysis concluded the structure to be a two-dimensional surface alloy with a 50:50 Cu/Pd

composition in the outermost layer [20, 21]. There was evidence of a small rippling of the Pd atoms in the top layer (0.02±0.03 Å outward). The initial studies reported a "best" c(2x2)-Pd for a Pd coverage of ~0.8 ML [19, 20]. This was subsequently revised to ~0.5 ML [21], which is in better agreement with the suggested two-dimensional model. A LEED and Rutherford back-scattering spectroscopy (RBS) study done by Pope *et al* [22] favoured an optimal c(2x2) pattern at θ_{Pd}=0.55±0.05 ML. However, they reported that the LEED pattern remained sharp for adsorption of an additional 0.1-0.2 ML making visual determination of the peak maximum difficult. Theoretical calculations have confirmed that surface alloying is expected for sub-monolayer coverages of Pd on Cu {100} [23, 24].

2. EXPERIMENTAL:

2.1. CuPd [85:15] {110}:

The p(2x1) surface was formed by argon ion bombardment of the bulk alloy followed by annealing to 670 K for 15 minutes. This was done in a preparation chamber (base pressure ~$5x10^{-10}$ torr) prior to transfer into an analysis chamber (base pressure ~$5x10^{-11}$ torr). The analysis chamber was equipped with LEED optics, a dual anode (Mg, Al) X-ray sources and a hemispherical electron energy analyser.

Polar XPD scans were measured by rotating the sample. Azimuthal motion allowed polar scans to be measured along the three high symmetry azimuths of the {110} surface. The azimuths were aligned to within ±2° via LEED. The analyser had a 2 mm wide slit in the plane of polar rotation, yielding an acceptance half angle of ~1-2°. Polar XPD curves were measured using emission from both Pd and Cu core levels. Electron emission was stimulated using Al K_α radiation ($h\nu$=1486.6 eV). The Pd XPD curves were measured by monitoring the Pd $3d_{5/2}$ photo-emission intensity (KE~1150 eV) while the Cu curves were measured by monitoring the Cu $L_3M_{4,5}M_{4,5}$ Auger emission (KE~917 eV). The intensity at a given polar angle was determined from the integrated area under emission peak after subtraction of a linear background. The peak intensities were normalised to the intensity measured at a point on the high kinetic energy side of the peaks.

Polar XPD curves were measured in 2° steps, except across the forward focusing peaks which were measured in 1° steps. Each data point was measured several times and the experimental curves shown represent an average of the multiple measurements. Normal emission was determined from the maximum of the 0° forward focusing peak. Polar XPD curves were also measured from a clean Cu {110} single crystal, using the $L_3M_{4,5}M_{4,5}$ Auger emission. These spectra allowed the method of XPD measurement to be checked and provided a reference for the position of the forward focusing peaks measured from the bulk alloy.

2.2. Cu {100}-c(2x2)-Pd:

The measurements were performed in an ADES-400 spectrometer with a base pressure of ~$5x10^{-11}$ torr. The chamber was equipped with a 4-grid LEED optics, a rotatable energy analyser (acceptance half-angle of ~1.5°) and a dual anode X-ray source. A Balzer QMG 420 mass spectrometer fitted with a glass entrance aperture allowed thermal desorption experiments to be carried out. The Cu {100} sample was cleaned in-situ, by cycles of argon ion bombardment and annealing to 700 K, over a period of several days after which no contaminants were detectable above the Auger or XPS noise level and the sample exhibited a sharp, bright p(1x1) LEED pattern. The sample could be cooled rapidly to 100 K by liquid nitrogen, and heated at a controlled rate to 800 K by resistive heating via the crystal support wires.

Palladium was evaporated from a 0.125 mm diameter high-purity Pd wire which was wound around a 0.25 mm diameter tungsten filament. The homogeneity of the Pd flux was checked using the Pd (330 eV) to Cu (920 eV) Auger ratio at different points on the surface. The rate of adsorption of Pd was calibrated using an Auger signal versus time (As-*t*) plot and by monitoring the intensity of the (1/2, 1/2) LEED beams. Figure 1 shows the resulting As-*t* and LEED intensity plots. The intensity of the half-order LEED beam has been reported to pass through a clear maximum at a Pd coverage of 0.55±0.05 ML [22]. The deposition rate resulted in the formation of an optimal c(2x2) pattern after a deposition time of 100 seconds.

CO TPD spectra were obtained from the clean Cu and the CuPd alloy surfaces. CO adsorption was carried out at ~100 K and desorption was performed with a linear heating rate of 2.5 Ks^{-1}. Gas dosing was achieved via a supersonic molecular beam source [25] to ensure no adsorption on the sample sides or back face. The sample was mounted directly off the liquid N_2 cooling tank resulting in a monotonically increasing background being superimposed on the TPD spectra due to desorption from the tank. This background was removed by empirically fitting an exponential background to the raw spectra. Imperfections in the subtraction technique left some small features, which are not derived from the sample surface, at desorption temperatures >200K (see figure 22).

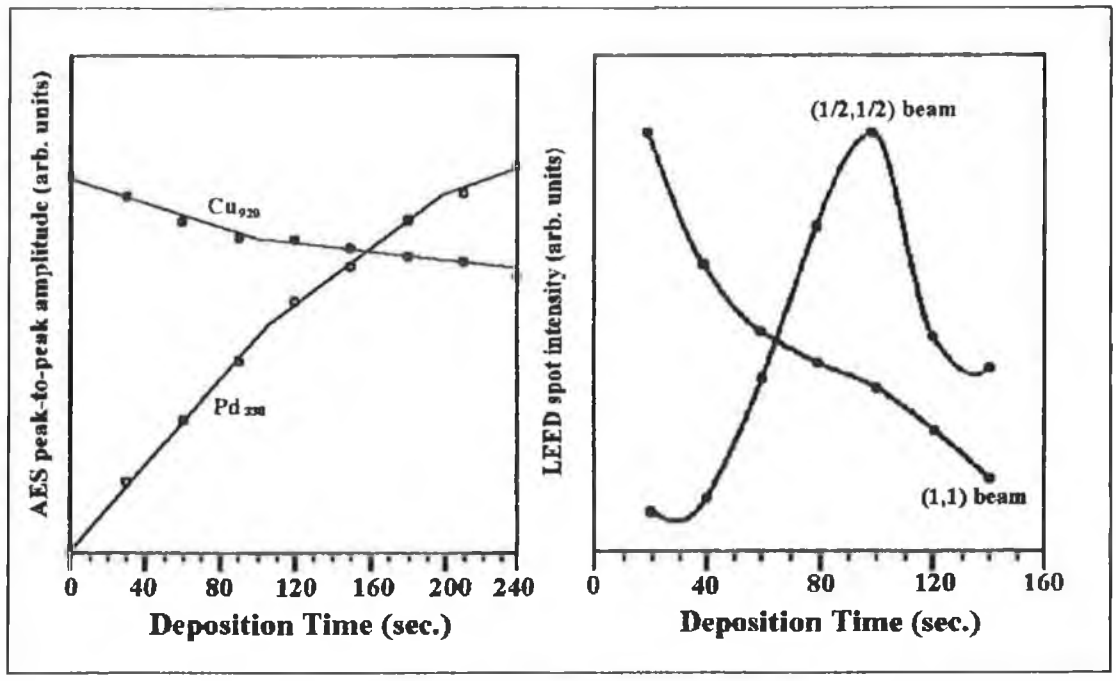

Figure 1: As-*t* plot and the variation of the integrated LEED (1/2,1/2) and (1,1) beam intensities at 80 eV for Pd deposition on Cu {100} at 300 K.

Polar XPD plots were measured along the {100} azimuth of the crystal surface. The azimuth was aligned to within ±2° via LEED. Electron emission was stimulated using the Al K_α X-ray source. Normal emission was located on the clean surface using the 0° forward focusing peak of the Cu $2p_{3/2}$ emission (KE~550 eV). Polar XPD curves were collected from Pd by monitoring the Pd $3d_{5/2}$ emission intensity (KE~1150 eV) in 2.5° steps. The plotted XPD intensities correspond to the integrated emission peak areas after subtraction of a linear background. Division by the background intensity, which was measured on the high kinetic energy side of the emission peak, was used to normalise out the instrument response function.

2.3. Single Scattering Cluster Calculations (SSCC's):

The electron emission for both alloys surfaces was modelled using single scattering theory and assuming the out-going electron wave was s-like. These approximations are valid for the high out-going kinetic energies used (Cu=917 eV; Pd=1150 eV). Phase shifts were calculated using Herman-Skillman wavefunctions [26]. A total of 26 and 29 phase shifts respectively were used in the SSCC's for electron kinetic energies of 917 (Cu emission) and 1150 (Pd emission) eV. The Debye temperatures (θ_D) of Cu

and Pd were set at their respective bulk values of 315 and 274 K. The inner potential of the cluster was set at 10 eV. Inelastic-mean-free-paths (IMFP's) of 13.5 Å and 15.1 Å were calculated for the Cu and Pd emissions respectively, using the formula of Seah and Dench [27]. The cluster size was limited to twice the valve of the IMFP in all directions. Convergence tests on larger clusters showed this to be a valid approximation. The spherical wave approximation and an analyser acceptance cone of half-angle=2° were utilised in the calculations.

In the case of the CuPd [85:15] bulk alloy cluster, the compositional profile of the Pd in the selvedge was set according to the values previously determined by Newton *et al* [15]. The outermost layer was pure Cu. The 2nd layer contained 50% Pd in a p(2x1) structure. The 3rd and 4th layers contained 5% and 25% Pd respectively and all deeper layers were set at the bulk composition of 15%. The Pd in the 3rd and deeper layers was randomly distributed within the layer. The initial lattice parameters of the cluster were initially set according to Vergard's law. Details of how these parameters were varied during the optimisation of the experiment-theory fit are included in the text.

For the Cu {100}-c(2x2)-Pd alloy, the bulk cluster lattice parameters were set at those of pure Cu [28]. On the basis of the compositional studies outlined above, the total amount of Pd in the cluster selvedge was maintained at 0.5 ML. The Pd distribution in the top 3 layers of the cluster and the selvedge inter-layer spacing was varied during the optimisation of the experiment-theory fit (details in text). In all cases the Pd in the different layers was inserted in a c(2x2) structure. All deeper layers were set as pure Cu in a bulk Cu {100} lattice structure.

3. RESULTS:

3.1. Clean Cu {110}:

Figure 2 shows a schematic representation of the Cu {110} single crystal surface. The 3 high symmetry azimuths ([1$\bar{1}$0],[1$\bar{1}$2] and [001]) are indicated. The major forward focusing peaks which would appear on polar XPD scans along these azimuths are shown on the cross-sections through the 3 azimuths. The in-plane lattice parameters of Cu {110} are 2.553 Å and 3.61 Å, and the bulk inter-layer spacing is 1.277 Å as shown in figure 2. A contraction of the outermost layer spacing to a value of 1.18±0.03 Å has been determined experimentally. This is an average of the values determined by several independent measurements of the Cu {110} surface utilising

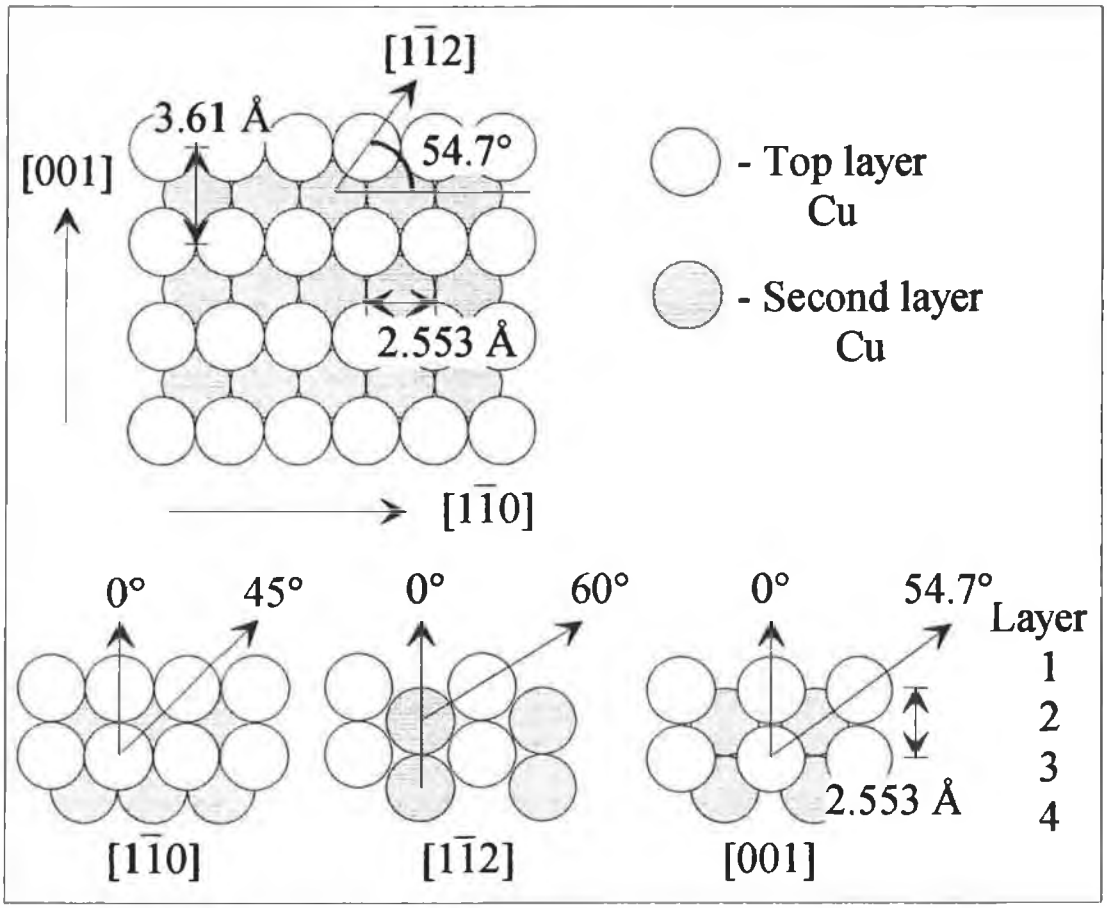

Figure 2: Schematic diagram of the Cu {110} single crystal. The origin of the main forward focusing peaks are shown on the cross-sections through the 3 high symmetry azimuths.

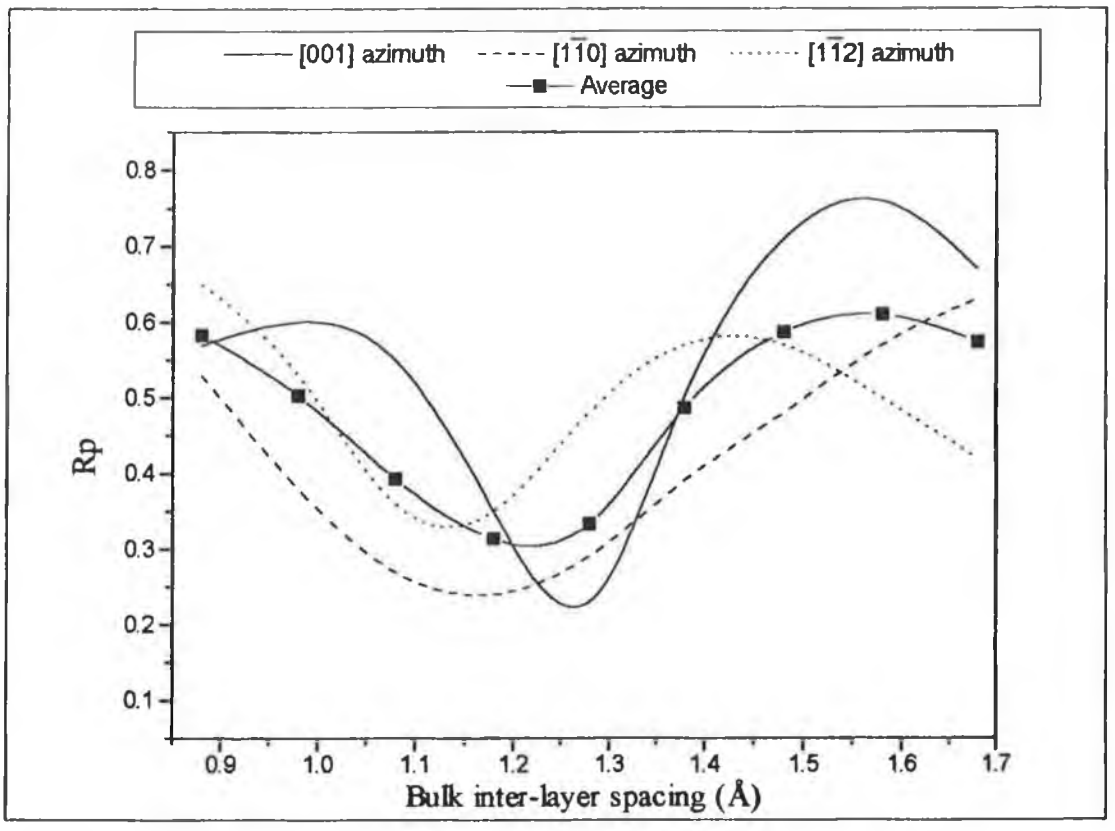

Figure 3: Pendry R-factors [33] plots for the comparison of SSCC's with experimental polar XPD curves along the 3 high symmetry surface azimuths of Cu {110} and the average of the 3 curves.

dynamical LEED calculations (~1.16 Å [29]; ~1.17 Å [30]) and single alignment ion scattering (RBS) ~1.21 Å [31]. These studies also reported a small expansion (~0.03-0.04 Å) of the 2nd-to-3rd layer spacing.

The polar angles of the peak maxima calculated in figure 2 neglect effects such as surface relaxations (the model is bulk terminated) and refraction of the emitted electrons at the surface. Surface relaxation of the magnitude outlined above would cause the position of the forward focusing peaks *due to emission from the outermost layers only* to shift to 45.7°, 62° & 55.4° for the [1$\bar{1}$0], [1$\bar{1}$2] & [001] azimuths respectively. Of course, emission from the bulk is largely unaffected, so such large shifts would not be observed in reality. Surface refraction typically leads to a shift of <0.5° toward normal emission at KE=917 eV [32].

Polar XPD curves were measured along the 3 high symmetry azimuths of the clean Cu {110} surface. The Cu LMM Auger emission intensity (KE~917 eV) was monitored

as a function of polar emission angle. SSCC's were performed for a Cu {110} cluster with the in-plane lattice parameters fixed at those of bulk Cu and the bulk inter-layer spacing (all layers in the cluster) varied between 0.88 and 1 68 Å in 0.1 Å steps. The calculated curves were compared with the experimental measurements by means of the Pendry R-factor. We can gauge the accuracy and sensitivity of our calculations by observing how well our best fit analysis agrees with the known structure of Cu {110}.

Figure 3 shows the R-factor plots obtained for the comparison of theory with experiment. The curves for each of the 3 high symmetry azimuthal directions and the average of those curves are shown. For a bulk terminated single crystal the minimum R-factor is expected at a layer spacing of ~1.28 Å. The R-factor plot for the [001] azimuth clearly minimises at the bulk inter-layer value. Along the other two azimuths the minimum position occurs at a contraction of the bulk spacing. The R-factor plot for the [1$\bar{1}$0] azimuth is relatively shallow indicating that the sensitivity to changes in the inter-layer spacing is not as good as that of the other polar scans. The [1$\bar{1}$2] azimuth R-factor plot minimises at the smallest inter-layer spacing (1.13±0.05 Å).

Additional SSCC's were carried out in which only the two outermost inter-layer spacings were allowed to (independently) vary and the spacing of the lower layers was maintained at the bulk value (~1.277 Å). Subsequent R-factor analysis was insensitive to the changes that occurred in the calculated curves as a result of varying these outermost layer spacings only. This insensitivity can be attributed to the calculated patterns being dominated by emission from the deeper (bulk) layers of the cluster. Such dominance is a consequence of the neglect of defocusing along 'chains' of atoms by single scattering theory [34].

Due to defocusing, the forward focusing peaks observed experimentally are significantly more surface sensitive than would be expected based purely on inelastic scattering considerations. Multiple scattering analysis by Xu *et al* [35] (shown in chapter 1), illustrated that at KE=917 eV a chain length of 5 Cu atoms (4 scatterers) should effectively eliminate the forward focusing effect. The failure of single scattering theory to account for defocusing means that it overestimates the contribution of deeper layers to the XPD forward focusing features. The result is, as

noted above, that calculations for clusters where only the spacing of the outermost layers is varied are dominated by features that originate from the cluster bulk. Full multiple scattering theory would increase the contribution to the calculated XPD pattern from emitters in the selvedge relative to the contribution from emitters deeper in the crystal. Although it was not done in the current work, the emission from the different layers could be weighted by factors determined from the multiple scattering analysis of the defocusing effect done by Xu *et al* [35]. This would improve the surface sensitivity of the SSCC's. However, it would not be ideal since defocusing reduces the intensity of the forward focusing peaks relative to the higher-order features whereas a fixed factor reduces the intensity of all curve features.

In the {110} crystal structure forward focusing between atoms in adjacent layers only occurs along the $[1\bar{1}2]$ azimuth. As a consequence, polar XPD scans measured along this azimuth are more sensitive to changes in the outermost inter-layer spacing than scans along the [001] or $[1\bar{1}0]$ azimuths. The fact that the R-factor plot for the $[1\bar{1}2]$ azimuth shown in figure 3 minimises for a bulk contraction of the crystal structure may be considered as indicating that the Cu {110} single crystals have a contracted outermost layer spacing.

Figure 4 shows the comparison of the best-fit SSCC's with the experimentally measured XPD polar plots. The theory curves are calculated for a Cu cluster with bulk Cu {110} in-plane spacings and an inter-layer spacing of 1.18 Å (obtained from the minimum of the averaged R-factor plot in figure 3). In the case of the [001] and $[1\bar{1}0]$ theory curves the forward focusing peaks at normal emission have been arbitrarily reduced by a factor of 5 to aid the comparison of the off-normal features. On the experimental curves, the positions of the off-normal forward focusing peaks are in good agreement with those predicted in figure 2 on the basis of simple geometry.

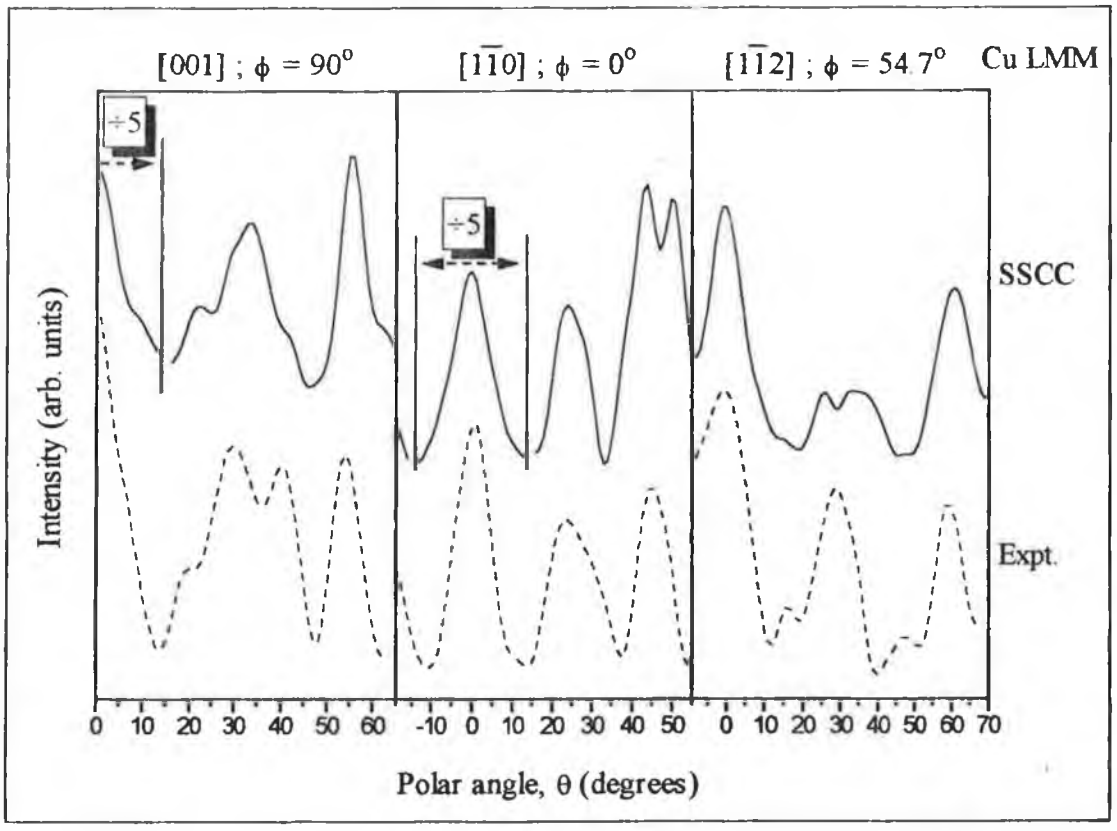

Figure 4: Comparison of SSCC's (solid lines) with experimental polar XPD curves (dashed lines) for polar scans along the [001], [1$\bar{1}$0] and [1$\bar{1}$2] azimuths of Cu {110}.

3.2. Clean CuPd [85:15] {110} p(2x1):

Equivalent polar XPD scans to those measured from Cu {110} were measured from the p(2x1) alloy surface of a CuPd [85:15] bulk alloy. In this case, the scans were measured by monitoring the electron emission from the Cu LMM Auger and from the Pd $3d_{5/2}$ photo-peak (KE~1150 eV). As mentioned in the introduction, it has been demonstrated that the p(2x1) structure formed on the CuPd [85:15] bulk alloy results from a CuPd-p(2x1) ordered 2nd layer. Studies of the Pd depth profile in the bulk alloy upon formation of the p(2x1) surface structure have shown that the Pd concentration modulates into its bulk layer value of 15% [15]. The outermost layer is pure Cu. The 2nd layer consists of approximately 50% Pd forming a p(2x1) structure. The 3rd layer is depleted of Pd while the 4th is enriched relative to the bulk composition (5% and 25% Pd respectively). Deeper layers have effectively bulk composition, although a small concentrations modulation may persist in the 5th and 6th layers.

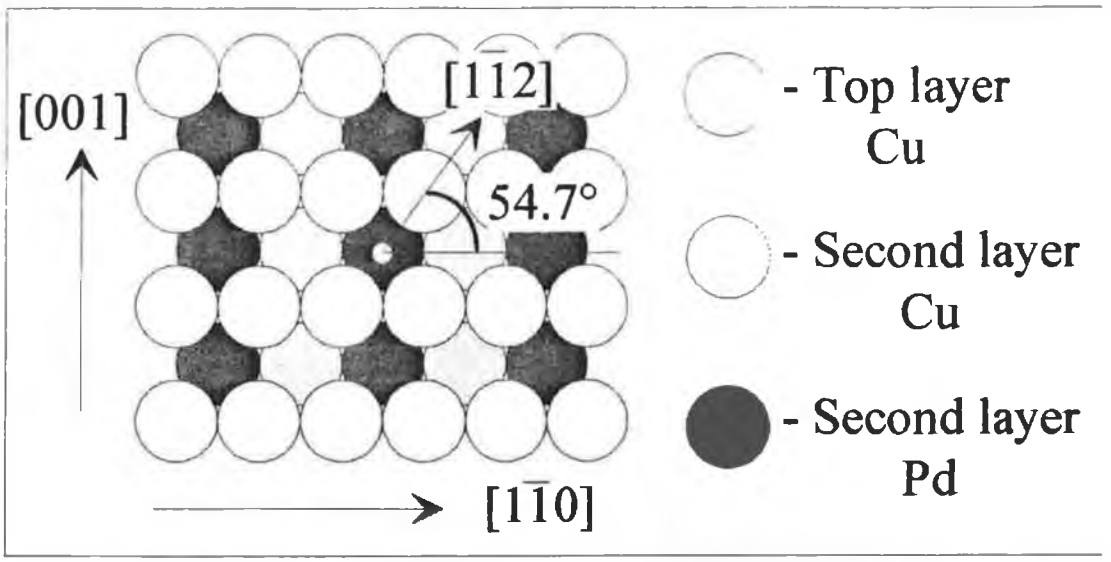

Figure 5: Schematic of the CuPd [85:15] p(2x1) surface. Electrons emitted from the 2nd layer Pd atoms can only be forward scattered by the top layer Cu atoms along the [1$\bar{1}$2] surface azimuth.

Figure 5 shows an illustration of the CuPd [85:15]-p(2x1) surface. Due to the relatively high concentration of Pd in the crystal 2nd layer, polar scans along the [1$\bar{1}$2] crystal azimuth using Pd emission should be strongly sensitive to the outermost layer spacing. This sensitivity is enhanced by the depletion of 3rd layer Pd. No forward focusing features originate from 2nd layer atoms along the [001] or [1$\bar{1}$0] azimuths. Polar XPD curves measured using Pd emission along these azimuths will be significantly less surface sensitive than the [1$\bar{1}$2] azimuth, since the Pd concentration is more uniform below the 3rd layer. In the case of polar XPD scans measured using Cu emission, the layer-wise contribution to the forward focusing features should be similar to that from a bulk Cu {110} single crystal along all azimuths.

Figure 6 shows experimentally measured polar XPD curves from the CuPd [85:15] {110} bulk alloy and from Cu {110} using Cu LMM emission. Because the emission energy is the same in both cases the curves can be compared directly The most notable change is the large shift in the position of the off-normal forward focusing peak on the polar scan measured along the [001] azimuth. On the curve measured from Cu {110} this peak is located at the expected position of ~55°. However, on the curve measured from the bulk alloy this peak is strongly shifted to ~51°. This shift

indicates a deviation of the crystal structure from bulk fcc. It may be due to a selvedge localised effect, although a bulk structural change is also possible. The off-normal forward focusing peak does not appear to consist of two component, as would be expected if the bulk structure was substantially different from that of the selvedge.

On the curves measured along the $[1\bar{1}2]$ azimuth there is no detectable change in the position of the off-normal forward focusing peak. The off-normal forward focusing peak measured from the bulk alloy along the $[1\bar{1}2]$ azimuth is significantly broader than the equivalent peak measured from the Cu {110}. This may be an indicator of multiple local scattering geometries (disorder) within the surface selvedge. There are two small peaks on the $[1\bar{1}2]$ azimuth scan measured from Cu {110} (at θ=20° & 50°) that are absent from the equivalent scan measured from the bulk alloy. The absence of these peaks is an indicator of structural differences between the Cu {110} and the CuPd {110} single crystals.

Figure 7 shows the polar XPD curves measured from the CuPd [85:15] crystal using Pd $3d_{5/2}$ emission. The arrow on each plot indicates the expected off-normal forward focusing peak position for a bulk terminated fcc {110} crystal structure neglecting refraction effects (see figure 2). As was the case for the Cu emission in figure 6, there is a large shift in the off-normal peak position on the polar scan along the [001] azimuth. The peak is shifted by ~5° toward normal emission. This compares well with the ~4° shift observed for Cu emission. In the case of the $[1\bar{1}0]$ azimuth there is a small shift of the forward focusing peak toward normal emission. However, this shift (~2.5°) is significantly smaller than that observed for the polar scans along the [001] azimuth. In the case of the $[1\bar{1}2]$ azimuth there is no observable shift in the position of the off-normal forward focusing peak, also in agreement with the Cu emission scan along this azimuth.

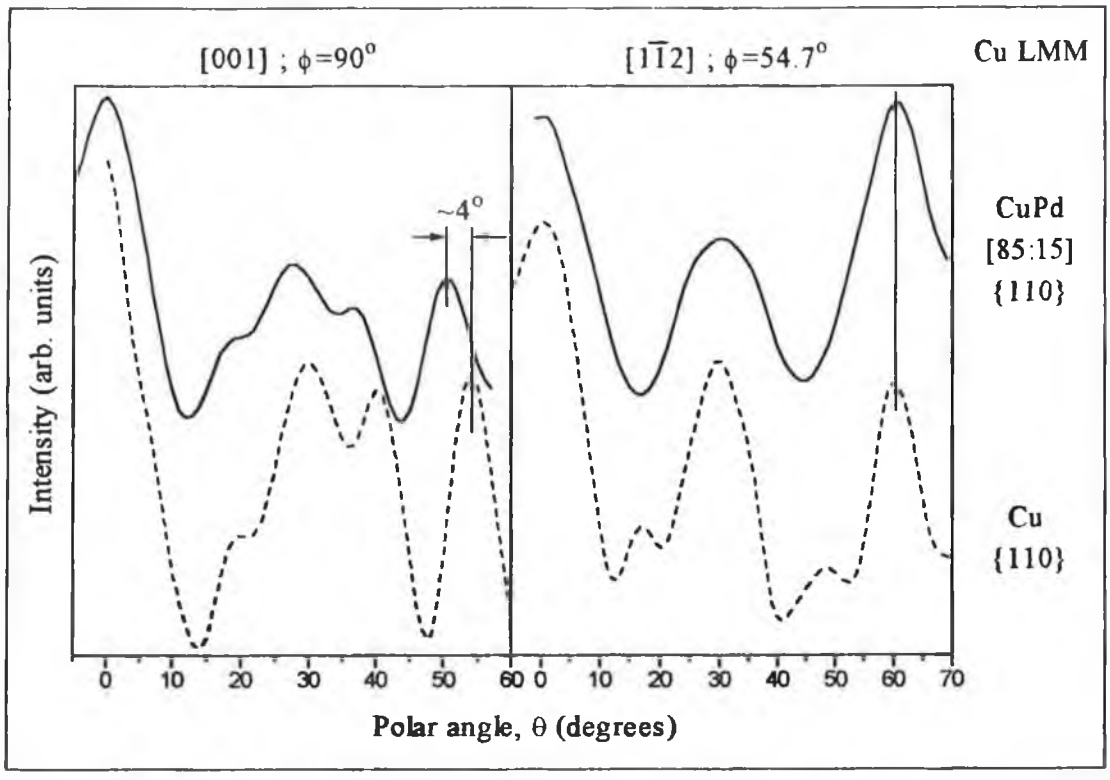

Figure 6: Polar XPD curves measured from the CuPd [85:15] {110} bulk alloy and from Cu {110} using Cu LMM emission.

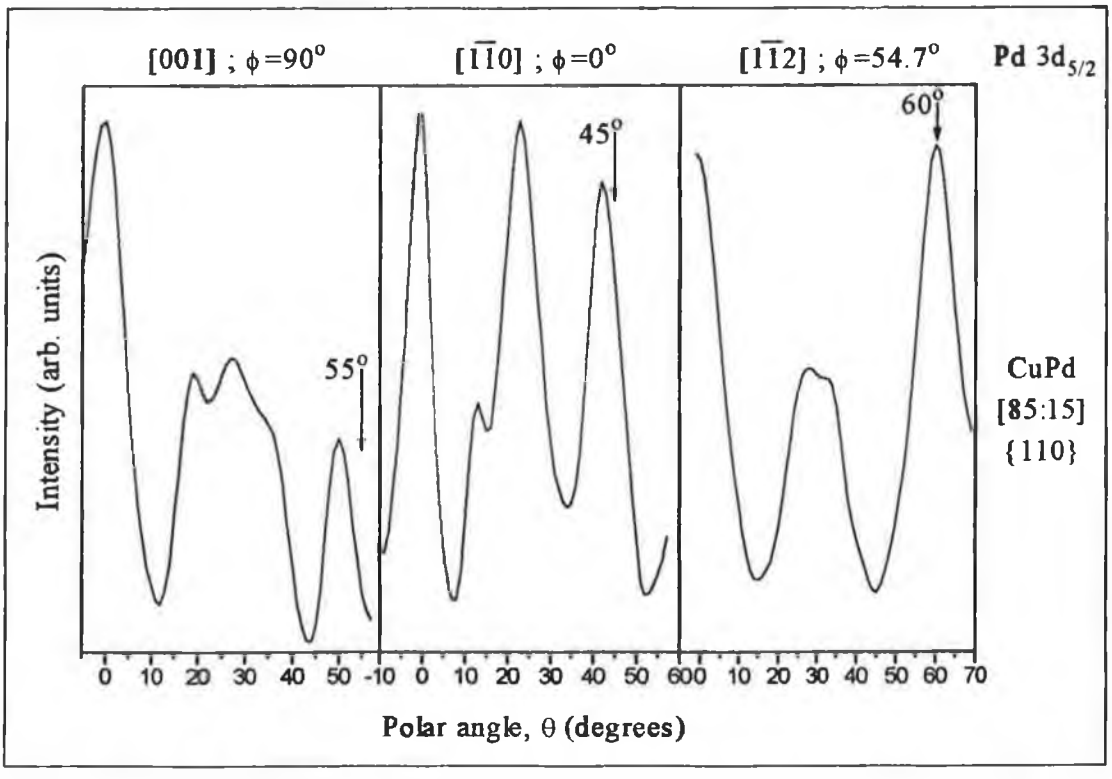

Figure 7: Polar XPD curves measured from the CuPd [85:15] (110) bulk alloy using Pd $3d_{5/2}$ emission. The arrows correspond to the ideal off-normal forward focusing peak positions for a bulk {110} lattice.

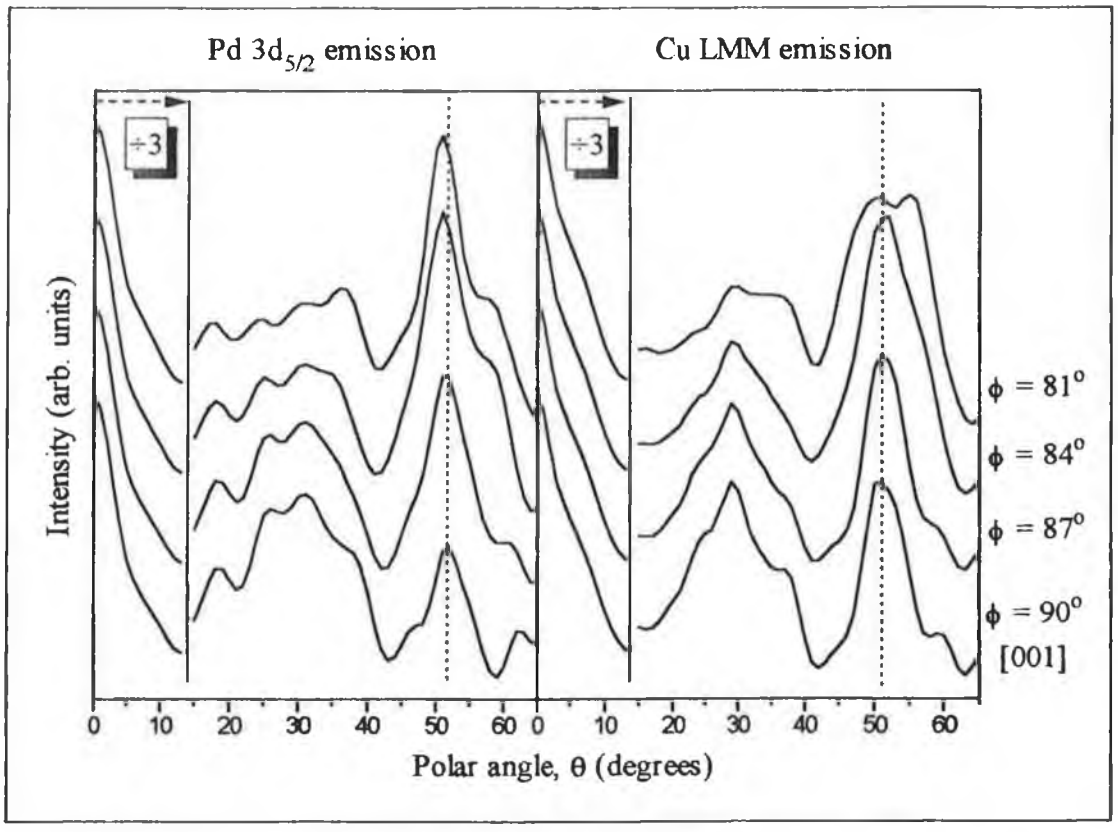

Figure 8: SSCC's done for a CuPd cluster at azimuthal angles of 81°, 84°, 87° and 90° using Pd 3d and Cu LMM emission. ϕ=90° corresponds to the [001] azimuth.

The first point that it is necessary to address is whether the large peak shift observed on the polar scans along the [001] azimuth could arise from a misalignment of the crystal azimuthal direction. This can tested simply by doing a series of SSCC's for different azimuthal rotations of the cluster. Polar XPD SSCC's from a CuPd [85:15] alloy cluster were calculated at azimuthal angles (ϕ) of 90° ([001] azimuth) and 87°, 84° and 81° (3°-, 6°- and 9°-off [001] azimuth respectively) utilising both Pd and Cu emission. The Pd composition was modulated into the bulk as outlined in the experimental section.

The resultant curves are shown in figure 8. Clearly, while there are changes in peak shape, there is no significant shift in the peak maximum for polar scans along azimuths up to 9°-off the [001] azimuth. A second component does appear strongly at a *higher* polar angle on the curves calculated for ϕ=81°, but there is no evidence of any new feature *nearer* to normal emission. Experimentally, the azimuthal alignment was

estimated to be accurate to within ±2°. Hence, we can conclude that azimuthal misalignment cannot cause the large peak shift observed.

Bulk alloys of Cu and Pd form across the entire range of compositions. The lattice parameters of the alloys approximately follow Vergard's law. Consequently, for the CuPd [85:15] {110} crystal the expected in-plane parameters are ~2.583 Å and ~3.652 Å with an expected bulk inter-layer spacing of ~1.291 Å. For the purpose SSCC modelling of electron emission from the alloy, the in-plane parameters were fixed at those listed above. The number of layers and the in-plane size was twice the IMFP of the appropriate emitter (Cu or Pd, see experimental). A preliminary set of polar SSCC's was carried out using a bulk terminated cluster and varying the bulk inter-layer spacing between 0.89 Å and 1.89 Å in 0.1 Å steps.

Figure 9 shows the R-factor plots obtained by comparison of these calculations with the experimental XPD curves. The averaged R-factor plots minimise at 1.39±0.05 Å.

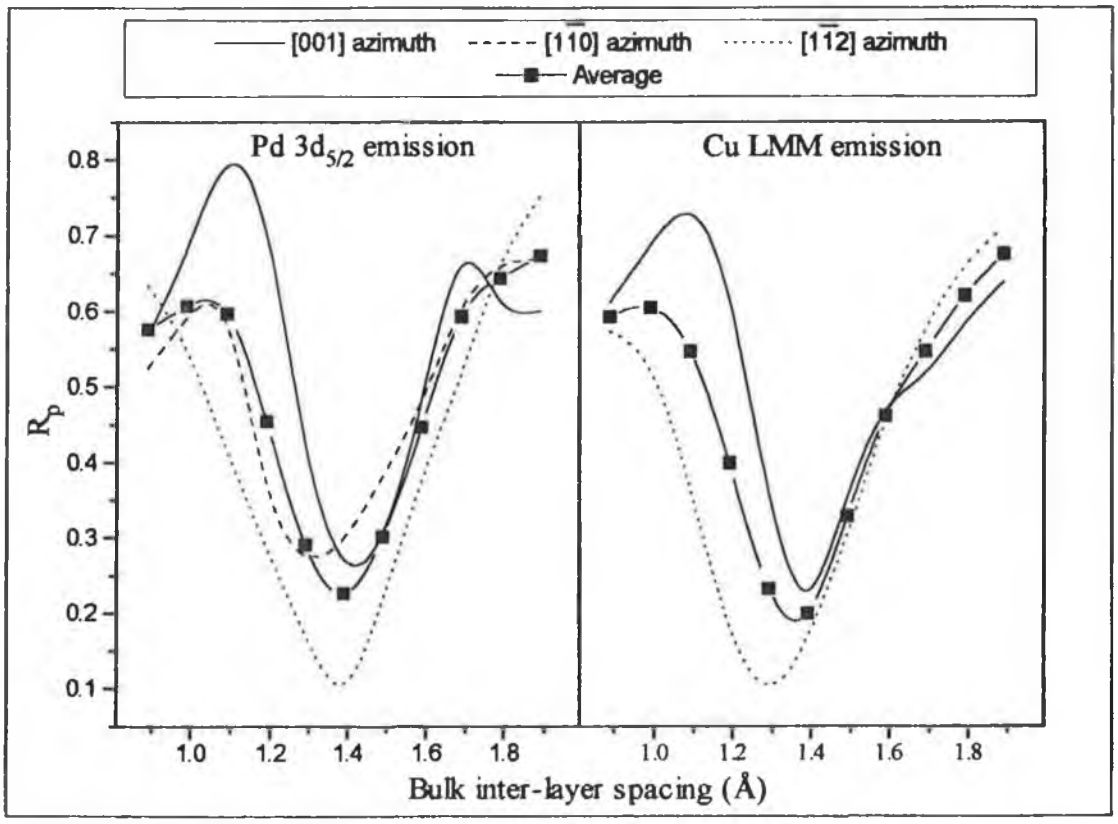

Figure 9: R-factors plots for comparison of SSCC's (see text) with polar XPD curves measured from the CuPd [85:15] bulk alloy. The curves due to Pd and Cu emission are shown separately.

This is observed for the comparison of theory with experiment for both Pd emission and Cu emission. The R-factor plots for the polar scans along [001] azimuth agree well with the averaged plot. The sharpness of the minima obtained for the [001] scans are undoubtedly strongly influencing the overall average minimum. The R-factor curves for the $[1\bar{1}0]$ and $[1\bar{1}2]$ azimuths minimise at lower values of the bulk inter-layer spacing. In particular, the curves for emission from Cu along the $[1\bar{1}2]$ azimuth and from Pd along the $[1\bar{1}0]$ azimuth both minimise at ~1.29 Å, which is the expected bulk inter-layer spacing for a CuPd [85:15] alloy following Vergard's law. The minimum indicated by the [001] azimuth and the averaged plots of ~1.39 Å correspond to an expansion of ~7.75% from the bulk value.

The minima obtained for the individual azimuthal directions display the trend which would be expected on the basis of the position of the off-normal forward focusing peaks seen on the experimental curves. A shift in the peak position toward normal emission equates with an expansion of the inter-layer spacing *if* the in-plane lattice parameters are fixed at bulk values. The larger the shift, the greater the corresponding expansion.

The R-factor analysis points to an expansion of the CuPd inter-layer spacing from the expected bulk value by ~0.1 Å. However, a number of discrepancies exist between this result and the forward scattering peak positions shown in figures 6 & 7. Firstly, the shift of the off-normal peak on the [001] polar scan (55°→50°) is, on the basis of simple geometric considerations, indicative of a much larger expansion of ~0.4-0.5 Å. Secondly, a simple expansion of the inter-layer spacing should be observed as a shift in the position of the off-normal forward focusing peak along all 3 high symmetry azimuths and this shift should be of approximately equal magnitude along each of the azimuths. While there is a small shift of ~2.5° along the $[1\bar{1}0]$ azimuth, there is no observable shift along the $[1\bar{1}2]$ azimuth. It is arguable that the high local concentration of Pd in the 2nd layer of the alloy could mask a peak shift in the Pd emission polar scan along the $[1\bar{1}2]$ azimuth *provided* there is no change in the 1st-to-2nd layer spacing (i.e. if the expansion is solely in the 2nd-to-3rd and/or deeper layer

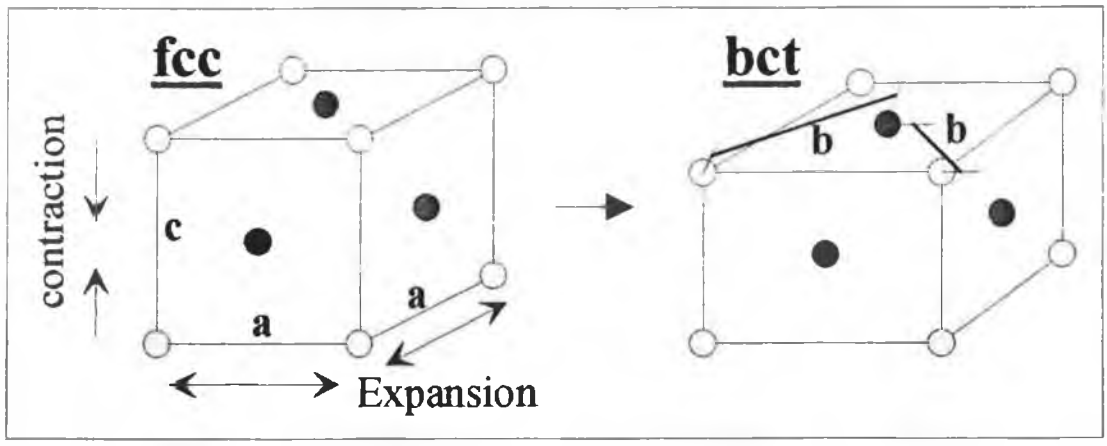

Figure 10: Illustration of the distortion of a fcc unit cell to a bct structure.

spacings). However, this argument does not hold for the Cu emission scan, which also shows no peak shift along the [1$\bar{1}$2] azimuth.

One possible explanation for the above discrepancies is that the CuPd lattice structure is *body centred tetragonal* (bct). This is basically a distorted fcc lattice structure as discussed for Co overlayers grown on Pd {100}. It is formed by expanding two axes of the crystal unit cell while simultaneously contracting the third axis. Taken to an extreme, it eventually converts an fcc structure into a bcc structure. The distortion of an fcc to a bct structure is shown in figure 10. The fcc structure has a unit cell with sides of equal length (i.e. c=a). Upon distortion to a bct structure this no longer holds true. If the expansion/contraction is sufficiently large, c will become equal to b and the structure becomes bcc.

The existence of the CuPd alloy in a bct crystal lattice structure can provide a more consistent explanation of the peak positions observed on the polar scans shown in figures 6 & 7. In order for a bct single crystal to have a {110} surface the 'contracted' side of the unit cell must lie along the surface [001] azimuth. The two expanded sides can be considered as lying along the surface [1$\bar{1}$0] azimuth and along the surface normal. It is worth noting at this point that the unit cell does not require a simultaneous contraction/expansion in order to be bct. Merely contracting one (or expanding two) of the fcc unit cell sides will yield a bct-like structure. However, a simultaneous contraction/expansion is required if the unit cell (and the bulk crystal) is to maintain its density.

If we assume a simultaneous contraction/expansion of the CuPd 'fcc' unit cell sides then the large shift in the off-normal forward focusing peak on the [001] polar scan can be readily explained. The contraction acts along the [001] azimuth of the single crystal while one of the expansions acts along the surface normal (i.e. increases the inter-layer spacing). Both these effects would serve to shift the off-normal forward focusing peak on the [001] polar scan toward normal emission. The cumulative effect would be a peak shift substantially greater than would be expected from a simple contraction or expansion of a single lattice parameter.

For a bct structure, two of the original fcc unit cell sides are expanded by an equal amount. One of these expansions would act along the $[1\bar{1}0]$ azimuth of a {110} crystal and the other along the surface normal. The cumulative effect of an equal expansion along the $[1\bar{1}0]$ azimuth and along the surface normal should be no net change in the position of the forward focusing peaks on the $[1\bar{1}0]$ polar XPD scan (i.e. the off-normal forward focusing peak should remain at ~45°). The small shift actually observed on the $[1\bar{1}0]$ Pd polar XPD should not appear for an ideal bct structure.

The situation for a polar scan along the $[1\bar{1}2]$ azimuth of a bct crystal is most complicated. In this case, the in-plane expansion/contraction and the expansion normal to the surface will all affect the relative position of the emitter-scatterer atoms. The in-plane expansion/contraction will shift the polar angle of the main off-normal scattering direction from 54.7° toward a value of 45° (both angles measured with respect to the $[1\bar{1}0]$ azimuth). Changes will occur in the polar scan features as a result of this change in position of the high symmetry azimuthal direction. The in-plane expansion will shift the off-normal forward focusing peak toward normal emission, but the effect will not be as large as for the [001] polar scan.

A series of SSCC's were performed in order to evaluate how well a bct structure matches the XPD measurements made from the CuPd crystal. The in-plane spacing along the [001] azimuth (D_x) was varied between 3.65 Å (bulk Vergard's law) and 3.0 Å in 0.05 Å steps. The in-plane spacing along the $[1\bar{1}0]$ azimuth and the inter-layer spacing were both expanded uniformly in order to maintain the unit cell density for a

given value of D_x. The cluster composition was the same as for the previous calculations. The cluster was bulk terminated (i.e. all layers had the same inter-layer spacing).

Figure 11 shows the R-factor plots obtained for the comparison of the bct SSCC curves with experiment. The R-factor plots for Cu emission show a broad minimum at values of D_x between 3.55 and 3.25 Å. In the case of Pd emission, the $[1\bar{1}2]$ azimuth also shows a broad minimum in this region. The R-factor calculated for the $[1\bar{1}0]$ azimuth is virtually unchanged across the entire range of D_x studied. This is due to the fact that the angle of the off-normal forward focusing peak along the $[1\bar{1}0]$ azimuth is relatively unaffected by the bct distortion, and reflects the degree to which forward focusing dominates single scattering theory. This is especially true when the forward focusing occurs along a chain of atoms as in a bulk cluster. The only curve that demonstrates a well defined minimum is that for Pd emission along the [001] azimuth,

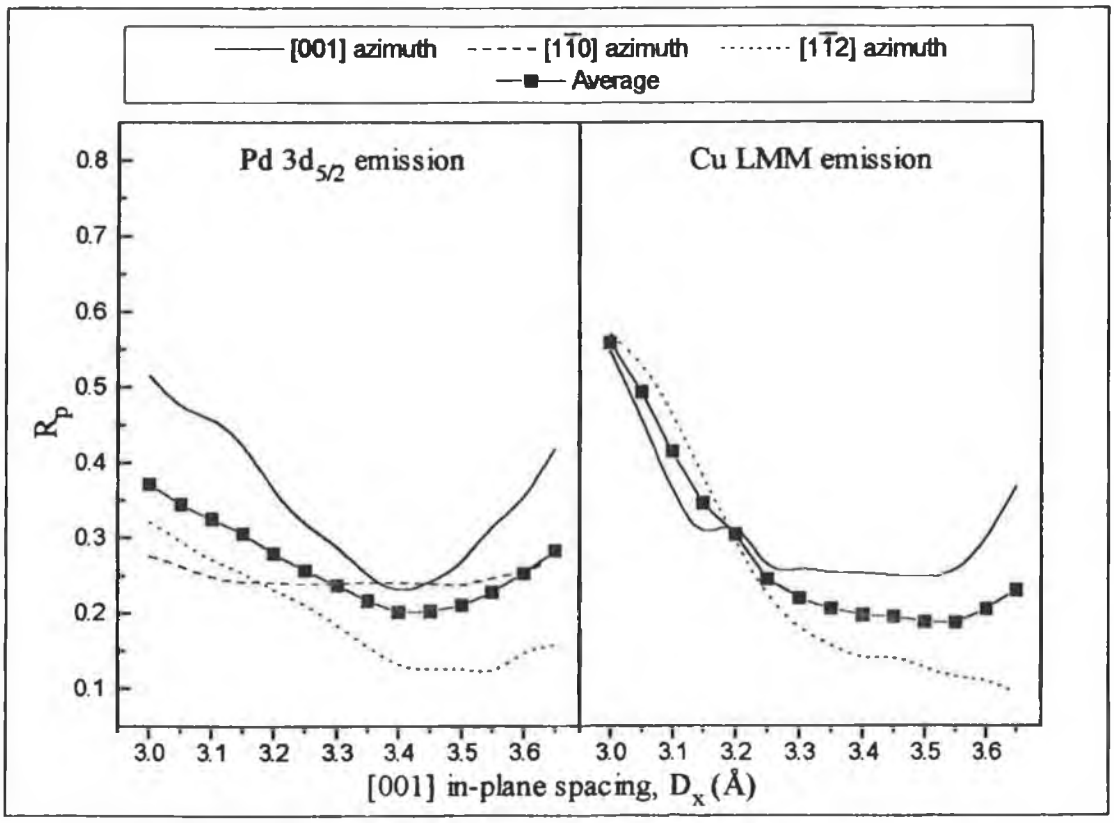

Figure 11: R-factor plots for comparison of bct SSCC's with experimental polar XPD curves. D_x corresponds to the in-plane lattice spacing along the [001] azimuth of the clusters.

which occurs at D_x=3.4 Å. The minimum R-factor obtained is of similar quality to that obtained previously for minimisation using a bulk expansion of the inter-layer spacing (figure 9). On the basis of maintaining the unit cell density, the lattice parameters corresponding to the minimum in figure 11 are 2.676 Å and 3.4 Å in-plane and 1.338 Å inter-layer spacing.

Figures 12 & 13 show the comparison of the experimental curves with SSCC's for Pd and Cu emission respectively. The theory curves correspond to the best fit determined from figures 9 & 11 on the basis of the averaged R-factor plots. In the case of the 'bulk expansion' curves, the in-plane lattice parameters are fixed at those determined by Vergard's law (2.583 Å and 3.652 Å) with a expanded inter-layer spacing set at 1.39 Å. The lattice parameters of the bct phase were as outlined above. The level of agreement between experiment and both theoretical structures is similar, as can be judged from the R-factors for the individual SSCC's quoted on the figures. On the basis of the R-factors and visual comparison, the bct model yields a slightly better fit.

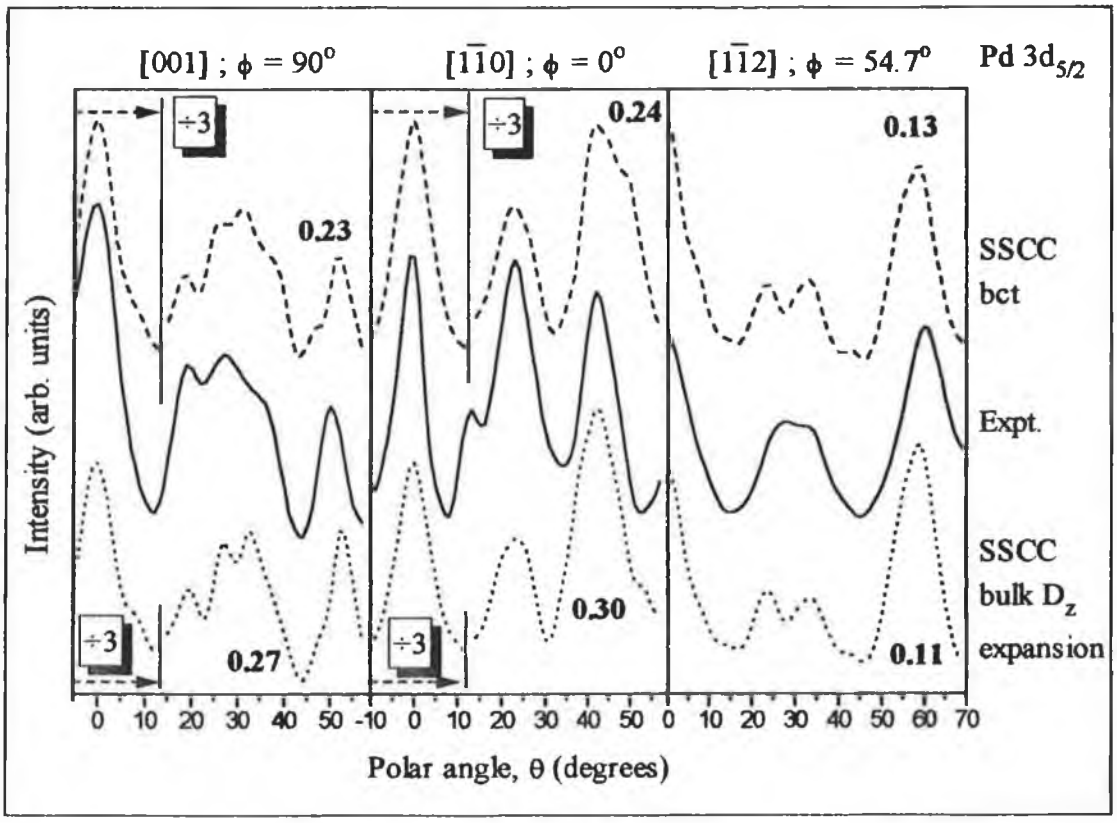

Figure 12: Comparison of polar XPD curves, measured using Pd 3d emission from CuPd [85:15], with the best fit SSCC's for a bct cluster lattice and a cluster with a bulk expansion of the inter-layer spacing.

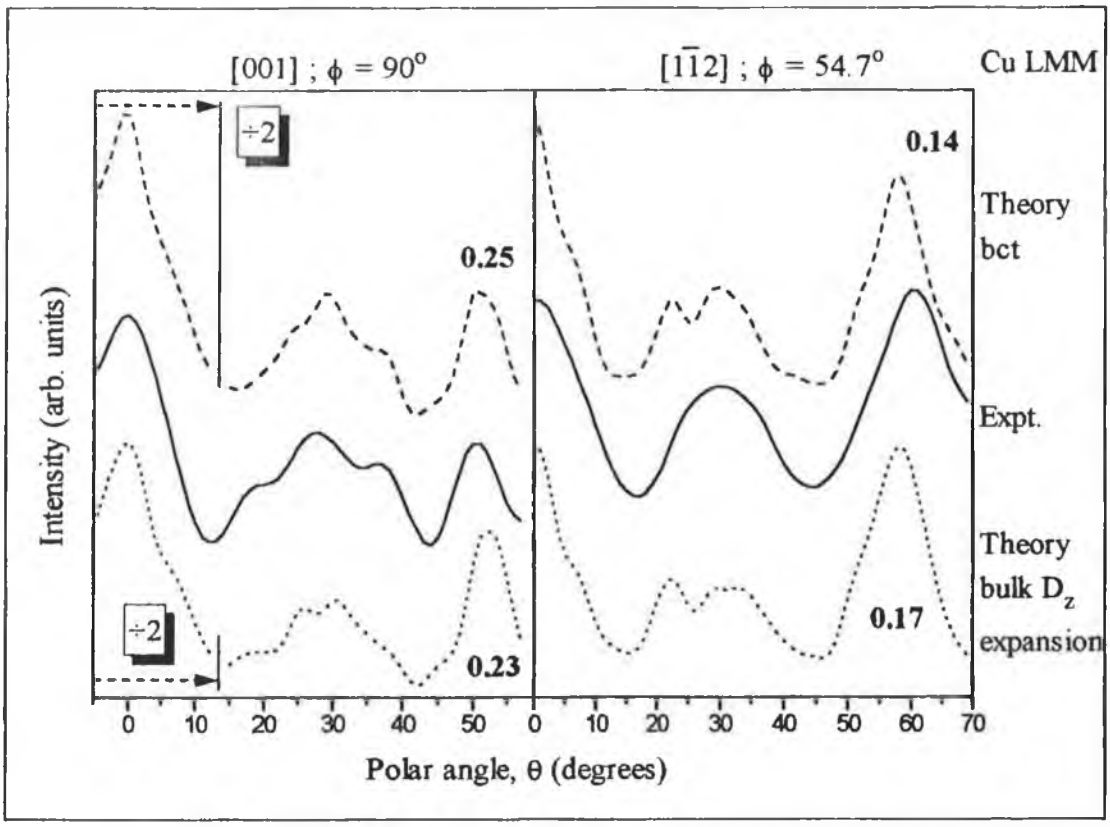

Figure 13: Comparison of polar XPD curves, measured using Cu LMM emission from CuPd [85:15], with the best fit SSCC's for a bct cluster lattice and a cluster with a bulk expansion of the inter-layer spacing.

However, considering the average of the 5 R-factors (bct=0.198, bulk expansion=0.216), both models must be regarded as adequately fitting the measured spectra.

Both the models considered above (bct distortion and D_z spacing change) have involved bulk structural changes (i.e. they occur uniformly throughout the cluster used to perform the SSCC's). For the bct model this is a realistic assumption. It is difficult to envisage the CuPd selvedge adopting a bct structure if the bulk crystal is fcc. However, in the case of the inter-layer spacing change, it is probable that the change may be localised in the crystal selvedge, with the bulk crystal adopting the 'ideal' inter-layer spacing. This could occur as a result of the unusually high concentration of Pd in the 2nd layer of the crystal. Merely considering the size differential between Cu and Pd (Pd~7.7% larger) leads to the conclusion that an expansion of the 1st-2nd (D_{12}) and 2nd-3rd (D_{23}) inter-layer spacings is possible.

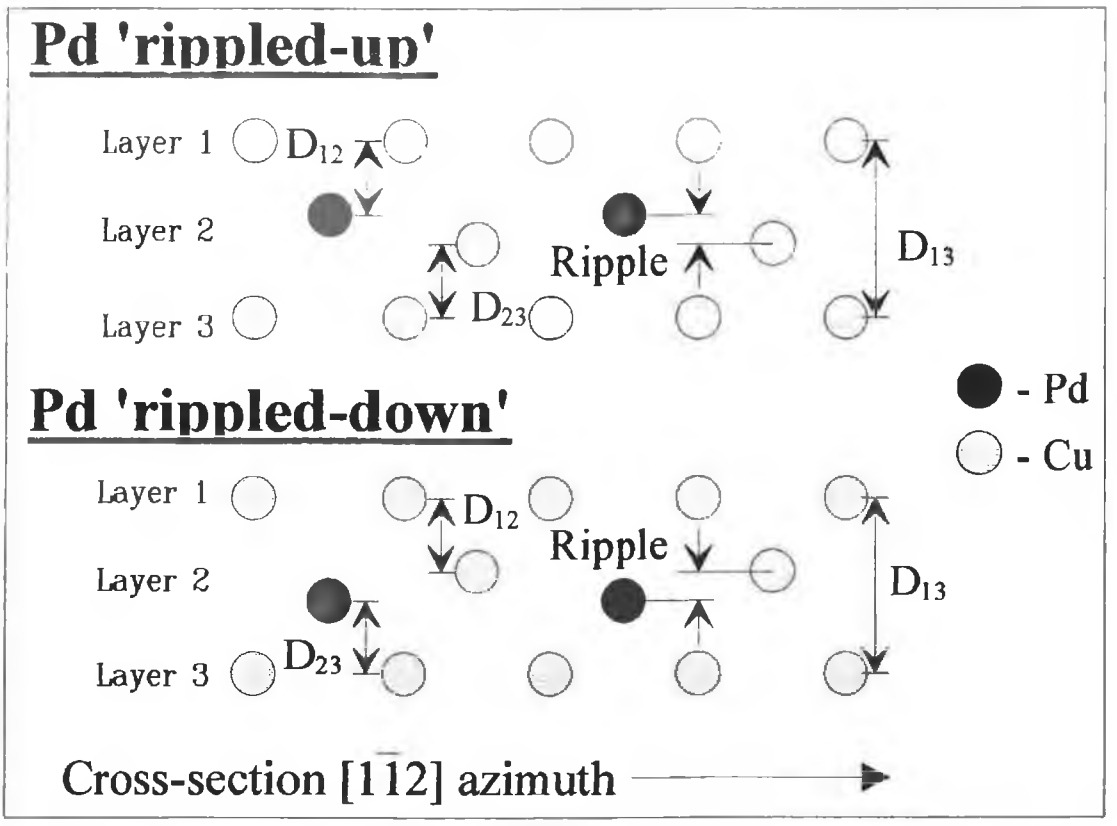

Figure 14: Illustration of the rippling done on the 2nd layer atoms in the SSCC clusters, as outlined in the text.

Furthermore, if the Pd is 'rippled' within the 2nd layer as a result of the difference in atomic size, then an expansion becomes more likely.

A series of SSCC's were carried out on a CuPd alloy cluster (composition as before) where only the 2 outermost layer spacings and the relative position of the Cu and Pd in the 2nd layer were varied. The inter-layer spacing for deeper layers was maintained at 1.29 Å (Vergard's law). The in-plane parameters of all layers were also set to values determined by Vergard's law. The layer spacings, D_{12} and D_{23}, were varied independently of each other between values 0.9 Å and 1.7 Å in 0.1 Å steps. In addition, the Pd atoms within the 2nd layer of the cluster were rippled between 0.0 Å (no rippling, co-planar with the Cu atoms) and 0.6 Å in 0.1 Å steps. SSCC's were performed with the Pd atoms rippled both above and below the Cu atoms. For the calculations where the 2nd layer Cu and Pd atoms were not co-planar, D_{12} denoted the spacing between the top layer and the 'rippled-up' atoms of the 2nd layer, whereas D_{23} denotes the spacing between the 3rd layer and the 'rippled-down' atoms of the 2nd

layer. Hence the 1^{st}-3^{rd} layer separation (D_{13}) is given by D_{12}+D_{23}+Ripple (see figure 14 for illustration).

As was noted earlier, the forward focusing features calculated by SSCC's are less surface sensitive than is actually experimentally observed. Hence, calculations done for a bulk cluster (many layers) tend to be dominated by features originating from the bulk. As a consequence the calculations are relatively insensitive to change solely in the outermost layer spacings of the cluster. In an attempt to counteract this effect the clusters used in the current set of calculations have been limited to a thickness of 6 layers. The in-plane cluster size is restricted based on the calculated IMFP's. Four of the 6 layers used in the calculation can be considered as 'bulk'. These should be sufficient to simulate the main XPD features originating from the crystal bulk. The use of a limited cluster thickness is a mechanism, albeit imperfect, through which the effect due to the neglect of defocusing by single scattering theory can be minimised. As the cluster is only 6 layers thick defocusing is no longer a significant factor in the

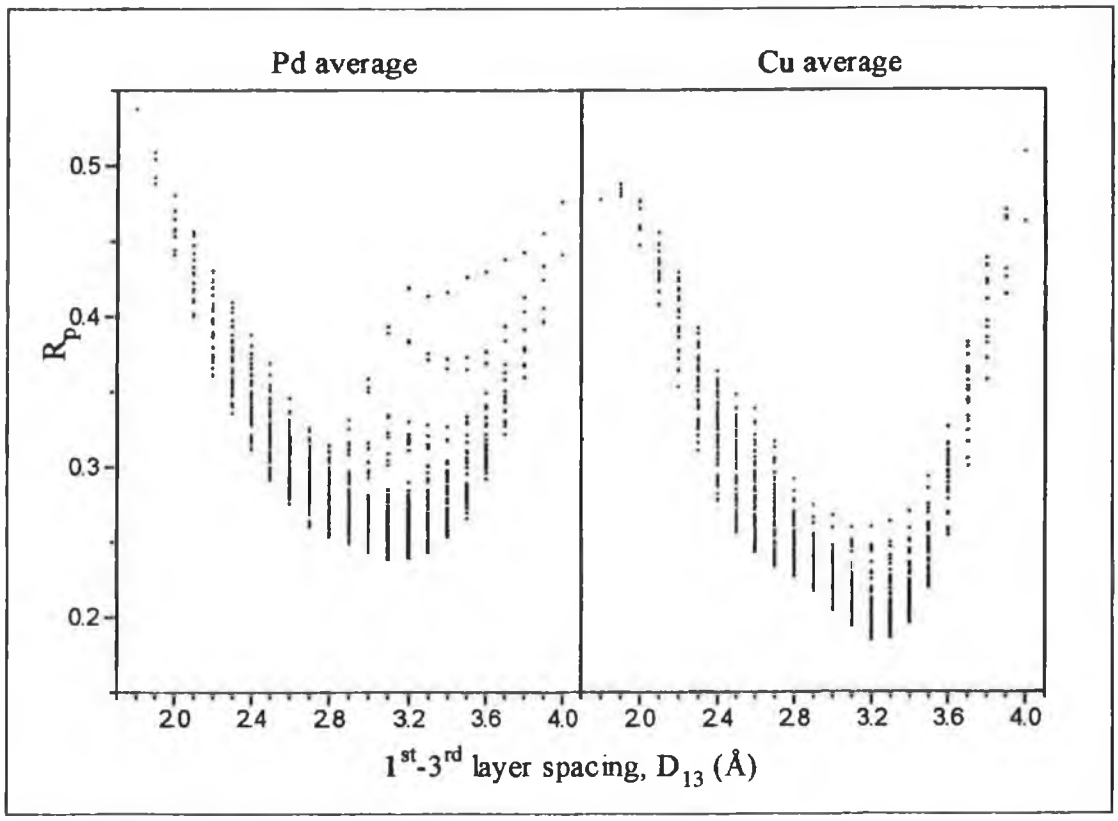

Figure 15: R-factor scatter plot with respect to D_{13}. The averaged R-factors for the comparison of Pd and Cu SSCC's with experiment are shown separately.

scattering process due to the absence of long 'chains' of scattering atoms

Due to the large number of different structures inherent in the range of parameters outlined above (1053 separate calculations), the determination of the level of agreement between theory and experiment relies heavily upon R-factor analysis. Three independent structural parameters can be identified in the calculation set. These are, the separation between layer 1 and layer 3 (D_{13}), the separation between layer 1 and the Pd in the 2nd layer (D_{1Pd}) and the separation between layer 1 and the Cu in the 2nd layer (D_{1Cu}). All other parameters, such as the rippling of the 2nd layer atoms, can be obtained from these 3 parameters.

All curves were compared with the experimental curves by means of Pendry R-factor analysis. The R-factors calculated for the comparison of the 3 Pd azimuths were averaged, as were those calculated for the 2 Cu azimuths. Figure 15 shows the R-factors obtained for different values of D_{13} using Pd and Cu emission. For any given value of D_{13} there are numerous data points. These correspond to different combinations of D_{12}, D_{23} and Ripple that sum to the same value of D_{13}. Structural information can be deduced on the basis of trends in the R-factor plots. A trend is clearly visible in the scatter plots shown in figure 15. In the case of the Pd plot the points tend to a minimum at values of D_{13} between 2.7-3.4 Å. In the case of the Cu plot the minimum is some what sharper, falling between 3.0-3.4 Å. Both indicate an expansion from the bulk termination value (~2.6 Å).

Plotting the variation of the R-factor points versus D_{1Pd} and D_{1Cu} in the same manner does not reveal a clear minimum similar to that seen for D_{13} in figure 15. This can be attributed largely to the fact that forward scattering between the 1st and 2nd layers of the crystal occurs only along the $[1\bar{1}2]$ azimuth. The scans along the other azimuths are relatively insensitive to changes in the outermost inter-layer spacing (and hence in the two parameters D_{1Pd} and D_{1Cu}). As a consequence the averaged R-factor plots are also insensitive to changes in these parameters.

The fact that there is an unusually high concentration of Pd in the 2nd layer of the alloy selvedge can be used to determine the D_{1Pd} spacing. The Pd enrichment of the 2nd layer coupled with the depletion of the 3rd layer makes Pd emission polar scans along the [1$\bar{1}$2] azimuth uniquely sensitive to the value of D_{1Pd}. Figure 16 shows R-factor scatter plots versus D_{1Pd} for the comparison of the Pd emission [1$\bar{1}$2] polar scan only with theory. The comparison of the experimental curve with SSCC's where the 2nd layer Pd is rippled *above* the Cu atoms is shown separately from those where it is rippled *below* the Cu atoms. Both plots in figure 16 tend to a minimum at values of D_{1Pd}=1.4-1.7 Å. On the basis of figure 15 & 16, R-factors points which did not match the criteria of 2.7Å<=D_{13}<=3.5Å and 1.4Å<=D_{1Pd}<=1.7Å were discarded. Further points were discarded on the basis of the R-factor value in order to leave only those with the lowest value. The remaining points are plotted with respect to D_{1Cu} in figure 17.

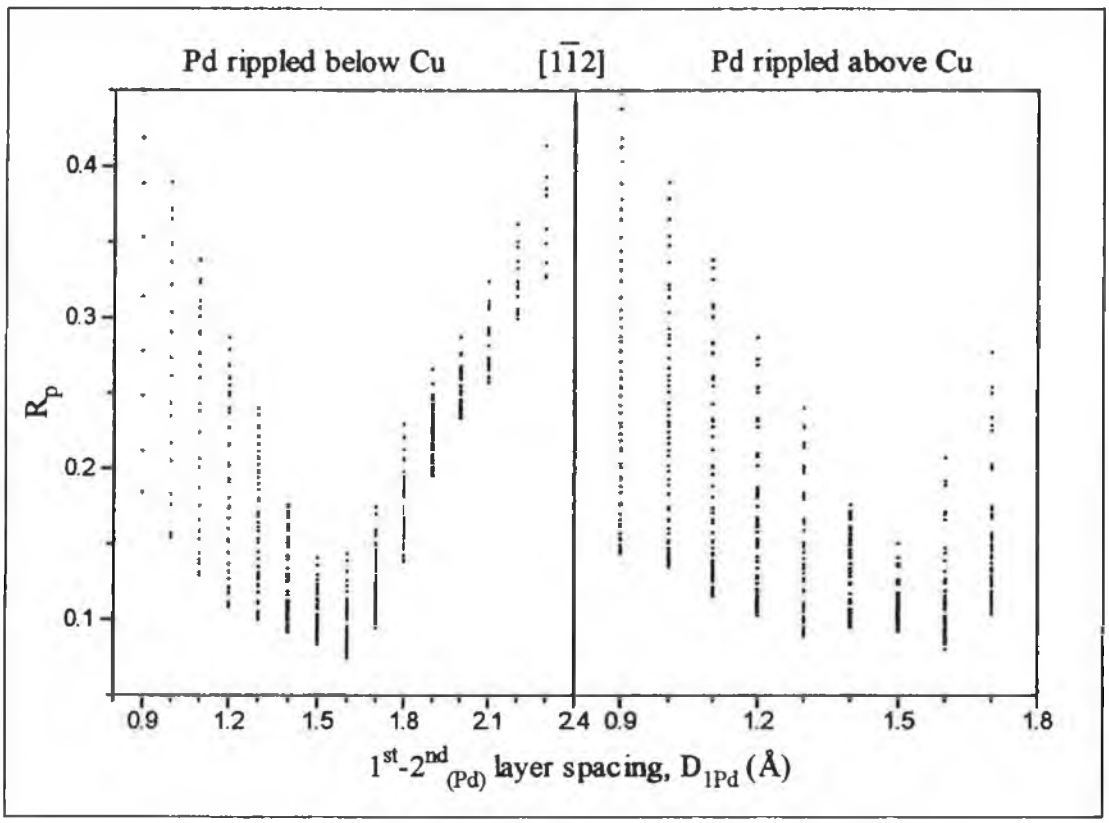

Figure 16: R-factor scatter plots with respect to D_{1Pd}. The points are the result of the comparison of the SSCC's of the Pd polar XPD scan along the [1$\bar{1}$2] azimuth with experiment.

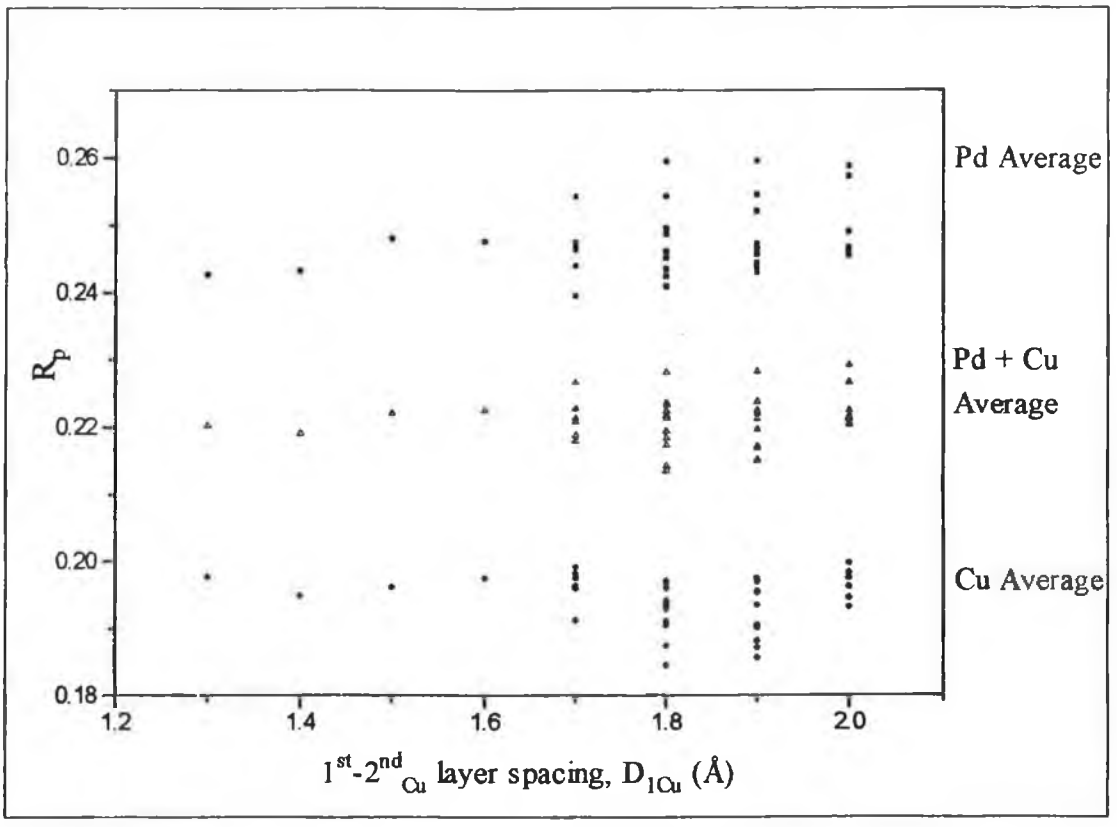

Figure 17: Plot of averaged R-factor points versus D_{1Cu} after points have been discarded on the basis of D_{13}, D_{1Pd} and R-factor values.

The first point to note about figure 17 is that 'minimum' R-factor values are obtained across a broad range of D_{1Cu} (1.3-2.0 Å). This reflects a general insensitivity to the position of the Cu atoms in the 2nd layer. Unlike the situation for the Pd atoms, Cu is depleted in the 2nd layer. Hence, Cu emission polar scans along the $[1\bar{1}2]$ azimuth have a smaller contribution due to emission by 2nd layer atoms in comparison to emission from a bulk Cu crystal. This means that this scan has reduced sensitivity to the 1st-to-2nd layer spacing. and as a consequence none of the Cu polar XPD scans are well suited to probing the D_{1Cu} spacing.

In spite of the factors outlined above, the bulk of the 'minimum' R-factor points are concentrated at values of D_{1Cu} of 1.7-2.0 Å. Although not conclusive, this is an indication that D_{1Cu} lies between these values. After elimination of the points which do not fall within this range the remaining points are defined by the limits:

$$3.1 \text{ Å} <= D_{13} <= 3.3 \text{ Å}$$

$$1.4\ \text{Å} <= D_{1Pd} <= 1.7\ \text{Å}$$

$$1.7\ \text{Å} <= D_{1Cu} <= 2.0\ \text{Å}$$

The absolute minimum occur at values of D_{13}=3.2 Å, D_{1Pd}=1.6 Å and D_{1Cu}=1.8 Å. The result indicates a small rippling of the 2nd layer, with the Pd above the Cu atoms. Figures 18 & 19 show the comparison of the SSCC's calculated for this set of geometric parameters with the experimental XPD curves. The level of agreement (as indicated by the R-factor values shown on the figures and visually) is similar to that obtained by varying the bulk structural parameters (figures 12 & 13). The average of the five R-factor values (0.220) is similar to the averages obtained for the bulk structural change models (0.198 & 0.216). Overall, a slight preference exists for the bulk bct structural model, but it is by no means conclusive.

The analysis outlined above demonstrates some of the limitations of XPD in the study of bulk alloy surfaces. The most fundamental limitation is a lack of surface sensitivity. For emission from atoms within a single crystal a large portion of the electron intensity in XPD plots originates from the crystal bulk. The result is uniform forward focusing features, upon which relatively small changes are super-imposed by variations in the layer spacings within the selvedge. This makes accurate quantification of effects such as contractions or expansions of the sample selvedge difficult. In such situations XPD is somewhat inferior to more surface sensitive techniques such as LEED. XPD becomes much more useful in situations where its surface sensitivity is artificially enhanced (such as by the enrichment of Pd within the CuPd [85:15] 2nd layer). It is also better suited to the analysis of bulk effects, such as the bct distortion proposed above, where the local geometry of all atoms is approximately identical.

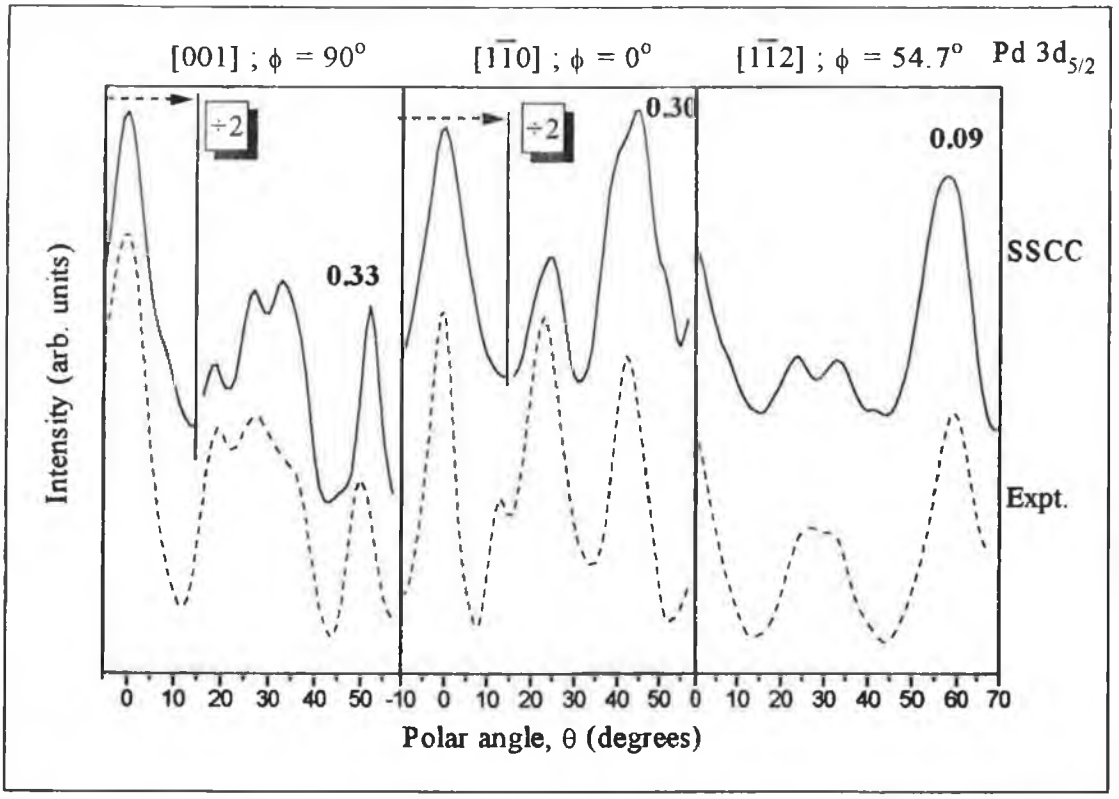

Figure 18: Comparison of polar XPD curves, measured using Pd 3d emission from CuPd [85:15], with the SSCC's for the structural parameters outlined in the text.

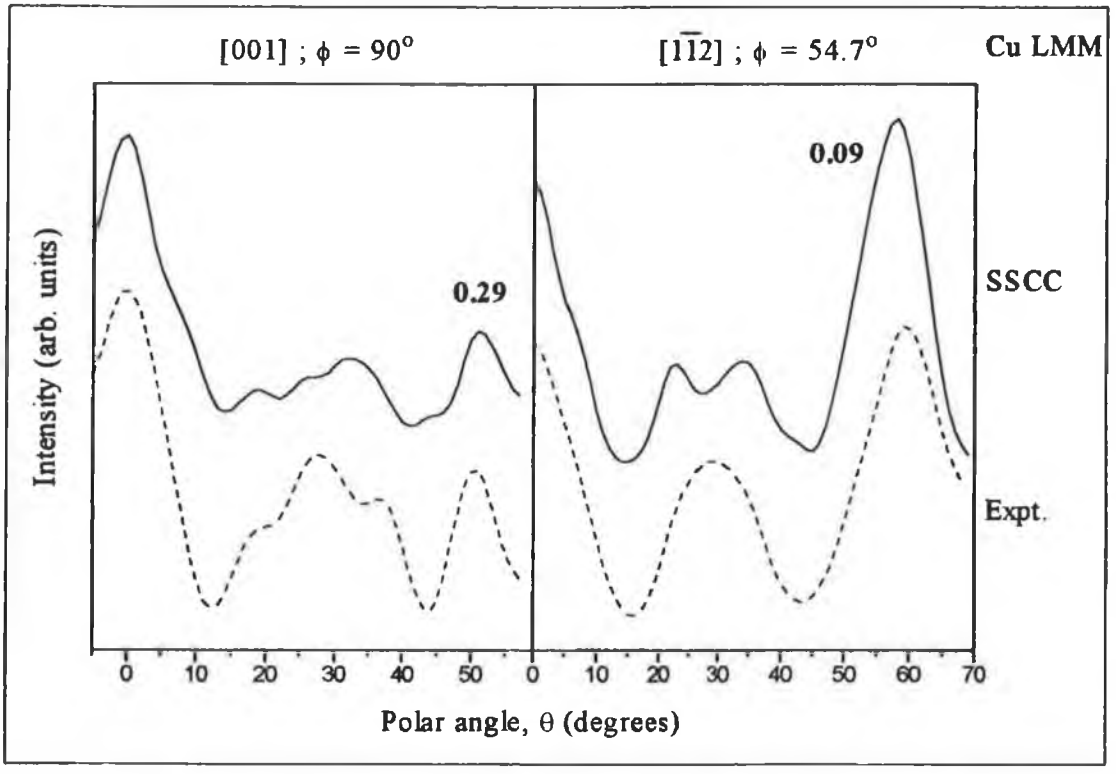

Figure 19: Comparison of polar XPD curves, measured using Cu LMM emission from CuPd [85:15], with the SSCC's for the structural parameters outlined in the text.

3.3. Cu {100}-c(2x2)-Pd surface alloy:

A good example of the power of XPD in situations where the emitting atom is surface localised is provided by the Cu {100}-c(2x2)-Pd surface alloy formed by adsorption of ~0.5 ML of Pd onto a clean Cu {100} surface. A number of studies have found that the optimum c(2x2) LEED pattern is formed just above the half-monolayer coverage (0.55 ML) [21, 22]. The model initially proposed for the surface alloy was a homogenous c(2x2)-Pd outermost layer (see figure 20) [19]. Subsequent LEED-I(V) analysis also favoured this model, although models in which the Pd substituted into deeper Cu layers were not tested [20, 21]. However, application of TPD and XPD to the study of the alloy surface clearly demonstrates that the structure is more complex than the proposed homogenous surface alloy.

Following formation the Cu {100}-c(2x2)-Pd structure, a LEED-I(V) curve was measured from the (1/2,1/2) beam and compared with an equivalent scan measured by Wu *et al* [21] as shown in figure 21. The similarity of the two curves indicates that the c(2x2)-Pd structures obtained in the two studies are quite similar. Comparison of the symmetry equivalent LEED beams indicated that the sample was close to normal incidence (±1°). No sample tilt mechanism was available to allow the crystal to be

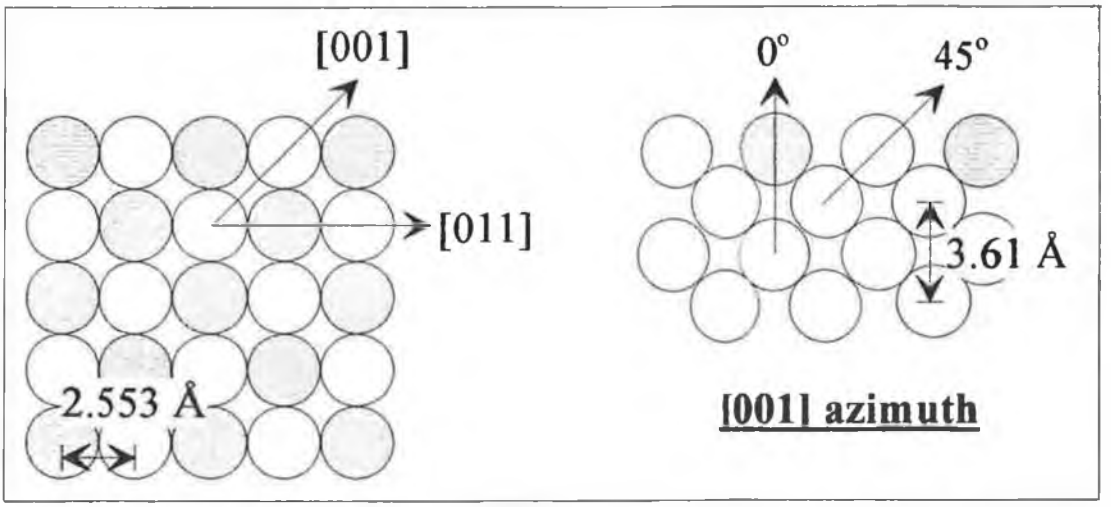

Figure 20: Proposed model of the Cu c(2x2)-Pd two-dimensional alloy (all Pd atoms localised in the outermost layer). The cross-section along the [001] azimuth illustrates the expected forward focusing peaks for a bulk terminated structure (no surface refraction). The lattice parameters shown are for a Cu {100} single crystal structure.

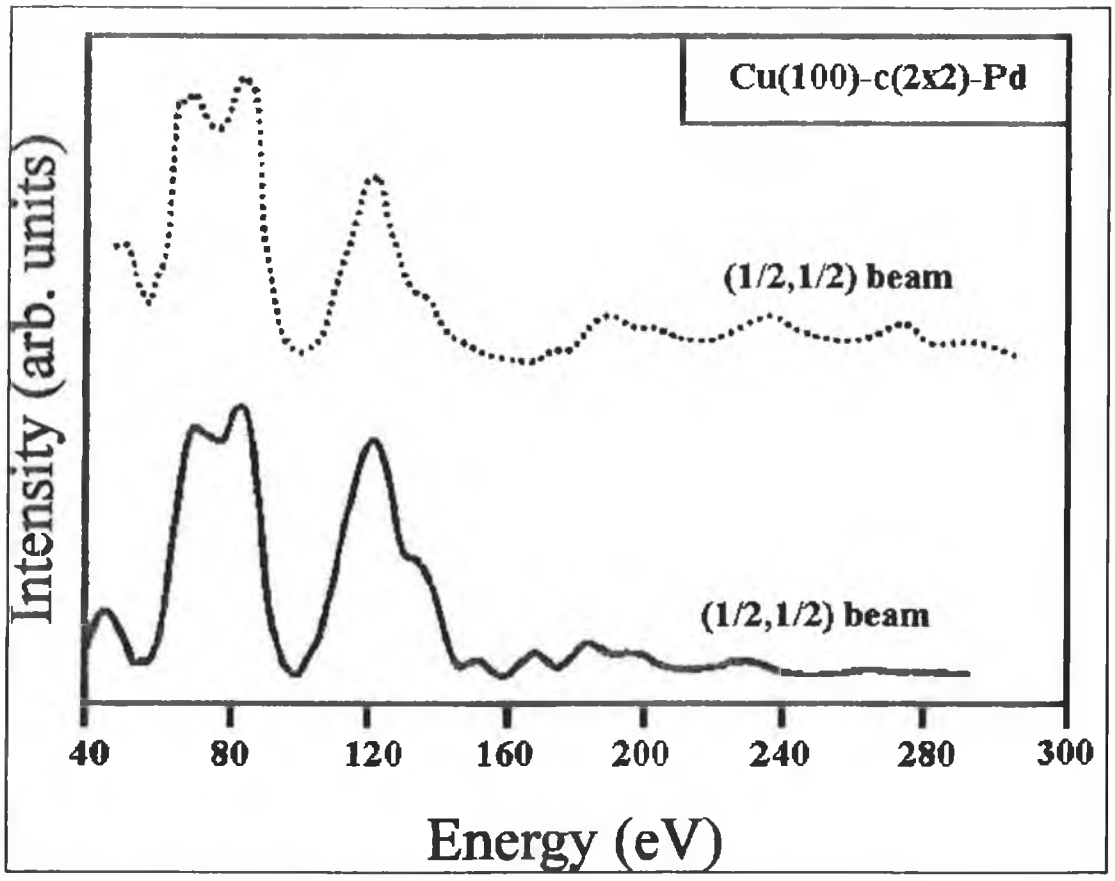

Figure 21: LEED-I(V) spectrum of the (1/2,1/2) beam from the c(2x2)-Pd surface alloy (lower curve). The upper curve is the corresponding spectrum measured by Wu *et al* [21].

oriented in exactly normal emission, however, the curves shown on figure 21 were obtained by averaging of symmetry equivalent beams thereby reducing the effect of any slight sample misalignments.

Figure 22 shows CO TPD spectra measured from clean Cu {100} and from the c(2x2)-Pd surface alloy. The TPD spectra measured from the clean Cu show a main desorption peak at ~173 K which saturates at θ_{CO}~0.5 ML. Lower coverages of CO lead to a symmetric desorption peak with a maximum at ~176 K. As the CO exposure increases the desorption peak maximum and the leading edge shift to lower temperatures indicating weak repulsive CO interactions in the overlayer. At θ_{CO}~0.5 ML the terrace sites on the Cu surface are saturated and a c(2x2) LEED pattern is observed. For higher coverages an additional sharp desorption peak is observed at ~140 K. This is associated with the formation of a compression structure that results in the splitting of the c(2x2) superstructure beams. At saturation, the intensity of this

peak is ~10% of the intensity of the main peak. The features at >200K are due to imperfect background subtraction (see experimental).

At low exposures the TPD spectra measured from the c(2x2)-Pd surface alloy contain a single desorption peak with a maximum at ~300K, which we assign to CO desorbing from regions of c(2x2)-Pd alloy. However, as the CO coverage is increased a second desorption state emerges at ~171 K. This corresponds well with the main desorption peak from clean Cu {100} and suggests the presence of domains of pure Cu on the alloy surface. These results are in good agreement with the TPD measurements of Pope *et al* [36]. Based on the integrated areas under the desorption peaks and the assumption that saturation θ_{CO} on the domains of Cu {100} and Cu {100}-c(2x2)-Pd are equal, then the pure Cu regions were estimated to comprise ~40% of the total surface area. As a consequence ~0.2-0.25 ML of Pd must be incorporated within deeper layers of the crystal. XPD provides a mechanism by which to probe the composition of the Pd atoms in the deeper layers of the selvedge. Pd atoms in the outermost layer have only a relatively minor contribution to the diffraction features at high kinetic energies.

The two high symmetry azimuthal directions ([001] & [1$\bar{1}$0]) of the {100} surface are indicated on figure 20. Polar XPD scans along these azimuths will result in two main

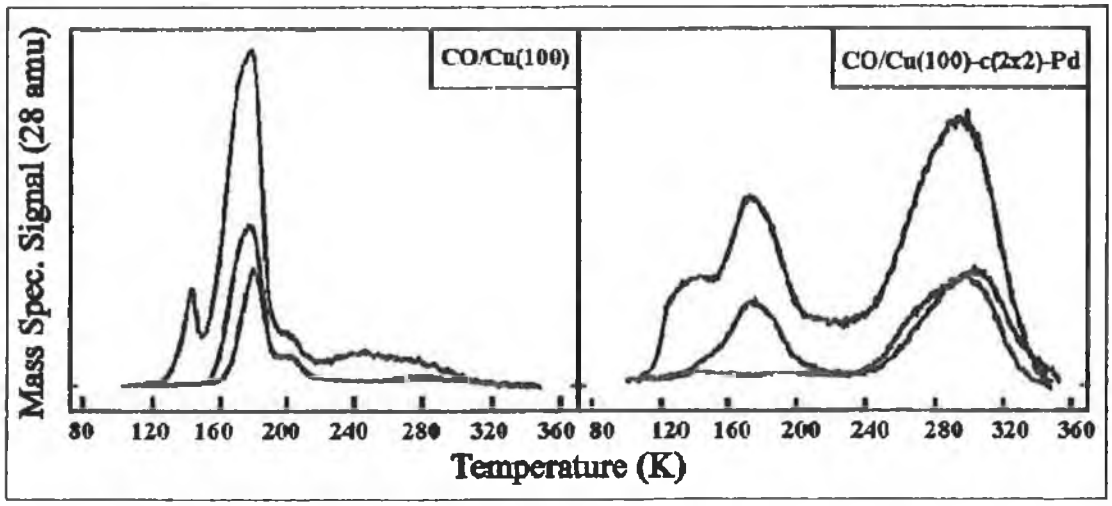

Figure 22: TPD spectra measured from Cu {100} (left-hand plot) for θ_{CO} of 0.12, 0.21 and 0.55 ML and from the c(2x2)-Pd surface alloy (right-hand plot) for θ_{CO} of 0.12, 0.16 and 0.50 ML.

forward focusing peaks, one at normal emission and one off-normal. The cross-section shown on figure 20 is for the [001] azimuth, where the off-normal peak is expected at ~45° for a bulk terminated structure. As can be seen, scattering by 1st layer atoms of electron emission from the 2nd layer can contribute to the 45° forward focusing peak but not to the 0° peak, which only originates due to electron emission from 3rd or deeper layers. Along the [1$\bar{1}$0] azimuth no forward focusing peaks arise due to emission from 2nd layer atoms. Clearly polar XPD scans, measured along the [001] azimuth of the surface alloy and utilising emission from a Pd core level, offer the possibility of distinguishing between Pd atoms in the 2nd layer of the selvedge and Pd atoms in deeper layers.

Figure 23 shows a polar XPD scan measured along the [001] azimuth of the surface alloy. The intensity of the emission from the Pd $3d_{5/2}$ core levels using Al K_α excitation (KE~1150 eV) was monitored as a function of emission angle. The experimental plot shown on figure 23 is an average of 3 independent measurements along the [001] azimuth. The most immediately obvious feature of the experimental plot is the strength of the forward focusing peak around 40°-45° and the relative weakness of the features at all other polar emission angles. This is direct evidence that the bulk of the sub-surface Pd atoms are localised in the 2nd layer of the selvedge. The broad feature between 10°-25° is due to higher-order diffraction peaks and contributions from out-of-plane scatterers. There is evidence of a small rise in intensity at normal emission which suggests that a small fraction of the Pd atoms may have entered the 3rd or deeper layers of the crystal. However, this feature is very weak and it could arise from the same processes that generated the feature around 10°-25°.

The theory curves shown on figure 23 correspond to SSCC's calculated for Pd 3d emission from a perfect c(2x2)-Pd layer located exclusively in the top, 2nd and 3rd layers respectively of a bulk Cu {100} cluster. All cluster lattice parameters were frozen at those of a bulk terminated Cu single crystal. As expected, emission from Pd in the top layer of the cluster at such a high outgoing kinetic energy (~1150 eV) results in an essentially featureless curve. If the c(2x2)-Pd is in the 2nd layer of the crystal then there is a strong forward focusing feature centred around ~45°. As the polar angle moves away from this peak the electron intensity goes through a series of

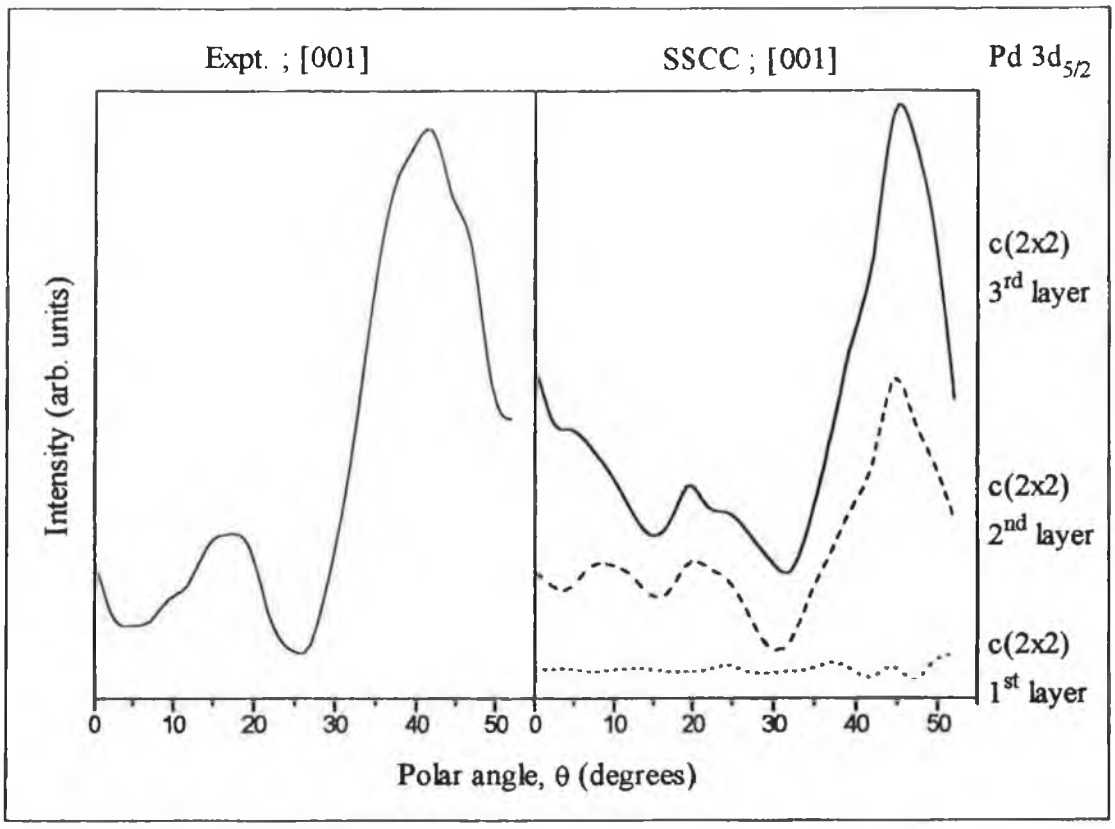

Figure 23: Polar XPD plot measured along the [001] azimuth of the Cu {100}-c(2x2)-Pd surface alloy using Pd 3d emission. Also shown are SSCC's for Pd emission from a perfect c(2x2)-Pd in the 1st, 2nd or 3rd layers only of a bulk Cu cluster.

minima and maxima corresponding to higher-order diffraction features. When the c(2x2)-Pd is in the 3rd layer of the cluster there is an increase in the intensity of the peak at 45° and the emergence of the normal emission forward focusing peak. The higher-order features, located at a polar angle of ~20°, are significantly weaker than both of the forward focusing peaks.

The maximum of the experimental forward focusing peak shown in figure 23 occur at ~41°-42°. This constitutes a significant shift of this feature from its expected position of ~45°. It should however be noted that, due to the large step size used while measuring the XPD scans, there is an uncertainty of ±1.5° in the peak position. Because of the absence of a significant normal emission peak on the experimental curve, it is reasonable to assume that the bulk of the intensity in the peak at 41°-42° arises due to emission from 2nd layer Pd. Hence, the shift in the peak position from the bulk termination position is a strong indicator of an expansion of the 1st-to-2nd layer

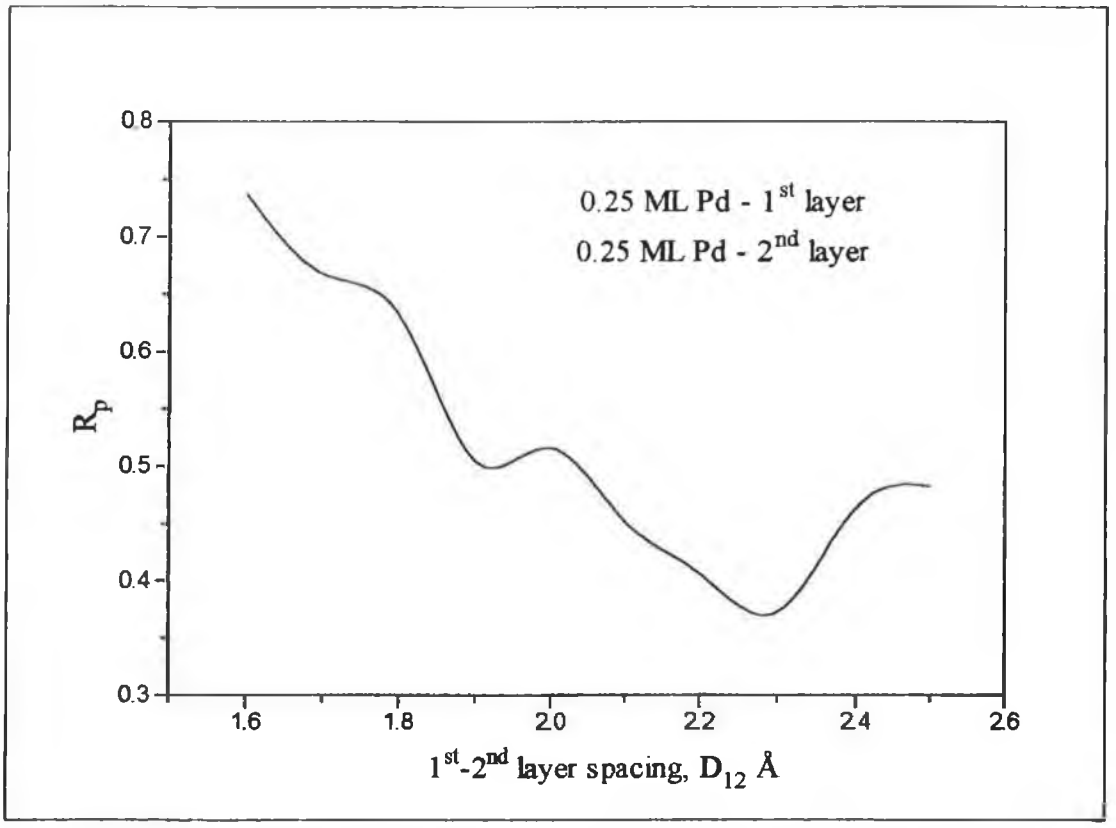

Figure 24: R-factor for comparison of experiment with SSCC's done for a range of values of D_{12} (see text for details of cluster).

spacing (D_{12}). In a study of the vibrational modes of the Cu {100}-c(2x2)-Pd surface, Hannon *et al* [37] reported that strong Cu-Pd bonding within a c(2x2)-Pd alloy layer results in a weakening of the bonding between the Cu atoms and adjacent layers. For a top layer c(2x2) alloy over a pure Cu 2nd layer, the bonding of the top layer Cu to the 2nd is found to be reduced by 5% relative to the clean surface. This making an expansion of the outermost layer spacing more probable for domains of c(2x2)-Pd in the outermost layer than for domains of pure Cu.

SSCC's were performed while varying D_{12} in an attempt to quantify the expansion in the outermost layer spacing. For the purposes of the SSCC's the surface alloy was assumed to contain exactly 0.5 ML of Pd. Of this, 0.25 ML was fixed in the outermost layer of the cluster and 0.25 ML was in the 2nd layers. In both layers the Pd was in an ordered c(2x2) structure. The Pd in the 2nd layer was covered by a layer of pure Cu. SSCC's were done for the range of D_{12} values between 1.6-2.5 Å in 0.1 Å steps. The level of agreement between theory and experiment was judged by Pendry R-factor analysis. The results are shown in figure 24, which shows a plot of the R-

factor values versus D_{12}. The R-factor minimum (R_p=0.37) occurs for values of D_{12}=2.3 Å, representing a large expansion from bulk Cu inter-layer spacing of ~1.8 Å.

Figure 25 shows a comparison of SSCC curves corresponding to different values of D_{12} with the experimental data. As expected the forward focusing peak shifts towards normal emission with increasing D_{12}. Comparing the SSCC's solely on the basis of the position of the forward focusing peak, as shown in figure 25, indicates a "best-fit" at a value for D_{12} of 2.1-2.2 Å. This corresponds to an expansion of 16-22% from the bulk Cu inter-layer spacing. On the basis of Vergard's law, applied solely to the selvedge, the expansion from the expected bulk value is 12-17%. The forward focusing peak on the SSCC curve corresponding to the R-factor analysis minimum (D_{12}=2.3 Å, bottom curve in figure 25) is clearly shifted to too low a polar angle. The reason that the R-factor minimum occurs at this point can be attributed to the level of agreement between the higher-order features of the SSCC and experimental curves. However, due to the complexity of the processes that contribute to these higher-order features,

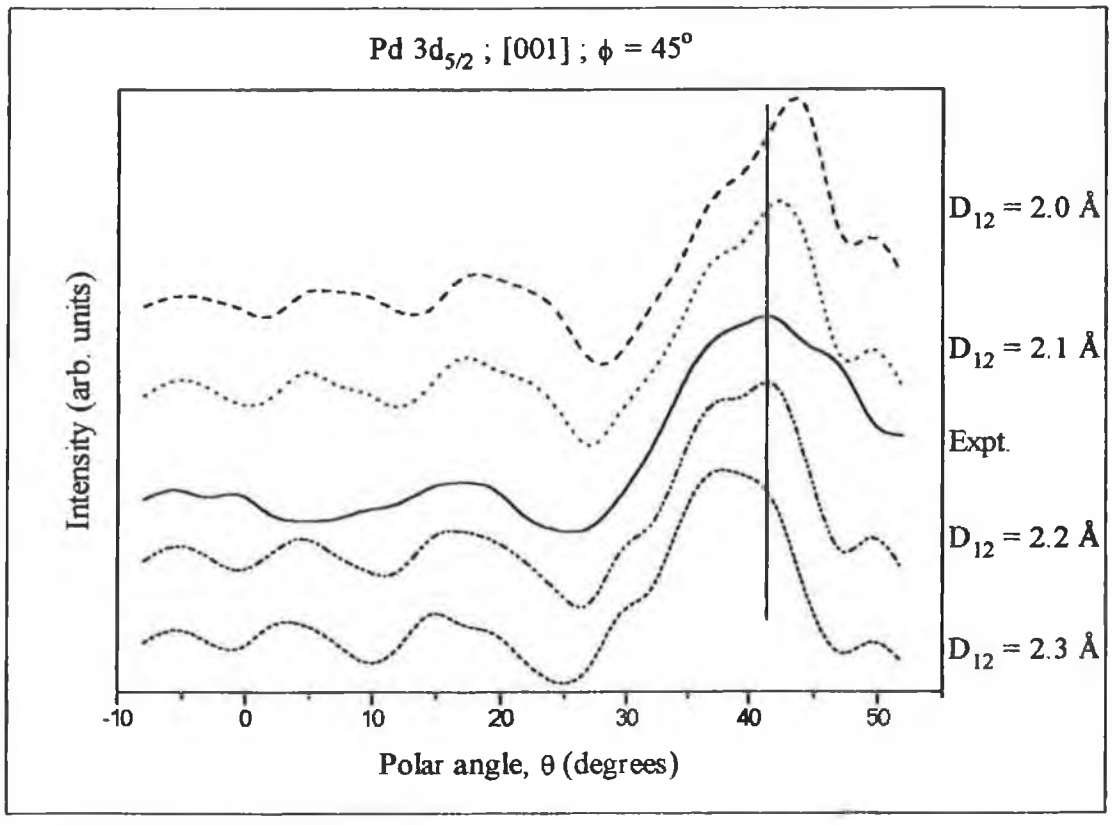

Figure 25: Comparison of experimental curve with SSCC's on the basis of the position of the forward focusing feature. The cluster consisted of 0.25 ML Pd in the 1st layer and 0.25 ML Pd in the 2nd layer.

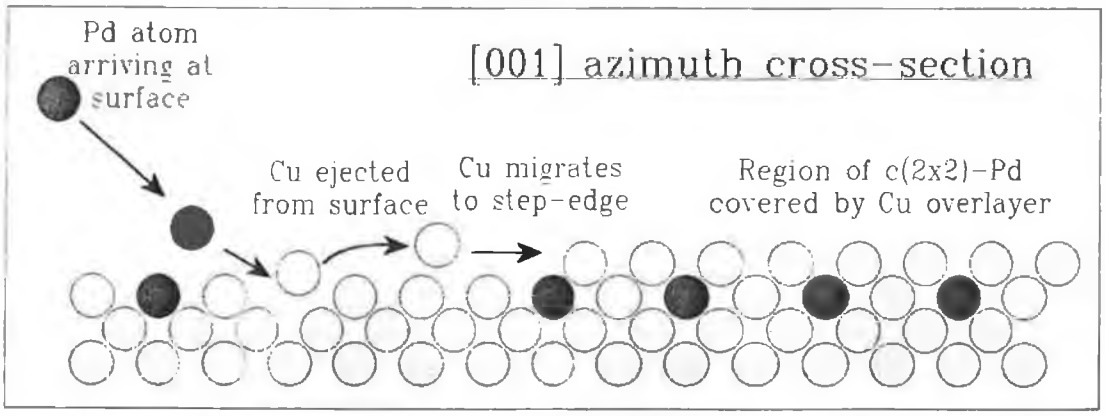

Figure 26: Schematic of a possible mechanism of generating 2nd layer Pd. Pd atoms arriving at the surface eject Cu atoms. These migrate to step-edges on the surface. The growth of the step-edge across the surface may cover regions of pre-formed c(2x2)-Pd.

they may be less accurately predicted than the forward focusing features because of the approximations employed in the SSCC's. For instance, as discussed in chapter 1, correct treatment of initial/final state effects and the precise nature of the scattering atoms is more important when calculating higher-order features than when calculating zero-order peaks. Hence, it is reasonable to assume that the expansion of the outer layer spacing may not be as large as predicted by the R-factor analysis.

One possible explanation for the existence of a significant quantity of 2nd layer Pd is that it is due to regions of 'top layer' c(2x2)-Pd being covered by Cu atoms which are ejected from the surface by Pd. The 'hot' Pd atoms arrive at the surface and replace Cu atoms. These Cu atoms may then diffuse across the surface to step edges and surface defects. This results in the creation of a new 'top layer'. As this layer grows it may cover regions of pure Cu and regions of c(2x2)-Pd, thereby resulting in '2nd layer' Pd. A simple schematic of this process is illustrated in figure 26. In addition, further Pd arriving at the surface may incorporate within the growing Cu top layer. The result is that some 2nd layer Pd may be covered either by a pure Cu overlayer or by a c(2x2)-Pd overlayer. Clearly this represents a very heterogeneous model for the c(2x2)-Pd surface alloy.

A molecular dynamics study of Pd atoms on a Cu {100} surface has been performed by Black and Tian [38]. This study revealed several mechanisms by which Pd atoms may exchange with Cu atoms in the 1st layer as shown in figure 26. In addition, some

evidence was found of Cu-Pd interactions keeping ejected Cu atoms associated with Pd atoms that was incorporated within the 1st layer of the crystal. Such interactions would provide a mechanism for the preferential covering of CuPd regions by Cu atoms. No evidence was found in the study of Pd atoms entering the 2nd layer of the Cu crystal. A theoretical study of the alloying of Pd with Cu {100} by Black [23] showed that displaced Cu atoms tend to form islands on the surface which is in-keeping with the model shown in figure 26.

The initial LEED investigations on the c(2x2)-Pd alloy surface [20, 21] reported the possibility of some Pd atoms existing subsurface or on-top of the alloy surface, but found no evidence that these atoms formed an ordered structure. This additional Pd was used to account for the discrepancy between the quoted θ_{Pd} of ~0.8 ML and the expected value of 0.5 ML for a perfect c(2x2) alloy. The high θ_{Pd} and the relatively broad range across which a good quality c(2x2) pattern is obtained [36] is more consistent with a c(2x2) structure in the top layer of the substrate that is partially covered by c(2x2) 'islands' (i.e. ordered domains in two rather than just one layer).

The size of the expansion indicated by figures 24 & 25 can be partially attributed to the difference in size between the Cu and Pd atoms. It may also be a reflection of the heterogeneity inherent in the model outlined above. Clearly, if the 2nd layer Pd atoms exist in two forms (i.e. covered by pure Cu and covered by c(2x2)-Pd), then it is conceivable that domains exist on the surface with different local values of D_{12}. As a result, the forward focusing peak observed experimentally would represent an average of several domains, rather than a single domain as modelled in the SSCC's. There is also the possibility that the Pd atoms in both the 1st and 2nd layers are 'rippled'. Rippling of the Pd sub-lattice for the c(2x2) alloy surface has been observed by STM [39] and from comparison of the surface vibrational frequencies with slab calculations employing the effective medium theory [37]. In the latter case, an outward expansion of the Pd atoms by 0.12 Å was reported. The broadness of the forward focusing peak on the experimental curve is suggestive of several domain structure (i.e. slightly different off-normal forward focusing directions) and also of some possible disorder within the surface structure.

4. DISCUSSION:

4.1. CuPd [85:15] {110}:

It is not possible on the basis solely of the polar XPD measurements presented in this chapter to make definitive statements regarding the exact structure of the bulk alloy selvedge. However, certain conclusions can be drawn and proposals made regarding the structure which are amenable to confirmation by independent techniques.

Clearly, the large shift in the off-normal forward focusing peak on the polar scans measured along the [001] azimuth of the alloy surface indicates a strong distortion of either the bulk crystal or the selvedge structure. The observed shift toward the normal emission direction is consistent with an inter-layer spacing expansion. A comparable level of agreement can be obtained for comparison of the experimental XPD curves with SSCC's done for a bulk cluster inter-layer expansion and with SSCC's done for an expansion limited to the two outermost layers of the cluster. For the bulk expansion of the cluster inter-layer spacing the R-factor minimum occurred at D_z~1.4 Å, which represents an expansion of ~0.1 Å (8%) from the expected bulk value based on Vergard's law. In the case of the selvedge expansion, the minimum was found at a much larger expansion of the inter-layer spacing. The analysis minimised at D_{13}~3.2 Å (23% expansion), with the 2nd layer Pd being equidistant between the 1st and 3rd layers (D_{1Pd}=D_{Pd3}=1.6 Å). There was evidence of a rippling of the 2nd layer Cu below the centre of gravity of the Pd atoms by ~0.2 Å.

The difference in the expansion found for the bulk inter-layer change versus that found for the selvedge-localised inter-layer change can be attributed to the XPD features originating from the 'bulk' of the cluster in the SSCC's. For a bulk expansion the forward focusing peaks due to emission from all layers vary in a similar fashion with the inter-layer spacing. However, when the spacing change is restricted to the selvedge the XPD features calculated from the bulk remain 'constant'. As a result they skew the off-normal forward focusing peaks toward the bulk position and the expansion in the selvedge must be significantly greater in order to achieve the same

net shift in peaks as observed for a bulk cluster expansion. The reason for the large 'interference' due to bulk emission in the SSCC's is due to the lack of defocusing in the theory. This can be partially overcome by artificially limiting the cluster thickness, although this is not ideal.

Of the 2 expansion models tested, the selvedge localised expansion is the one that intuitively seems more plausible. There is a clear physical phenomenon (the Pd enrichment of the 2nd layer) to which such an expansion may be attributed. The large size differential (~8%) between Cu and Pd makes an expansion of D_{13} seem probable. However, a number of problems arise with regard to the determination of a net expansion, either bulk or selvedge localised, in the CuPd alloy. The first is that a previous quantitative LEED study on the alloy surface found no evidence of an expansion of the selvedge layer spacings [11]. In fact, a small contraction was reported. Further evidence to support the LEED conclusions is derived from first principle total energy calculations of the surface relaxation of the alloy [40]. These also found no evidence of an expansion at the alloy surface. Some indication of a small rippling within the 2nd layer Pd was found.

Further reason to doubt the existence of an expansion arises from the XPD curves themselves. By its very nature, an expansion of the inter-layer spacing (either bulk or surface localised) acts equally in all azimuthal directions of the surface. Hence, a forward focusing peak shift observed along any given azimuthal direction of the surface should be observed to essentially the same degree along all other azimuths. Slight changes in the amount of the shift along the various azimuths due to differences in the polar angle position of the off-normal forward focusing features are essentially unobservable experimentally. This is clearly not the case for the experimental plots shown in figures 6 & 7. There is a large shift along the [001] azimuth (~4-5°), a significantly smaller shift along the $[1\bar{1}0]$ azimuth (~2.5°) and no apparent shift along the $[1\bar{1}2]$ azimuth. The lack of a peak shift along the $[1\bar{1}2]$ azimuth for emission from Pd could be attributed to the high concentration of Pd in the 2nd layer, if the 1st-to-2nd layer spacing is not expanded. However, this does not explain the lack of a shift in the Cu emission forward focusing peak along this azimuth, given that a shift is seen for

Cu emission along the [001] azimuth. Using the expansion models, the SSCC's do show equivalent shifts of the off-normal forward focusing peaks on the polar scans calculated along the 3 high symmetry surface azimuths for a given lattice expansion.

The XPD curves can be better explained in terms of a bct distortion of the bulk CuPd alloy as proposed in the results section. Such a distortion would result in a contraction of the in-plane lattice parameter along the [001] azimuth coupled with an expansion of the inter-layer spacing (both effects leading to a large shift in the off-normal forward focusing peak along the [001] azimuth). The bct distortion would also result in an expansion of the in-plane lattice parameter along the $[1\bar{1}0]$ azimuth. The net effect should leave the off-normal forward focusing peak along this azimuth effectively unchanged, while a small shift should be observed in the off-normal peak along the $[11\bar{2}]$ azimuth. Clearly, this model does not fit the experimental data ideally. Contrary to what would be expected, on the basis of a purely geometric consideration of the bct structure, a small shift is observed along the $[1\bar{1}0]$ azimuth, while no shift is apparent along the $[11\bar{2}]$ azimuth. However, since the model does predict different shifts along various surface azimuths, it is in better agreement with the experimental results than a simple expansion model. The LEED pattern from a bct lattice would appear fcc-like and, unless quantitative measurements were performed to ensure the ratio of the in-plane lattice parameters was correct, a bct distortion could be missed.

Studies on the ordering reaction of poly-crystalline CuPd alloys with ~20 *at.*% Pd have reported the existence of an ordered tetragonal structure [41, 42]. If the ordered structure is considered in terms of a fcc cell (c=a), the axial ratio was reported at c/a=0.986 [41] and c/a=0.994 [42]. These values represent a relatively small tetragonal distortion. The results of the SSCC's analysis indicate that a bct structure is possible. The level of agreement for the 'best-fit' SSCC's is comparable with that obtained for both of the expansion models. The R-factor analysis yielded a broad minimum region for in-plane lattice parameters along the [001] azimuth of 3.3-3.6 Å. The absolute minimum occurred at an in-plane lattice parameter along the [001] azimuth of ~3.4 Å (7% contraction), with an inter-layer spacing of ~1.34 Å (3.5%

expansion). The axial ratio determined based on these values is c/a=0.9±0.04, which is substantially larger that any distortion that has been reported for CuPd bulk alloys.

The R-factor analysis of the three models tested favours the bct model slightly. The overall averages of the R-factor minima obtained for comparison of experiment with theory were 0.198 (bct), 0.216 (bulk D_z expansion) and 0.220 (D_{12} expansion). It should be noted that the bct model was bulk terminated (i.e. no surface relaxations/deformities were included). Hence, it is conceivable that the inclusion of such effects might result in an improved fit between experiment and theory. One limitation of high-energy scanned-angle XPD, which is highlighted by the bulk alloy models tested, is its relative inability to distinguishing between structural models that produce similar diffraction patterns. It can identify gross structural changes, such as fcc {111}→hcp {0001} transformations, but more subtle changes, such as the expansion versus bct models, are not as easily distinguished. For any give structural model, the geometric parameters can be optimised to fit the experimental data on the basis of R-factor analysis. However, when different models yield similar levels of agreement it is necessary to rely on additional techniques to conclusively identify the correct structure. On the other hand, the fact that structural changes can be observed directly on polar XPD curves is one of the technique's major strengths. The large shift of the off-normal forward focusing peak along the [001] azimuth, coupled with non-uniform shift along the different surface azimuths was readily observable by XPD. Such an effect may be missed by less direct techniques such as LEED. Because the forward focusing peaks are a direct indicator of the selvedge structure, they are ideally suited to identifying unexpected structural changes.

4.2. Cu {100}-c(2x2)-Pd:

Although Pd polar XPD scans were only measured along a single azimuth of the c(2x2)-Pd surface alloy these, in conjunction with TPD, clearly illustrates that the structure is not the homogenous two-dimensional alloy that was initially suggested [19-21]. The TPD demonstrates that ~40% of the surface layer is pure Cu. The polar XPD curve shows that the bulk of the sub-surface Pd is in the 2nd layer. This can be explained in termed of Cu atoms, which are ejected from the surface, covering

domains of Cu/Pd as shown in figure 26. The conclusion that appreciable amounts of pure Cu are present at the alloy surface is supported by a recent STM study [39].

The alloy surface is probably kinetically frozen rather than at its thermodynamic equilibrium structure. The main factors which determine surface segregation in dilute transition metal alloys are the difference in the pure metal surface free energies and the elastic size mismatch energy [43]. The surface free energies of Cu and Pd have been calculated, from their internal free enthalpies of atomisation, as 1.934 and 2.043 Jm^{-2} respectively [44]. Although not a huge difference, these values favour incorporation of Pd within a Cu crystal. The heat of solution of Pd in Cu is negative (-43 $KJmol^{-1}$ [43]), also favouring adatom incorporation. Finally larger atoms incorporated within a surface layer will have a positive elastic size mismatch energy (which hinders surface segregation) since it is energetically unfavourable to expand the metal-vacuum surface [43]. In addition, factors such as surface stress and surface elasticity usually favour incorporation of atoms larger than the substrate atoms [45]. Various theoretical studies on surface segregation in dilute transition metal alloys find that Pd should not segregate to the surface [46-48]. Clearly there should be a thermodynamic driving force for the incorporation of Pd within the crystal bulk. The reason that this does not occur must be ascribed to the slow kinetics of the atom exchange process at room temperature. Hence, although it is thermodynamically more favourable, the most likely source of 2^{nd} layer Pd is due to coverage by displaced Cu rather that through direct atomic exchange.

While the structural analysis is not conclusive, there is evidence for an expansion of the outermost layer spacing in the Cu {100}-c(2x2)-Pd surface alloy. This expansion can be attributed in part to the larger size of the Pd atoms. Furthermore, it is likely that the Pd is rippled within the c(2x2)-Pd structure, which would also contribute to a D_{12} expansion. The broadness of the forward focusing peak indicates that there may be some degree of disorder in the overlayer structure. This may be due to regions of 2^{nd} layer c(2x2)-Pd being covered by pure Cu while other regions are covered by top layer c(2x2)-Pd. The result would be domains with different local D_{12} values, causing a broadening of the forward focusing peak and a shifting of the peak maximum.

5. CONCLUSIONS:

Given the results of the previous LEED-I(V) study, the first principle total energy calculations and the inconsistencies between the polar XPD scans taken along the various azimuths of the CuPd [85:15] {110} alloy, it is reasonable to discount an expansion model as an explanation for the observed peak shift. The bct model is a better qualitative fit to the observed peak shifts in the polar XPD data, although it is not perfect. In addition, the R-factor analysis find that the bct model is quantitatively a better fit, although the difference between the various models is minor. A large bct distortion (c/a=0.9) is required to explain the observed forward focusing peak shifts. However, at present there is no plausible explanation or independent experimental evidence to support such a large distortion in a bulk crystal. The tetragonal structures found in poly-crystalline CuPd alloys represent only a comparatively minor distortion of the normal fcc structure. The true bulk lattice parameters of the CuPd [85:15] bulk alloy should be re-determined by an X-ray diffraction study. This is a routine measurement. The reason that it was not performed prior to the XPD analysis was because of the, seemingly reasonable, assumption that the alloy crystal would retain an fcc structure. The motivation to test a bct model against the measured XPD scans arose from the need to reconcile the different shifts in the off-normal forward focusing peaks along the different surface azimuths. This highlights the direct nature of scanned-angle XPD, where the correctness of certain fundamental structural assumptions (e.g. the existence of a fcc lattice structure) may be determined merely from a cursory inspection of the measured spectra.

In the event that the bct model is proven incorrect, then the possibility arises that the shifts in the XPD curves observed are due to heterogeneity in the p(2x1) structure. The LEED study may have been swayed by regions of pure Cu in a mixed domain selvedge structure. LEED has the inherent disadvantage that it is species insensitive and scattering occurs from all ordered domains in the surface being probed. XPD, on the other hand, is species sensitive and may, in the case of Pd emission, be probing only a single domains in the selvedge that contains Pd atoms (or preferentially probing Pd rich domains). At the time of writing no other realistic models for the selvedge of

the bulk alloy were readily apparent. The accuracy of the XPD analysis may be limited by the possibility that there are a number of Pd sites with different local order and hence a different contribution to the overall diffraction curve. Heterogeneity within a surface structure remains a problem for most surface science techniques, including XPD.

The analysis of the Cu {100}-c(2x2)-Pd surface alloy clearly shows that the structure 'as formed' is quite heterogeneous and is not a single-phase 2-D surface alloy. The possibility of increasing the order and two-dimensional nature of the alloy layer by such approaches as gentle heating was not examined. A nearly pure Cu outer layer can be formed by heating the Cu/Pd surface alloy to ~420 K [49, 50]. This surface still exhibited a good c(2x2) LEED pattern [49], which was attributed to an ordered Pd-containing subsurface layer. The existence of an ordered c(2x2) structure was proposed to provide some stabilisation against incorporation of Pd within the crystal bulk. It is likely that this subsurface ordered layer is in the 2nd layer of the crystal and that it is already partially formed by room temperature deposition as demonstrated by the XPD results.

There is evidence of an expansion of the outermost layer spacing in the c(2x2) alloy structure. This can be attributed to the large size of the Pd atom and also to a weakening of the bond strength between surface Cu and the bulk due to strong Cu-Pd interactions in the c(2x2) layer [37]. An EXAFS study by Weightman *et al* [51] found that there is a local lattice expansion around Pd atoms in CuPd alloys that are dilute in Pd. This indicates that an expansion of the outer layer may occur in the c(2x2)-Pd surface alloy and also possibly in the CuPd [85:15] bulk alloy. In any event, the high Pd concentrations in the selvedge of these alloys is likely to result in lattice distortions both in-plane and inter-layer.

6. REFERENCES:

[1] D.W. Goodman in: Characterization and Catalyst Development, Eds. S.A. Bradley, M.J. Gattuso and R.J. Bertolacini, American Chemical Society, Washington, DC, (1989) pp. 191-202.

[2] J.H. Sinfelt, J.L. Carter and D.J.C. Yates, J. Catal., 24 (1972) 283.

[3] C.R. Helms, J. Catal., 36 (1975) 114.

[4] C.T. Campbell, Annu. Rev. Phys. Chem., 41 (1990) 775.

[5] U. Bardi, Rep. Prog. Phys., 57 (1994) 939.

[6] P.A. Dowben and A. Miller, Surface Segregation Phenomena, CRC Press, Boca Raton,Florida, (1990).

[7] M. Hansen and K. Anderko, Constitution of Binary Alloys, Schenectady, New York, (1985).

[8] J.H. Sinfelt and J.A. Cusumano in: Advanced Materials in Catalysis, Eds. J.J. Burton and R.L. Garten, Academic Press, London, (1977) pp. 1-31.

[9] M. Valden, J. Aaltonen, M. Pessa, M. Gleeson and C.J. Barnes, Chem. Phys. Lett., 228 (1994) 519.

[10] D.J. Holmes, D.A. King and C.J. Barnes, Surf. Sci., 227 (1990) 179.

[11] M. Lindroos, C.J. Barnes, M. Bowker and D.A. King, Springer Series Surf. Sci., 24 (1991) 287.

[12] R.H. Bergmans, M.van de Grift, A.W. Denier van der Gon, R.G.van Welzenis, H.H. Brongersma, S.M. Francis and M. Bowker, Nucl. Instr. and Meth. in Phys. Res. B, 85 (1994) 435.

[13] Y. Gauthier and R. Baudoing in: Surface Segregation Phenomena, Eds. P.A. Dowben and A. Miller, CRC press, Boca Raton, Florida, (1990) pp. 169-206.

[14] M.A. Newton, S.M. Francis, Y. Li, D. Law and M. Bowker, Surf. Sci., 259 (1991) 45.

[15] M.A. Newton, S.M. Francis and M. Bowker, Surf. Sci., 259 (1991) 56.

[16] M.A. Newton, S.M. Francis and M. Bowker, Phys. Rev. B, 45 (1992) 9451.

[17] M.A. Newton, S.M. Francis and M. Bowker, Surf. Sci., 269/270 (1992) 41.

[18] M. Bowker, M.A. Newton, S.M. Francis, M. Gleeson and C.J. Barnes, Surf. Rev. Lett., 1 (1994) 569.

[19] G.W. Graham, Surf. Sci., 171 (1986) L432.

[20] S.H. Lu, Z.Q. Wang, S.C. Wu, C.K.C. Lok, J. Quinn, Y.S. Li, D. Tian, F. Jona and P.M. Marcus, Phys. Rev. B, 37 (1988) 4296.

[21] S.C. Wu, S.H. Lu, Z.Q. Wang, C.K.C. Lok, J. Quinn, Y.S. Li, D. Tian, F. Jona and P.M. Marcus, Phys. Rev. B, 38 (1988) 5363.

[22] T.D. Pope, G.W. Anderson, K. Griffiths, P.R. Norton and G.W. Graham, Phys. Rev. B, 44 (1991) 11518.

[23] J.E. Black, Phys. Rev. B, 46 (1992) 4292.

[24] J. Kudrnovsky, S.K. Bose and V. Drchal, Phys. Rev. Lett., 69 (1992) 308.

[25] M. Valden, Licentiate Thesis, Tampere University of Technology, Tampere, (1993).

[26] F. Herman and S. Skillman, Atomic Structure Calculations, Englewood Cliffs, N.J. Prentice Hall Inc., New York, (1963).

[27] D. Briggs and M.P. Seah, Practical Surface Analysis, John Wiley & Sons, New York, (1990).

[28] J.M. MacLaren, J.B. Pendry, P.J. Rous, D.K. Saldin, G.A. Somorjai, M.A. van Hove and D.D. Vvedensky, Surface Crystallographic Information Service: A Handbook of Surface Structures, D. Reidel publishing company, Dordrecht, Holland, (1987).

[29] H.L. Davis and J.R. Noonan, Surf. Sci., 126 (1983) 245.

[30] D.L. Adams, H.B. Nielsen and J.N. Andersen, Surf. Sci., 128 (1983) 294.

[31] I. Stensgaard, R. Feidenhans'l and J.E. Sorensen, Surf. Sci., 128 (1983) 281.

[32] S.A. Chambers, H.W. Chen, I.M. Vitomirov, S.B. Anderson and J.H. Weaver, Phys. Rev. B, 33 (1986) 8810.

[33] J.B. Pendry, J. Phys. C: Solid State Phys., 13 (1980) 937.

[34] S.Y. Tong, H.C. Poon and D.R. Snider, Phys. Rev. B, 32 (1985) 2096.

[35] M.-L. Xu, J.J. Barton and M.A. van Hove, Phys. Rev. B, 39 (1989) 8275.

[36] T.D. Pope, K. Griffiths and P.R. Norton, Surf. Sci., 306 (1994) 294.

[37] J.B. Hannon, H. Ibach and P. Stoltze, Surf. Sci., 355 (1996) 63.

[38] J.E. Black and Z.-J. Tian, Comments Cond. Mat. Phys., 16 (1993) 281.

[39] P.W. Murray, I. Stensgaard, E. Laegsgaard and F. Besenbacher, Phys. Rev. B, to be published, (1996).

[40] P. Hu, Private Communication, (1996).

[41] F.W. Jones and C. Sykes, J. Inst. Metals, 65 (1939) 419.

[42] A.H. Geisler and J.B. Newkirk, Trans. AIME, 200 (1954) 1076.

[43] A.R. Miedema, Z. Metallkde., 69 (1978) 455.

[44] L.Z. Mezey and J. Giber, Jap. J. Appl. Phys., 21 (1982) 1569.

[45] M. Schmid, W. Hofer, P. Varga, P. Stoltze, K.W. Jacobsen and J.K. Norskov, Phys. Rev. B, 51 (1995) 10937.

[46] A.R. Miedema and J.W.F. Dorleijn, Surf. Sci., 95 (1980) 447.

[47] J.R. Chelikowsky, Surf. Sci., 139 (1984) L197.

[48] P.M. Ossi, Surf. Sci., 201 (1988) L519.

[49] G.W. Graham, P.J. Schmitz and P.A. Thiel, Phys. Rev. B, 41 (1990) 3353.

[50] A.R. Koymen, K.H. Lee, G. Yang, K.O. Jensen and A.H. Weiss, Phys. Rev. B, 48 (1993) 2020.

[51] P. Weightman, H. Wright, S.D. Waddington, D. van der Marel, G.A. Sawatzky, G.P. Diakun and D. Norman, Phys. Rev. B, 36 (1987) 9098.

Chapter VII

Conclusions.

This thesis has dealt with the application of scanned-angle XPD to quantitatively examine a range of surface structural problems, including strain-induced stabilisation of novel crystal structures in metal-on-metal systems (Chapters III & IV), the determination of the structure of catalytically relevant co-adsorption systems illustrated by a 2-D co-adsorption phase (Chapter V) and the structure of clean CuPd alloys (Chapter VI). The work serves to highlight the particular strengths, as well as some of the limitations, of this technique at its current stage of development.

In Chapters III & IV, scanned-angle XPD (both polar and azimuth) was used to study the growth of strained thin films, using a laboratory based X-ray source. In this mode (the high kinetic energy forward focusing regime), the technique proved an excellent probe of the thin film growth mechanism. In conjunction with As-*t* plots, low energy ion scattering and LEED, XPD allows the three growth modes, Frank-van der Merwe (FM), Stranski-Krastanov (SK) and Volmer-Weber (VW), to be easily differentiated. With proper coverage calibration, XPD on its own can differentiate FM/SK/VW merely on the basis of the point of emergence of the forward focusing features. Used in conjunction with As-*t* plots, very subtle deviation from perfect FM growth mode can be detected (c.f. Chapter IV). XPD is shown to be a more reliable method of determining thin film growth modes than the more traditional method of construction of Auger-time plots. XPD is also an excellent, direct probe of thin film structure, i.e. whether the stacking pattern is bcc, hcp or fcc. Subtle distortions of the lattice structure of metal overlayers can be readily detected, and the relaxation of the metal overlayers as a function of coverage can be monitored. One of XPD's greatest strengths is its ability to give direct evidence of profound structural changes in metal overlayers, which are imposed due to interfacial strain (e.g. the stabilisation of bct Co grown on Pd {100} - Chapter III). One criticism that may be levelled against indirect techniques, such as LEED, is that the structure determined may be limited by the imagination of the investigator, (i.e. novel structural changes may be missed merely because they remained unconsidered). The directness of the forward focusing phenomenon in scanned-angle XPD helps to eliminate this problem.

There is a valid argument to be made for the routine application of scanned-angle XPD to the study of metal-on-metal overlayers. Even in the absence of cluster

modelling, general structural information can be obtained with relatively little effort. From a quantitative point of view, the fact that single scattering cluster calculations are well suited to modelling the high energy XPD process serves to enhance the appeal of the technique. However, the structural accuracy which is realistically achievable from a laboratory-based systems is ±0.1 Å. Hence, the technique cannot rival the accuracy of quantitative LEED at present.

The use of XPD in forward focusing mode has, over the past few years, become an established technique in the armoury of the surface science community. A newer and still very much a probationary technique is low-energy scanned-angle XPD, which was applied to the study of (K+CO) co-adsorbed on Co $\{10\bar{1}0\}$ (Chapter V). At first glance, this technique may appear as merely a poor relation of scanned-energy XPD, which has been successfully utilised to study a number of adsorbate systems with an accuracy approaching that of full LEED-I(V) analysis. However, except in specific cases, scanned-energy XPD has difficulty studying systems containing multiple atomic species. The problem stems from Auger peaks (fixed KE) being swept through or over the XPS peak whose intensity is being monitored during data collection. Regions in which the kinetic energy of the emitted XPS electrons coincides with an Auger emission must be discarded from the data-set. As a system's chemical complexity increases, so does the number of Auger peaks with the result that scanned-energy measurements are not viable for a large range of chemically interesting systems. Because scanned-angle measurements are made at fixed energies, this problem is circumvented.

The results of the low-energy XPD study of the c(2x2)-(K+CO) system were encouraging. The geometric structure determined was in good agreement with the results of a full quantitative LEED study. The fact that the structural analysis was done using single scattering modelling makes the technique even more attractive. The prospect of obtaining detailed structural information from a straight forward set of measurements, and by utilising a comparatively rapid modelling system, is clearly appealing. However, low-energy scanned-angle XPD needs further study before definitive statements can be made about its accuracy and suitability for full structural

determination. A further, larger data-set should be collected from the K/CO system, utilising a broader range of photon energies and several different azimuthal scan directions. This would allow a much more detailed judgement on the accuracy and usefulness of this technique. Given the wealth of alternative useful measurements that can only be performed using synchrotron radiation, low-energy scanned-angle XPD is likely to receive limited attention until it becomes better established.

The application of scanned-angle XPD to surface and bulk alloys (c.f. Chapter VI) has much in common with the study of metal overlayers. In the case of surface alloys, polar XPD is a useful probe of the selvedge composition, particularly when the minority component of the alloy undergoes concentration within the selvedge of the crystal. In conjunction with CO TPD measurements, a single polar XPD scan has been shown to conclusively demonstrate that a "surface alloy" formed by deposition of ~0.5 ML of Pd on Cu {100} is not a "homogeneous" c(2x2) top layer structure as modelled in a previous LEED-I(V) analysis. The data clearly indicates that ~50% of the deposited Pd is localised in the crystal 2nd layer. In the case of a CuPd [85:15] {110} bulk alloy, polar XPD shows evidence of an unusual surface crystal phase both from direct observation and from quantitative forward scattering modelling. Again, this highlights the fact that when using traditional indirect techniques, such as LEED, "unexpected" structures may remain undetected simply because the authors have not considered these structures as a viable possibility. Polar XPD allows rapid and partially (via study of zero-order forward focusing features) "real space" visualisation of the surface structure by simple triangulation.

The range of systems studied, and the ease with which data analysis was performed, clearly demonstrates the versatility of scanned-angle XPD. In so far as laboratory based scanned-angle XPD at medium outgoing kinetic energies (>400 eV) is concerned, the technique appears to have reached maturity. Cluster modelling theory is well developed, hence the accuracy of a structural determination is now largely governed by the quality of the experimental measurements. From the point of view of future development, utilisation of synchrotron radiation in scanned-angle XPD experiments is likely to increase. As mentioned earlier, scanned-energy experiments are quite well established, although utilised by only a small number of established

practitioners. Low-energy scanned-angle XPD, where the atomic scattering factor becomes more isotropic (hence sensitive to the 3-D structure), is likely to develop into a useful tool for studying complex systems that are not amenable to scanned-energy measurements. This is particularly true if, as indicated by the study of the co-adsorption system, single scattering is an adequate approximation of diffraction process even at low outgoing kinetic energies. A second option made available by synchrotron radiation is to utilise very high energy photons, thus increasing the kinetic energy of the emitted electrons. This makes the forward focusing process even more dominant and reduces the width of forward scattering peaks. This would increase the accuracy with which inter-atomic bond directions can be determined, and may make subtle structural changes more apparent.

Recently, the technique of photo-electron holography has provided a means of obtaining a real-space image of the local structure around an emitting atom via phased Fourier transformation of full hemispherical XPD patterns. Photo-electron holography is closely related to the studies performed here, differing only in the details of data analysis (and that a smaller experimental data-set is used in non-holographic applications). Only time will tell which of the approaches will serve scientists best in surface structural studies.

"..... be not sad my friends,
for there are no beginnings without ends,
and though life is short and love is fleeting
both are challenges worth meeting.
There are struggles to be fought,
sins to be forgiven
and a fragile sense to form
from the little we are given."

Igor Goldkind, *The Clown.*